Study of two-dimensional nanostructured materials for electrochemical energy storage applications

Maciej Tobis

Doctoral Dissertation

Scientific Supervisor:

Professor Elżbieta Frąckowiak

Institute of Chemistry and Technical Electrochemistry
Poznan University of Technology
Poland, 2024

The author would like to acknowledge **National Science Centre** in Poland for financial support within the **OPUS** project no. 2018/31/B/ST4/01852 "*Study of electrode/electrolyte interface of high stability and quick charge response*" and within the **Preludium** project no. 2021/41/N/ST5/01364 "*Influence of redox pairs on hydrogen evolution overpotential of dichalcogenides*".

The author would like to acknowledge **Polish National Agency for Academic Exchange (NAWA)** under **STER programme,** Towards Internationalisation of Poznan University of Technology Doctoral School (2022-2024) for funding the scientific internship at Karlsruhe Institute of Technology (KIT), Helmholtz Institute Ulm (HIU) in Ulm, Germany for realisation of the research project "*Investigation of energy storage mechanism of transition metal dichalcogenides (TMDs) with designed interlayer spacing*".

Acknowledgements

This PhD thesis could not have been realized without the presence of some important people in my life, to whom I would like to dedicate a part of this thesis.

I would like to sincerely thank Professor Elżbieta Frąckowiak for all the care and her unwavering scientific support she has shown to me throughout my PhD studies.

I would like to acknowledge Professor Francois Beguin for his scientific help.

I am thankful to Professor Krzysztof Fic for his scientific and non-scientific discussions, for his advices and kind help.

I would like to acknowledge all the current and past members of the PowerSourcesGroup. Special thanks go to Adam M., Jakub, Paweł, Justyna, Anetta, Paulina, Adam Ś., Sylwia, Bartosz G., Bartosz N., Masoud, Amelia and Przemek for their significant help in the realization of this PhD dissertation.
- Thank you guys!

I would like to also acknowledge Adam Maćkowiak, my office mate and a friend for his presence and help during the daily life.
- May the ŁekuPoweł be with us!

I would like to also mention my dearest family which supported me throughout my PhD studies time. Sincere gratitude goes to my father Przemysław, mother Bernadeta, my brother Wojciech and his lovely family (Asia, Antek and Stefek).

My appreciation also goes to the dearest people around me: Daria, Reyhan, Mateusz, Emilia, and Michał. I would like to also acknowledge my friend Dawid, whose memory will always stay with me.

Table of contents

Acknowledgements 4

Table of contents 5

List of recurring abbreviations 7

Abstract 8

Streszczenie 10

Motivation and context of the research 12

Chapter I Literature review 15

Electrochemical capacitors (ECs) 16

1 Principle of ECs operation 16

2 Electrical double-layer models 19

3 Emergence of pseudocapacitance in electrode materials 22

4 Electrolytic solutions for ECs 32

5 Electrode materials for ECs 36

5.1 Carbonaceous materials 36

5.2 Two dimensional transition metal dichalcogenides (TMDs) . 39

Chapter II Dissertation outline 47

Aim of the dissertation 48

Dissertation structure 49

Chapter III Evaluation of the electrochemical properties of 2D materials 50

P1. *Electrochemical Capacitor Performance of Nanotextured Carbon/Transition Metal Dichalcogenides Composites* 51

P2. *Supercapacitors with Carbon/MoS_2 Composites* 65

P3. *Electrochemical Capacitor Based on Reduced Graphene Oxide/NiS_2 Composite* 79

Chapter IV Covalent modification of 2D material by redox-active species 82

P4. *Nanostructured MoS_2 grafted by anthraquinone for energy storage* 95

Chapter V Emergence of pseudocapacitive properties of 2D materials 112

5. *Controlling structure and morphology of MoS_2 via sulfur precursor for optimized pseudocapacitive lithium intercalation hosts* 113

Chapter VI Concluding remarks 141

General summary 142

Scientific track records 144

References 149

Co-authorship statements 161

Copyrights 177

List of recurring abbreviations

2D – Two-dimensional

AC – Activated carbon

AQ – Anthraquinone

CB – Carbon black

C – Capacitance [F]

GCPL – Galvanostatic cycling with potential limitation

CV – Cyclic voltammogram

CNTs or NTs – Carbon nanotubes

ECs – Electrochemical capacitor

EDL – Electrical double-layer

EIS – Electrochemical impedance spectroscopy

n-BuLi – n-buthyllithium

OER – Oxygen evolution reaction

HER – Hydrogen evolution reaction

rGO – reduced graphene oxide

SSA – Specific surface area [$m^2\ g^{-1}$]

SEM – Scanning electron microscopy

TEM – Transmission electron microscopy

TMDs – Transition metal dichalcogenides

TAA – Thioacetamide

TU – Thiourea

LC – L-cysteine

XPS – X-ray photoelectron spectroscopy

XRD – X-ray diffraction

Abstract

Due to the intermittent nature of renewable energy sources, the development of energy storage devices is paramount for the successful transition towards sustainable future. Electrochemical capacitors (ECs) offer several advantages over standard lithium-ion batteries (LiBs), including exponential longevity and power density, but they suffer from moderate energy density. This PhD dissertation addresses the main issue of ECs, i.e., low energy density, by utilizing novel two-dimensional (2D) electrode materials characterized by high capacitance.

The first part of the dissertation (Chapter I) focuses on a theoretical introduction to the current *state-of-the-art* in ECs. It will provide an in-depth explanation of their fundamental charge storage mechanisms, including the formation of electrical double-layer (EDL) at the electrode/electrolyte interface and the emergence of pseudocapacitance. The standard components of ECs cells, such as electrolytes and electrode materials are thoroughly discussed. Special attention is given to introducing 2D materials, such as transition metal dichalcogenides (TMDs), as electrodes in ECs. Novel trends in the use of 2D materials and how to understand their electrochemical performance are also described.

In Chapter II, the objective and structure of this PhD dissertation are explained. The *Motivation* for pursing this research is provided before each subsequent chapter.

Chapter III, consisting of three research papers (**P1, P2, P3**), introduces the concept of using 2D materials as electrode materials in aqueous-based ECs. Synthesis protocols for obtaining different TMDs materials (ReS_2, MoS_2, NiS_2, FeS_2) and their integration with carbon into composite materials have been developed. The relationship between the materials' morphology and electrochemical behavior is thoroughly discussed. The advantages and disadvantages of using TMDs as electrode material are also explained.

Chapter IV consists of one research paper (**P4**) and aims to address the issues identified in Chapter III. Based on the synthesis methodology developed in Chapter III, MoS_2 has been obtained for further functionalization with redox-active compound, i.e., anthraquinone (AQ). These grafted AQ species have been found to improve the capacitance and longevity of the electrode material. Power-law relationship and electrochemical impedance spectroscopy (EIS) studies reveal the ion movement kinetics and dominant charge storage mechanism. Given the disadvantages observed

for symmetrical cells in Chapter III, an asymmetrical setup was utilized to prevent the oxidation of MoS_2, thus capacitance decay. Preliminary electrochemical studies in an organic medium have also been performed.

Based on the interesting electrochemical behavior of MoS_2 in organic media, different sulfur precursors, i.e., thiourea (TU), thioacetamide (TAA), L-cysteine (LC), were used for their hydrothermal synthesis in Chapter V, which includes additional data (**5**). Chapter V reveals that depending on the sulfur precursor used for the hydrothermal synthesis of MoS_2, different physicochemical, structural, morphological, and porous properties are obtained. Induced by the nanostructured particle size, MoS_2 shows slightly different pseudocapacitive electrochemical behavior. Additional *operando* measurements, such as X-ray diffraction and dilatometry, were used to study crystal structure and electrode height changes during electrochemical operations. Dependent on the particle size, different results were found.

The thesis is concluded with general conclusions, followed by a presentation of the scientific track record and a list of references.

Streszczenie

Ze względu na niestabilny sposób dostawy energii ze źródeł odnawialnych, rozwój urządzeń do magazynowania energii ma kluczowe znaczenie dla zrównoważonej przyszłości. Kondensatory elektrochemiczne (KE) mają kilka zalet w porównaniu ze standardowymi akumulatorami litowo-jonowymi (Li-ion), w tym wysoką trwałość i gęstość mocy. Niestety charakteryzują się one umiarkowaną gęstością energii. Niniejsza rozprawa doktorska porusza główny problem niskiej gęstości energii, poprzez wykorzystanie nowatorskich dwuwymiarowych (2D) materiałów elektrodowych charakteryzujących się dużą pojemnością.

Pierwsza część rozprawy (rozdział I) skupia się na teoretycznym wprowadzeniu do aktualnego stanu wiedzy o KE i zawiera szczegółowe wyjaśnienie ich podstawowych mechanizmów magazynowania ładunku, w tym tworzenie podwójnej warstwy elektrycznej na granicy faz elektroda/elektrolit oraz zjawisko pseudopojemności. Omówiono szczegółowo standardowe składniki KE: elektrolity oraz materiały elektrodowe. Szczególną uwagę poświęcono wprowadzeniu materiałów 2D, takich jak dichalkogenki metali przejściowych (ang. *transition metal dichalcogenides* – TMD), jako elektrody w KE. Zostały opisane również nowe trendy w stosowaniu materiałów 2D oraz sposoby wykorzystania ich właściwości elektrochemicznych.

W Rozdziale II wyjaśniono cel i strukturę rozprawy doktorskiej. Przed każdym kolejnym rozdziałem przedstawiono motywację do podjęcia badań.

Rozdział III, składający się z trzech artykułów naukowych (**P1, P2, P3**), wprowadza koncepcję wykorzystania materiałów 2D jako materiałów elektrodowych w wodnych KE. Opracowano metodologie syntez hydrotermalnych umożliwiających otrzymywanie różnych materiałów TMDs (ReS_2, MoS_2, NiS_2, FeS_2) i ich integrację z węglem w celu tworzenia kompozytów. Szczegółowo omówiono związek pomiędzy morfologią materiałów a zachowaniem elektrochemicznym. Wyjaśniono także zalety i wady stosowania TMDs jako materiałów elektrodowych.

Rozdział IV składa się z jednego artykułu naukowego (**P4**) i ma na celu wyjaśnienie problemów zidentyfikowanych w Rozdziale III. W oparciu o metodologię syntezy opracowanej w Rozdziale III, otrzymano MoS_2 do dalszej funkcjonalizacji związkiem o aktywności redoks, tj. antrachinonem (AQ). Wykazano, że funkcjonalizacja MoS_2 antrachinonen zwiększa pojemność oraz stabilność materiału elektrodowego. Badania

wykorzystujące techniki woltamperometryczne oraz spektroskopii impedancyjnej pozwoliły na oszacowanie wpływu obecności grup funkcyjnych na kinetykę oraz dominującego mechanizmu magazynowania ładunku. Biorąc pod uwagę wady zaobserwowane dla ogniw symetrycznych w rozdziale III, zastosowany został układ asymetryczny w celu uniknięcia utleniania MoS_2, a tym samym szybkiej utraty trwałości ogniwa. Przeprowadzono również wstępne badania elektrochemiczne w elektrolicie organicznym.

Bazując na interesujących właściwościach elektrochemicznych MoS_2 w elektrolitach organicznych, w rozdziale V (**5**), wykorzystano do syntezy hydrotermalnej różne prekursory siarki, tj. tiomocznik (TU), tioacetamid (TAA) i L-cysteinę (LC). Wykazano, że w zależności od wykorzystanego prekursora, uzyskuje się różne właściwości fizykochemiczne, w tym strukturalne, morfologiczne oraz porowatości otrzymywanego materiału. Różnice w wyżej wymienionych właściwościach, powodują, że zachowanie elektrochemiczne MoS_2 jest nieco różne. Zostały również wykonane dodatkowe badania typu *operando*, badające zmiany struktury krystalicznej, ekspansji oraz kurczenia się elektrody podczas pracy elektrochemicznej. W zależności od wielkości cząstek materiału uzyskano różne wyniki.

Ostatnią część dysertacji są wnioski ogólne, po których następuje prezentacja dorobku naukowego oraz wykaz literatury.

Motivation and context of the research

The climate is a set of expected weather conditions at a specific time of year. While it naturally varies over the years due to factors such as volcanic eruptions, solar radiation fluctuation or tectonic movements, since 1950s a gradual increase in surface average temperatures has been observed. This phenomenon was termed '*global warming*' by NASA (*National Aeronautics and Space Administration*) in the 1980s and further expanded to '*climate change*' in the 2000s, defined as changes in climate patterns [1, 2]. The last decade (2011-2020) was identified as the warmest on record, with average global temperatures being 1.1 °C higher than those in the pre-industrial era. If this trend continues, with temperatures rising by about 0.2 °C per decade, reaching 2 °C could lead to severe consequences for the natural environment and human health [3]. In response, nearly 195 countries, including Poland, signed the Paris Agreement in 2015, aiming to keep the global temperatures increase well below 1.5 °C above pre-industrial levels.

CO_2 is the largest contributor to global warming, with its concentration having increased by nearly 48% compared to the pre-industrial era [4]. It is primarily produced by burning fossil fuels for energy production. As the energy consumption rises exponentially with human population growth, there is a significant need for development of efficient methods to harvest sustainable energy sources. Sustainable energy can be produced from renewable sources such as wind, water, and geothermal energy. Various technologies convert these renewable sources into electrical energy, for instance, solar cells use the photovoltaic effect to convert solar to electrical energy, wind turbines convert kinetic energy from the wind to electrical energy. However, these renewable sources often depend on weather conditions and regional climate, meaning they do not consistently deliver a steady current load, even though continuous energy is needed [5].

To maintain continuous and reliable access to electrical energy, energy storage devices have been developed such as rotating flywheels, hydraulic lift systems, etc. Among these, **electrochemical energy storage devices** have emerged as a promising solution. These devices bridge the gap between energy generation and consumption by storing surplus energy for later use, thus improving grid stability and reliability.

There are various types of devices capable of efficient storing and releasing electrical energy, including batteries, fuel cells and capacitors (**Fig. 1**). Despite their differences, they are 'electrochemically' comparable, i.e., the electrochemical process of charge storage/generation occurs at the electrode/electrolyte interface [6].

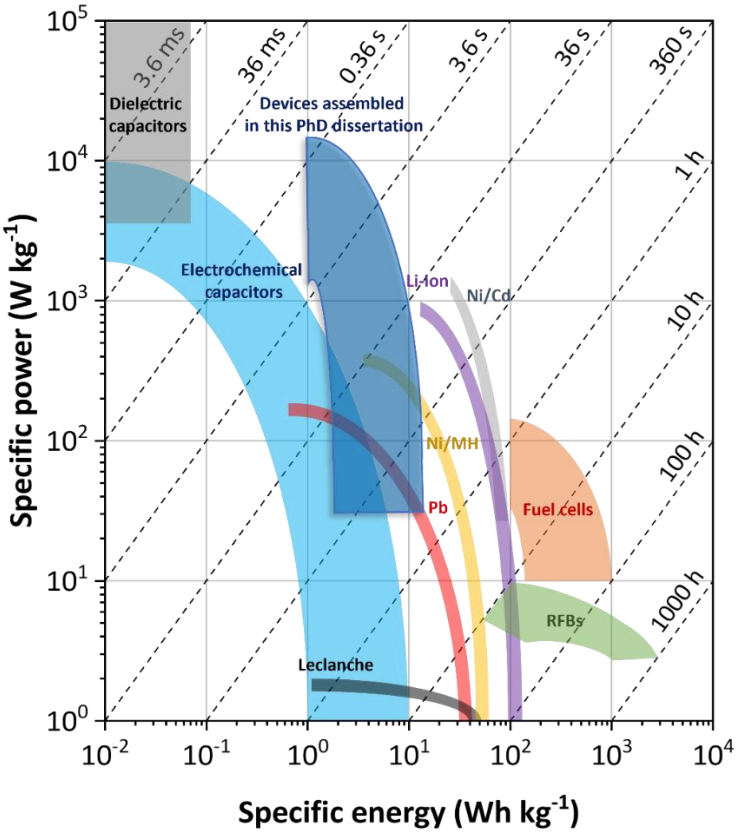

Figure 1 Ragone plot presenting different electrochemical energy storage systems.

Fuel cells, for example, convert energy by breaking down hydrogen molecules into water during electrochemical processes. They are scalable devices used in transportation and some stationary applications.

Batteries store chemical energy and release it as electrical energy on demand. They are categorized into primary cells, such as Leclanché, where electrochemical processes are non-reversible meaning they can be only used once, and secondary cells, such as lead-acid (Pb), nickel-metal hydride (Ni/MH), lithium-ion (LiBs), nickel-cadmium (Ni/Cd), and redox-flow batteries (RFBs), where the redox processes are reversible, and they can be used many times. Batteries can supply stable power output during long discharges. Two contrary devices among the batteries are LiBs and RFBs. LiBs are used in portable electronics and electric cars due to their high energy density, light weight,

and relatively high power, allowing for quick charging. RFBs store energy *via* charge transfer processes in electrolyte ions, achieving high energy levels depending on the tank size storing the electrolytes. In general, batteries show high energy density, but their electrochemical performance is often kinetically limited by sluggish ion transport within the electrode material, giving usually low power density.

Contrary, there are devices which can deliver the energy much quicker, in form of burst of energy. Initially, dielectric capacitors were used for small devices where the charge is stored on metal plates. By adding electrolyte solution and high-area electrodes, ECs were developed. Their energy storage mechanism is based on the reversible adsorption of ions at the electrode/electrolyte interface. Due to the physical nature of this mechanism, the energy values reached by these systems are usually intermediate, but the specific power values are typically extremely high. This mechanism allows for quick charging and discharging, making ECs ideal for applications where quick burst of energy is needed, such as regenerative braking in electric vehicles.

Hybrid devices, combining the charge storage mechanism of ECs and batteries, are also possible. There are different levels of hybridization, e.g. on electrode, electrolyte, device, or connection level, each allowing for reaching higher energy density than standard systems.

This dissertation will focus on the development of the ECs components, especially electrode materials showing battery-like behavior will be tailored to the ECs needs.

Chapter I

Literature review

Electrochemical capacitors (ECs)

Electrochemical capacitors (ECs) belong to a class of electrochemical energy storage devices capable of quickly storing and releasing energy, much faster than conventional batteries. However, in contrast to batteries, ECs exhibit significantly lower energy density. In this context, many researchers are focusing on enhancing the ECs energy values, while maintaining their high-power characteristics. Consequently, the development of ECs components, such as, electrode materials, electrolyte solutions, or membranes is paramount when designing a novel EC device. Currently, there are numerous ways for enhancing the operational parameters of ECs. To address these effectively, the following paragraphs will introduce the operational principles of ECs and provide insights into the current *state-of-the-art* related to the ECs components, with a special attention on electrode materials technology.

1 Principle of ECs operation

Generally, ECs are composed of two current collectors coated with highly porous electrodes, submerged in an electrolyte solution, and separated by a non-conducting membrane to prevent short-circuiting. (**Fig. 2 a**) [5]. Capacitors operate through electrostatic adsorption of ions at the electrode/electrolyte interface, induced by the polarization of the current collectors [7]. The nature of the ion adsorption process is purely physical, meaning that there is no chemical or phase changes during charging and discharging [8]. Consequently, it allows the capacitors to reversible store energy for thousands of cycles without any loss of the initial capacitance [9]. The term, capacitance (C_{ele}), refers to the ability of a capacitor to store charge and is expressed by the amount of charge (Q in A s) accumulated within operational voltage window (U in V) (**eq. 1**) .

$$C_{ele} = \frac{Q}{U} = \left[\frac{A\ s}{V}\right]\ [F] \qquad (\textbf{eq. 1})$$

Consequently, capacitance linearly increases when applying a higher potential range (**Fig. 2 b**). When referring to a device, it should be noted that a full capacitor (C_{cell}) consists of two electrodes which are considered as separate capacitors connected *via* series circuit as shown by the equation below (**eq. 2**).

$$C_{cell} = \left(\frac{1}{C_{ele-}} + \frac{1}{C_{ele+}}\right)^{-1} \quad \textbf{(eq. 2)}$$

With C_{ele-} and C_{ele+} being the capacitance of the negative and positive electrode, respectively. In this way, the electrode with smaller capacitance determines the total capacitance of a system. Consequently, the capacitance expressed per electrode (C_{ele}) is 4 times bigger than the capacitance expressed per device (C_{cell}), assuming the same electrodes were used in terms of mass and capacitance [10].

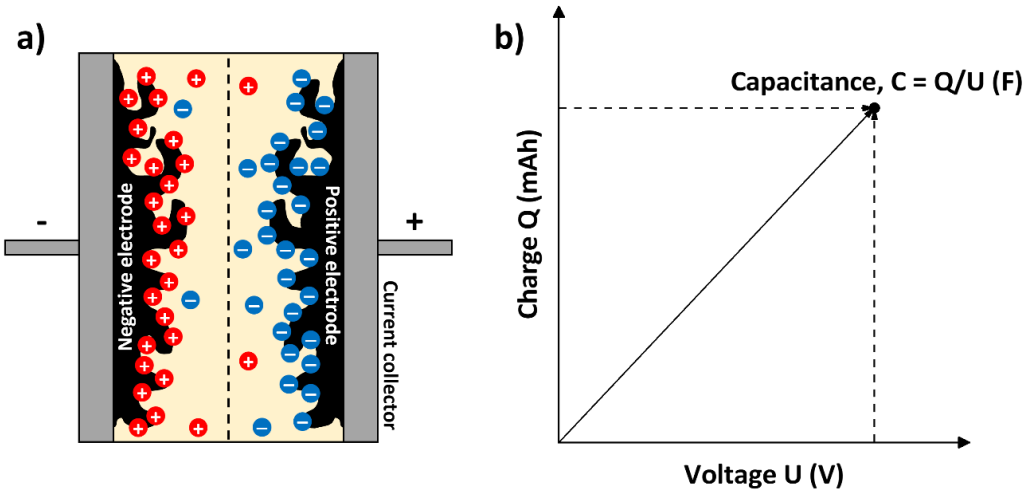

Figure 2 (a) Schematic drawing of a capacitor. (b) linear relationship between accumulated charge and capacitor voltage range.

However, the capacitance of a device does not directly reflect the practical application of capacitor as an energy storage system. Therefore, other parameters, such as energy (E_{Cell} in Wh) and power (P_{Cell} in W), allow for the comparison of energy storage systems in terms of how much energy they can store and how quickly they can release it [11]. Based on the relationship between energy and power, different energy storage devices can be compared on a chart called Ragone plot (**Fig. 1**) [12]. The energy of a cell can be expressed by the equation (**eq. 3**) [13].

$$E_{Cell} = \frac{CU^2}{2} \ [Wh] \quad \textbf{(eq. 3)}$$

Consequently, the energy of a capacitor is dependent on the capacitance (C in F) and operational voltage range (U in V) of a device. The energy improvement can be realized through increasing the system capacitance (e.g., **by introducing pseudocapacitive electrode materials** or using redox-active electrolyte solutions) and/or increasing the voltage range (e.g., by using different electrolyte media) [14].

The power of a device expresses how quickly energy can be extracted from it. It can be determined at the maximum voltage range and divided by the resistance of the capacitor cell (**eq. 4**).

$$P_{Cell} = \frac{U^2}{4R} \ [W] \qquad (\textbf{eq. 4})$$

It can also be expressed in relationship to energy, where the energy is divided by the discharge time (t) (**eq. 5**).

$$P_{Cell} = \frac{E}{t} \ [W] \qquad (\textbf{eq. 5})$$

Nevertheless, there is a general practice in academia to demonstrate the values of energy and power of a device while referring to the active mass of electrode materials, rather than the total mass of a device, i.e., including mass of the separator, electrolyte solution, coatings, or casings. For example, in the energy storage devices industry, crucial improvements are made by reducing the '*dead mass*' of a cell (i.e., mass which does not actively participate in energy storage processes), where the weight of the cell components is reduced, such as limiting the mass of a current collectors [15, 16]. Another important parameter of an energy storage device is time constant (τ), which indicates the time required to release half of the energy stored in the device and is expressed by the capacitance of the system multiplied by resistance of a cell. The following sections focus on the introduction to the charge storage phenomena.

2 Electrical double-layer models

The primary energy storage mechanism of ECs involves the reversible electrostatic accumulation of ions at the electrode/electrolyte interface upon polarization of the electrodes. However, the concept explaining this phenomenon has evolved over the years. The first model was proposed by Helmholtz in 1853 [17]. It describes that after polarization of current collectors, the separation of charges occurs at the surface of electrodes, forcing ions of opposite sign in the vicinity of the electrolyte to diffuse toward the electrodes. Ions at the electrode/electrolyte interface form a stiff layer, a few nanometers in thickness, in a plane parallel to the electrode surface. Such charge storage phenomenon is called the electrical double-layer (EDL) [18]. As observed in **Figure 3 a**, the electrical potential of the electrode (φ_e) linearly decreases as the distance between the positively charged surface and negatively charged ions (two, or double layers) increases. The ability to store charge by the electrode is expressed as capacitance (C in F). In this case, the capacitance of such simplified EDL model (C_H) is expressed in the same way as that of a capacitance of a conventional electrical capacitor (operating through separation of charges without the electrolyte solution) given by the equation below (**eq. 6**) [19].

$$C_H = \frac{\varepsilon_0 \cdot \varepsilon_r \cdot A}{d} \text{ [F]} \qquad \textbf{(eq. 6)}$$

where, ε_0 is the vacuum permittivity (ε_0=8.854·10^{-12} F m^{-1}), ε_r is the dielectric constant given for the specific electrolyte, A is the available specific surface area of the electrode material [m^2], and d is the effective thickness of the double-layer [m]. The Helmholtz model encompasses the electronic structure of the electrode material, its polarization, and the electrolyte effect, giving a relationship between the capacitance and the type of electrode (i.e., accessible surface area) and the type of the electrolyte (i.e., dielectric constant).

However, the equation introduced by Helmholtz was a simplified model that does not consider several factors such as the diffusion of ions in the electrolyte vicinity and the interaction between the dipole moment of the solvent and the electrode material. Consequently, the Gouy model was introduced in 1910 and later improved by Chapman in 1913 [20]. They used the Boltzmann and Poisson equations to describe diffusion phenomena. However, their model was valid only for diluted electrolytes. At higher concentrations, other phenomena such as layering effects, ion pairing formation,

or ion crowding occur which do not allow for correct approximation of a model. The Gouy-Chapman model (C_{GC}) assumed ions as a point-like charged non-interacting with each other particles, where the solvent is a continuous dielectric medium with uniform electrical permittivity. Consequently, the electrical potential of the electrode exponentially decreases from the electrode surface to the electrolyte bulk vicinity (**Fig. 3 b**).

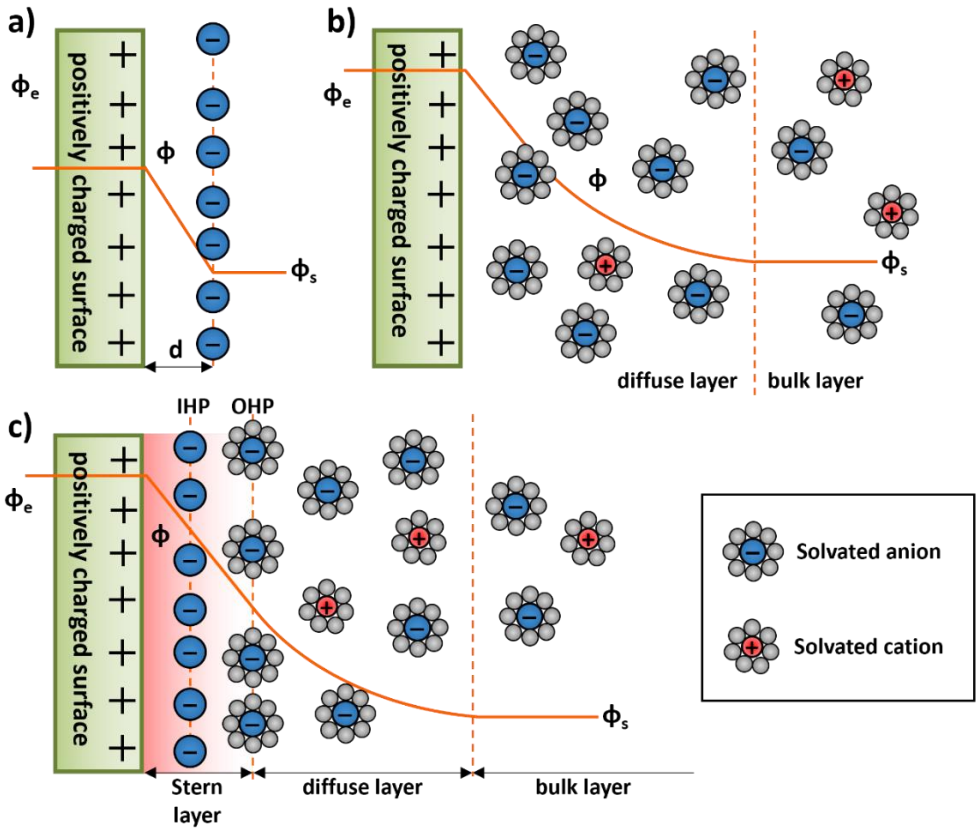

Figure 3 (a) Helmholtz, (b) Gouy-Chapman, and (c) Stern models of the electrical double-layer formed at a positively charged electrode in an electrolyte. The electrical potential (φ) decreases when going away from electrode (φ_e) to the bulk electrolyte (φ_s). (Adapted from Ref. [18]).

The Gouy-Chapman theory was improved by Stern in 1924, which introduced the concept accounting for the dimensions of ions and solvent molecules existence in the bulk electrolyte [21]. Finally, the Stern model consider the EDL phenomenon as a combination of Helmholtz (C_H) and Gouy-Chapman (C_{GC}) models (**Fig. 3 c**). The Stern model derives the capacitance (C_{EDL}) as equivalent to two capacitors in series combining C_H and C_{GC} to a total capacitance of the EDL model as given below (**eq. 7**)

$$\frac{1}{C_{EDL}} = \frac{1}{C_H} + \frac{1}{C_{GC}} \quad [\mathrm{F}] \qquad \textbf{(eq. 7)}$$

Further theory was introduced by Grahame in 1947, which presented the concept of specifically adsorbed ions at the surface of the electrode material [22]. Basically, the ions in the electrolyte bulk are surrounded by the solvation shell. However, when solvated ions are approaching the electrode surface, the solvation sheath can be dropped upon specific adsorption. Graham introduced the division of the Stern layer into the inner Helmholtz plane (IHP) and outer Helmholtz plane (OHP), where IHP forms by the centres of the specifically adsorbed ions, whereas OHP represents the rigid plane formed at the centres of the solvated ions. The final component of the Graham model was introduced by Bockris, Devanthan and Müller (BDM) in 1963, which included the action of the solvent molecules at the electrode/electrolyte interface [23]. The dipoles of the solvent molecules are specifically oriented in accordance with the nature of the ions charge. The IHP passes through the centres of the specifically adsorbed ions at the surface of the electrode and the solvent molecules, which are oriented accordingly to the nature of the surrounding ions. It means that the surface of the electrode submerged in the electrolyte solution is being surrounded by the solvent molecules. The OHP passes through the centres of the solvated ions near the electrode surface. Outside of the OHP there is a diffuse layer with solvated ions. The BDM model is presented in the **Figure 4**.

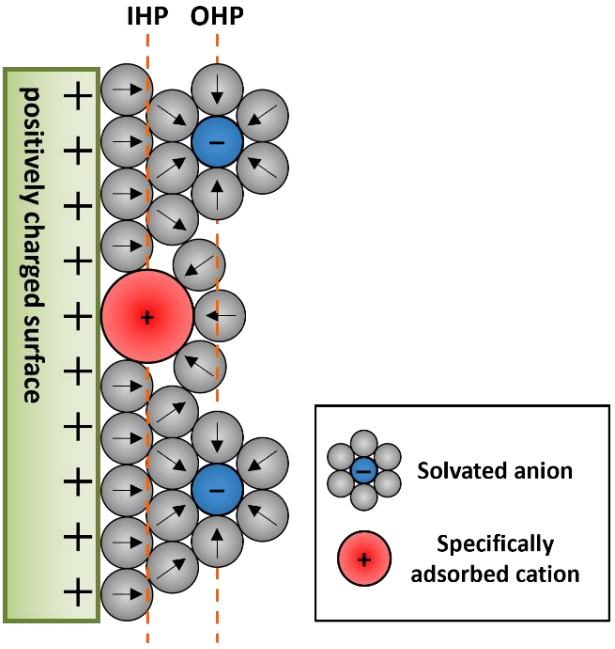

Figure 4 Schematic representation of the Bockris, Devanthan and Müller (BDM) double-layer model on a negatively polarized electrode.

3 Emergence of pseudocapacitance in electrode materials

The process of charge storage in ECs is not exclusively limited to the EDL phenomenon but can also involve charge transfer between the electrode and electrolyte components. Capacitance, which originates from processes other than EDL, was called '*pseudo-capacity*' in 1941 by Graham [24]. Conway introduced the concept that the electrode capacitance can arise from two phenomena, i.e., involving non-specifically adsorbed ions (charge is induced, not transferred) and adsorption pseudocapacitance (charge is transferred) [8]. It was later identified that mainly three processes could be occurring at the electrode/electrolyte interface which involve charge transfer phenomena (other than EDL), i.e., **surface redox reactions**, **electrochemical intercalation reaction**, and **conversion/alloying reactions** [25]. These reactions are faradaic in nature, meaning that they adhere to Faraday's laws and are accompanied by the clear and distinct signs of a charge transfer processes during electrochemical operation [26]. However, some of these processes show electrochemical features typical for capacitive, potential-dependent relationship while being faradaic in origin [27]. This phenomenon is described as '*pseudocapacitance*', where the electrochemical behavior seems to be capacitive in nature, while kinetically and thermodynamically adhere to the Faraday's laws [28]. Charge transfer processes can generally be explained by an equation corresponding to an electron transfer process between the oxidized (Ox) and reduced (Red) forms of the reagents (**eq. 8**).

$$\mathrm{Ox} + \mathrm{ze}^{-} \leftrightarrow \mathrm{Red} \qquad (\textbf{eq. 8})$$

According to Conway, pseudocapacitance can be classified into three different types **(Fig. 5)**: **adsorption pseudocapacitance**, **redox pseudocapacitance**, and **intercalation pseudocapacitance**. Each of these pseudocapacitance phenomena occur *via* different physical processes and arise from various types of materials. However, they show comparable electrochemical signatures due to relationship between the potential and charge that develops as a result of adsorption/desorption process at the electrode/electrolyte interface (**eq. 9**) [29].

$$\mathrm{E} \sim \mathrm{E}^{0} + \frac{\mathrm{RT}}{\mathrm{zF}} \ln\left(\frac{\mathrm{X}}{1-\mathrm{X}}\right) \ [\mathrm{V}] \qquad (\textbf{eq. 9})$$

Where, E is the electrochemical potential [V], E^0 is the standard electrochemical potential [V], R is the gas constant, 8.314 [J mol^{-1} K^{-1}], T is the temperature [K], n is the number of electrons transferred during redox reaction, F is the Faraday constant, 96 485 [C mol^{-1}], and X is the extent of the fractional coverage of the surface/inner structure [29, 30]. This relationship highlights that such adsorption/desorption phenomena are hindered by the thermodynamic kinetics of the processes [29-31]. The relationship between voltage and charge is not totally linear, as in the EDL capacitor, thus the capacitance does not remain constant with increasing potential, which is why it is referred as pseudocapacitance. The total amount of charge stored *via* pseudocapacitive electrodes can be expressed as capacitance (C in F) by the equation below (**eq. 10**), when the relationship of U *vs.* Q (**Fig. 2 b**) becomes linear.

$$C = \left(\frac{nF}{m}\right) \qquad \textbf{(eq. 10)}$$

Where, m is the molar mass of active material in the electrode. From a theoretical point of view, the capacitance realized in pseudocapacitive systems is substantially higher (10 to 100 times) than those observed for purely EDL-based systems for the same weight or volume [8]. For that reason, it is often observed to overuse the term pseudocapacitance and refer the battery-like materials showing plateaus of electrochemical reaction as a pseudocapacitor and refer to capacitance, not capacity [32, 33]. A comparison of potentially reachable capacitance by materials showing different natures is presented in **Table 1**.

Table 1. Comparison of the number of stored charges through double-layer, pseudocapacitance, and in battery-like electrode materials. (Based on [8]).

Type of material in mechanism context	**Stored charge**
Electrical double-layer	i.e., 0.17-0.20 electrons per 1 atom of electrochemically active surface area
Pseudocapacitive	Based on 500 μF cm^{-2}, ≈ ca. 500 μC V^{-1} i.e., 2.5 electrons per 1 atom. For hydrogen chemisorption, 1 electron per 1 atom.
Battery-like	i.e., 1-3 electrons per 1 atom or molecule of bulk phase

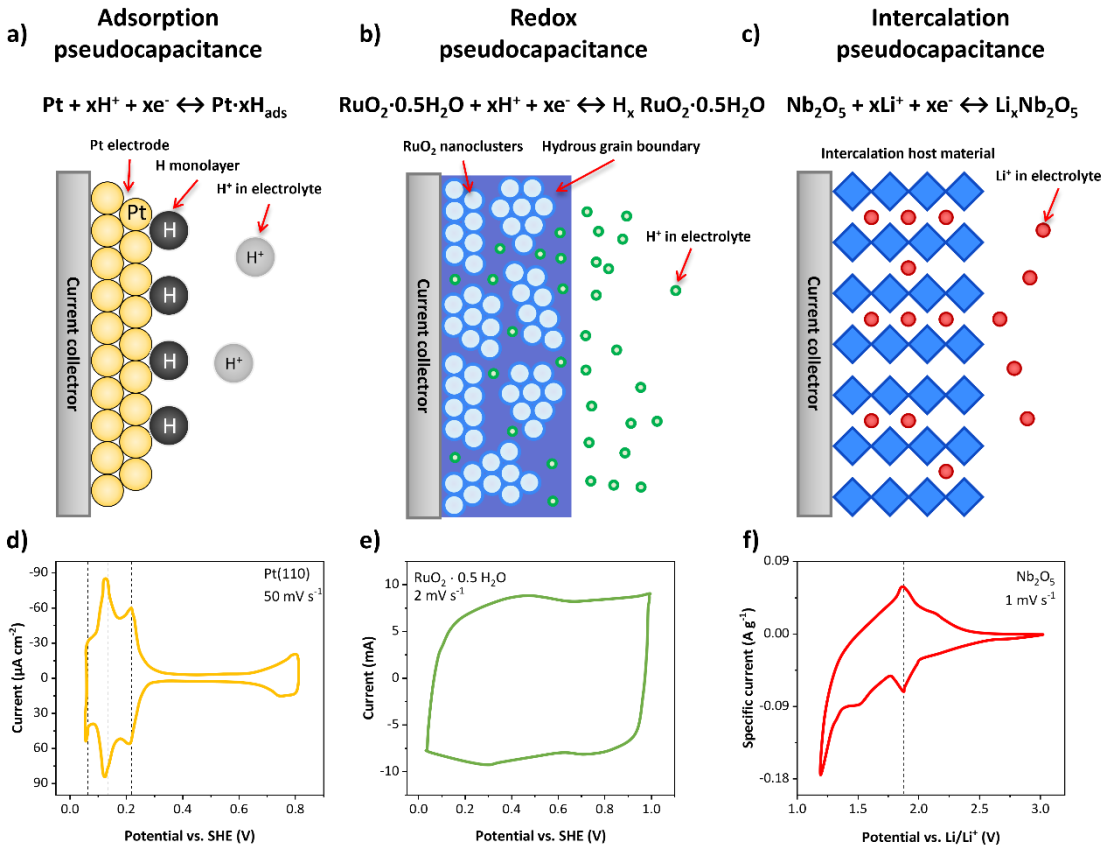

Figure 5 Three different types of pseudocapacitance with their corresponding cyclic voltammogram response, a), d) adsorption of H^+ ions on Au surface, b), e) surface redox reaction of hydrous RuO_2 with protons, c), f) intercalation pseudocapacitance of Li^+ into layered structure of Nb_2O_5. (Adapted from Ref. [34]).

The adsorption pseudocapacitance occurs through the electrosorption of cation A^+ onto the surface of the electrochemically conductive surface M (**eq. 11**) [34].

$$\mathrm{M} + A^+ + e^- \rightarrow MA_{ads} \qquad \textbf{(eq. 11)}$$

This electrosorption process is assumed to follow a Langmuir-type (monolayer) isotherm of adsorption [35]. A classic example is the electrochemical adsorption of Pb^{2+} ions on the surface of a gold electrode [36]. It is also known to occur at the surface of noble metals such as Pt, Rh, Ru, and Pd with the adsorption of hydrogen ions [37]. The reversible electrosorption of hydrogen ions is observed just before the cathodic recombination of adsorbed H^+ into H_2, hence, it is called '*underpotential pseudocapacitance*' (**Fig. 5 a**).

In the energy storage context, hydrogen electrosorption appears to be the most relevant in aqueous ECs utilizing microporous carbon-based electrode materials [38]. Hydrogen storage occurs through electrochemical electrolyte decomposition and subsequent electrosorption of nascent hydrogen in the porous texture of the negative electrode [39]. The reactions can be summarized in equations below (**eq. 12-14**) [40, 41].

$$\mathrm{H_2O + e^- \rightarrow H + OH^-} \qquad \textbf{(eq. 12)}$$

$$H_3O^+ + e^- \rightarrow \mathrm{H} + \mathrm{H_2}O \qquad \textbf{(eq. 13)}$$

$$< \mathrm{C} > + H_2O + e^- \rightarrow < C > H_{ads} + OH^- \qquad \textbf{(eq. 14)}$$

When polarization is reversed, adsorbed hydrogen is released, forming water together with the OH^- anion present in the electrolyte.

Thanks to the hydrogen storage in the microporous texture of the carbon electrode, aqueous ECs can operate above the thermodynamic potential limitation of water decomposition (i.e., 1.23 V). It is caused by the locally alkalized pH of the electrode/electrolyte interface due to the formation of OH^- ions during hydrogen storage (**eq.14**) [40]. It causes the shift of the Nernst potential for the H_2 evolution and subsequently the shift of the H_2 evolution overpotential [42].

The amount of stored hydrogen is dependent on the physicochemical properties of carbon material (i.e., porous texture, specific surface area, elemental composition, and surface functionality), but also on the electrolytic medium as well as the electrochemical experiment conditions [43] [44]. The additional capacitance originating from the hydrogen storage is dependent on the amount of stored hydrogen. Calculated from Faraday's law, ca. 1 % of stored hydrogen corresponds to 274 mAh g^{-1} [45]. For that reason, carbon electrodes utilizing pseudocapacitive hydrogen storage can be utilized as an anode in a full secondary cell [46].

Surface redox pseudocapacitance arises from redox reactions between the electrode material and electrolyte ions (**Fig. 5b**). The first materials exposed as pseudocapacitive in nature were ruthenium oxide (RuO_2) in acidic and manganese oxide (α-MnO_2) in neutral electrolytes, both displaying higher values of capacitance than typically available for carbon materials [47-49]. The charge storage mechanism in these materials is limited to the electrode surface, as demonstrated by X-ray photoelectron spectroscopy (XPS) analysis of the electrode's oxidation state during charge/discharge.

In thin electrodes, changes of the oxidation state of MnO_2 from Mn^{4+} to Mn^{3+} during charging was observed [50]. In turn, no changes for bulk electrode were detected indicating that only thin layer electrodes are electrochemically active.

It was found that the electrochemical properties of RuO_2 are strongly dependent on the crystalline structure. Especially, structural water in RuO_2, in form of RuO_2 0.5 H_2O, was also proved to be important. It allows for the redox behavior of the Ru^{4+} cations, the metallic-like conductivity of RuO_2, rapid proton transfer during charge storage, and a larger specific surface area which shortens the diffusion path length of ions [51-53].

In the context of electrodes showing surface redox pseudocapacitance, the high reversibility of an electrochemical process at all applied potential ranges was noticed. The anodic and cathodic voltammograms are almost mirror images (RuO_2), whereas battery-like materials, such as $Pb/PbCl_2$, show irreversible electrochemical process at certain potentials. This is common for any battery materials as they involve phase changes that are subject to kinetic limitations of ion movement in the host material [54].

However, pseudocapacitance does not have to be limited to the surface. **Intercalation pseudocapacitance** occurs when the ions are inserted into the bulk structure of a host material (**Fig. 5c**). This type of pseudocapacitance is associated with at surface or near-surface reversible redox reactions which are not burdened by solid-state ion diffusion. The shortened ions diffusion pathway allows for rapid charge/discharge, usually within minutes, thanks to the surface-controlled mechanism. Consequently, it excludes the existence of phase transformation, since the ions can instantly occupy the reaction sites upon entering the host material [55, 56] .

Orthorhombic T-Nb_2O_5 shows pseudocapacitive intercalation of lithium ions in non-aqueous electrolytes at potentials below 2 V *vs.* Li/Li^+ [55]. The galvanostatic charge/discharge profiles are almost linear, which allows T-Nb_2O_5 to be classified as a pseudocapacitive material. The electrochemical behavior is strongly dependent on its crystalline structure [57, 58]. In T-Nb_2O_5, the charge is stored via redox couple of the Nb^{5+}/Nb^{4+} [57]. The reaction is facilitated by the low energy barrier of (001) plane in the T-Nb_2O_5 crystal lattice [59].

There is a significant increase in the number of scientific works that are referring the electrochemical behavior of electrode material as pseudocapacitive in nature, while in fact, they are exhibiting battery-like behavior. For this reason, novel nomenclature has been introduced by *P. Simon* and *B. Dunn* to describe the materials that show pseudocapacitive properties because of their intrinsic properties as **intrinsic pseudocapacitive materials**. Otherwise, if the pseudocapacitance occurs due to extrinsic properties of electrode material and is caused as a result of its structure, such material is referred to as an **extrinsic pseudocapacitive material** [60]. Performance of both materials is demonstrated in **Fig. 6**.

Intrinsic pseudocapacitive materials show the capacitive electrochemical response regardless of a crystallite size, disorder, or morphology. These materials include RuO_2 0.5 H_2O, MnO_2, Nb_2O_5 [61-63].

Extrinsic pseudocapacitive materials exhibit a strong dependency on the aforementioned properties in regard to their electrochemical behavior. This is primarily due to reduction of ion diffusion length path, or suppression of phase transformations. In these materials, the bulk electrodes show slow solid-state diffusion of ions, controlled by the diffusion mechanism, which hinders the redox reaction kinetics and influences the very slow charge/discharge rates [32]. The movement of Li^+ concentration within the host crystal lattice induces stress, often leading to phase transformation, e.g., disorder transitions, two-phase reactions, or crystal lattice rearrangement, which can affect the electrode's longevity [54, 64].

The pseudocapacitive effect can be achieved upon nanosizing the crystallites [65]. As a result, charge is stored and released much quicker with comparable capacity values to the bulk electrode materials. Electrochemically, the material exhibits nearly linear galvanostatic charge/discharge profiles and lacks of redox reaction plateaus [54]. Additionally, square-shaped cyclic voltammograms can be also distinguished, resembling capacitive behavior [27].

The nanosizing effect is already well reported in the literature to allow for the transformation of the electrochemical response of a battery-like material to pseudolinear performance which resembles a capacitor.

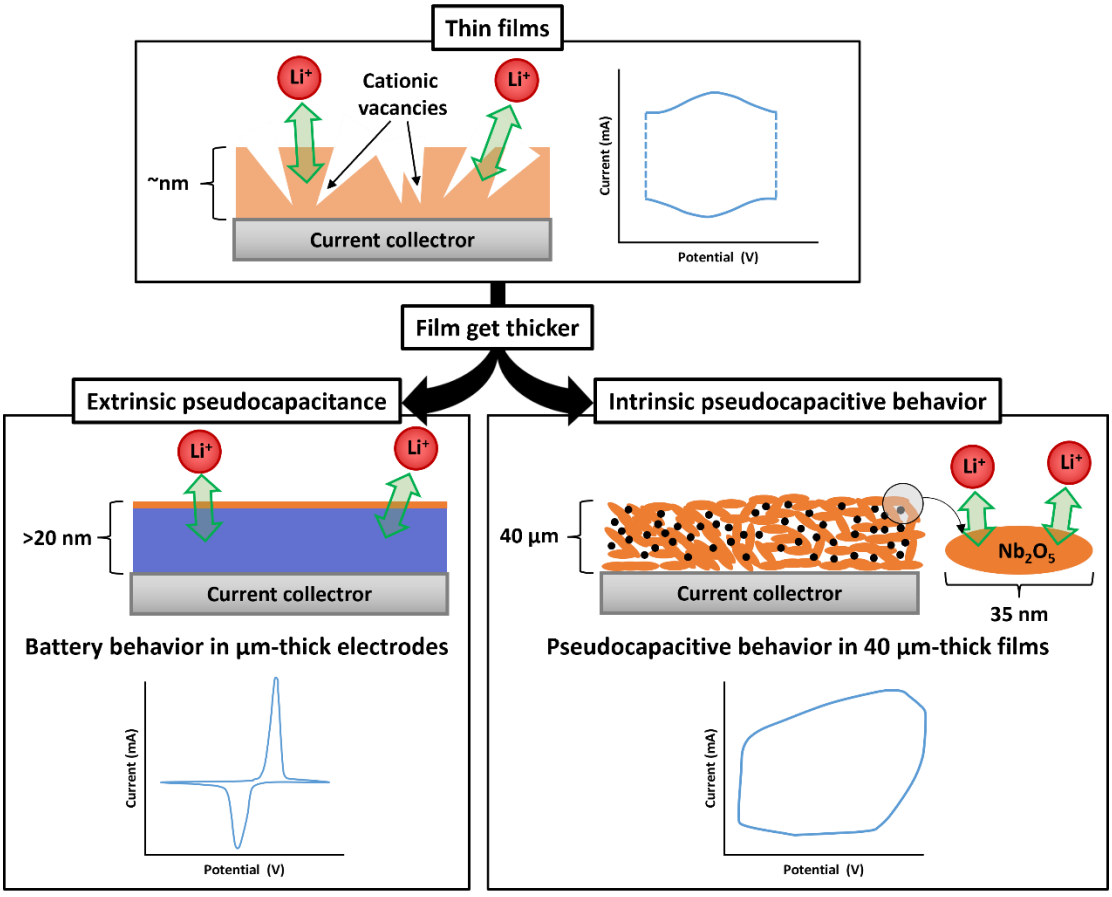

Figure 6 Electrochemical behavior of intrinsic and extrinsic pseudocapacitive materials. (Adapted from Ref. [60]).

Exemplary material is Li_xCoO_2 (a cathode material used in LiBs) (**Fig. 7**), where for the bulk material, plateaus of electrochemical reaction is noticed [66]. Upon nanosizing the particle sizes, the transition from a plateau to isosceles galvanostatic charge/discharge profiles can be observed [67].

Recently, two-dimensional (2D) materials such as transition metal carbides (MXenes) or transition metal dichalcogenides (TMDs) were reported to exhibit capacitive features in both aqueous and organic media. Molybdenum disulfide (MoS_2), a typical representative of the TMDs family, shows linear galvanostatic charge/discharge profiles and square-shaped cyclic voltammograms resembling a capacitive response in aqueous media. In organic media, it presents features of battery-like behavior such as electrochemical plateaus during galvanostatic charge/discharge and distinct peaks during cyclic voltammetry measurements.

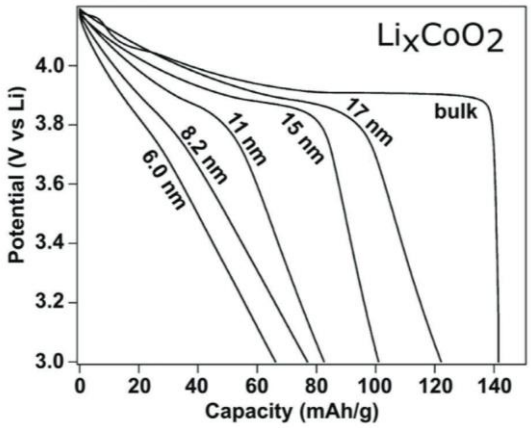

Figure 7 Cyclic Discharge curves for crystalline Li_xCoO_2 as a function of a particle size where a transition from a battery-like behavior to nearly linear, a pseudocapacitive-like behavior is observed with decreasing of a particle size. (Adapted from Ref. [68]).

Upon nanostructuring, MoS_2 exhibits improved lithium intercalation kinetics due to shortened diffusion path length of ions and suppression of a first-order phase transition. Consequently, the material gives electrochemical features resembling a capacitive response. However, it will be in-detail explained in the next paragraph. **Figure 8** presents a brief comparison of different electrochemical responses based on phenomena including, EDL, pseudocapacitance and battery-like.

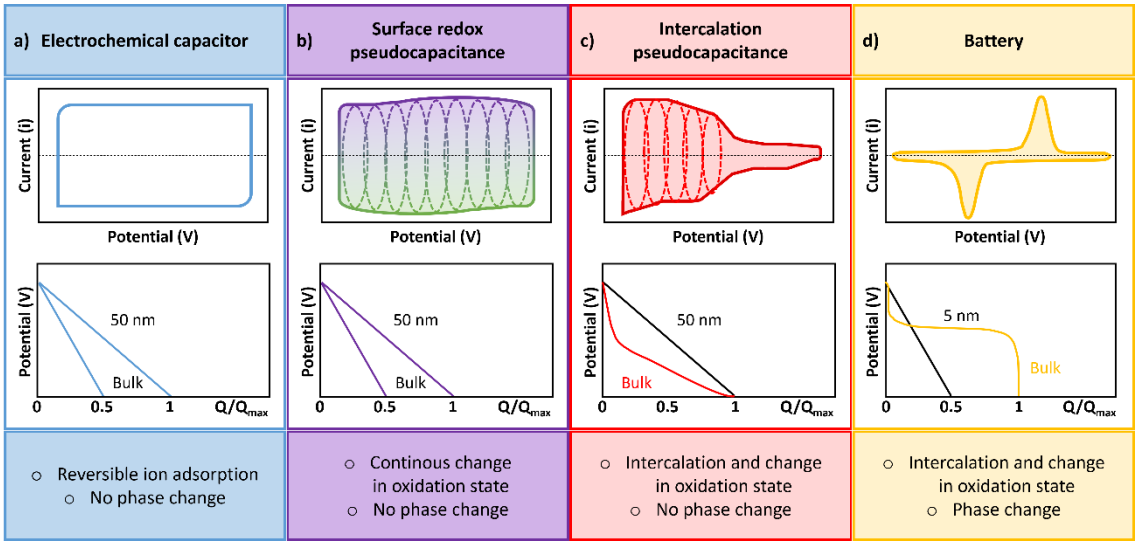

Figure 8 Comparison of different electrochemical behavior. a) Electrochemical capacitor, b) Surface redox pseudocapacitance, c) Intercalation pseudocapacitance, d) Battery. (Adapted from Ref. [69]).

Due to the attractive capacity/capacitance values presented by pseudocapacitive materials, a vast number of scientific works focus on the utilization of such materials in full cell applications. For this reason, different composites with capacitive, pseudocapacitive, or battery-like components are prepared, and their electrochemical behavior is evaluated. Thus, the necessary characterization methods needed to be developed to correctly evaluate the dominant charge storage of a material.

To this day, electrochemical characterization remains the most important tool to describe the phenomena occurring in a pseudocapacitive material. The first-line tool is based on the cyclic voltammetry studies. The power-law relationship (known as *b-value analysis*) between the applied scan rate and electrochemical peak current can be applied to assess whether the process has a dominant surface-controlled (capacitive) or diffusion-controlled (battery-like) kinetics (**eq. 15**).

$$i(V) = av^b \qquad \textbf{(eq. 15)}$$

Where *i(V)* is the peak current density, *a* and *b* are diffusion parameters, and *v* is the scan rate. By plotting a *log(i) vs. log(v)* function, dependent on the b values determined from the slope of the function, it is possible to probe if the process has a dominant diffusion-controlled (*b=0.5*), mixed, finite diffusion-controlled (*b=0.6-0.8*), or surface-controlled (*b=1*) kinetics (**Fig. 9)**.

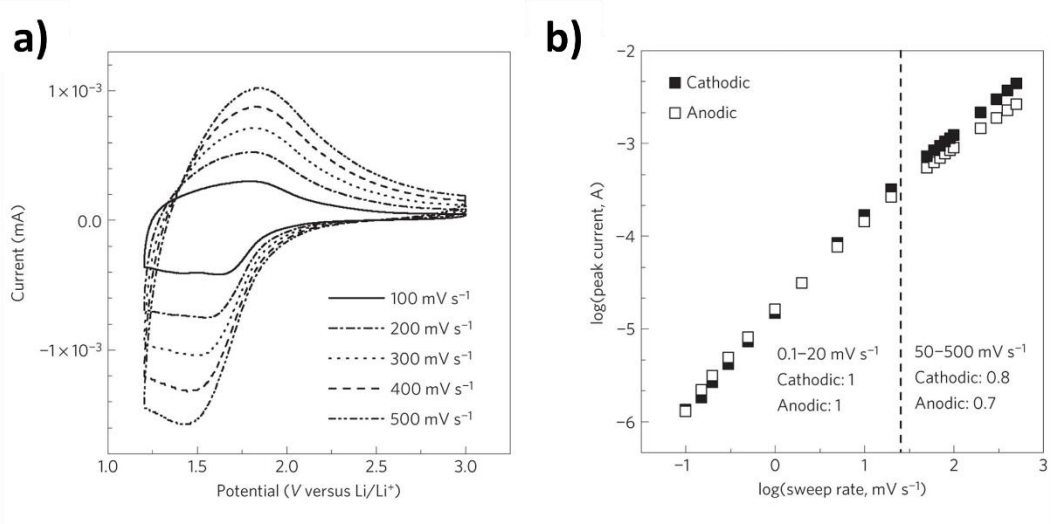

Figure 9 a) Cyclic voltammetry obtained at different scan rates, b) resulted logarithmic peak current variations obtained at different scan rates from CV analysis. (Adapted from Ref. [55]).

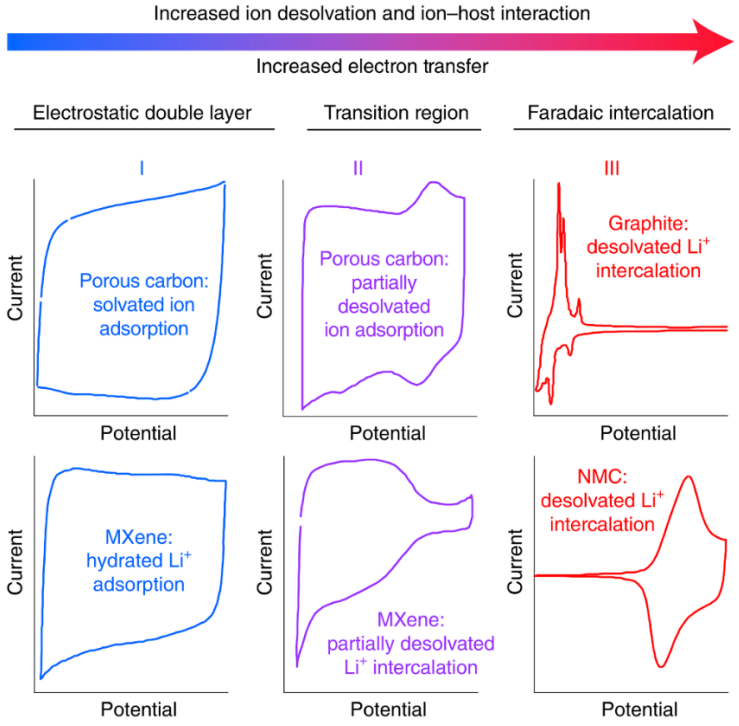

Figure 10 Matrix of CVs demonstrating a continuous transition from (I) electrostatic double-layer, through a (II) transition region, to (III) Faradaic intercalation in nanoconfined environment. (Adapted from Ref. [70])

Finally, there is a vigorous discussion in scientific community of the cross-sectional understanding of the pseudocapacitance in terms of theory and utility. Some researchers link these two processes (EDL and redox) as phenomenon, where one could not exist without another. Recently, the concept of confined electrolytes has been developed where the faradaic phenomena can be observed related to the dropping of the solvation sheath upon adsorption in microporous carbons with tuned porosity. This viewpoint has been extended to layered materials with intercalation charge storage mechanism. From the practical point of view, the electrochemically active surface area of layered electrode materials in non-uniform. The existence of the porous texture and tortuosity of pores in electrode cannot be excluded. Consequently, it evolved into a new concept of a continuous transition from double layer to faradaic charge storage in confined electrolytes (**Fig. 10**) where different phenomena could be occurring in the layered system dependent on the ion desolvation and ion-host interaction. Thus, the need towards fundamental works focusing on the explanations of the phenomena occurring in such systems is especially important [70].

4 Electrolytic solutions for ECs

Regardless of the phenomena occurring in the ECs, the cell construction requires using the electrolyte solution, which serves as the source of ions capable of transporting charges from the electrolyte bulk to the electrode/electrolyte interface. Various types of electrolytes have been proposed, including liquid, solid-state, and quasi-solid electrolytes [71, 72]. In the context of this thesis, mainly liquid electrolytes will be considered. We can differentiate three different groups of liquid electrolytes: **aqueous, organic, and ionic liquids** [73, 74]. The choice of electrolyte significantly impacts the electrochemical performance of ECs, particularly in terms of their energy and power density values. Depending on the application, the ideal electrolyte should be characterized by a wide operational voltage window (to achieve high energy, **eq. 3**) and high ionic conductivity (to achieve high power, **eq. 4**). However, specific utilization of ECs requires consideration of other aspects such as flammability, environmental issue, or price [74]. Characteristics of different electrolytes are presented in **Table 2**.

Table 2. Characteristics of electrolytes for EC applications (Based on Ref. [74]).

Electrolyte	**Aqueous**	**Organic**	**Ionic liquids**
Ionic conductivity at 25 °C	~1000 mS cm^{-1}	~60 mS cm^{-1}	~10 mS cm^{-1}
Voltage range	1-1.6 V	2.5-3.7 V	> 3 V
Assembly	Air	Inert	Inert
Safety	High	Low	High
Price	Low	Moderate	High

Aqueous electrolytes are environmentally friendly and inexpensive compared to other types. However, they are limited by the thermodynamic potential of water decomposition, i.e., 1.23 V. Exceeding this voltage may lead to hydrogen evolution on the negative electrode and oxygen evolution on the positive electrode [75]. Certainly, the electrode materials affect the realization of a voltage extension. Hydrogen storage on the negative electrode in microporous carbons can locally change the pH of the electrode/electrolyte interface, altering the hydrogen evolution overpotential [76]. On the positive electrode, oxidation of the electrode is considered prior to oxygen evolution [77]. The surface chemistry of carbon electrode affects the porous texture of an electrode material, capacitance, and thus longevity [78, 79].

First reported electrolytes used for ECs construction were acid-(H_2SO_4) and alkali-(KOH) based solutions, demonstrating high conductivity (~1 S cm^{-1} at 25 °C), significantly higher than the common organic electrolytes (e.g., ~ 60 mS cm^{-1} for 1 M TEA BF_4 in ACN at 25 °C) [80-82]. In a consequence, the capacitance of carbon-based materials is also relatively high (~150-200 F g^{-1}) in comparison to other type of aqueous electrolytes [83]. The operational voltage window of H_2SO_4 and KOH electrolytes is ca. 0.8-1.2 V, depending on the electrode material, current collector, and electrolyte concentration. Due to the low operational voltage window and corrosion problem of current collectors and cell components, H_2SO_4 and KOH were disregarded for the practical application [84, 85].

Acid and alkali-based electrolytes were replaced with neutral salts such as sulfates [86, 87], nitrates [78, 88, 89], or perchlorates [90, 91] to mitigate the issues of low operational voltage window and corrosion. The voltage window can be increased due to hydrogen sorption within the porous texture of electrode material, shifting the overpotential of hydrogen evolution towards more negative values [92]. On the positive electrode, oxidation of the surface can be observed upon cycling, depending on the anion used and voltage applied [78]. ECs based on sulfates (e.g., 1 M Li_2SO_4) can reach up to 2.2 V due to the strong solvation shell of Li^+ cations and SO_4^{2-} anions, providing long-term stability of over 15 000 galvanostatic cycles. Generally, the electrode capacitance values in sulfate salts are slightly lower than those observed in H_2SO_4 or KOH (~100-150 F g^{-1}) [87].

To increase capacitance, hybrid devices employing Faradaic components can be considered. In the context of electrolytes, an increase in cell capacitance is realized through the implementation of redox active species in the electrolyte [93, 94].

A representative of halides, i.e., iodides have been shown to participate in reversible redox reactions at the electrode/electrolyte interface, contributing to the total charge stored through the following redox reaction occurring on the positive electrode (**eq. 13**) [95, 96].

$$2I^- \leftrightarrow I_2 + 2e^- \quad \textbf{(eq. 13)}$$

The theoretical capacity calculated from Faraday's law is 211 mAh g^{-1}, which shows a competitive value compared to other pseudocapacitive materials [97]. When I_2 is present at the electrode/electrolyte interface, it can also form polyiodides (I_3^- and I_5^-) during long-term cycling (**eq. 14-15**) [98, 99].

$$I^- + I_2 \leftrightarrow I_3^- \quad \textbf{(eq. 14)}$$

$$I_3^- + I_2 \leftrightarrow I_5^- \quad \textbf{(eq. 15)}$$

Redox active electrolytes have usually limited longevity due to the formation of insoluble deposits (e.g., IO_3^-). They also suffer from a low operational voltage window (ca. 1.2 V for 1 M KI in carbon//carbon systems) due to the near thermodynamic H_2 evolution potential window of the negative electrode [100]. Low concentration redox-active electrolytes (e.g., 0.2 M KI) or binary solutions of neutral and redox-active electrolytes (e.g., 0.2 M KI with 1 M Li_2SO_4 have been found to improve capacitance without affecting longevity (over 10 000 cycles) and voltage window (~1.5 V) [99-101].

Organic electrolytes offer a significantly higher operational voltage window of about 2.5-3.0 V compared to aqueous solutions. Most organic electrolytes consist of ammonium salts (e.g., tetraethylammonium tetrafluoroborate – TEA BF_4) dissolved in organic solvents such as acetonitrile (ACN) or propylene carbonate (PC) [102-104]. They exhibit a wide range of applicable temperatures (-30 to 80 °C) and good ionic conductivity (~60 mS cm^{-1}) [82]. Therefore, organic electrolytes are commonly used in commercial cells [105]. However, ACN or PC solvents are flammable and toxic, prompting research into developing safer and more environmentally friendly organic electrolytes.

Ionic liquids (ILs), which consist solely of ions without any solvent, offer a 'green' alternative to toxic organic electrolytes [106]. For EC applications, ILs must be liquids at room temperature, hence the term room temperature ILs (RTILs). ILs offer high heat conductivity, low vapor pressure, chemical and thermal stability (between -60 to 100 °C) [107, 108]. Their physicochemical properties can be tuned, to some extent, by matching the cations and anions or combining ILs into binary or ternary solutions [109-111]. As solvent-free solutions, ILs' ions are not solvated by solvent molecules. Instead, ions are surrounded by layers of opposite charge shells in a phenomenon called Coulombic ordering [112]. In bulk solutions and on flat polarized surfaces, the concept is simple. However, in confined spaces such as micropore or layered environment, Coulombic ordering partially breaks upon electrode polarization, leading to increased concentrations of oppositely charged ions at the electrode/electrolyte interface [113]. Consequently, IL-based ECs show improved performance when the micropores match the ion sizes of the ILs [114]. Commonly used cations include 1-ethyl-3-methylimidazolium [EMI], 1-butyl-3-methyl-imidazolium [BMI], N-butyl-N-methyl-pyrrolidinium [BMP]. Anions consist of bis(trifluoromethylsulfonyl)imide [TFSI], bis(trifluorosulfonyl)imide [FSI], and tetrafluoroborate [BF_4] [115, 116]. However, ILs are complex and require advanced purification techniques, resulting in high costs. They must also be stored under inert conditions to prevent electrolyte decomposition, which can limit their operational voltage window [117]. ILs' drawbacks include high viscosity and often low ionic conductivity due to large ion sizes. Consequently, even with high operational voltage windows (sometimes up to 4.0 V), the capacitance of microporous carbon electrodes in IL-based ECs typically does not exceed 100 F g^{-1} [118-120].

5 Electrode materials for ECs

The selection of an appropriate electrolytic solution is only halfway towards designing a stable, high-energy, and high-power device. Equally important is the selection of an adequate electrode material. Not all electrolytes suit every electrode material, and vice versa. In recent studies, carbonaceous materials have been predominantly used in two-electrode cell assemblies due to their wide abundance, different dimensionalities, and high electrical conductivity. However, the dominant charge storage mechanism of carbon-based electrode materials is physisorption of ions at the electrode/electrolyte interface. Therefore, materials with faradaic properties have emerged as attractive alternatives. The following sections introduce different energy storage materials.

5.1 Carbonaceous materials

Carbonaceous materials are highly appealing for EC applications due to their ability to form various allotropes with different architectures. They exhibit various dimensionalities, ranging from zero-dimensional (0D) to three-dimensional (3D) structures, each with unique properties (**Table 3**). Depending on their dimensionality, they possess diverse thermal and electrical conductivities, specific surface areas (SSA), and crystallinities.

Table 3. Different carbon-based materials used as electrodes in ECs. (Based on Ref. [121]).

Material	**Carbon onion** [122]	**Carbon nanotubes** [123]	**Graphene** [124]	**Activated carbon** [125]
Dimensionality	0D	1D	2D	3D
Electrical conductivity	High	High	High	Moderate
Relative capacitance	Low	Low	Moderate	High
Structure	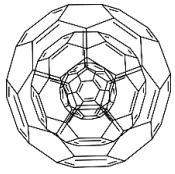		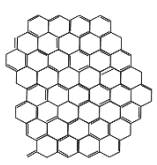	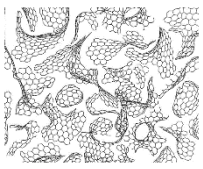

Among different carbon materials, **carbon nanotubes (CNTs)**, **activated carbons (ACs)**, and **graphene** have emerged as particularly significant electrode materials, offering an attractive balance between electrical conductivity, capacitance, [126-130]. **CNTs** exhibit a tubular structure composed of sheets of sp^2 carbon atoms rolled into seamless cylinders with nanometric dimensions [131]. Depending on the preparation method, they can be produced as single layer carbon nanotubes (SWCNTs) or multiwalled carbon nanotubes (MWCNTs) [132]. However, achieving a strict control over the number layers is challenging and often accompanied by the formation of amorphous carbon or metal catalyst residues. For energy storage application, CNTs present ballistic electrical conductivity values, allowing for quick charging of the electrode/electrolyte interface [133]. However, the most critical parameter for their application as an electrode material in ECs is the SSA [134]. CNTs typically exhibit relatively low SSA, dependent on the number of walls and nanotube diameter, with theoretical values ranging from 50 to 1315 $m^2 g^{-1}$ [135]. Despite their high electrical conductivity, only CNTs are not optimal material for ECs. Instead, they serve as a high conductive support for the deposition of materials with faradaic response, facilitating rapid charge/discharge processes. Consequently, oxides such as MnO_2 [136-138], RuO_2 [139, 140], Nb_2O_5 [141], and many others have been integrated with nanotubes in a composite electrode material for ECs application [142-147].

ACs offer high SSA (ranging from 1 000 to 2 000 $m^2 g^{-1}$) due to their porous texture, generated by the disoriented structure of graphitic-like sheets randomly linked with each other [148]. The linkage between such fragments generates slits and tunnels throughout the AC matrix [149, 150]. ACs can be produced at moderate costs from various naturally abundant resources such as coke, coal, wood, or coconut shells. Subsequent activation, typically by carbon dioxide, steam, or air, generates their porosity [151-153]. Additionally, ACs can be obtained in different shapes, including powders, fibers, or granulates. Their porous texture can be controlled to some extent by using various templating methods, making ACs suitable for numerous commercial applications [154-157]. Despite their popularity, ACs-based electrode materials primarily exhibit purely capacitive charge storage behavior. Modifying the surface chemistry of ACs can introduce pseudocapacitance, thereby enhancing their electrochemical performance [87]. ACs enriched with heteroatoms such as nitrogen, oxygen, sulfur and phosphorous show altered local electronic density of the carbon matrix, influencing the polarity of the surface [158]. Mainly nitrogen and oxygen are introduced to ACs for electrochemical applications. Nitrogen can be introduced by thermal treatment of AC

in the presence of nitrogen-rich compounds such as urea, ammonia, or melamine, improving the capacitance, stability and voltage window of ACs electrode materials [159-162]. Oxygen functionalities enhance the wettability of the carbon surface and act as redox-active species, improving total specific capacitance. Li *et al.* found that carboxyl and carbonyl groups increase the wettability and charge propagation of AC-based electrodes at certain concentrations [163, 164]. Later, it was found that the redox activity of oxygen functionalities is also pH dependent. For example, quinones and carbonyl groups show redox activity in acidic media, while carboxylic, lactone, or phenol groups react in alkaline media [165]. However, the main drawback of such systems is the relatively low operational voltage window due to the necessity of using sulfuric acid or potassium hydroxide solutions [166]. Pamete et al. introduced low pH electrolytes (i.e., 1 M $BeSO_4$) for use with anthraquinone-functionalized carbon material. The constructed ECs operated at 1.6 V for 10 000 cycles [167]. Although ACs are relatively well-studied as electrode materials for EC applications, other materials are extensively investigated to find those with beyond-capacitive behavior.

Graphene is a 2D material that was isolated from graphite in 2004 by Novoselov using the scotch tape method [168]. This discovery was awarded the Nobel Prize in 2010. Graphene was considered a material of the future due to its outstanding mechanical strength, excellent thermal and electrical conductivity, and lightness. However, its production costs are high, since graphene consists of a single sheet of carbon atoms connected by strong sp^2 bonding in a honeycomb lattice [169]. Producing high-quality graphene is often difficult and neither cost- nor time-efficient. During production, defects can be introduced, altering the local electronic structure, and affecting its extraordinary physicochemical properties and electrochemical behavior [170, 171]. Theoretical SSA of graphene is approximately 2600 m^2/g, making it attractive for EC applications as an electrode material [172]. Due to its high electrical conductivity, graphene has also been integrated with materials that exhibit faradaic properties to create composite electrode materials [173-176].

5.2 Two dimensional transition metal dichalcogenides (TMDs)

Since the development of methods for isolating graphene layers from graphite, researchers, motivated by the promising properties of graphene, have broadened their exploration to include other 2D materials. Transition metal dichalcogenides (TMDs) are a rapidly emerging family of 2D materials that consist fundamentally two layers of chalcogen atoms (e.g., S, Se, or Te) sandwiching one layer of metal atoms (e.g., Mo, Re, V, etc.) and can be represented by a general formula of MX_2 (where M is a metal atom and X is a chalcogen atom) (**Fig. 11 a**) [177, 178]. They can exist in different crystallographic forms depending on the atomic arrangement in the crystal lattice and the number of successive layers in the crystal unit (i.e., 1T, 2H and 3R). As there are various materials, e.g., molybdenum disulfide (MoS_2), vanadium disulfide (VS_2), rhenium disulfide (ReS_2), etc., each can exhibit slightly different physicochemical properties [179]. One of the most studied materials in the literature is **molybdenum (IV) disulfide (MoS_2)** due to its wide natural abundance and extraordinary optoelectronic, catalytic and energy storage properties [180-183]. MoS_2 naturally crystallizes in a hexagonal order (2H) with a monolayer bandgap of ca. 1.9 eV, which renders its semi-conductive properties [183] (**Fig. 11 b**). In the context of energy harvesting, the metallic trigonal (1T) form of MoS_2 is particularly attractive due to its high electrical conductivity (approximately 10^7 times more conductive than a semiconductive form) [184]. Single sheets of MoS_2 can be prepared by various **bottom-up (chemical vapor deposition – CVD,** or **wet-chemical synthesis)**, and **top-down (exfoliation) methods**. CVD involved the formation of MoS_2 on a substrate from gaseous precursors (such as molybdenum oxides/chlorides and sulfur) at high temperatures (above 600 °C) in a flow of inert gas [185, 186]. This method requires separate heating zones to control the reaction kinetics [187]. Even if this method allows for preparation of high quality continuous films of single sheeted MoS_2, it is more expensive than other. Wet chemical methods allow for preparation of large quantities of MoS_2 *via* hydrothermal or solvothermal syntheses. Those methods employ different soluble (in organic solvents – solvothermal, in water – hydrothermal) molybdates and sulfur precursors to prepare MoS_2 at high temperatures in a sealed container called an autoclave [188-190]. Depending on the temperature, pressure, types of precursors, and reaction time, the resultant material can exhibit different morphologies, and physicochemical and crystallographic properties. Thus, resultant functional properties such as catalytic, charge storage properties in aqueous medium, or even

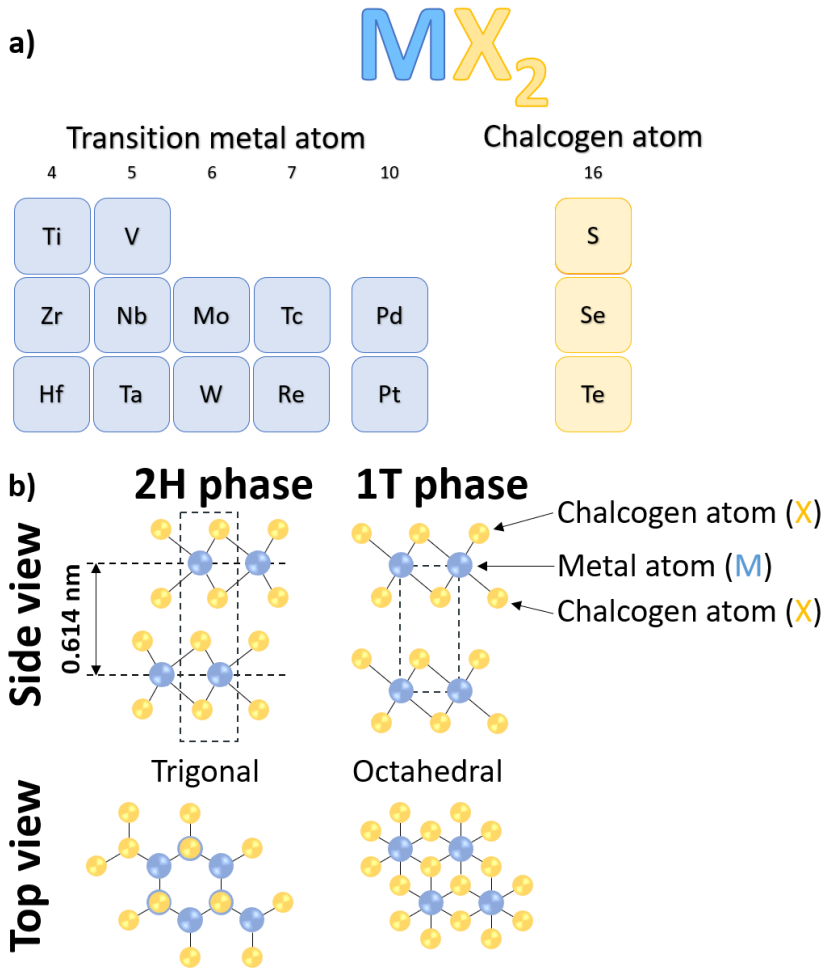

Figure 11 a) Known layered TMDs in the periodic table with a general formula of MX_2, b) stick-balls model of 2H and 1T phases of MoS_2 in side and top view. Yellow and blue balls represent S and Mo atoms, respectively. (Adapted from Ref. [180])

lithium storage can be altered [191-195]. The top-down approach involves exfoliating bulk materials down to single layers and include mechanical, liquid phase, chemical and electrochemical methods [196]. Mechanical methods are based on delaminating single layers of MoS_2 bulk crystallites down to single layers and are comparable to scotch-tape method used for obtaining graphene [197]. Liquid phase exfoliation allows for a high yield of single-sheeted MoS_2 with the assistance of sonication in an adequate solvent. It is necessary to match the solvent's surface tension with the surface energy of MoS_2 to achieve high exfoliation yields [198, 199]. Solvent such as N-methyl-2-pyrrolidone (NMP), or dimethylformamide (DMF) were mostly reported due to matched surface tension energies to the surface energy of MoS_2 [200-202].

MoS_2 can be also exfoliated using chemical approaches, including organolithium treatment. This method involves the chemical intercalation of lithium ions derived from organolithium compounds (e.g., n-buthyllithium – n-BuLi) and subsequent exfoliation of lithiated MoS_2 (Li_xMoS_2) in water with sonication assistance [203, 204]. Organolithium treatment yields high quantities of MoS_2 with flake thickness of about 1 to 5 layers [205]. The charge transfer during Li^+ intercalation causes the transformation from 2H to the 1T phase, leading to the emergence of metallic properties in the exfoliated MoS_2 [206]. After exfoliation and purification, MoS_2 layers are found to bear a negative charge, stabilizing the aqueous suspension [207]. Interestingly, negatively charged layers of MoS_2 (or TMDs in general) can react with various organic and inorganic molecules [208]. Consequently, it is possible to functionalize MoS_2 with diazonium salts, amines, thiols, and other compounds with a formation of different bonding such as covalent, coordination or 'ligand conjugation' (**Fig. 12**) [209-211]. Such modified materials with different molecules were found to show altered physicochemistry which broadens the range of TMDs application and improve their functional properties [212].

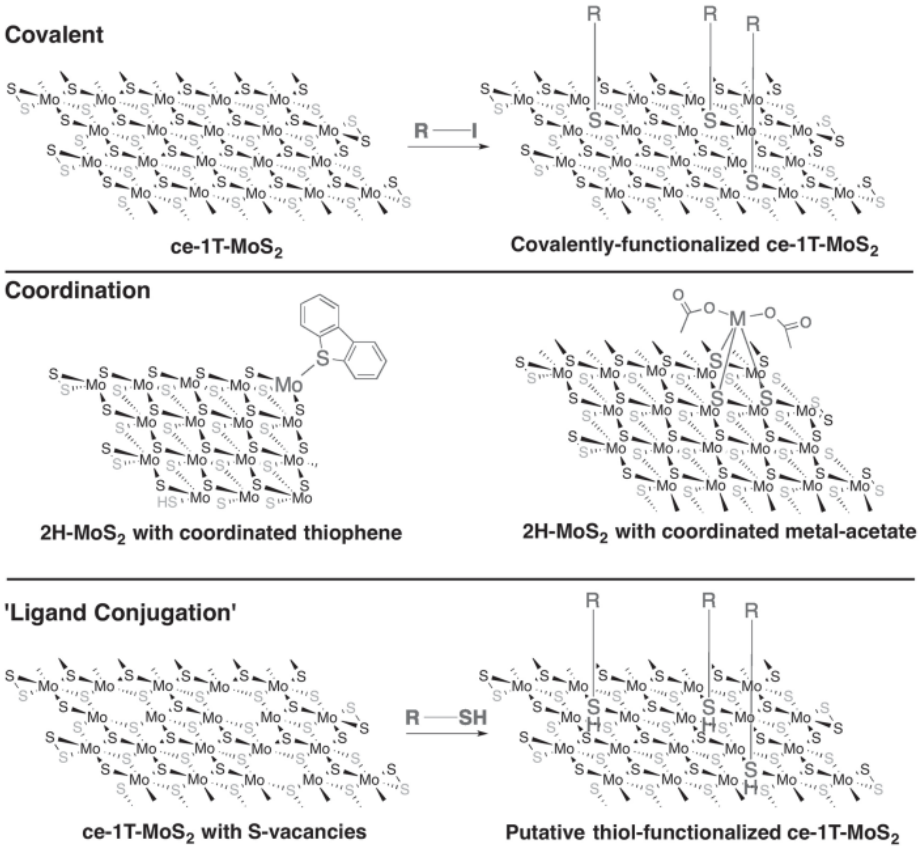

Figure 12 Ways to functionalize TMDs with small molecules. (Adapted from Ref. [209] with permission from John Wiley and Sons).

In the context of energy storage, layered MoS_2, along with other TMDs (such as TiS_2, or VS_2), has been extensively studied as a host material for electrochemical metal ion storage. The intercalation chemistry of TMDs has been well known since 1970s when Whittingham investigated TiS_2 as a potential cathode material for future lithium-ion batteries [213]. In fact, TiS_2 is the lightest of all dichalcogenides, why it was initially introduced as positive electrode material in a battery pilot plant [213, 214]. The charge storage mechanism of TiS_2 is based on the reversible intercalation of lithium ions. TiS_2 naturally occurs in the metallic 1T phase, which excludes the phase transformation upon de/lithiation [215]. Based on the electrochemical behavior of TiS_2, it was initially assumed that TiS_2 exhibits a pseudocapacitive charge storage mechanism, but it was unclear if bulk structures could show comparable electrochemical properties. It was later confirmed by Müller et al. that few-layered nanocrystalline TiS_2 shows improved lithiation kinetics when the bulk structure is reduced to few-nanolayers [216]. Later, it occurred that TiS_2 shows pseudocapacitive behavior with two different lithiation kinetic regions (non-limited and limited by the diffusion) [217].

In the case of the MoS_2, the situation is more complex. Naturally occurring bulk MoS_2 crystallizes in the 2H phase, which transforms to the 1T phase upon electrochemical intercalation of lithium ions at 1.1 V *vs.* Li/Li^+ via a first order phase transition [218]. Subsequent lithiation/delithiation cycles proceed within the potential range of 1 – 3 V *vs.* Li/Li^+ (**eq. 16**) [219, 220]:

$$MoS_2 + xLi^+ + xe^- \rightarrow Li_xMoS_2, \qquad where\ 0 \leq x \leq 1 \qquad \textbf{(eq. 16)}$$

Bulk MoS_2 shows distinct plateaus during galvanostatic cycling and high current humps on cyclic voltammograms, indicating phase transformations occurring in the crystal lattice (**Fig. 13**) [218]. Consequently, the movement of such ion concentration gradient, is responsible for the sluggish kinetics of lithium intercalation, leading to low charge propagation at elevated current densities. However, when MoS_2 crystallites are nanostructured, first order phase transition is suppressed, giving rise to solid-solution intercalation behavior, which shows pseudocapacitive characteristics. Due to the lack of phase transformations, nanostructured MoS_2 demonstrates fast lithium intercalation kinetics allowing for quick charge/discharge [221].

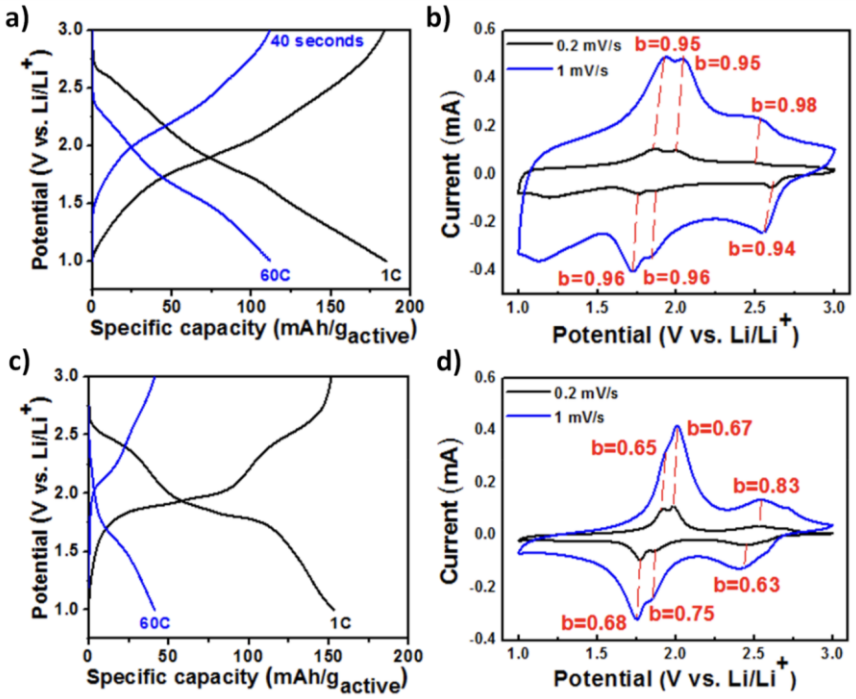

Figure 13 Electrochemical behavior of Nano and Bulk MoS_2. a) Galvanostatic profiles of Nano MoS_2, b) cyclic voltammograms of Nano MoS_2, c) galvanostatic profiles of Bulk MoS_2, d) cyclic voltammograms of Nano MoS_2. Cyclic voltammograms present values obtained for b-value analysis. (Adapted from Ref. [218] with permission from American Chemical Society).

TMDs have also gained significant attention for ECs applications in aqueous media. Commercially available bulk (2H) MoS_2 exhibits rather poor electrochemical performance, with an electrode capacitance of ca. 15 F g^{-1} at a 0.6 V window in symmetrical cell in 1 M Na_2SO_4 [222]. Due to its layered structure, MoS_2 is assumed to store charge *via* electrochemical intercalation of ions. However, the relatively weak van der Waals forces cannot be broken to convert this structure into 1T phase upon electrochemical intercalation reaction within a reasonable potential window. As described previously, the conversion reaction occurs at 1.1 V *vs.* Li/Li^+ (ca. -2 V *vs.* SHE), which is above the thermodynamic potential for hydrogen evolution (especially in sulfuric acid when referring to hydrogen storage). In addition, TMDs are also known for their exceptional hydrogen evolution catalytic properties due to unsaturated sulfur atoms present at the edges of their structure, which is also unfavorable for energy storage in aqueous media [223]. Therefore, it is assumed that the charge storage mechanism in 2H MoS_2 is mostly based on adsorption of ions at the basal planes, not on intercalation within the interlayer spacing.

Instead, researchers have shifted towards the metallic form, which shows much more attractive charge storage properties than the bulk counterpart. Bulk MoS_2 can be converted to metallic form *via* n-BuLi treatment, as presented by Acerce et al. [184]. They prepared self-standing electrodes *via* filtration of an aqueous suspension of exfoliated MoS_2 (**Fig. 14 a**). X-ray diffraction patterns revealed a broader (002) peak after exfoliation, indicating that the layers of MoS_2 are randomly arranged in the crystal lattice (**Fig. 14 b**) with a high content of the 1T MoS_2 phase (**Fig. 14 c**).

After conversion of bulk MoS_2 to the metallic form, it showed capacitive square-shape behavior with significantly increased capacitance, from ca. 70 F cm^{-3} to 650 F cm^{-3} (**Fig. 14 d-e**). The authors studied the electrochemical behavior of restacked MoS_2 in different electrolytes, which showed comparable capacitive features. In comparison to carbon-based electrode materials, TMDs show improved values of capacitance showing higher values of energy and power (**Fig. 14 f**).

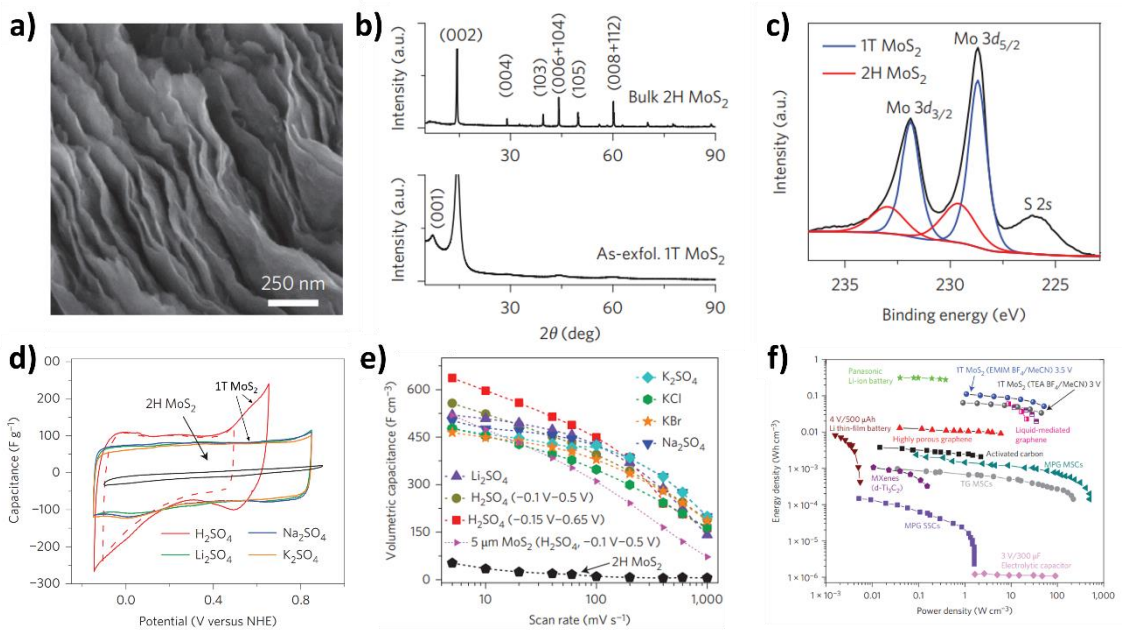

Figure 14 Physicochemical and electrochemical characterization of bulk and chemically exfoliated MoS_2, a) scanning electron microscopy image, b) X-ray crystallographic diffraction (XRD) patterns of bulk and exfoliated MoS_2, c) X-ray photoelectron spectroscopy (XPS) results, d) three-electrode cell electrochemical results of bulk and exfoliated MoS_2, e) volumetric capacitance *vs.* scan rate, f) Ragone plot expressed per volumetric energy density. (Adapted from Ref. [184]).

Chhowalla group conducted ex situ XRD analysis of the cycled electrodes in different electrolytes (**Fig. 15**). Interestingly, they showed that upon cycling, the position of the (002) peak, indicating interlayer spacing (d_{002}), shifts according to the dimensions of the cation used. Electrodes cycled in sulfuric acid revealed a lack of (002) peak position changes, indicating that small, mobile protons can easily diffuse between the interlayer spacing. After cycling in neutral aqueous salts, i.e., Li_2SO_4, Na_2SO_4, and K_2SO_4, the position of the (002) peak shifts accordingly to the solvated cation size. In organic electrolyte, (002) peak position shifts according to the presence of the sole cation. These results indicate that the MoS_2 electrode can dynamically expand to accommodate cations during the intercalation process, suggesting the capacitive nature of the charge originated in the 1T MoS_2.

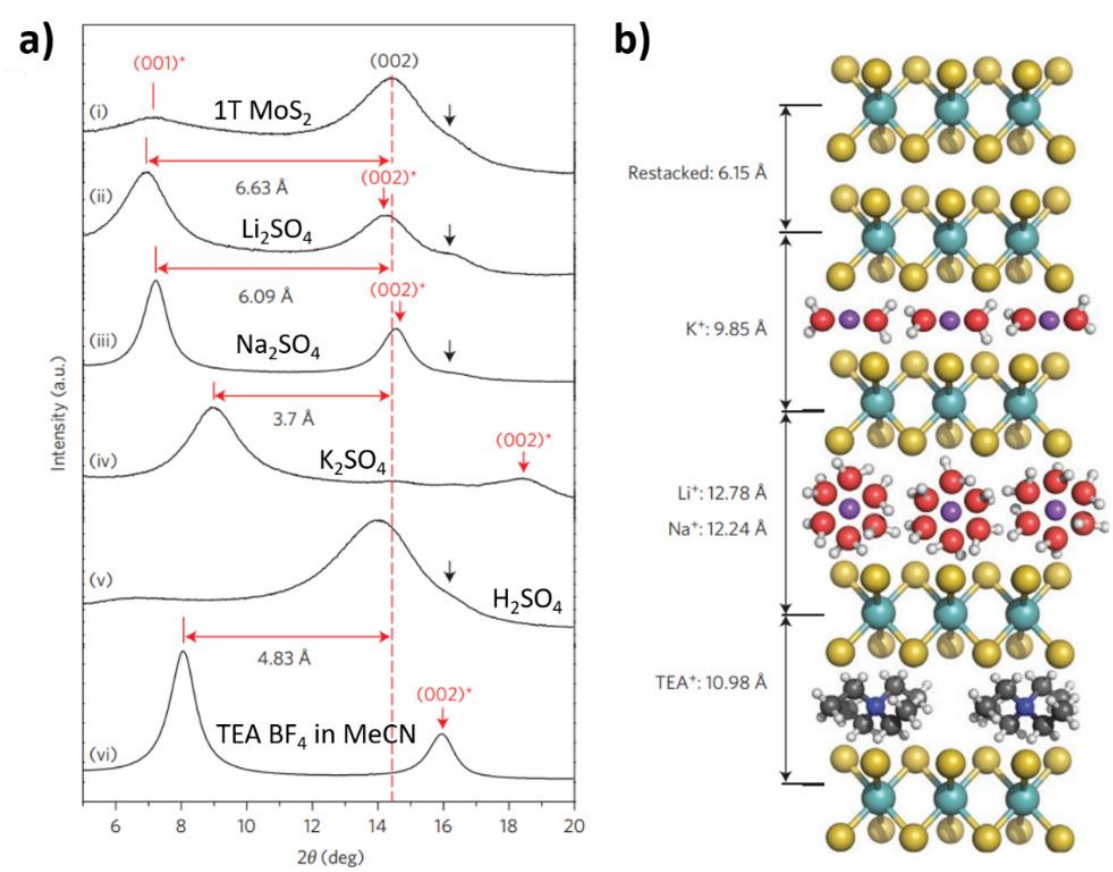

Figure 15 Ex-situ XRD results from different exfoliated MoS_2 films and cycled electrodes. a) XRD patterns from: (i) exfoliated MoS_2, (ii)-(v) electrodes of exfoliated MoS_2 cycled in aqueous electrolytes, Li_2SO_4, Na_2SO_4, K_2SO_4 and H_2SO_4, respectively, (vi) electrode cycled in organic electrolyte, TEA BF4 in MeCN. b) Modelling of the MoS_2 structure with solvated and desolvated cations within the interlayer spacing. (Adapted from Ref. [184]).

However, the detailed mechanism of charge storage in aqueous media is still unclear. The potential-dependent pseudolinear character of electrochemical behavior and changes in interlayer spacing suggest a pseudocapacitive sign with a solid-solution mechanism, but it remains unclear whether the originated charge is faradaic. Some works suggest that the electrochemical performance of MoS_2 is purely capacitive and occurs only based on adsorption of ions within the interlayer spacing of MoS_2 [224]. Other works consider the redox behavior of 1T MoS_2, involving two different possible mechanisms: proton insertion/desertion into the MoS_2 interlayers (**eq. 17**), and the redox deposition of protons on the interlayer surface of the MoS_2 nanosheets (**eq. 18**) [225].

$$MoS_2 + H^+ + e^- \rightarrow MoS - SH \qquad \textbf{(eq. 17)}$$

$$MoS_2 + H^+ + e^- \rightarrow MoS_2 - H \qquad \textbf{(eq. 18)}$$

Overall, the detail mechanism of charge storage in aqueous media is still under consideration, as not all TMDs are the same in terms of defects, structure, morphology, porous texture, and defect sites. As reviewed above, there are different methods to obtain TMDs in various structures, and depending on the intended application, it is possible to control their physicochemical properties. These properties can be further adjusted by altering their surface chemistry, which can expand their tunability.

In the context of energy storage, TMDs exhibit improved capacitance values compared to commercially available carbons. They can display pseudocapacitive properties, which can be enhanced when paired with different conductive carbon substrates. The development of novel TMDs composites is crucial for advancing electrochemical energy storage technologies, especially in ECs and batteries. Future research should continue to explore new synthesis methods, functionalization techniques, and hybrid composites to utilize the full potential of TMDs in energy storage applications.

Chapter II

Dissertation outline

Aim of the dissertation

ECs are promising energy storage devices which offer significant advantages over conventional LIBs in reachable power-density and longevity. Nevertheless, there is a significant gap between the energy-density of ECs and LIBs. Consequently, the main direction of ECs research is the development of ways to improve their energy density.

The energy density of a EC can be improved by enhancing the capacitance of the system and by widening its operational voltage window. Within the electrode materials, research focuses on the development of novel electrode materials able to show attractive values of capacitance and wide potential window.

Recently, 2D materials such as transition metal dichalcogenides (TMDs) have been demonstrated to give high values of the capacitance (above than carbons) which could improve the overall energy density of a device.

Considering the above, the research hypothesis arises – **can 2D materials such as TMDs be used for ECs application to effectively increase their device capacitance?**

Chapter III presenting three published articles (P1, P2, P3) focuses on the development of hydrothermal synthesis protocol for the synthesis of novel 2D TMDs. Due to their low electrical conductivity, they were paired with highly conductive carbon supports which effectively improved their electrochemical performance in symmetrical cell. However, due to the hydrogen evolution reaction (HER) catalytic activity of TMDs, the voltage window of such device was limited to below 1 V.

Chapter IV presenting one published article (P4) addresses the HER catalytic activity issue and highlights the possibility of covalent functionalization of 2D TMDs with redox active species. Such modified TMD is utilized as the EC negative electrode material which significantly improves the electrochemical cell performance. As TMDs are layered materials, they were also exploited as a host for lithium-ion storage in organic electrolyte.

Chapter V presenting additional results (5) highlights the importance of a sulfur precursor choice during hydrothermal synthesis of TMDs. Dependent on the utilized precursor, different structure, morphology, and porous texture properties were found which affected the electrochemical lithium intercalation behavior. *Operando* measurements, i.e., XRD and dilatometry were utilized to study the charge storage properties.

Dissertation structure

Results obtained in this PhD dissertation are divided into three parts. **Chapter III consists of three published articles attached** and focus on the implementation of the 2D materials as electrode materials in ECs application.

Chapter III Evaluation of the electrochemical properties of 2D materials

P1. *Electrochemical Capacitor Performance of Nanotextured Carbon/Transition Metal Dichalcogenides Composites*

P2. *Supercapacitor with Carbon/MoS_2 Composites*

P3. *Electrochemical Capacitor Based on Reduced Graphene Oxide/NiS_2 Composite*

Chapter IV **consists of one published article attached**, which focus on the functionalization of layered nanostructured MoS_2 with redox active molecules. This chapter describes the electrochemical performance of such modified MoS_2 in different aqueous and organic media.

Chapter IV Covalent modification of 2D material by redox-active species

P4. *Nanostructured MoS_2 grafted by anthraquinone for energy storage*

Chapter V **consists of additional publicly open data, but not peer reviewed yet (sent for review)**. The results presented in this chapter was obtained during scientific internship in *Helmholtz Institute of Ulm,* Germany. They are consistent to the PhD dissertation topic and are complementary data. This chapter focuses on the utilization of different sulfur precursors during hydrothermal synthesis of MoS_2. Dependent on the properties of the resultant MoS_2, the pseudocapacitive behavior of MoS_2 will vary in organic media.

Chapter V Emergence of pseudocapacitive properties of 2D materials

5. *Controlling structure and morphology of MoS_2 via sulfur precursor for optimized pseudocapacitive lithium intercalation hosts*

Chapter III

Evaluation of the electrochemical properties of 2D materials

P1. *Electrochemical Capacitor Performance of Nanotextured Carbon/Transition Metal Dichalcogenides Composites*

Authors: Elżbieta Frąckowiak, Masoud Foroutan Koudahi#, Maciej Tobis#

Journal: Small, **2021**, 17, 2006821

DOI: https://doi.org/10.1002/smll.202006821

License: The content is available under CC BY 4.0

Contribution: Synthesis of ReS_2-based composites, physicochemical analysis, electrochemical characterization, data plotting, writing original draft

# The authors have contributed equally

Graphical abstract

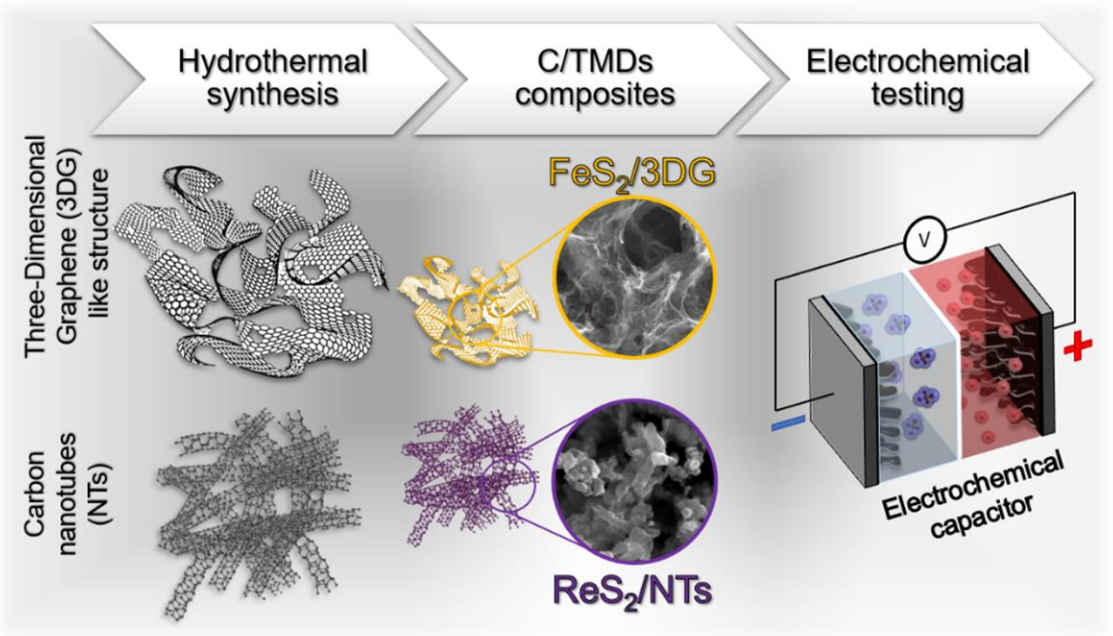

Context of research & summary

Generally, electrode material research predominantly focuses on carbon-based materials such as ACs, CNTs, and graphene. These materials offer significant advantages such as low cost, developed SSA, and excellent electrical conductivity. However, their charge storage mechanism is limited to the physisorption of ions at the electrode/electrolyte interface, resulting in moderate capacitance values. Consequently, many studies aim to integrate carbon-based materials with redox active components to enhance their capacitance, and thereby, the energy density of a device. A prime example is Skeleton Technologies, a company known for the commercial production of ECs based on carbon materials operating in organic electrolytes. However, to broaden their range of application, they introduced a device called *SuperBattery,* which integrates carbon-based materials with metal oxides, enabling fast reversible redox reactions and achieving high energy and power densities [226].

In this context, TMDs are emerging as promising layered materials capable of exhibiting faradaic behavior, potentially reaching higher capacitance values than those observed for carbon-based materials. However, TMDs generally suffer from moderate electrical conductivity, and for that reason they are paired with conductive supports such as carbonaceous materials to enhance capacitance and charge propagation.

This study presents the integration of TMDs, specifically rhenium disulfide (ReS_2) and iron disulfide (FeS_2), with a carbonaceous matrix to obtain composite materials with improved electrochemical performance.

Among the TMD family, ReS_2 has been poorly studied. It was recently synthesized through hydrothermal route, allowing to obtain nanostructured few-layered flakes of ReS_2 [227]. ReS_2 naturally crystallizes in the 1T phase, avoiding the formation of 1T/2H phases mixture, where the 2H phase offers limited charge storage properties as explained before in the case of MoS_2 [228]. Both composites (ReS_2 and FeS_2) were fabricated using a hydrothermal synthesis method, with multiwalled carbon nanotubes (NTs) and a three-dimensional graphene-like network (3DG) serving as the substrates for the deposition of ReS_2 and FeS_2, respectively.

Scanning electron microscopy (SEM) imaging revealed that the ReS_2/7wt% NTs composite resembles morphology of the NT support, with surface well covered by the perpendicularly positioned ReS_2 nanolayers. For the FeS_2/3DG composite,

FeS_2 was deposited on the hierarchical porous structure of 3DG. The morphology was found to significantly influence the electrochemical properties of the composite material.

A symmetrical cell containing the ReS_2/NTs-based composite electrode material displayed square-shaped cyclic voltammograms (CVs) at low voltage (0.5 V), characteristic for capacitive phenomena. Hybridization of ReS_2 and NTs also led to increased capacitance and conductivity confirmed by CV, constant current charging, and electrochemical impedance spectroscopy (EIS) measurements. During voltage extension, the cell exhibited a high current density peak at 0.8 V, indicating hydrogen evolution at the negative electrode and oxygen evolution at the positive electrode. This suggests that the perpendicularly positioned ReS_2 nanolayers may induce catalytic effects related to electrolyte decomposition. At 0.8V, the symmetrical cell exhibited a high capacitance of 110 F g^{-1} at 0.2 A g^{-1} current density.

Conversely, the FeS_2-based composite exhibited a higher voltage limit of 1.5 V, highlighting the importance of material selection in optimizing electrochemical performance, with a high capacitance of 240 F g^{-1} at current density of 0.2 A g^{-1}. Furthermore, the study examined the cyclic stability and rate performance of the composites. The ReS_2/CNTs composite retained about 85% of its initial capacitance after 13 000 charge-discharge cycles at 0.8 V and 1 A g^{-1} current load. The 3DG/FeS_2 composite showed minimal capacitance loss over 8 000 cycles at 1.5 V and 10 A g^{-1}. Rate performance tests revealed that both composites maintained a significant fraction of their capacitance at higher current densities.

In conclusion, integrating nanotextured carbon with TMDs such as ReS_2 and FeS_2 offers a promising pathway for developing high-performance electrodes for ECs. The results of this study suggests that the catalytic nature of certain TMDs could limit their practical application and need to be appropriately addressed in further studies.

Publication

P1. *Electrochemical Capacitor Performance of Nanotextured Carbon/Transition Metal Dichalcogenides Composites*

FULL PAPER

NANO · MICRO small
www.small-journal.com

Electrochemical Capacitor Performance of Nanotextured Carbon/Transition Metal Dichalcogenides Composites

Elżbieta Frąckowiak, Masoud Foroutan Koudahi, and Maciej Tobis*

Transition metal dichalcogenides (TMDs) are emerging low-dimensional materials with potential applications for electrochemical capacitors (EC). Here, physicochemical and electrochemical characterizations of carbon composites with two sulfides ReS_2 and FeS_2 are reported. To enhance conductivity, multiwalled carbon nanotubes (NTs) serve as a support for ReS_2 while 3D graphene-like network (3DG) is utilized for FeS_2 deposition. Unique structure of carbon/TMDs composites allows a faradaic contribution of sulfides to be exploited. Capacitance values, charge/discharge efficiency, capacitance retention, charge propagation, cyclabilty, and voltage limits of EC with carbon/sulfide composites in aqueous neutral solutions (Li_2SO_4, Na_2SO_4) are analyzed. Special attention is devoted to energetic efficiency of capacitive charge/discharge processes. Structure-to-capacitance correlation for the composites with various TMDs loading is thoroughly emphasized. The more defected structure of layered NTs/ReS_2 composite is responsible for the lower capacitor voltage (0.8 V) owing to quicker electrolyte decomposition. Additionally, the catalytic effect of Re for hydrogen evolution reaction plays a crucial role in EC voltage restriction. Contrary, the operating voltage of capacitor based on 3DG/FeS_2 is able to be extended until 1.5 V in sodium sulfate electrolytic solution.

1. Introduction

Electrochemical capacitors (ECs) are high-power energy storage devices that are expected to play a significant role in various future applications, for example, electrical cars, shuttles, cell phones, or power plants. It is worth noting that EC escape battery safety and disposal issues. The energy storage in ECs occurs mainly through the electrostatic accumulation of charges at the electrode/electrolyte interface, hence, it is required that the electrode materials should possess a developed specific surface area and high conductivity.[1–3] Many representatives of carbons such as activated carbon, carbon fibers, carbon NT/composites, or graphene fit those characteristics and are mostly used in ECs. However, they offer moderate capacitance due to the limited specific surface area and non-uniformly distributed pores which hinder the accessibility of the vacant sites for ions. Therefore, more efforts are directed into developing new composites with redox phenomena which will meet the requirements of high energy and power density as well as high cyclability.[4–6] 2D transition metal dichalcogenides (2D-TMDs) are promising candidates due to their layered structure, a large variety of metal-dichalcogenide combinations, and exposed active sites.[7–12] Yet, they offer moderate conductivity and stability which limits their application in long-term operating devices. So far, molybdenum disulfide (MoS_2) and tungsten disulfide (WS_2) are the most often reported as EC electrode materials.[13–15] Application of carbon materials as a conducting substrate for TMDs is indispensable. Deposition of a thin layer of TMDs on carbon scaffold (e.g., carbon nanotubes (NTs), graphene) improves not only the power rate but also capacitive behavior of the composite. For example, electrode based on MoS_2-carbon nanoplates have been prepared by hydrothermal-calcination method and symmetric capacitor cell with such composite demonstrated a specific capacitance of 248 F g^{-1} at a current density of 0.1 A g^{-1}.[16] Moreover, the aforementioned electrode showed a fast response, that is, even at high scan rate of 300 mV s^{-1} the electrode preserved its rectangular shape. In another study, Chen et al. designed a composite based on carbonaceous materials such as CNTs, graphene, and carbon black as the substrate and MoS_2 as the redox active material. Among the synthesized electrodes, CNTs/MoS_2 showed a high specific capacitance of 402 F g^{-1} at a current density of 1 A g^{-1}. Also, this electrode exhibited a good cyclability by maintaining nearly 80% of its initial capacitance after continuous 10 000 charge–discharge cycles at a current density of 1 A g^{-1}.[17] WS_2/composites have been widely investigated in EC application. For instance, Rout et al. tailored a hybrid electrode based on reduced graphene oxide (GO) and WS_2 through one-step hydrothermal procedure. A high specific capacitance of 350 Fg^{-1} was achieved at a scan rate of 2 mV s^{-1}.[18] Additionally, other types of TMDCs such as CoS_2,[19] SnS_2,[20] and VS_2[14] were utilized for EC application. For example, Jun et al. synthesized electrode materials based on CoS_2 deposited on S and N co-doped nanosheets and such electrodes delivered a high specific capacitance of 283 F g^{-1} at a current density of 1 A g^{-1}. Furthermore, this

Prof. E. Frąckowiak, M. Foroutan Koudahi, M. Tobis
Institute of Chemistry and Technical Electrochemistry
Poznan University of Technology
Poznan 60965, Poland
E-mail: elzbieta.frackowiak@put.poznan.pl

The ORCID identification number(s) for the author(s) of this article can be found under https://doi.org/10.1002/smll.202006821.

© 2021 The Authors. Small published by Wiley-VCH GmbH. This is an open access article under the terms of the Creative Commons Attribution License, which permits use, distribution and reproduction in any medium, provided the original work is properly cited.

DOI: 10.1002/smll.202006821

ADVANCED SCIENCE NEWS
www.advancedsciencenews.com

NANO · MICRO small
www.small-journal.com

electrode showed no capacitance decrease after 5000 cycles of constant charge–discharge at a high current density of 20 A g^{-1} which indicates its favorable stability at harsh conditions.

Even if in the literature cited above, the high capacitance values are indicated, very often only cyclic voltammetry (CV) results in a three-electrode cell are shown without comparison to galvanostatic data from a two-electrode cell (real system). Additionally, capacitance values are frequently calculated taking only Coulombic efficiency (discharge time) but not energetic efficiency where capacitance is estimated from integrating the galvanostatic discharge curve. Especially if discharge curve is concave, the capacitance value calculated from discharging time is highly overstated. Some studies are performed with the electrode mass below or equal to 1 mg what is practically not applicable, long-term cycling by CV in a three-electrode cell has no sense as well. Hence, the critical point of view is necessary during literature analysis.

Aside from the most popular TMDs mentioned, rhenium disulfide (ReS_2), which has rarely been explored in the case of energy storage devices has recently gained significant attention in metal-ion batteries (MIBs).[21–23] ReS_2 is popular in MIBs due to similar interlayer spacing to MoS_2 (0.614 to 0.615 nm) and more than 25 times weaker interlayer energy coupling.[24] However, in the case of EC, it has been never reported.

Here, the original composites with a various proportion of multiwalled carbon NTs and ReS_2 have been prepared by hydrothermal method to study capacitor performance. Additionally, novel material based on 3D graphene network (3DG) like structure as a matrix for iron sulfide has been designed. Interestingly both carbon networks (CNTs and 3DG) are characterized by different structure/texture, hence, composites supplied distinct electrochemical performance. The target of this research is to synthesize the composites which show synergistic properties of both materials, that is, carbons and TMDs, to exploit their electrochemical performance, conductivity, and unique structure. The reason of different operating voltage limits for both composites has been revealed. Voltage range, in turn, is an important metric that affects the energy of capacitor device.

2. Results and Discussion

Low-dimensional materials such as graphene and TMDs have been under significant consideration as novel materials for the ECs. Herein, we report on the hydrothermal synthesis of composites based on rhenium disulfide with multiwalled carbon NTs and iron disulfide with 3DG. The scheme of TMD/carbon composite preparation via a hydrothermal synthesis is presented in **Figure 1**, where carbon NTs and 3DG materials play a scaffold role for deposition of Fe and Re sulfides.

First, different proportions of NTs and Re sulfide in composite were studied to find the optimal composition. It is well known that carbon NTs, as highly mesoporous material, provide negligible capacitance (a few F g^{-1}); generally the more pure and well organized structure of NTs, the lower capacitance values.[25,26] Hence, the very moderate amount of NTs (7 wt%) was the most beneficial. In fact, ReS_2 was the main component (93 wt%) in this composite. Mesoporous character of the nanotextured ReS_2/7 wt% NTs and NTs was proven by N_2 adsorption/desorption. Figure S1, Supporting Information presents the isotherms and inset with a pore size distribution. Isotherms show a steep increase of N_2 adsorbed at low relative pressure exhibiting limited presence of micropores and a peak at high relative pressure region indicating presence of bigger pores. During desorption a significant hysteresis is observed. Type IV isotherms demonstrate clearly a mesoporous character of both materials. The volume of N_2 adsorbed/desorbed by ReS_2/7 wt% NTs is significantly lower than for the pure NTs. It means that the deposited TMD layers have decreased the overall surface area mainly in the range of mesopores. Specific surface area and porosity features are compiled in Table S1, Supporting Information.

The distribution of elements and the morphology/texture of such composite (**Figure 2**) was studied by scanning electron microscopy (SEM) combined with energy dispersive spectroscopy (EDS).

The SEM images with different scales show that the composite exhibits derivative morphological shape to the NTs with

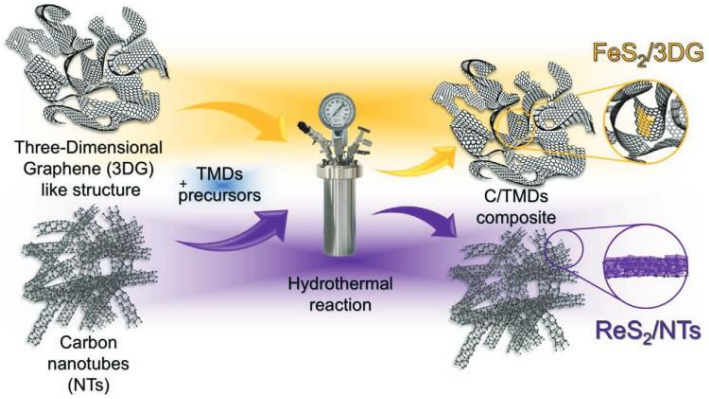

Figure 1. The simplified scheme of synthesis for two different composites: 3DG/FeS_2 and CNTs/ReS_2.

 © 2021 The Authors. Small published by Wiley-VCH GmbH

ADVANCED SCIENCE NEWS
www.advancedsciencenews.com

NANO · MICRO small
www.small-journal.com

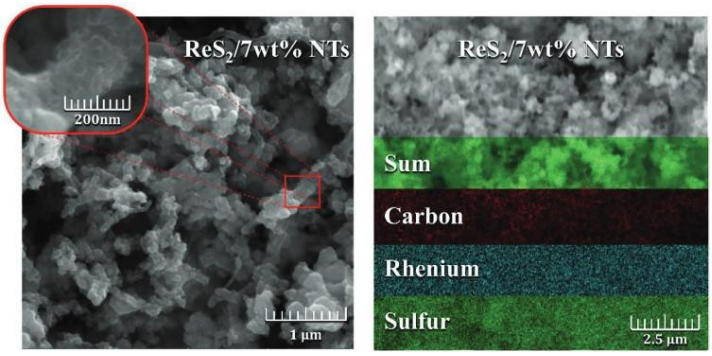

Figure 2. SEM images (left) and EDS mapping (right) of ReS_2/7 wt% NTs composite.

cauliflower-like structure. However, at high magnification the perpendicular flakes with exposed edges are well visible. EDS mapping shows that the individual atoms of ReS_2 are well distributed on the surface of the NTs, it means that the carbon NTs are firmly covered by ReS_2 layers. During the synthesis of the composite, ReS_2 layers are being formed on the surface of the NTs favorably at the structural defect sites. Typically, during deposition process the defect sites play a nucleation role. This unique morphology allows the electrolyte to penetrate through the whole electrode. Thus, the dense layered structure creates many active sites for ions to be freely adsorbed and desorbed during ECs charge/discharge. Generally, the layers can be directed perpendicularly or parallel to the NTs plane.[27] In this case, due to the low controllability of the hydrothermal synthesis process the layers are distributed randomly and most likely vertically to the NTs surface as it can be observed in the inset of Figure 2.

To analyze the crystal structure of the powdered materials, both samples (ReS_2 and ReS_2/7 wt% NTs composite) were investigated by the X-ray diffraction (XRD) technique. As shown in the **Figure 3**, peaks at 14.5°, 32.5°, 43.5°, and 60.9° (2θ) are observed and can be attributed to ReS_2 (JCPDS # 00-063-0205) namely (100), (002), (006), and (008) planes, respectively. The lack of intense peak confirms the disordered layered structure of the composite.

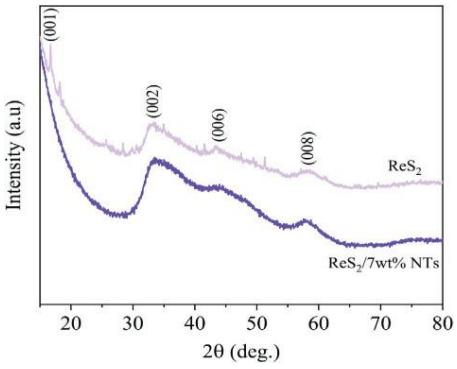

Figure 3. XRD diffractograms for ReS_2 and ReS_2/7 wt% NTs composite.

After a detailed physicochemical characterization, synthesized materials were successfully employed as electrodes in electrochemical capacitor (EC) cells and investigated by CV, galvanostatic charge/discharge with potential limitation (GCPL), and electrochemical impedance spectroscopy (EIS). For the two-electrode electrochemical investigations, Swagelok cell with two stainless steel pistons was used. Two separated electrodes of similar mass were soaked with 1 mol L^{-1} Li_2SO_4 electrolyte. Detailed investigation of the individual electrodes was performed utilizing a cell combined additionally with Hg/Hg_2SO_4 reference electrode.

Deposited ReS_2 onto carbonaceous materials improved the overall performance of the assembled EC system due to the exhibition of faradaic reactions. Cells prepared with ReS_2/7 wt% NTs demonstrated a capacitance of 108 F g^{-1} (**Figure 4**). For comparison, the cells with pure carbon materials (NTs) were also investigated.

The performances of the ECs cells were evaluated accordingly to the very well-known methodology.[28] At the beginning, the symmetrical cell assembled with ReS_2/7 wt% NTs was studied by CV. The window voltage was extended by 0.1 V beginning from 0.5 V with the 1 mV s^{-1} sweeping rate (Figure 4a). The performance of the full cell with the separate behavior of positive and negative electrodes is presented in Figure 4b. It can be observed that at low scan rates the electrodes exhibit nearly rectangular square shape which is characteristic for the capacitive behavior of electric double-layer capacitors. Further voltage extension shows no faradaic contribution until 0.8 V where the characteristic peaks, which can be attributed to oxygen and hydrogen evolution are appearing on the positive and the negative electrode, respectively. While it is understandable that the oxygen evolution appears close to the calculated potential value for the water decomposition, the hydrogen evolution limit is much further from what is observed experimentally. Layered ReS_2 and most of other representatives of 2D-TMDs family, are consisting of inert basal plane and active edge sites.[29–31] TMDs

 © 2021 The Authors. Small published by Wiley-VCH GmbH

ADVANCED SCIENCE NEWS
www.advancedsciencenews.com

NANO · MICRO small
www.small-journal.com

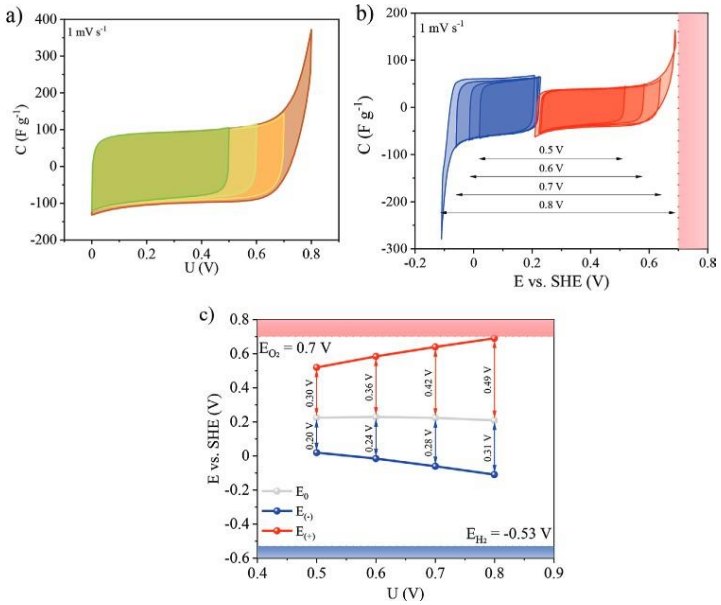

Figure 4. a) Electrochemical characterization of symmetric EC with ReS_2/7 wt% NTs by cyclic voltammetry (1 mV s^{-1}) with a gradual voltage extension. b) Electrochemical behavior of individual electrodes is depicted, c) with the thermodynamic limit of O_2 and H_2 evolution. Electrolyte—1 mol L^{-1} Li_2SO_4.

will promote hydrogen evolution, dependent on the amount of edge site exposed.[32–33] Additionally, Figure 4c shows that the positive electrode works on a wider potential window than the negative one. From characteristics of the negative electrode, it looks that the hydrogen storage does not proceed at all, just contrary this material has a tendency to catalyze hydrogen evolution reaction (HER) during the voltage extension. It should be considered that the NTs as typical mesoporous material cannot store hydrogen, additionally NTs amount is very low. On the other hand, hydrogen evolution is governed by a balance between the surface coverage and reactivity illustrated by the so called volcano plot, that is, M—H bond strength versus log i_0 (exchange current). Re as metal occurs close to noble metals (Pt, Pd) which greatly catalyze HER. Due to the high evolution peaks indicating oxygen and hydrogen evolution at higher voltage, it was decided to perform other electrochemical investigations at 0.8 V.

The voltammetry characteristics of cells assembled with ReS_2/7 wt% NTs at various scan rate from 2 to 200 mVs^{-1} are shown in **Figure 5a**. The rectangular shape of the voltammograms at all sweeping rates indicates the capacitive behavior of the electrodes. Thanks to the intimate interconnection of the ReS_2 nanolayers to the NTs, the composite electrode exhibits higher conductivity from NTs and increased capacitance due to the TMD presence as well as because of the higher specific surface area of composite. It can be stated that the composite possesses the intermediate properties to the parent materials. NTs significantly improve the charge propagation of the electrode. GCPL characteristics for the cells with ReS_2/7 wt% NTs limited to 0.8 V at different current loading from 0.2 to 2 Ag^{-1} are shown in Figure 5b. The curves represent close to ideal triangular lines which are associated with capacitive behavior. The integrated capacitance values for ReS_2/7 wt% are 108, 94, 82, and 73 F g^{-1} at 0.2, 0.5, 1, and 2 A g^{-1}, accordingly.

The same voltammetry test was conducted for the cell with pure ReS_2 (Figure S2, Supporting Information). The ReS_2 alone showed a high capacitance but with much lower charge propagation and inferior conductivity. Cell with ReS_2 comparably to composite shows nearly squared shape profile but only at lower scan rates. At higher sweeping rates, the voltammograms lose the squared shape because of the diffusion limits. The EC in both cases (ReS_2 and ReS_2/NTs) did not show redox peaks. It is well known that some electrochemically active materials do not show redox peaks (e.g., ruthenium oxide, nitrogenated carbons). Hence, in that case, the faradaic reactions of TMD should not be excluded. The following reaction can be considered: $ReS_2 + Li^+ + e^- \leftrightarrow ReS - SLi$

EIS is very valuable, complementary technique for capacitor investigation. Nyquist plots and the analog circuit diagrams for capacitor built with all materials, that is, NTs, ReS_2, and ReS_2/7 wt% are presented in Figure S3, Supporting Information. EIS results were measured within the frequency range of 1 mHz–10 kHz. Pure NTs in comparison to composites showed significantly smaller capacitance but exhibited superior charge propagation and great conductivity. The capacitor working with NTs exhibited

 © 2021 The Authors. Small published by Wiley-VCH GmbH

ADVANCED SCIENCE NEWS
www.advancedsciencenews.com

NANO · MICRO small
www.small-journal.com

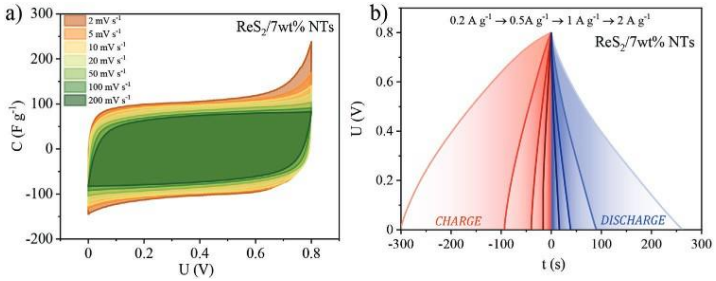

Figure 5. a) Voltammetry and b) galvanostatic characteristics for the capacitor built from ReS_2/7 wt% NTs composite. Electrolyte—1 mol L^{-1} Li_2SO_4.

negligible values of ESR and EDR (0.77 and 1.58 Ohms). The imaginary part of the impedance characteristics grows in parallel to the *y*-axis meaning that there is no effect of redox reactions especially for NTs. However, for the composite clear diffusion limitation is observed. In case of the cell constructed with ReS_2/7 wt% NTs, the system showed comparable values of ESR and an increase of EDR value (0.8 and 8.2 Ohms, respectively). Such an increase in resistance of the cell comes from the addition of ReS_2 to the composite material. Also, the shape of the impedance curve is no longer parallel to the *y*-axis. Cell assembled with ReS_2 exhibited distinct semi-circle due to the redox reactions and lower conductivity of the material. Charge propagation is an important EC metric. EIS technique is perfectly adapted for monitoring this property. In addition to Nyquist plots, the capacitance versus frequency chart has been presented in **Figure 6**. Due to a significant difference between the capacitance values depicted for NTs in comparison to other materials, capacitance has been replaced with capacitance retention. Fast response of the NTs cell can be explained by the very high conductivity of the material. For NTs the capacitance remains stable up to 3 Hz while gradually drops for ReS_2, the composite still preserves 50% value at 1 Hz. As

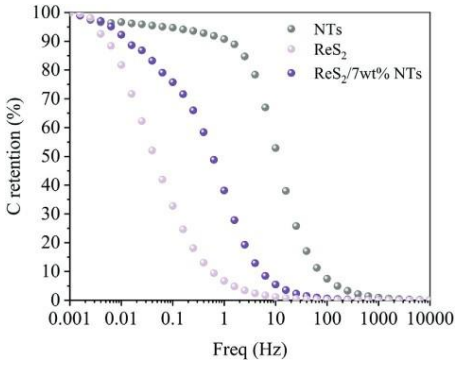

Figure 6. Capacitance retention versus frequency for ReS_2/NTs composite and its components.

expected, the composite possesses the intermediate characteristics. In conclusion, a proportion of components in composite has a fundamental influence on charge propagation.

The cyclability of the ReS_2/7 wt% NTs were also studied (Figure S4, Supporting Information) by performing 13 000 galvanostatic cycles at 0.8 V with current rate of 1 A g^{-1}. Capacitance retention was found to be 85% of the initial value.

The second TMD/composite material studied in this work is graphene-like 3DG/FeS_2. This unique carbon skeleton characterized by an interconnected, porous structure including pores with various size, ranging from a few micrometers to nanometers, provides excellent electron and ion conductivity.[34] Considering the chemical stability and physical robustness of 3DG-like structure, it can be used as the promising scaffold for deposition of other active material[35–39] such as FeS_2. The structure of 3DG is affected by its precursor, that is, graphite oxide. The proper oxidation of graphite powder to graphite oxide is important, since it affects the dispersion of GO layers inside the solution.[40] Graphite oxides with high content of different oxygenated functionalities guarantee the creation of 3DG matrix with interconnected porous structure. Subsequently, the dispersion level of GO layers has the main influence on the size of the pores, in the porous skeleton of 3DG.[41] Deposition of a thin layer of the TMDs on 3DG network improves not only the power rate but also the capacitive behavior of the TMDs-based electrodes, since all of the TMDs content will be accessible to ions for surface electrochemical interactions.

For physicochemical characterization of graphene-like 3DG/FeS_2 composite, N_2 sorption measurements were performed. Figure S5, Supporting Information presents the isotherms and the pore size distribution for the nanotextured 3DG/FeS_2. Specific surface area and the porosity properties are displayed in Table S1, Supporting Information. A moderate drop of porosity is observed for composite material. **Figure 7** shows the SEM images of freeze-dried 3DG and 3DG/FeS_2 composites. 3DG sample consists of a hierarchical highly porous structure. The pores are connected to each other and are spread in the internal structure of this substrate. The walls of the graphene-like network are thin and majority of the internal space is occupied by void, which implies the minimal aggregation of graphene layers.[42] Deposition of the active materials on such a porous structure, including pores with

 © 2021 The Authors. Small published by Wiley-VCH GmbH

ADVANCED SCIENCE NEWS
www.advancedsciencenews.com

NANO · MICRO small
www.small-journal.com

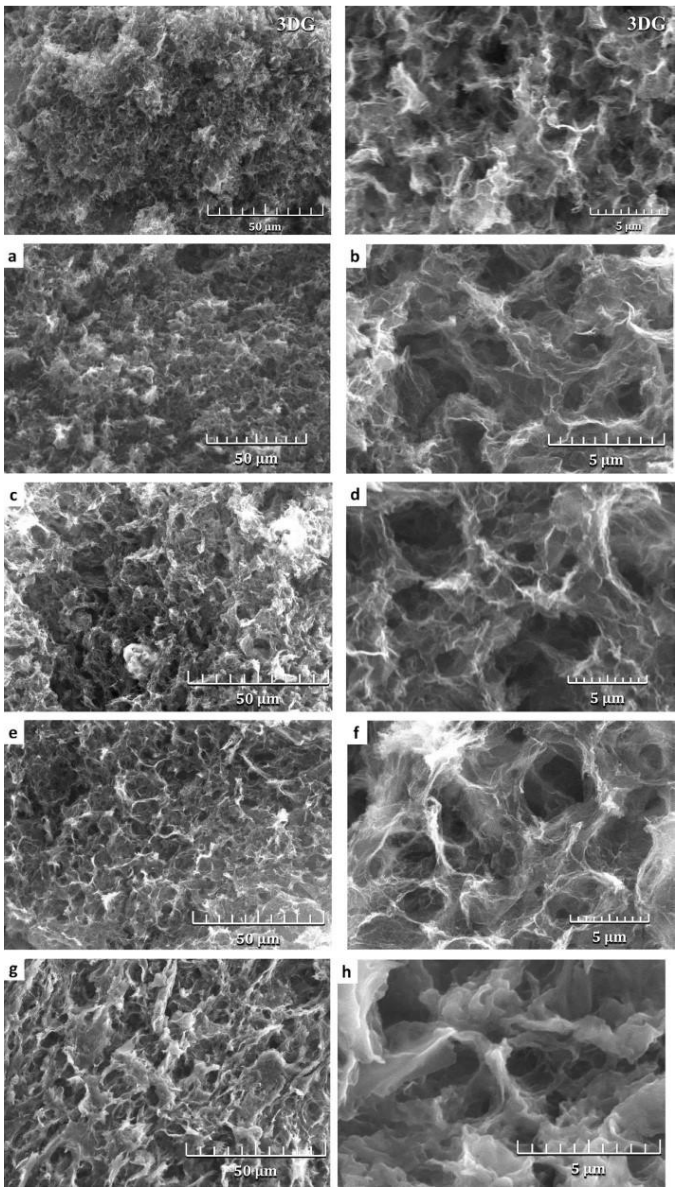

Figure 7. SEM images of freeze-dried 3DG and 3DG/FeS_2 composites at different magnifications a,b) 5, c,d) 10, e,f) 15, g,h) 20 wt% FeS_2.

 © 2021 The Authors. Small published by Wiley-VCH GmbH

ADVANCED SCIENCE NEWS
www.advancedsciencenews.com

NANO · MICRO small
www.small-journal.com

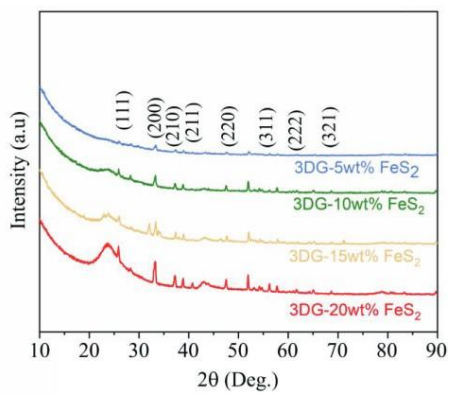

Figure 8. XRD structural characterization of 3DG/FeS_2 composites with various content of sulfide.

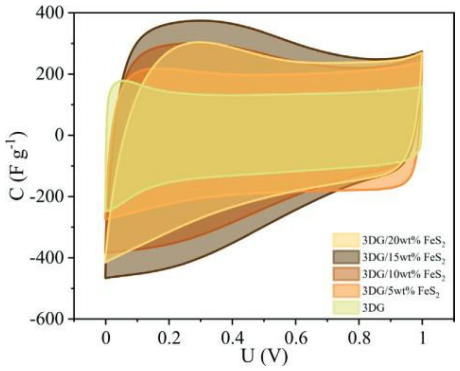

Figure 9. Comparison of CVs at 2 mV s^{-1} for composites with a different FeS_2 content. Electrolyte—1 mol L^{-1} Na_2SO_4.

a wide range size, can be challenging, since high percentage of loading will result in losing a majority of small pores which plays a crucial rule in capacitive applications based on sorption/desorption. Figure 7 displays the images taken from the inner space of 3DG-5 wt% FeS_2 (a,b), 3DG-10 wt% FeS_2 (c,d), 3DG-15 wt% FeS_2 (e,f), and 3DG-20 wt% FeS_2 (g,h), respectively. All the samples are highly porous and they are comparable to the internal structure of 3DG skeleton. Inhomogeneous deposition of FeS_2 is observed especially for higher sulfide percentage with a thickness of ≈30–50 nm. It can be suggested that too high loading of active material (20%) can severely deteriorate the transportation of adsorbed ions into the bulk of capacitor electrode. This fact was proven further by the electrochemical evaluations.

Figure 8 reveals the XRD pattern of 3DG-FeS_2 with different percentage of loaded active materials. The characteristic peaks which appear at 26°, 34°, 39°, 44°, 57°, 62°, and 65° (2θ) are allocated to (111), (200), (210), (211), (311), (023), and (321) planes of FeS_2 with JCPDS Card Number of 98-005-9067. The peaks are quite sharp, it means that all the samples have a well-structured crystal lattice. From 3DG-5% FeS_2 to 3DG-20% FeS_2, the intensity of the characteristic peaks increases, that confirms the different amounts of deposited active materials over the surface of the 3DG substrate.

EDS mapping of C, Fe, and S elements for 3DG-5 wt% FeS_2 to 3DG-20 wt% FeS_2 proved a gradual increase of sulfide in composite. All elements have been uniformly scattered at entire surface of the surveyed area, which verifies the hierarchical structure of the composites. No significant agglomeration was spotted while monitoring a broad area of the surface. Moreover, the elemental characterization of the EDS spectrum is aligned with the observations from the maps, and further indicates the presence of Fe, and S elements at the surface of graphene substrate. Figure S6, Supporting Information shows example of EDS results for 3DG-15 wt% FeS_2.

The capacitive performance of the porous carbonaceous electrodes can easily be affected by structural transformation. As already discussed, deposition of active materials higher than an optimum amount decreases the accessible surface area of the substrate. To specify the proper percentage of loading, the prepared samples were evaluated by CV analysis. **Figure 9** represents the capacitive/faradaic behavior of the assembled symmetric cells based on each composite in comparison with the ideal behavior of 3DG which has most EDLC profile among all the other samples. As it can be seen, all the samples show almost a rectangular CV graph with a low resistance. At applied scan rate of 2 mVs^{-1} redox reactions are well observed in the form of a wide hump from 0 to 0.6 V. It enhances with the percentage of FeS_2 from 5% to 20%. This ill-defined peak is the result of redox activities in the composites. The surface area under the voltammograms for electrodes based on 3DG and with a higher content of FeS_2 until 15 wt% gradually increases. However, 3DG-20 wt% FeS_2 shows no further charge expansion in comparison with 3DG-15 wt% FeS_2. This observation may suggest that 3DG-20 wt% FeS_2 has an inferior porous structure compared to the other samples. Surely, the sample with the higher content of FeS_2 lost a part of microporosity at the sacrifice of having a higher content of redox active materials.

Faradaic reactions have been confirmed by running a three-electrode cell investigation of capacitor based on 3DG-15 wt% FeS_2 in various voltage windows (**Figure 10**a–d). It seems that hydrogen storage could be considered for the negative electrode in the range of potential from −0.33 to −0.7 V versus SHE (Figure 10c). Redox activity of Fe species is also well observed from 0.2 to 0.4 V versus SHE.

The quality of interconnected porous structure of composite can be studied through analyzing the capacitive behavior at the scan rates from 2 to 200 mV s^{-1} and at the current densities from 0.2 to 2 A g^{-1}. Interconnected porous structure allows a fast charge response for the 3DG/15 wt% FeS_2 composite (Figure S7a,b, Supporting Information). However, at very high rates a significant aggravation of characteristics is observed for both dependences. EIS, in the form of Nyquist plot, for 3DG material and all composites with FeS_2 clearly shows the difference between materials with various loading (Figure S8, Supporting Information). To study the charge propagation, capacitance

 © 2021 The Authors. Small published by Wiley-VCH GmbH

ADVANCED SCIENCE NEWS
www.advancedsciencenews.com

NANO · MICRO small
www.small-journal.com

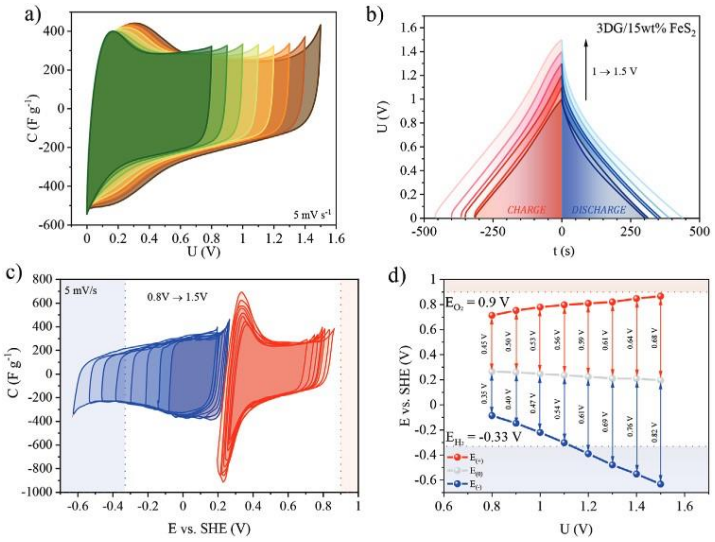

Figure 10. a) Voltage extension of 3DG/15 wt% FeS_2 electrode material in two-electrode cell, b) galvanostatic charge/discharge at 0.5 A g^{-1}, c) with separation of performance for (+) and (–) electrodes and d) indication of hydrogen and oxygen evolution.

versus frequency has been reported in Figure S9, Supporting Information for 3DG and composite with 15 wt% FeS_2. 3DG material supplies 50% capacitance at 1 Hz but for the composite with redox activity capacitance drops rapidly already at 50 mHz.

The cyclability of the 3DG/15 wt% FeS_2 composite were also investigated. Figure S10, Supporting Information presents 8000 galvanostatic cycles with current rate of 10 A g^{-1}.

For the comparison of both capacitor materials based on Re and Fe sulfides, the detailed charts of capacitance versus current loading are represented in Figure S11, Supporting Information. Energetic and Coulombic efficiencies for all materials are also indicated. As a rule of thumb, the higher redox activity, that is, higher capacitance, the lower charge propagation as well as energetic efficiency.

3. Conclusion

Two different composites based on carbon materials (NTs or 3DG) and TMDs were successfully prepared by hydrothermal synthesis and used as EC electrode materials. After detailed physicochemical characterization, their electrochemical performance was tested in ECs two- and three-electrodes cells. Mechanism of the energy storage has been elucidated. It was proven that type of transition metal such as rhenium restricts the voltage range of the capacitor (0.8 V). The composites show a specific capacitance of ≈110 F g^{-1} for ReS_2/7 wt% NTs at 0.2 A g^{-1} and 240 F g^{-1} for 3DG/15 wt% FeS_2. The composition of the prepared composite differed completely. 3DG/FeS_2 consisted of mainly highly porous carbon matrix, with a small loading of TMDs while in ReS_2/7 wt% NTs, the majority of the composite was ReS_2 and NTs served as a conductive additive. The two different approaches of using TMD as an additive or as a fundamental component have brought different results based on the initial properties of the matrix. Selection of the carbon support and method of composite preparation affect the final electrochemical performance. Energetic efficiency of charge/discharge process was exploited for true capacitance evaluation. It has been proven that voltage extension in aqueous medium is affected by materials structure, that is, edge sites strongly restrict operational window, type of metal. The species of the most noble metals catalyze water decomposition.

4. Experimental Section

Preparation of ReS_2 and CNTs/ReS_2 Composite: First, 0.6 g of ammonium perrhenate (Sigma Aldrich), 0.25 g of hydroxylamine hydrochloride (Sigma Aldrich), and 1.6 g of L-Cysteine (Sigma Aldrich) were dissolved in 40 mL of distilled water. The substrate solution was mixed for 2 h before the autoclave reaction. Then, 0.039 g of (which constituted a 7 wt% of ReS_2 material) MWCNTs (OD: 20–40 nm; L: 5–15 µm; 95+%, Iolitec) were dispersed in 40 mL of distilled water by the ultrasonic device (Hielscher—UP50H) for 30 min. The as-prepared mixtures were transferred into a stainless steel autoclave (Parr Instruments—High-Pressure Compact Reactor 5521) and kept at 180 °C for 48 h with stirring (125 rpm). After the reaction, a black precipitate was collected by filtration and then dried at 70 °C for 12 h. The same procedure was adopted for the synthesis of ReS_2, but without using NTs.

Preparation of 3DG and 3DG/FeS_2: Tailoring 3D porous structure based on graphene was carried out using one-step hydrothermal self-assembly treatment. GO was prepared according to the modified

 © 2021 The Authors. Small published by Wiley-VCH GmbH

Hummers' method.[41] GO aqueous dispersion (4 mg mL^{-1}) was prepared by sonication of graphite oxide solution using ultrasonic bath for 1 h. Next, the GO solution was transferred into a Teflon-lined stainless steel autoclave (100 mL), and was kept without any stirring at 180 °C for 24 hr. Then, the autoclave was cooled down to 25 °C, and the formed cylindrical hydrogel was extracted and was stored in DI water to replace the undesired by-products inside the pores with water molecules. The purified hydrogel was freeze-dried prior the structural and elemental characterizations. The synthesis of 3DG/FeS_2 was carried out using a one-step hydrothermal reaction. For this purpose, different amounts of $FeCl_3$ 4 H_2O were dissolved in 20 mL ethylene glycol. Then, 60 mg of GO was dissolved into 30 mL of DI water. Later, the $FeCl_3$ and GO solutions were homogeneously dispersed in each other using ultrasonic bath. The samples contained 5, 10, 15, and 20 wt% of $FeCl_3$ in GO solution. Then, 15 mg of elemental sulfur was added to all the mixtures. The pH of the mixture was tuned to 9 before it was transferred into a 100 mL Teflon-lined stainless steel autoclave, and maintained at 200 °C for 24 h. After, the autoclave was cooled down to the room temperature and the 3DG/FeS_2 hydrogels were rinsed with water and ethanol before electrochemical analysis. Prior to physicochemical characterizations, the samples were freeze-dried.

Physical Characterization: Morphology of the samples was determined with the use of SEM Tescan Vega 5135 coupled with the PGT Avalon X-ray microanalyzer adapter for the evaluation of the EDS.

Diffractograms were obtained from aparatus, BRUKER D8 Advanced, equipped with Johansson monochromator using Cu Kα radiation (Cu Kα, λ = 1.5406 Å) and silicon strip detector LynxEye. The minimum measurement angle was 0.6 2Θ deg.

The specific surface area of samples were determined during N_2 adsorption/desorption at 77 K by using porosity analyzer ASAP 2460 (Micromeritics, USA). The samples were degassed for 24 h at 100 °C (He atmosphere and then for 5 h under the high vacuum) prior the measurements. Pore size distribution was evaluated using 2D-NLDFT model. The range of 0.01–0.05 relative pressure (p/p_0) was used for calculation of the specific surface area.

Electrode Preparation and Electrochemical Characterization: All the electrodes based on ReS_2/7 wt% NTs composite contained 90 wt% of active material, 5 wt% of binder, that is, polytetrafluoroethylene (60 wt% dispersion in water, Sigma Aldrich) and 5 wt% of conducting agent (C-NERGY Super C65, Imerys). Components were mixed in a mortar until dough-like material was obtained. Then it was rolled on a calendaring machine in order to obtain 200 µm thickness sheet of electrode material. Electrodes in a shape of discs with the diameter of 10 mm were cut from the foil, followed by drying in 70 °C for 24 h. The electrodes of similar mass separated by a glass microfiber membrane (GF/A, Whatman, diameter of 12 mm) were soaked with 1 mol L^{-1} Li_2SO_4 aqueous electrolyte.

For 3DG self-standing samples 1 mol L^{-1} Na_2SO_4 was used. Active materials loading per electrode was 8–10 mg for NT_S/ReS_2 and 2.5–3 mg for 3DG/FeS_2 composites.

All the electrochemical cells were investigated by using VMP3 multichannel potentiostat/galvanostat (Biologic, France) with the EC-lab software.

Supporting Information

Supporting Information is available from the Wiley Online Library or from the author.

Acknowledgements

M.F.K. and M.T. contributed equally to this work. E.F. supervised this project. The authors would like to acknowledge OPUS project financed by National Science Centre, Poland (project no. 2018/31/B/ST4/01852) for the financial support of the research.

Conflict of Interest

The authors declare no conflict of interest.

Data Availability Statement

The data that support the findings of this study are available from the corresponding author upon reasonable request.

Keywords

3D graphene, carbon nanotubes, electrochemical capacitors, transition metal-dichalcogenides

Received: October 31, 2020
Revised: January 22, 2021
Published online: March 19, 2021

[1] E. Frackowiak, F. Beguin, *Carbon* **2001**, *39*, 937.
[2] K. Fic, A. Platek, J. Piwek, E. Frackowiak, *Mater. Today* **2018**, *21*, 437.
[3] P. Simon, Y. Gogotsi, *Nat. Mater.* **2010**, *7*, 845.
[4] M. Yang, B. Cheng, H. Song, X. Chen, *Electrochim. Acta* **2010**, *23*, 7021.
[5] D. Guan, Z. Gao, W. Yang, J. Wang, Y. Yuan, B. Wang, M. Zhang, L. Liu, *Mater. Sci. Eng. B* **2013**, *178*, 736.
[6] D. Liang, Z. Tian, J. Liu, Y. Ye, S. Wu, Y. Cai, C. Liang, *Electrochim. Acta* **2015**, *182*, 376.
[7] H. Wang, D. Tran, J. Qian, F. Ding, D. Losic, *Adv. Mater. Interfaces* **2019**, *6*, 1900915.
[8] W. Choi, N. Choudhary, G. H. Han, J. Park, D. Akinwande, Y. H. Lee, *Mater. Today* **2017**, *20*, 116.
[9] N. Choudhary, M. A. Islam, J. H. Kim, T.-J. Ko, A. Schropp, L. Hurtado, D. Weitzman, L. Zhai, Y. Jung, *Nano Today* **2018**, *19*, 16.
[10] L. Lin, W. Lei, S. Zhang, Y. Liu, G. G. Wallace, J. Chen, *Energy Storage Mater.* **2019**, *19*, 408.
[11] S. Ding, D. Zhang, J. S. Chen, X. W. D. Lou, *Nanoscale* **2012**, *4*, 95.
[12] S. Wang, J. Zhu, Y. Shao, W. Li, Y. Wu, L. Zhang, X. Hao, *Chem. Eur. J.* **2017**, *23*, 3438.
[13] K. Gopalakrishnan, S. Sultan, A. Govindaraj, C. Rao, *Nano Energy* **2015**, *12*, 52.
[14] Q. Ji, C. Li, J. Wang, J. Niu, Y. Gong, Z. Zhang, Q. Fang, Y. Zhang, J. Shi, L. Liao, *Nano Lett.* **2017**, *17*, 4908.
[15] N. Choudhary, C. Li, H.-S. Chung, J. Moore, J. Thomas, Y. Jung, *ACS Nano* **2016**, *10*, 10726.
[16] T. Quan, N. Goubard-Bretesché, E. Härk, Z. Kochovski, S. Mei, N. Pinna, M. Ballauff, Y. Lu, *Chem. Eur. J.* **2019**, *25*, 4757.
[17] X. Chen, J. Ding, J. Jiang, G. Zhuang, Z. Zhang, P. Yang, *RSC Adv.* **2018**, *8*, 29488.
[18] S. Ratha, C. S. Rout, *ACS Appl. Mater. Interfaces* **2013**, *5*, 11427.
[19] S. Liu, D. Gao, J. Li, K. San Hui, Y. Yin, K. N. Hui, S. C. Jun, *J. Mater. Chem. A* **2019**, *7*, 26618.
[20] P. Asen, M. Haghighi, S. Shahrokhian, N. Taghavinia, *J. Alloys Compd.* **2019**, *782*, 38.
[21] X. Xie, M. Mao, S. Qi, J. Ma, *CrystEngComm* **2019**, *21*, 3755.
[22] Q. Zhang, S. Tan, R. G. Mendes, Z. Sun, Y. Chen, X. Kong, Y. Xue, M. H. Rümmeli, X. Wu, S. Chen, *Adv. Mater.* **2016**, *28*, 2616.
[23] M. Mao, C. Cui, M. Wu, M. Zhang, T. Gao, X. Fan, J. Chen, T. Wang, J. Ma, C. Wang, *Nano Energy* **2018**, *45*, 346.
[24] S. Liu, W. Lei, Y. Liu, Q. Qiao, W.-H. Zhang, *ACS Appl. Mater. Interfaces* **2018**, *10*, 37445.

 © 2021 The Authors. Small published by Wiley-VCH GmbH

[25] G. Lota, K. Fic, E. Frackowiak, *Energy Environ. Sci.* **2011**, *4*, 1592.
[26] H. Pan, J. Li, Y. Feng, *Nanoscale Res. Lett.* **2010**, *5*, 654.
[27] J. Gao, L. Li, J. Tan, H. Sun, B. Li, J. C. Idrobo, C. V. Singh, T.-M. Lu, N. Koratkar, *Nano Lett.* **2016**, *16*, 3780.
[28] A. Laheäär, P. Przygocki, Q. Abbas, F. Béguin, *Electrochem. Commun.* **2015**, *60*, 21.
[29] H. Li, C. Tsai, A. L. Koh, L. Cai, A. W. Contryman, A. H. Fragapane, J. Zhao, H. S. Han, H. C. Manoharan, F. Abild-Pedersen, *Nat. Mater.* **2016**, *15*, 48.
[30] Q. Zhang, W. Wang, J. Zhang, X. Zhu, Q. Zhang, Y. Zhang, Z. Ren, S. Song, J. Wang, Z. Ying, *Adv. Mater.* **2018**, *30*, 1707123.
[31] W. Shi, G. Li, Z. Wang, *J. Phys. Chem. C* **2019**, *123*, 12261.
[32] Q. Sun, B. Zhang, L. Diao, B. Chen, K. Song, L. Ma, F. He, *J. Mater. Chem. A* **2020**, *8*, 11607.
[33] J. Pan, R. Wang, X. Xu, J. Hu, L. Ma, *Nanoscale* **2019**, *11*, 10402.
[34] Y. Xu, Z. Lin, X. Zhong, X. Huang, N. O. Weiss, Y. Huang, X. Duan, *Nat. Commun.* **2014**, *5*, 4554.
[35] K. Yao, Z. Xu, M. Ma, J. Li, F. Lu, J. Huang, *Adv. Funct. Mater.* **2020**, *30*, 2001484.
[36] X. Zhang, J. Zhang, Y. Chen, K. Cheng, J. Yan, K. Zhu, K. Ye, G. Wang, L. Zhou, D. Cao, *J. Colloid Interface Sci.* **2019**, *536*, 291.
[37] Y. Zou, R. Liu, W. Zhong, W. Yang, *J. Mater. Chem. A* **2018**, *6*, 8568.
[38] D. Wu, W. Zhong, *J. Mater. Chem. A* **2019**, *7*, 5819.
[39] Y. Wang, M. Zhang, T. Ma, D. Pan, Y. Li, J. Xie, S. Shao, *Mater. Lett.* **2018**, *218*, 10.
[40] B. Konkena, S. Vasudevan, *J. Phys. Chem. Lett.* **2012**, *3*, 867.
[41] M. Foroutan, L. Naji, *Electrochim. Acta* **2019**, *301*, 421.
[42] J. Li, G. Zhang, C. Fu, L. Deng, R. Sun, C.-P. Wong, *J. Power Sources* **2017**, *345*, 146.

 © 2021 The Authors. Small published by Wiley-VCH GmbH

P2. *Supercapacitors with Carbon/MoS_2 Composites*

Authors: Maciej Tobis, Sylwia Sroka, Elżbieta Frąckowiak

Journal: Frontiers in Energy Research, **2021**, 9, 647878

DOI: https://doi.org/10.3389/fenrg.2021.647878

License: The content is available under CC BY 4.0

Contribution: Conceptualization of the article, planning experiments, synthesis of carbon/MoS_2 composites, physicochemical analysis of prepared samples (Raman spectra, XRD, SEM/EDX, TEM), electrochemical investigation (two, and three-electrode cells), data plotting, writing original draft

Graphical abstract

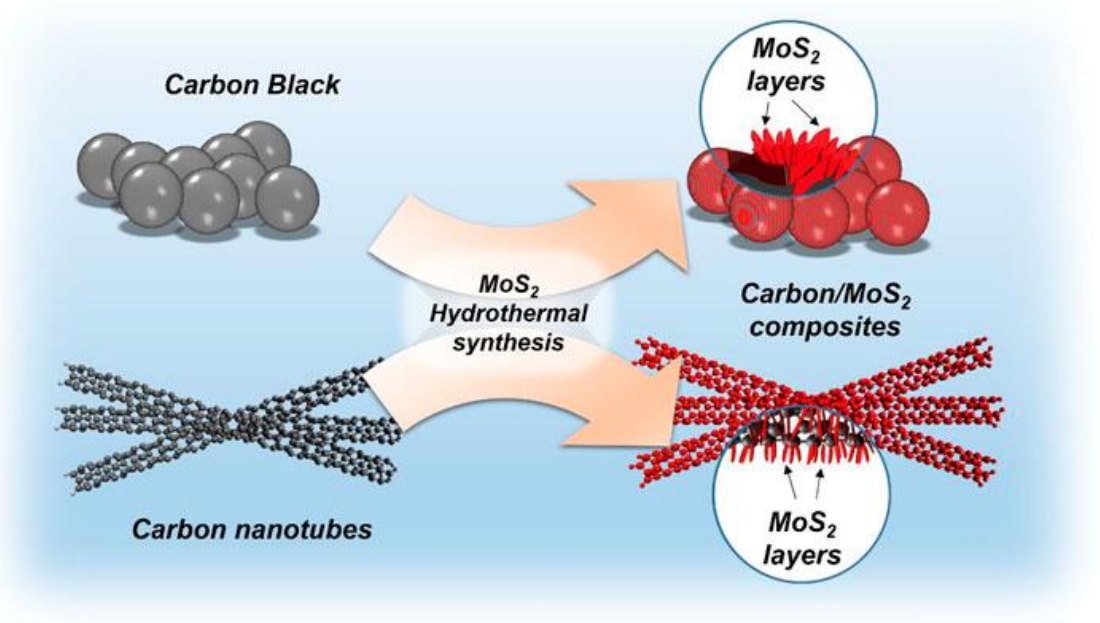

Context of research & summary

Previous study showed that ReS_2/CNTs revealed catalytic properties towards HER and potentially OER which limited its practical application in the ECs. However, there are other TMDs, such as MoS_2, which shows attractive electrochemical properties for ECs application.

MoS_2 is relatively well documented in the literature, however, most of the reports highlight the electrochemical behavior of a single electrode (very often the active mass loading is below 1 mg) operating in the sulfuric acid. Therefore, it is difficult to evaluate if the MoS_2 material could be practically used as an EC electrode. Having in mind the moderate conductivity of the TMDs, the results of this study present the integration of MoS_2 with different carbonaceous materials with open porosity such as carbon nanotubes (NTs) and carbon black (CB) to omit the blockage of microporous texture and allows for homogenous distribution of layered MoS_2. By combining MoS_2 with different carbon materials, it could be expected to observe enhanced electrochemical performance, improved conductivity, and optimized voltage window of the ECs.

MoS_2-based composites were prepared by using hydrothermal method assisted by L-cysteine, which acts as a sulfur source. This process led to the formation of MoS_2 nanolayers on the carbon substrates which morphology, structure and porous texture were investigated by nitrogen sorption at 77 K, X-ray diffraction (XRD), Raman spectroscopy, scanning electron microscopy (SEM) imaging coupled with energy dispersive spectroscopy (EDS) and transmission Electron Microscopy (TEM).

Electrochemical studies were conducted by using symmetric ECs assembled with the prepared composites. The MoS_2/CNTs exhibited the highest capacitance of 150 F g^{-1}, while the MoS_2/BP2000 reached 110 F g^{-1} at current load of 0.2 A g^{-1} at 0.8 V. The performance was compared to pure carbon supports, demonstrating the superiority of the composites.

Additional tests in two-electrode cells equipped with a reference electrode allowed for monitoring the electrochemical behavior of both electrodes during voltage extension. These tests revealed that the MoS_2 show some signs of the hydrogen evolution reaction (HER) on the negative electrode and high redox peak on the positive electrode during potential extension. Because of this, the electrochemical voltage window of the cells with MoS_2-based materials was limited to below 1 V.

The study suggests that further optimization of the composite materials and their synthesis process is necessary to fully exploit the potential of MoS_2-based electrodes in energy storage applications.

Publication

P2. *Supercapacitors with Carbon/MoS_2 Composites*

frontiers in Energy Research

ORIGINAL RESEARCH
published: 21 May 2021
doi: 10.3389/fenrg.2021.647878

Supercapacitor with Carbon/MoS_2 Composites

*Maciej Tobis, Sylwia Sroka and Elżbieta Frąckowiak**

Institute of Chemistry and Technical Electrochemistry, Poznan University of Technology, Poznan, Poland

Transition metal dichalcogenides (TMDs) with a two-dimensional character are promising electrode materials for an electrochemical capacitor (EC) owing to their unique crystallographic structure, available specific surface area, and large variety of compounds. TMDs combine the capacitive and faradaic contribution in the electrochemical response. However, due to the fact that the TMDs have a strong catalytic effect of promoting hydrogen and oxygen evolution reaction (HER and OER), their usage in aqueous ECs is questioned. Our study shows a hydrothermal L-cysteine–assisted synthesis of two composites based on different carbon materials—multiwalled carbon nanotubes (NTs) and carbon black (Black Pearl-BP2000)—on which MoS_2 nanolayers were deposited. The samples were subjected to physicochemical characterization such as X-ray diffraction and Raman spectroscopy which proved that the expected materials were obtained. Scanning electron microscopy coupled with electron dispersive spectroscopy (SEM/EDS) as well as transmission electron microscopy images confirmed vertical position of few-layered MoS_2 structures deposited on the carbon supports. The synthetized samples were employed as electrode materials in symmetric ECs, and their electrochemical performance was evaluated and compared to their pure carbon supports. Among the composites, NTs/MoS_2 demonstrated the best electrochemical metrics considering the conductivity and capacitance (150 Fg^{-1}), whereas BP2000/MoS_2 reached 110 Fg^{-1} at a current load of 0.2 Ag^{-1}. The composites were also employed in a two-electrode cell equipped with an additional reference electrode to monitor the potential range of both electrodes during voltage extension. It has been shown that the active edge sites of MoS_2 catalyze the hydrogen evolution, and this limits the EC operational voltage below 1 V. Additional tests with linear sweep voltammetry allowed to determine the operational working voltage for the cells with all materials. It has been proven that the MoS_2/carbon composites possess limited operating voltage, that is, comparable to a pure MoS_2 material.

Keywords: molybdenum disulfide, transition metal dichalcogenide, 2D materials, carbon nanotubes, carbon black, electrochemical capacitors, neutral electrolyte

OPEN ACCESS

Edited by:
Ana Karina Cuentas Gallegos, National Autonomous University of Mexico, Mexico

Reviewed by:
Yong Zhang, Hefei University of Technology, China
Jeng-Yu Lin, Tatung University, Taiwan

****Correspondence:***
Elżbieta Frąckowiak
elzbieta.frackowiak@put.poznan.pl

Specialty section:
This article was submitted to Electrochemical Energy Conversion and Storage, a section of the journal Frontiers in Energy Research

Received: *30 December 2020*
Accepted: *23 April 2021*
Published: *21 May 2021*

Citation:
Tobis M, Sroka S and Frąckowiak E (2021) Supercapacitor with Carbon/MoS_2 Composites. Front. Energy Res. 9:647878. doi: 10.3389/fenrg.2021.647878

INTRODUCTION

The industry is constantly facing issues on advanced and more efficient energy storage systems for intermittent renewable energy harvesting that can successfully inhibit the overexploitation of natural reserves of fossil fuels. For this reason, a booming interest in the area of research and development of energy storage devices has been noted. Electrochemical capacitors (ECs) in particular, owing to their remarkable features such as superior cyclability and high-power density, can be successfully employed in this field (Sharma and Bhatti, 2010; Chen, 2016; González et al., 2016). However, in order to compete with modern batteries, the research aim is largely focused on increasing EC energy density while retaining their fast charge/discharge rate. The performance of such storage devices can be effectively improved through extension of voltage window or an increase of specific capacitance, as shown in the following equation (Simon and Gogotsi, 2008):

$$E = \frac{1}{2} C \cdot V^2$$

where E represents energy density, C capacitance, and V the operating voltage. As the energy in ECs is stored mainly through adsorption of ions at electrode/electrolyte interface, one of the major requirements for the electrode materials is developed specific surface area (SSA) and high conductivity. Electrode materials based on carbons have been already well known to possess those characteristic features (Frackowiak and Béguin, 2001; Pandolfo and Hollenkamp, 2006; Cherusseri et al., 2016; Ratajczak et al., 2019). Although, due to limitations related to a nonuniform distribution of pores and their availability for ions, they usually offer capacitance ca. 100 Fg^{-1} (Fic et al., 2012). For this reason, a regained interest in the field of electrode material development such as ones based on transition metal dichalcogenides (TMDs) has been observed. These two-dimensional inorganic materials, including MoS_2, WS_2, VS_2, or $MoSe_2$ (Acerce et al., 2015; Balasingam et al., 2015; Chen et al., 2019; Xu et al., 2020), can possess both "faradaic" and "non-faradaic" behaviors, very thin structure (which in turn leads to short transport length for electrons and ion migration), high conductivity, and large surface tunability (Coogan and Gun'ko, 2021; Lukatskaya et al., 2016; Bissett et al., 2016; Choi et al., 2017; Zhang and Huang, 2017). Thanks to these qualities, TMDs can be effectively employed as electrode materials for ECs. MoS_2, in particular, has been extensively studied in capacitor applications over the past few years. Layered MoS_2 consists of a single Mo atom sandwiched between two S atoms, with weak Van der Waals interactions stacking them together. One way in which the electronic conductivity of the composite can be noticeably improved is the incorporation of conducting materials, such as carbon blacks or carbon nanotubes (CNTs) (Yang et al., 2017; Lin et al., 2019; Sun et al., 2019). However, when paired with an aqueous electrolyte, the EC system is characterized by a narrow voltage window due to electrolysis of water, which, in turn, affects its energy density. In electrochemical systems, this process is governed by oxygen evolution reaction (OER) and hydrogen evolution reaction (HER). However, aqueous electrolytes have superior advantage in terms of safety, cost, feasibility of use, and eco-friendliness, as compared to organic electrolytes (Zhong et al., 2015). A lot of research has been devoted to TMD composites as EC materials and very high capacitance values exceeding even 400 Fg^{-1} have been reported, but most of these studies are performed only in a three-electrode system with an excess of electrolyte, the mass of electrode is often below 1mg, and calculations are not always correct. Hence, apart from the fundamental significance, practical application of some studies is meaningless. From our point of view, only investigation in a two-electrode system resembles a real capacitor performance. Estimation of safe operating voltage of capacitor with TMD-based electrodes is crucial. Unfortunately, the reason of voltage limitation was not studied in detail. Electrochemical reactions associated with activity of MoS_2 result in its inherent limited potential window. Nasir et al. have reported an electrochemical window of MoS_2 where both anodic and cathodic regions were investigated (Nasir et al., 2015). At the anodic potentials, oxidation of Mo^{4+} to Mo^{6+} occurs, while at the cathodic potentials, the reduction of H_3O^+ present in the solution results in electrocatalytic HER at the surface of MoS_2 (Nasir et al., 2015; Sangeetha and Selvakumar, 2018; Tseng and Lee, 2020; Yuan et al., 2020). Hence, even if interconnected network is created, such as in MoS_2/carbon-based materials, TMD presence can lead to enhanced HER activity due to its morphology and much faster movement of electrons (Sangeetha et al., 2020; Rendón-Patiño et al., 2020). All the parameters mentioned have a great impact on the potential window of MoS_2-based materials and have to be considered carefully.

In this study, the MoS_2 composites with 7 wt% amount of BP2000 or NTs were prepared with the use of hydrothermal process utilizing L-cysteine which acted as an effective and nontoxic source of sulfur in the reaction (Huang et al., 2013; Park et al., 2013; Huang et al., 2014). Synthetized composites and sole materials were physicochemically characterized, prepared in the form of electrodes, and further studied electrochemically in two-electrode and two-electrode with reference cells with a special attention to voltage frontiers.

EXPERIMENTAL

Material Synthesis

Layered MoS_2 was obtained during a hydrothermal reaction. 1.6 g of L-cysteine (Sigma Aldrich, 97%) and 0.6 g of $Na_2MoO_4{\cdot}2H_2O$ (Sigma Aldrich, ≥ 99%) were mixed in 80 ml of DI water. Then, the pH of the solution was adjusted to 6 with the use of 5% HCl which turned the solution from colorless to scarlet orange. The mixture of the precursors was then transferred into a stainless steel autoclave (Parr® 5500 Series compact reactor) for 24 h at 210°C. After the reaction, the solution was filtered and washed several times with DI water and isopropanol. Black powder was collected and dried at 70°C for 12 h. The composites of NTs/MoS_2 and BP2000/MoS_2 were synthetized accordingly but with the use of NTs (IoLiTec nanomaterials, outer diameter: 20–40 nm, length: 5–15 μm, and > 95% purity) and BP2000 (Cabot). 0.035 g of the NTs and BP2000 were sonicated (Hielsher UP50H) for 30 min and then mixed with the solution of precursors. The resulting solution was treated as prior, and composite sample was collected and dried. The process of

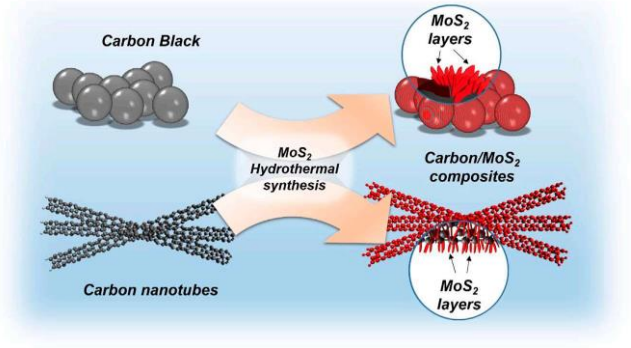

FIGURE 1 | Simplified process of carbon/MoS_2 synthesis.

synthesis (**Figure 1**) can be presented by the following equations (Chang and Chen, 2011).

$$HSCH_2CHNH_2COOH + H_2O \rightarrow CH_3COCOOH + NH_3 + H_2S$$

$$4MoO_4^{2-} + 9H_2S + 6CH_3COCOOH \rightarrow 4MoS_2 + SO_4^{2-} + 6CH_3COCOO^- + 12H_2.$$

Materials Characterization

Raman scattering spectroscopy was performed using a Thermo Scientific DXR Raman Microscope with a laser emitting at $\lambda = 532$ nm and power of 5 mW. The total exposure time was 60 s, carried out in 3 scans series, and each lasting 20 s. The measurements were repeated at least 3 times for each sample at different locations to ensure uniformity throughout.

Scanning electron microscope (SEM) Tescan Vega 5135 coupled with the PTG Avalon X-ray microanalyzer adapter for the evaluation of the energy dispersive spectroscopy (EDS) was employed to study the texture morphology and atomic content on the surface of the material at different magnifications.

Additional structural and morphological studies were performed by transmission electron microscopy (TEM) FEI Titan G2 80-300 equipped with an energy dispersive X-ray spectrometer (Hillsboro, OR, United Sates).

In order to confirm crystallographic structures, the samples were investigated by X-ray diffraction (XRD) technique employing BRUKER D8 Advanced, equipped with Johansson monochromator using Cu Kα radiation (Cu Kα, λ = 1.5406 Å) and silicon strip detector Lynx Eye. The minimum measurement angle was 0.6 of 2θ degree.

Electrode Preparation and Electrochemical Tests

The electrodes were prepared from 90wt% of an active material, 5 wt% of a conducting agent (C-NERGY™ Super C65, Imerys), and 5 wt% of polytetrafluoroethylene binder (60% dispersion in water

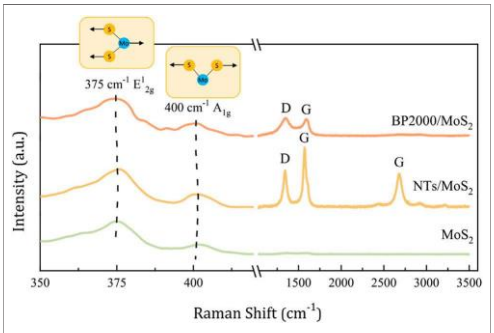

FIGURE 2 | Raman spectra of BP2000/MoS_2, NTs/MoS_2, and MoS_2.

PTFE, Sigma Aldrich). The materials were weighed and mixed with isopropanol and sonicated for 30 min. After isopropanol was evaporated and dough-like consistency of the material was obtained, it was then transferred in-between two sheets of plastic foil, rolled, and passed through a hot roller in order to obtain a uniform thickness of about 200 µm. Then, it was cut into disc electrodes of a 10mm diameter and dried at 70°C for 24 h in an oven.

Symmetric electrochemical capacitors with stainless steel 316L current collectors were assembled with two electrodes of equal mass (ca. 10 mg). They were soaked with an appropriate amount of electrolyte (1M Li_2SO_4), then separated with a glass microfiber membrane (GF/A, Whatman™, thickness of 260 µm and disc diameter 12 mm), and mounted under normal atmosphere using Teflon Swagelok® tube fitting. Hg/Hg_2SO_4 served as a reference electrode to monitor performance of both electrodes. The voltammetry response of each electrode was determined according to the previous investigations (Slesinski and Frackowiak, 2018). The specific capacitance per one electrode

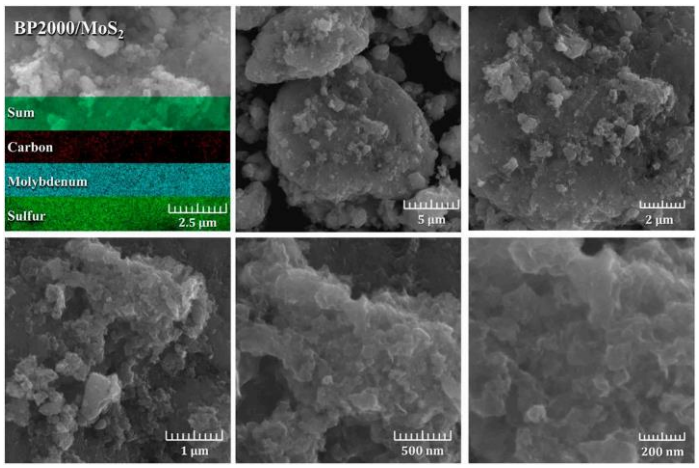

FIGURE 3 | EDS and SEM images of BP2000/MoS_2 at different magnifications.

was calculated according to a very well-known methodology (Laheäär et al., 2015). Taking into account the information gathered from all electrochemical measurements and calculations, a successful comparison between each material was completed.

RESULTS AND DISCUSSION

Material Characterization

Raman spectroscopy allowed to obtain information regarding a chemical composition of MoS_2 and its composites with BP2000 and NTs. **Figure 2** shows Raman spectrum of BP2000/MoS_2, NTs/MoS_2, and MoS_2 composites. Spectrum contains distinctive G and D band peaks at 1,604 and 1,345 cm^{-1}, respectively, with a loss of intensity for both peaks. Raman spectrum of NTs/MoS_2 composite showed three distinctive features: two sharp peaks at ~1,575 and ~1,345 cm^{-1} belonging to G (graphite in plane mode due to stretching vibrations of C–C bond) and D (disorder) band, respectively. D band of BP2000 is widened due to disordered structure and amorphous nature of the BP2000 instead of less defects than the CNTs. G′ second order harmonic is visible at ~2,685 cm^{-1} (Zdrojek et al., 2004). In both samples, the G band can be further divided into G1 and G2 bands at 1,572 and 1,608 cm^{-1}, respectively. These bands are related to lattice vibration of sp^2 bond carbon materials, as reported in other works (Rao et al., 1997; Duesberg et al., 2000). Raman spectrum bands at ~ 375 cm^{-1} can be assigned to an in-plane E_{2g} mode where sulfur atoms vibrate in one direction, whereas molybdenum in another direction, with a literature value of 400 cm^{-1} (Conley et al., 2013).

Figure 3 shows SEM and EDS images of BP2000/MoS_2. Carbon blacks are known to be created from the spherical particles which connected together form a complex micro- and mesoporous bead-like structure. SEM images revealed that the composite, comparable to NTs/MoS_2 (**Figure 4**), has remained in the original shape of BP2000 and NTs, accordingly. Higher magnifications show that the surface of the composites is covered by the MoS_2 nanolayers which form accessible structure favorable for transportation and diffusion of ions during adsorption/desorption. EDS mappings (**Figures 3** and **4**) show the elemental distribution on the surface of the composite. Presence of Mo, S, and C atoms is confirmed in both cases, that is, BP2000/MoS_2 and NTs/MoS_2. A low amount of carbon detected suggests tight and homogenous coverage of carbon supports by MoS_2 layers. During the synthesis process, MoS_2 layers are formed and deposited on the surface of the NTs favorably at the defect sites. The layers are directed perpendicularly or horizontally to the NTs surface. Generally, "bottom-up" methods such as hydrothermal synthesis are characterized by low controllability of the process, unlike chemical vapor deposition (CVD) (Gao et al., 2016). Therefore, it is most likely that the composite possesses randomly positioned layers with a major perpendicular orientation (inset of **Figures 3** and **4**). Such unique structure possesses many adsorption sites for ions created by deposited MoS_2 layers and quick diffusion routes originating mostly from NTs and BP2000.

Transmission electron microscopy (TEM) was conducted to determine the microstructure and crystallinity of the composites. TEM images in **Figures 5A,E** showed consistency with the SEM/EDX results in **Figure 4**. High

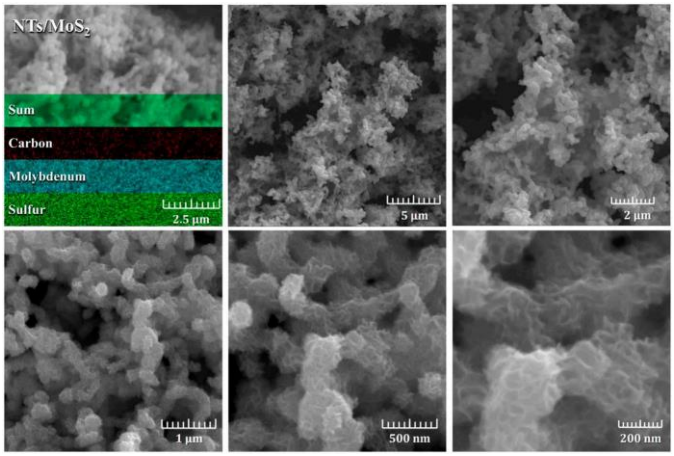

FIGURE 4 | EDS and SEM images of NTs/MoS_2 at different magnifications.

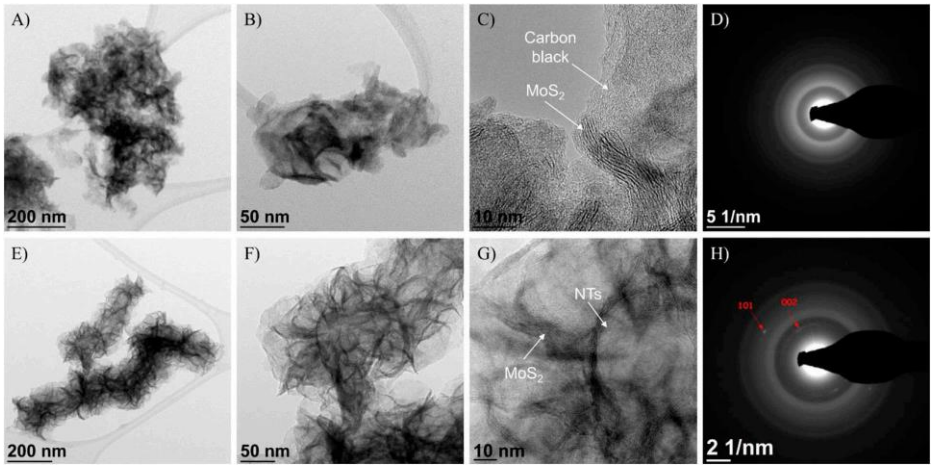

FIGURE 5 | TEM and SAED images of BP2000/MoS_2—**(A)–(D)** and NTs/MoS_2—**(E)–(H).**

magnifications of BP2000/MoS_2 (**Figure 5C**) show two significantly different sections in the image. Wide disordered area can be attributed to carbon black, while black lines can be considered as MoS_2 edged layers. Images show that the MoS_2 layers are predominantly grown in the vertical direction to the carbon support. Additionally, MoS_2 present in the form of few layers stacks is strongly linked to carbon support. Sample NTs/MoS_2 showed comparable stacking, although it seems that the MoS_2 are much better distributed on the NTs surface. It may origin from the mesoporous character of the NTs. The number of individual layers of MoS_2 appears to be lower which can also be attributed to the texture of NTs. In both cases, selected area electron diffraction (SAED—**Figures 5D,H**) patterns showed weak diffraction rings indicating low crystallization of MoS_2.

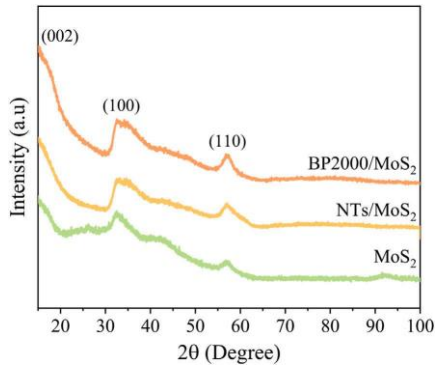

FIGURE 6 | X-ray diffractograms for different materials.

For the NTs/MoS_2 sample, it was possible to differentiate two weak diffraction rings, that is, 002 and 101 attributed to NTs. The XRD method allowed to investigate the crystallographic structure of the samples. **Figure 6** shows diffractogram patterns registered for MoS_2, $BP2000/MoS_2$, and NTs/MoS_2. Each sample exhibited peaks at 17°, 33°, and 58° indicating (002), (100), and (110) planes of MoS_2, respectively (JCPDS card number 37-1492). Low intensity of the peaks is related to the disordered and layered, differently oriented structure of the MoS_2 on the carbon supports.

Electrochemical Measurements

After physicochemical characterization, the composite materials and pure components were further investigated in the capacitor cells to evaluate the electrochemical properties. The fundamental electrochemical measurement consisted of electrochemical impedance spectroscopy (EIS) with a frequency between 100 kHz–10 mHz, followed by cyclic voltammetry (CV) from 0 to 0.8 V with varying scan rates 1, 2, 5, 10, 20, 50, 100, and 200 mVs^{-1}, galvanostatic charge/discharge at a current densities of 0.2, 0.5, 1, and 2 Ag^{-1}, and subsequent EIS measurement with the same parameters. Next, the two-electrode cell equipped with a reference electrode was subjected to a gradual CV extension of the voltage window starting from 0.6 to 1.5 V with increments of 0.1 V at a constant scan rate of 2 mVs^{-1} and galvanostatic measurements with a constant current density of 0.2 Ag^{-1}, finishing up by the EIS measurement. General comparison of capacitor metrics between each sample is shown in **Figure 7**. Additionally, the detailed electrochemical characterization including effect of scan rates and different current density applied was placed in **Supplementary Figures S1 and S2**.

A perfectly rectangular shape of the cyclic voltammetry profiles for the EC cells with carbonaceous materials is not a surprise in the low voltage ranges. Such materials are already known to be ideal capacitor materials with high conductivity. MoS_2 itself demonstrated higher capacitance than both carbons owing to the dual mechanism, that is, capacitive charge/discharge but also possible redox phenomena (lithium insertion and various oxidation state of Mo). However, the CV characteristics of MoS_2 and its composite derivatives exhibited slightly sloping shape that indicates higher intrinsic resistance of the TMD material. Both

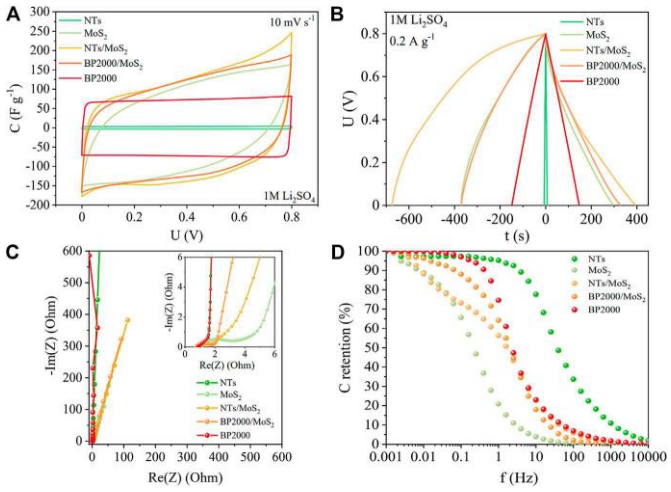

FIGURE 7 | Electrochemical performance of pure BP2000, NTs, MoS_2, and their MoS_2 composite materials. **(A)** Cyclic voltammograms, **(B)** galvanostatic charge/discharge, **(C)** electrochemical impedance spectroscopy, and **(D)** capacitance retention vs. frequency.

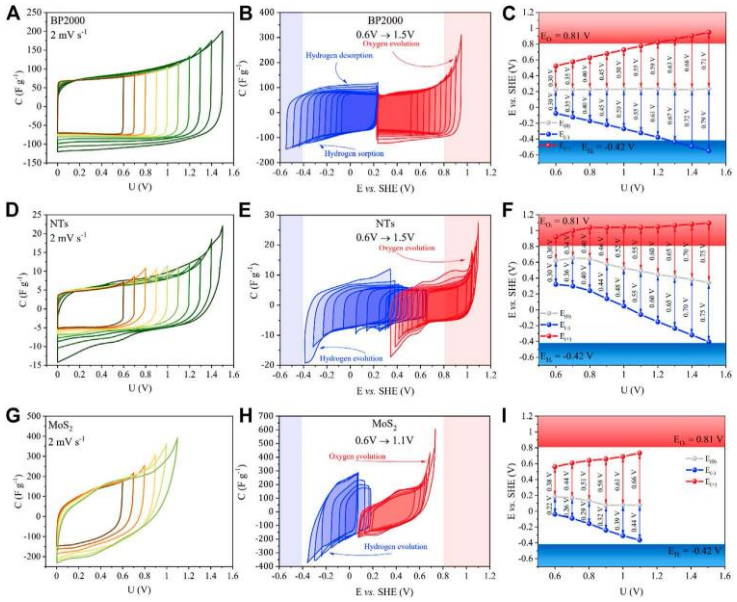

FIGURE 8 | Electrochemical characterization of symmetric EC cells. Cyclic voltammograms of gradual voltage extensions for BP2000, NTs, and MoS_2—**(A), (D),** and **(G)**. Individual cyclic voltammograms for (+) and (–) electrodes—**(B), (E),** and **(H)**. Operational potentials for both electrodes at each voltage—**(C), (F), and (I).**

EC cells with composites showed significantly higher capacitance than maternal materials. Nevertheless, the NTs/MoS_2 composite exhibited definitely better behavior than BP2000/MoS_2. **Figure 7C** presents a Nyquist plot for composites and precursor materials. Carbons in comparison to MoS_2 and its composites possessed significantly smaller intrinsic resistance. Carbon blacks and nanotubes are known to possess very high conductivity which reflects low equivalent series resistance (ESR) values (0.82 and 0.74 Ω, respectively). Fast capacitive charging of these carbons is proven by the parallel direction of line to the y-axis with equivalent distributed resistance (EDR) of 1.65 and 1.58 Ω. Oppositely, MoS_2 alone as a semiconductor possesses lower conductivity with ESR of 1.1 Ω with a distinct semicircle exhibiting EDR of 4.85 Ω. At low frequencies, MoS_2 line showed high slope reflecting diffusion effects. Such discrepancy between the values obtained from MoS_2 and carbons can be explained by the lower conductivity and high charge transfer resistance of MoS_2. Cells constructed with BP2000/MoS_2 and NTs/MoS_2 exhibited intermediate values of ESR to the parental materials (0.78 and 0.80 Ω, respectively). Additionally, slope character of the MoS_2 composites with EDR of (2.05 and 3.32 Ω, adequately) indicates diffusion effects of faradaic processes. To explain the charge propagation of the composites, the capacitance retention vs. frequency chart has been prepared (**Figure 7D**). It can be observed that the carbon black and nanotubes were able to hold their maximum capacitance up to 1 and 10 Hz, respectively. At 1 Hz, MoS_2 was able to retain only 20% of the initial capacitance which originates from its low conductivity and high charge transfer resistance. Composites prepared with BP2000 and NTs exhibited intermediate charge transfer properties as they were able to hold around 65% of the initial capacitance. It can be observed that such moderate addition of carbons (~7 wt%) to the composite has improved the overall performance of the cell. Different loadings of carbon supports in the composite mass have been studied separately (**Supplementary Figure S3**). It has been proven that 7 wt% of carbon support was an optimal amount. The morphology of both carbon supports is different; hence, the process of MoS_2 layers formation and deposition is dissimilar.

Taking into account the main goal of our research, we focused on the possibility of voltage extension and elucidation of electrochemical behavior of (+) and (–) electrode, separately. Hence, the further electrochemical performance of the samples was studied in a two-electrode cell with an additionally positioned Hg/Hg_2SO_4 reference electrode. At the beginning, operational voltage windows of the cells containing pure materials, that is, BP2000, NTs, and MoS_2 were studied. **Figure 8A** displays performance of the full cell containing BP2000 as an electrode material, whereas **Figures 8B,C** indicate performance of single electrodes. Cell with BP2000 showed steady window potential extension at both electrodes with stable rest potential. This carbon black is a micro- and mesoporous material with

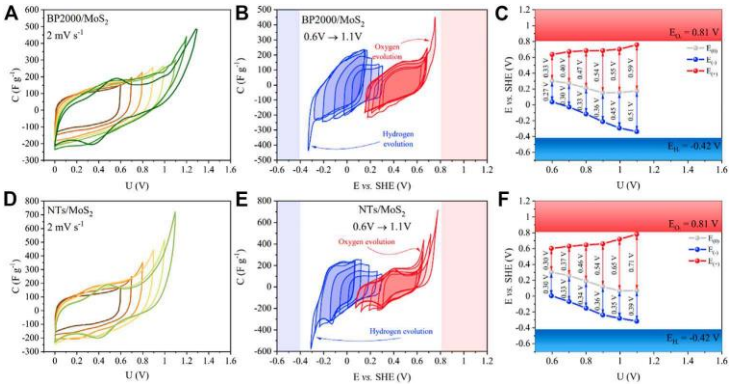

FIGURE 9 | Electrochemical characterization of symmetric EC cells based on MoS_2 composites. Cyclic voltammograms during gradual voltage extension—**(A)** and **(D)**. Individual cyclic voltammograms for (+) and (–) electrodes—**(B)** and **(E)**. Operational potentials for both electrodes at each voltage—**(C) and (F).**

developed surface area (1540 m^2g^{-1}). Due to such unique morphology, it possesses a smaller amount of sharp edges on which the electrolyte decomposition phenomena can occur, meaning that the material can withstand higher operational voltages. Contrary, for the cell with NTs (**Figures 8D–F**) at the low voltages (0.6–0.8 V), rest potentials of both electrodes remain stable. The maximum positive and negative potential values are gradually and equally extended. Beginning from 0.9 V, the rest potential is being shifted toward more negative values. The maximum positive potential remained more or less unchanged during the tests, and it was placed within the range of oxygen evolution. NTs possess essentially mesoporous structure (90 m^2g^{-1}) which excludes the hydrogen electrosorption, and the peaks are most likely related to the HER.

Figures 8G–I show results obtained for the cell with MoS_2. Opposite to the carbon-based materials, the cell with MoS_2 exhibited higher capacitance values (ca. 150 Fg^{-1}) and higher intrinsic resistance, seen at each step of the voltage extension. It can be observed that the positive electrode operates with a wider potential window than the negative one. It may be explained by the possible redox reactions occurring on the negative electrode involving hydrogen ion, for example, ($MoS_2 + H^+ + e^- \rightarrow$ MoS-SH^+) which further leads to its evolution (Soon and Loh, 2007; Ji et al., 2015; Cao et al., 2019). The additional charge flowing through the system is being balanced on the positive electrode. The system worked relatively stable up to 0.8 V, where the decomposition reactions started to occur. Further voltage extension resulted in peaks showing at both negative and positive sides. Those peaks can be attributed to hydrogen and oxygen evolution. Such phenomena could be understood in the situation where the positive and negative electrodes are working near the thermodynamic limit of O_2 and H_2 evolution. Additionally, from the characteristics of the negative electrode, it looks that the hydrogen storage does not take place, there is a lack of peak related to desorption of hydrogen. Generally, the layers of TMDs are composed of inert basal plane and edge sites which remain electrochemically active (Gao et al., 2016). Therefore, dependent on the number of active sites exposed, the layered MoS_2 will promote hydrogen decomposition definitely excluding its electrosorption (Hinnemann et al., 2005; Soon and Loh, 2007; Ji et al., 2015; Shi et al., 2015; Voiry et al., 2016; Cao et al., 2019). It is visible on the CV of the negative electrode that the hydrogen sorption/desorption is not observed. **Figures 9A–F** show CV for both electrodes and separate positive and negative electrode performance of BP2000/MoS_2 and NTs/MoS_2 composites.

Cell working with BP2000/MoS_2 started to exhibit faradaic reaction above 1V, which is relatively higher if we compare it with the cell containing MoS_2. Additionally, peaks which can be attributed to the HER and OER are significantly smaller than those for MoS_2 sample. It can be explained by the synergetic effect of capacitive behavior of BP2000 and faradaic processes of the deposited MoS_2. It can be interpreted that the BP2000 could be responsible for the hydrogen storage and MoS_2 for the hydrogen evolution. Despite of only 7 wt% of the carbon in the full composite, these processes can be distinguished. The cell showed comparable shifts of the rest potential during voltage extension which is comparable to the cell with pure MoS_2. On the contrary, cell with NTs/MoS_2 showed significantly higher hydrogen evolution peaks than BP2000/MoS_2 and MoS_2. Carbon nanotubes are mainly mesoporous materials which cannot store hydrogen; on the other hand, they are structurally defected that promotes electrolyte decomposition. Additional peaks on the positive electrode which occurred during extension of voltage prove it. As the final effect, the composite based on nanotubes has demonstrated a smaller operational voltage window. Positive electrodes of both composites exhibit small humps during charging/discharging near 0.3–0.5 V. It should be stressed that MoS_2 exhibits the typical electrical double layer even if the specific surface area is low (40 m^2g^{-1}) but also redox reactions connected with Li^+ insertion accordingly:

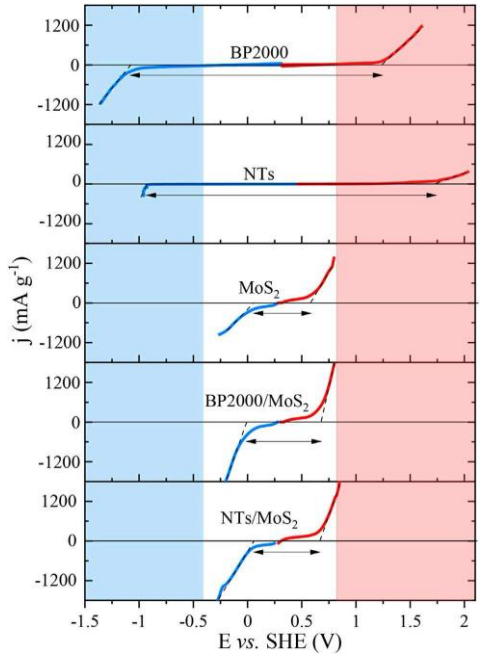

FIGURE 10 | Linear sweep voltammetry plots for different samples (pure materials and carbon/MoS_2 composites) at 2 mVs^{-1}.

$$MoS_2 + Li^+ + e^- \leftrightarrow MoS - SLi.$$

Redox reactions connected with the higher oxidation state of molybdenum should not be excluded.

Electrochemical stability of the electrodes working in a symmetrical two-electrode cell with reference was also determined with the use of linear sweep voltammetry (LSV). Voltage of the cell was extended from 0 to ± 1.5 V with a scan rate of 2 mVs^{-1} with simultaneous monitoring of electrodes potentials (Slesinski and Frackowiak, 2018). It was possible to observe real responses of each electrode since their performance are mutually governed. These investigations were conducted in two-electrode Swagelok cell with limited amount of electrolyte. This means that the local changes of the pH at electrode/electrolyte interface influence the electrodes behavior during voltage extension. The maximum operating window for each sample was determined by observing current increase related to hydrogen and oxygen evolution. The stability of each material with distinct electrodes is compiled in **Figure 10**. It can be marked that the BP2000 has the widest operational window. Thus, the potential was gradually extended in both directions, which is also reflected on CVs in **Figure 8**. LSV for NTs is characterized with narrower voltage window. In comparison to BP2000, hydrogen evolution on NTs occurs quicker, mostly due to the presence of defects and catalytic impurities, that is, Ni used for nanotubes production. MoS_2 in comparison to the carbon material showed much narrower voltage range of 0.6 V which is not a surprise due to its catalytic properties. What can also be observed is earlier evolution of hydrogen than in comparison with oxygen. Both composites, BP2000/MoS_2 and NTs/MoS_2, possess comparable HER and OER potentials. It can be also noticed that the composites possess slightly sharper anodic and cathodic responses. Such phenomena can be explained by significantly higher amount of vertically placed few-layered structures with exposed active edge sites which catalyze hydrogen and oxygen evolution reactions. Also, due to increased conductivity of the composites, the reaction of electrolyte decomposition can also occur earlier due to higher electron mobility.

CONCLUSION

Two morphologically different MoS_2 composites based on carbon nanotubes and carbon black have been prepared by a facile hydrothermal L-cysteine–assisted synthesis. Physicochemical characterization such as XRD and Raman spectroscopy proved that the desired materials were obtained. SEM/EDS and TEM analysis showed that the carbon supports are homogenously covered by the MoS_2 nanolayers. After physicochemical characterization, composites were prepared in a form of electrodes and their electrochemical performances in ECs cells were evaluated. NTs/MoS_2 and BP2000/MoS_2 demonstrated higher capacitance and intermediate conductivity to the parental materials—150 and 110 Fg^{-1} at 0.2 A g^{-1}, accordingly. MoS_2 was the major material in each composite; hence, main electrochemical responses were coming from the nanolayered structure of the TMD. Carbons served mainly as structural supports. Additional tests of the symmetric two-electrode cell with reference were performed. Investigation revealed that materials based on MoS_2 possess narrow range of operational voltage. On the contrary, carbon materials exhibited much wider operational voltage window. It was proven that MoS_2-based materials possess many active site edges which catalyze hydrogen evolution and restrict the operational voltage window to < 1 V. Additional experiments using the LSV method proved that pure MoS_2 possessed the narrowest voltage window of 0.6 V due to early hydrogen and oxygen evolution. BP2000/MoS_2 and NTs/MoS_2 composites exhibited comparable voltage range to MoS_2 but with slightly sharper anodic and cathodic responses caused by a vertical placement of few-layered structures with exposed active sites which catalyze HER and OER.

DATA AVAILABILITY STATEMENT

The original contributions presented in the study are included in the article/**Supplementary Material**, and further inquiries can be directed to the corresponding author.

AUTHOR CONTRIBUTIONS

EF contributed to research supervision, manuscript preparation, and results interpretation. MT contributed to planning and performing laboratory experiments and results interpretation. SS contributed to materials synthesis and manuscript preparation.

ACKNOWLEDGMENTS

The authors would like to acknowledge OPUS project of the National Science Center, Poland (Project No. 2018/31/B/ST4/01852) for the financial support of the research. The Polish Ministry of Science and Higher Education is also acknowledged for the 0911/SBAD/0399 project. The authors are sincerely thankful for performing TEM analysis to prof. Mirosława Pawlyta from Silesian University of Technology.

SUPPLEMENTARY MATERIAL

The Supplementary Material for this article can be found online at: https://www.frontiersin.org/articles/10.3389/fenrg.2021.647878/full#supplementary-material

REFERENCES

Acerce, M., Voiry, D., and Chhowalla, M. (2015). Metallic 1T Phase MoS2 Nanosheets as Supercapacitor Electrode Materials. *Nat. Nanotech.* 10, 313–318. doi:10.1038/nnano.2015.40

Balasingam, S. K., Lee, J. S., and Jun, Y. (2015). Few-layered MoSe2 Nanosheets as an Advanced Electrode Material for Supercapacitors. *Dalton Trans.* 44, 15491–15498. doi:10.1039/c5dt01985k

Bissett, M. A., Worrall, S. D., Kinloch, I. A., and Dryfe, R. A. W. (2016). Comparison of Two-Dimensional Transition Metal Dichalcogenides for Electrochemical Supercapacitors. *Electrochimica Acta* 201, 30–37. doi:10.1016/j.electacta.2016.03.190

Tseng, C.-A., and Lee, C.-P. (2020). Transition Metal Chalcogenides for the Electrocatalysis of Water. *Adv. Funct. Mater.* 19, 114. doi:10.5772/intechopen.92045

Cao, L., Yang, S., Gao, W., Liu, Z., Gong, Y., Ma, L., et al. (2019). Direct Laser-Patterned Micro-supercapacitors from Paintable MoS_2 Films. *Small* 9, 2905–2910. doi:10.1002/smll.201203164

Chang, K., and Chen, W. (2011). l-Cysteine-Assisted Synthesis of Layered MoS2/Graphene Composites with Excellent Electrochemical Performances for Lithium Ion Batteries. *ACS Nano* 5, 4720–4728. doi:10.1021/nn200659w

Chen, G. Z. (2016). Supercapacitor and Supercapattery as Emerging Electrochemical Energy Stores. *Int. Mater. Rev.* 62, 173–202. doi:10.1080/09506608.2016.1240914

Chen, W., Yu, X., Zhao, Z., Ji, S., and Feng, L. (2019). Hierarchical Architecture of Coupling Graphene and 2D WS2 for High-Performance Supercapacitor. *Electrochim. Acta* 298, 313–320. doi:10.1016/j.electacta.2018.12.096

Cherusseri, J., Sharma, R., and Kar, K. K. (2016). Helically Coiled Carbon Nanotube Electrodes for Flexible Supercapacitors. *Carbon* 105, 113–125. doi:10.1016/j.carbon.2016.04.019

Choi, W., Choudhary, N., Han, G. H., Park, J., Akinwande, D., and Lee, Y. H. (2017). Recent Development of Two-Dimensional Transition Metal Dichalcogenides and Their Applications. *Mater. Today* 20, 116–130. doi:10.1016/j.mattod.2016.10.002

Conley, H. J., Wang, B., Ziegler, J. I., Haglund, R. F., Pantelides, S. T., and Bolotin, K. I. (2013). Bandgap Engineering of Strained Monolayer and Bilayer MoS2. *Nano Lett.* 13, 3626–3630. doi:10.1021/nl4014748

Coogan, Á., and Gun'ko, Y. K. (2021). Solution-based "Bottom-Up" Synthesis of Group VI Transition Metal Dichalcogenides and Their Applications. *Mater. Adv.* 2, 146–164. doi:10.1039/d0ma00697a

Duesberg, G. S., Loa, I., Burghard, M., Syassen, K., and Roth, S. (2000). Polarized Raman Spectroscopy on Isolated Single-Wall Carbon Nanotubes. *Phys. Rev. Lett.* 85, 5436–5439. doi:10.1103/physrevlett.85.5436

Fic, K., Frackowiak, E., and Béguin, F. (2012). Unusual Energy Enhancement in Carbon-Based Electrochemical Capacitors. *J. Mater. Chem.* 22, 24213–24223. doi:10.1039/c2jm35711a

Frackowiak, E., and Béguin, F. (2001). Carbon Materials for the Electrochemical Storage of Energy in Capacitors. *Carbon* 39, 937–950. doi:10.1016/s0008-6223(00)00183-4

Gao, J., Li, L., Tan, J., Sun, H., Li, B., Idrobo, J. C., et al. (2016). Vertically Oriented Arrays of ReS2 Nanosheets for Electrochemical Energy Storage and Electrocatalysis. *Nano Lett.* 16, 3780–3787. doi:10.1021/acs.nanolett.6b01180

González, A., Goikolea, E., Barrena, J. A., and Mysyk, R. (2016). Review on Supercapacitors: Technologies and Materials. *Renew. Sustain. Energ. Rev.* 58, 1189–1206. doi:10.1016/j.rser.2015.12.249

Hinnemann, B., Moses, P. G., Bonde, J., Jorgensen, K. P., Nielsen, J. H., Horch, S., et al. (2005). Biomimetic Hydrogen Evolution: MoS_2 Nanoparticles as Catalyst for Hydrogen Evolution. *J. Am. Chem. Soc.* 127, 5208–5209. doi:10.1021/ja0504690

Huang, K.-J., Wang, L., Liu, Y.-J., Liu, Y.-M., Wang, H.-B., Gan, T., et al. (2013). Layered MoS2-Graphene Composites for Supercapacitor Applications with Enhanced Capacitive Performance. *Int. J. Hydrogen Energ.* 38, 14027–14034. doi:10.1016/j.ijhydene.2013.08.112

Huang, K.-J., Wang, L., Zhang, J.-Z., Wang, L.-L., and Mo, Y.-P. (2014). One-step Preparation of Layered Molybdenum Disulfide/multi-Walled Carbon Nanotube Composites for Enhanced Performance Supercapacitor. *Energy* 67, 234–240. doi:10.1016/j.energy.2013.12.051

Ji, H., Liu, C., Wang, T., Chen, J., Mao, Z., Zhao, J., et al. (2015). Porous Hybrid Composites of Few-Layer MoS2 Nanosheets Embedded in a Carbon Matrix with an Excellent Supercapacitor Electrode Performance. *Small* 11, 6480–6490. doi:10.1002/smll.201502355

Laheäär, A., Przygocki, P., Abbas, Q., and Béguin, F. (2015). Appropriate Methods for Evaluating the Efficiency and Capacitive Behavior of Different Types of Supercapacitors. *Electrochem. Commun.* 60, 21–25. doi:10.1016/j.elecom.2015.07.022

Lin, L., Lei, W., Zhang, S., Liu, Y., Wallace, G. G., and Chen, J. (2019). Two-dimensional Transition Metal Dichalcogenides in Supercapacitors and Secondary Batteries. *Energ. Storage Mater.* 19, 408–423. doi:10.1016/j.ensm.2019.02.023

Lukatskaya, M. R., Dunn, B., and Gogotsi, Y. (2016). Multidimensional materials and device architectures for future hybrid energy storage. *Nat. Commun.* 7, 12647. doi:10.1038/ncomms12647

Nasir, M. Z. M., Sofer, Z., Ambrosi, A., and Pumera, M. (2015). A Limited Anodic and Cathodic Potential Window of MoS2: Limitations in Electrochemical Applications. *Nanoscale* 7, 3126–3129. doi:10.1039/c4nr06899h

Pandolfo, A. G., and Hollenkamp, A. F. (2006). Carbon Properties and Their Role in Supercapacitors. *J. Power Sourc.* 157, 11–27. doi:10.1016/j.jpowsour.2006.02.065

Park, S.-K., Yu, S.-H., Woo, S., Quan, B., Lee, D.-C., Kim, M. K., et al. (2013). A Simplel-Cysteine-Assisted Method for the Growth of MoS2nanosheets on Carbon Nanotubes for High-Performance Lithium Ion Batteries. *Dalton Trans.* 42, 2399–2405. doi:10.1039/c2dt32137h

Rao, A. M., Ritcher, E., Bandow, S., Chase, B., Eklund, P. C., Williams, K. A., et al. (1997). Diameter-Selective Raman Scattering from Vibrational Modes in Carbon Nanotubes. *Science* 275, 187–191. doi:10.1126/science.275.5297.187

Ratajczak, P., Suss, M. E., Kaasik, F., and Béguin, F. (2019). Carbon Electrodes for Capacitive Technologies. *Energ. Storage Mater.* 16, 126–145. doi:10.1016/j.ensm.2018.04.031

Rendón-Patiño, A., Domenech-Carbó, A., Primo, A., and García, H. (2020). Superior Electrocatalytic Activity of MoS2-Graphene as Superlattice. *Nanomaterials* 10, 839. doi:10.3390/nano10050839

Sangeetha, D. N., and Selvakumar, M. (2018). Active-defective Activated carbon/MoS2 Composites for Supercapacitor and Hydrogen Evolution Reactions. *Appl. Surf. Sci.* 453, 132–140. doi:10.1016/j.apsusc.2018.05.033

Sangeetha, D. N., Santosh, M. S., and Selvakumar, M. (2020). Flower-like Carbon Doped MoS_2/Activated Carbon Composite Electrode for Superior Performance of Supercapacitors and Hydrogen Evolution Reactions, *J. Alloys Comp.* 831, 154745.

Sharma, P., and Bhatti, T. S. (2010). A Review on Electrochemical Double-Layer Capacitors. *Energ. Convers. Manage.* 51, 2901–2912. doi:10.1016/j.enconman.2010.06.031

Shi, S., Gao, D., Xia, B., Liu, P., and Xue, D. (2015). Enhanced Hydrogen Evolution Catalysis in MoS2 Nanosheets by Incorporation of a Metal Phase. *J. Mater. Chem. A.* 3, 24414–24421. doi:10.1039/c5ta08520a

Simon, P., and Gogotsi, Y. (2008). Materials for Electrochemical Capacitors. *Nat. Mater* 7, 845–854. doi:10.1038/nmat2297

Slesinski, A., and Frackowiak, E. (2018). Determination of Accurate Electrode Contribution during Voltammetry Scan of Electrochemical Capacitors. *J. Solid State. Electrochem.* 22, 2135–2139. doi:10.1007/s10008-018-3924-0

Soon, J. M., and Loh, K. P. (2007). Electrochemical Double-Layer Capacitance of MoS[sub 2] Nanowall Films. *Electrochem. Solid-state Lett.* 10, A250–A254. doi:10.1149/1.2778851

Sun, P., Wang, R., Wang, Q., Wang, H., and Wang, X. (2019). Uniform MoS2 Nanolayer with Sulfur Vacancy on Carbon Nanotube Networks as Binder-free Electrodes for Asymmetrical Supercapacitor. *Appl. Surf. Sci.* 475, 793–802. doi:10.1016/j.apsusc.2019.01.007

Voiry, D., Yang, J., and Chhowalla, M. (2016). Recent Strategies for Improving the Catalytic Activity of 2D TMD Nanosheets toward the Hydrogen Evolution Reaction. *Adv. Mater.* 28, 6197–6206. doi:10.1002/adma.201505597

Xu, D., Wang, H., Qiu, R., Wang, Q., Mao, Z., Jiang, Y., et al. (2020). Coupling of Bowl-like VS2 Nanosheet Arrays and Carbon Nanofiber Enables Ultrafast Na+-Storage and Robust Flexibility for Sodium-Ion Hybrid Capacitors. *Energ. Storage Mater.* 28, 91–100. doi:10.1016/j.ensm.2020.03.002

Yang, W., He, L., Tian, X., Yan, M., Yuan, H., Liao, X., et al. (2017). Carbon-MEMS-Based Alternating Stacked MoS2@rGO-CNT Micro-Supercapacitor with High 393 Capacitance and Energy Density. *Small* 13, 17000639. doi:10.1002/smll.201770144

Yuan, S., Pang, S. Y., and Hao, J. (2020). 2D Transition Metal Dichalcogenides, Carbides, Nitrides, and Their Applications in Supercapacitors and Electrocatalytic Hydrogen Evolution Reaction. *Appl. Phys. Rev.* 7–021304. doi:10.1063/5.0005141

Zdrojek, M., Gebicki, W., Jastrzebski, C., Melin, T., and Huczko, A. (2004). Studies of Multiwall Carbon Nanotubes Using Raman Spectroscopy and Atomic Force Microscopy. *Ssp* 99-100, 265–268. doi:10.4028/www.scientific.net/ssp.99-100.265

Zhang, W.-J., and Huang, K.-J. (2017). A Review of Recent Progress in Molybdenum Disulfide-Based Supercapacitors and Batteries. *Inorg. Chem. Front.* 4, 1602–1620. doi:10.1039/c7qi00515f

Zhong, C., Deng, Y., Hu, W., Qiao, J., Zhang, L., and Zhang, J. (2015). A Review of Electrolyte Materials and Compositions for Electrochemical Supercapacitors. *Chem. Soc. Rev.* 44, 7484–7539. doi:10.1039/c5cs00303b

Conflict of Interest: The authors declare that the research was conducted in the absence of any commercial or financial relationships that could be construed as a potential conflict of interest.

Copyright © 2021 Tobis, Sroka and Frąckowiak. This is an open-access article distributed under the terms of the Creative Commons Attribution License (CC BY). The use, distribution or reproduction in other forums is permitted, provided the original author(s) and the copyright owner(s) are credited and that the original publication in this journal is cited, in accordance with accepted academic practice. No use, distribution or reproduction is permitted which does not comply with these terms.

P3. *Electrochemical Capacitor Based on Reduced Graphene Oxide/NiS_2 Composite*

Authors: Andrii Kachmar, Maciej Tobis, Elżbieta Frąckowiak

Journal: ChemElectroChem, **2022**, 9, e202200834

DOI: https://doi.org/10.1002/celc.202200834

License: The content is available under CC BY 4.0

Contribution: Responsible for obtaining physicochemical characterization results (XRD patterns, N_2 sorption, SEM imaging, TEM imaging), evaluation of the physicochemical data (N_2 sorption, SEM and TEM imaging), performing electrochemical studies in two- and three-electrode cells by different techniques, data plotting, writing original draft

Graphical abstract

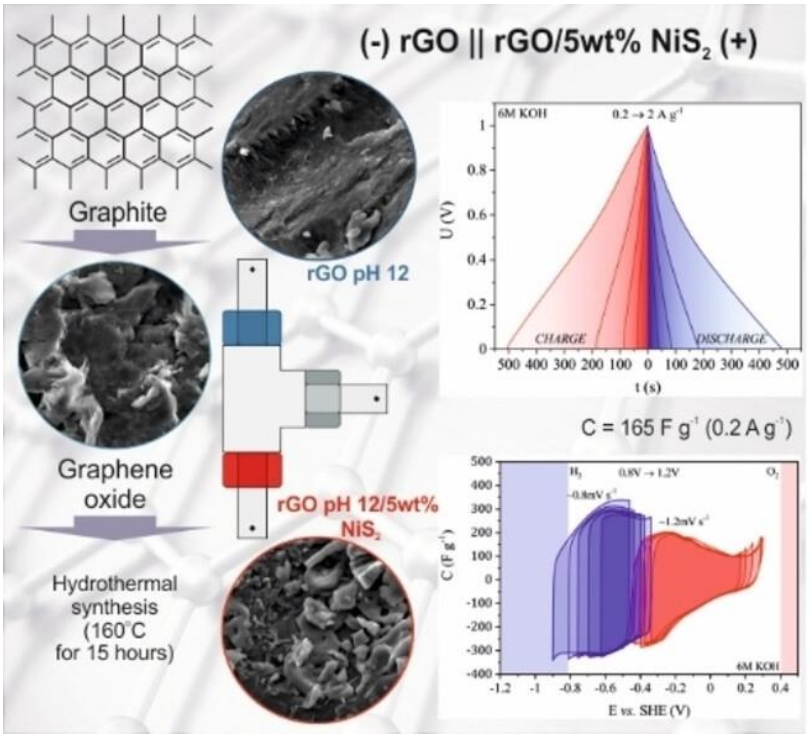

Context of research & summary

The utilization of 2D materials, specifically TMDs, as electrode materials presents an intriguing approach to enhance the electrochemical performance of energy storage devices.

Graphene, due to its extraordinary physicochemical characteristics (*Chapter I*), is a promising 2D material for electrodes in energy storage application. However, current methods of graphene production are not cost-effective. Instead, reduced graphene oxide (rGO), prepared through the oxidation and subsequent reduction of graphite flakes, constitutes an attractive alternative to graphene. However, such synthesis protocol can often lead into formation of structural defects potentially affecting its electrical conductivity. Nevertheless, rGO offers a good cost-effective ratio with satisfactory electrical conductivity comparable to graphene.

TMDs, in addition to their 2D form, can also exist in non-layered forms. A well-known example is nickel sulfide (NiS_2), which exhibits a pyrite-like structure. NiS_2 is known for its ability to participate in reversible redox reactions, significantly improving the energy storage properties of the system. However, due to its highly crystalline structure, most of the bulk electrode material remains electrochemically inactive. Therefore, these materials are often paired with conductive substrates during synthesis of composite to increase their electrochemically active SSA.

In this published article, contrary to previous papers, a pyrite-like TMD (NiS_2) material is deposited onto 2D (rGO) material. In the first step, the preparation protocol for obtaining rGO suitable for electrochemical application were developed. It was found that hydrothermally prepared rGO at pH 12 exhibited fewer oxygen functionalities and optimal structural properties for subsequent binding with NiS_2. Various weight percentages of NiS_2 were deposited onto the rGO, with 5wt% of NiS_2 identified as the most effective in enhancing the electrochemical performance of a device. In the context of previous research where the catalytic activity of TMDs were recognized, hybrid systems consisting of rGO negative electrode and rGO/NiS_2 positive electrode were assembled. Such system showed improved capacitance from 147 F g^{-1} to 165 F g^{-1} at 0.2 A g^{-1}. Consequently, TMDs offer various possibilities of improving the overall performance of the ECs system.

Publication

P3. *Electrochemical Capacitor Based on Reduced Graphene Oxide/NiS_2 Composite*

Check for updates

ChemElectroChem

Research Article
doi.org/10.1002/celc.202200834

Chemistry Europe
European Chemical Societies Publishing

www.chemelectrochem.org

Electrochemical Capacitor Based on Reduced Graphene Oxide/NiS_2 Composite

Andrii Kachmar, Maciej Tobis, and Elżbieta Frąckowiak*[a]

The use of a pyrite-like structure transition metal dichalcogenides (TMDs) such as NiS_2 is not reported as frequently as layered structured TMDs in electrochemical capacitors. Our study shows a reduced graphene oxide (rGO) preparation and its further use as a substrate for the deposition of NiS_2 during the hydrothermal reaction. The influence of pH for the GO solution on the structural and textural properties of the resultant rGO was explained in detail by using Raman spectroscopy, UV, X-ray diffraction (XRD), scanning electron microscopy (SEM) and nitrogen sorption at 77 K. The electrochemical response of the rGO samples obtained from various pH solutions was studied and compared in symmetric two electrode Swagelok® cells. As a result, rGO pH 12 was chosen for further modification with NiS_2. The average size of the crystallites, and electronic structure of the rGO/NiS_2 composite have been determined. The effect of the NiS_2 content in the composite on the electrochemical results was further investigated. It occurred that 5 wt% NiS_2 in the composite was sufficient for a significant improvement of the capacitive response. Interestingly, an asymmetric cell with rGO/5 wt% NiS_2 working as a positive electrode and rGO pH 12 as a negative electrode was able to reach a high capacitance of 165 $F g^{-1}$ at 0.2 $A g^{-1}$ with 92% coulombic and 79% energetic efficiency.

Introduction

In order to fulfil the increasing demand toward sustainable energy consumption, there is a strong need for development of devices that are able to efficiently generate/store energy. Among a wide variety of systems, high-power electrochemical capacitors (ECs) have found many commercial applications, e.g., in consumer electronics, heavy industry, automotive sector of hybrid electric vehicles (HEVs), or as power grid buffer in powerplants. Compared to other energy storage systems, they are characterized by superior cyclability, low maintenance needs, and favourable environmental profile.[1,2] Such devices are constructed with two porous electrodes, an ion permeable separator, and an electrolyte. The electrode materials are usually made of carbonaceous materials, e.g., activated carbons, carbon blacks, carbon nanotubes, or graphene derivatives. Carbons are usually able to provide high capacitance values due to the controlled distribution of pores and the developed specific surface area.[3–5] Yet, they cannot compete with metal-ion batteries in terms of specific energy density values. Primarily, the energy storage mechanism within ECs is purely based on the formation of an electrical double layer (EDL) at the electrode/electrolyte interface.[6,7] It means that ions are physically adsorbed on the surface of the carbon material. Thus, carbon-based systems usually reach around 100–150 $F g^{-1}$.[8,9] Enhancement of capacitance can be obtained from components of the electrolyte or electrode material that participate in fast reversible reduction/oxidation reactions. One of the exemplary materials that exhibit redox phenomena are transition metal dichalcogenides (TMDs).[10] They are chemically versatile materials which can be presented by the formula of MX_2, where M is a metal atom (e.g., Mo, V, Zr, Nb, Ni etc.), and X is chalcogen atoms (e.g., S, Se, or Te). The majority of TMDs crystallize in the layered structure with three different polymorphs, that is, 1T, 2H and 3R (number represents the amount of X–M–X units in a single unit cell).[11] Contrary, some TMDs are commonly found in non-layered structures (usually group 8–10 in the periodic table).[12] Recent development of TMDs within energy storage systems suggests great potential to fill the gap between modern requirements and final performance of the device.[13–16] Yet, numerous recent articles are describing the performance of the layered materials (e.g., MoS_2, WS_2, VS_2, etc.) within energy storage devices, with only few papers about non-layered, e.g., FeS_2, NiS_2. One of the interesting examples of the nonlayered TMD is nickel sulphide (NiS_2). It is characterized with a high-symmetry pyrite structure and a wide range of electrical, optical, and magnetic properties. Among a variety of potential applications, NiS_2 has found particularly use in energy storage devices. It was already described that NiS_2 is able to augment the specific capacitance of the system through the reversible redox reaction.[17] W. Ni et al. presented the preparation of NiS_2 during the high-pressure sulfidation process for its subsequent electrochemical study in a three-electrode system. The active material (NiS_2) was pressed in the nickel foam serving as the working electrode and investigated within the 0.6 V potential window. Such electrode exhibited 1545 $F g^{-1}$ at 1 $A g^{-1}$.[18] D. Zhang et al. showed preparation of NiS_2/NiO nanosheet grown on a nickel foam during the hydrothermal reaction. The

[a] *Dr. A. Kachmar, M. Tobis, Prof. E. Frąckowiak*
Faculty of Chemical Technology
Poznan University of Technology
Berdychowo 4, 60-965, Poznan, Poland
E-mail: elzbieta.frackowiak@put.poznan.pl

Supporting information for this article is available on the WWW under https://doi.org/10.1002/celc.202200834

© 2022 The Authors. ChemElectroChem published by Wiley-VCH GmbH. This is an open access article under the terms of the Creative Commons Attribution License, which permits use, distribution and reproduction in any medium, provided the original work is properly cited.

© 2022 The Authors. ChemElectroChem published by Wiley-VCH GmbH

ChemElectroChem | Research Article
doi.org/10.1002/celc.202200834
Chemistry Europe
European Chemical Societies Publishing

prepared nickel composite electrode was used as a working electrode in a three-electrode system and tested within a narrow potential window of 0.5 V reaching 2251 $F g^{-1}$ at 1 $A g^{-1}$.[19] Y. Ji et al. presented the hydrothermal preparation and electrochemical performance of heterostructured composite MnO_2@NiS_2/$Ni(OH)_2$. The electrochemical system was able to reach 1010 $F g^{-1}$ at 1 $A g^{-1}$.[20] The aforementioned authors tried to refer the visible redox response during electrochemical performance to the reaction given below (equation 1):

$$NiS_2 + OH^- \leftrightarrow NiS_2OH + e^- \quad (1)$$

It is worth underlining that TMDs are also recognized as hydrogen evolution reaction (HER) catalysts. Generally, each member of the TMDs family is able to promote HER due to presence of unsaturated sulphur atoms on the edge sites of the material structure.[21–23] NiS_2 was also recently recognized as an efficient hydrogen evolution catalyst.[24,25] It is necessary to underline that the catalytic properties of TMD materials cause shrinkage of negative electrode potential window. Therefore, due to the catalytic properties on the negative side (HER), TMD was recently implemented in asymmetric system as a positive electrode.[26] NiS_2 has great potential to be used as an electrode material additive for improving the overall EC performance. However, aforementioned studies present mainly use of NiS_2 composites in the three-electrode system which does not represent the conditions in the real EC cells. In addition, electrochemical characteristics in the form of well-defined peaks in cyclic voltammetry (CV) or wide plateau for galvanostatic discharge (GC/GD) should not be expressed in $F g^{-1}$, but rather $mAh g^{-1}$ typically for battery response. Moreover, nickel foam served as a current collector which in the very positive potential can exploit reversible redox reduction of nickel oxides. Hence, even if the literature values of capacitance for NiS_2 measured in the narrow potential range seem to be impressive, it is worth considering that calculations is often not truthful and apart from that mass of electrodes should be significantly higher than 0.5 mg.

In this paper, reduced graphene oxide (rGO) samples have been prepared and combined with NiS_2 to form composites. Different rGO were obtained during hydrothermal reduction whereas the pH of the GO solution varied from 8 to 12. Interestingly, if pH was higher the resultant rGO sample has a lower content of surface oxygen groups. Rich oxygen functionality affects the capacitance decay during cycling. Hence, the electrochemical performance of the cells with rGO samples dependent on the pH of GO solution was the criterion for rGO selection to prepare NiS_2 composite. Then, NiS_2/rGO composites were formed during hydrothermal reaction with various content of NiS_2. After adjusting the optimal NiS_2 content within the electrode matrix, asymmetric EC cells were assembled and tested.

Results and Discussion

The Raman spectra of graphite powder, GO, rGO samples hydrothermally reduced at different pH values and rGO/NiS_2 composite are presented in Figure 1A. The characteristic two peaks at around 1340–1360 cm^{-1} (D band) and 1565–1595 cm^{-1} (G band) correspond to breathing A_{1g} mode by a second order Raman scattering process and first-order scattering of E_{2g} mode, respectively.[27] The G band indicates the sp^2 carbon presence where D band corresponds to sp^3 carbon networks and its intensity grows with the enlarging of disordered carbon content.[28] Complex composition of the D band reflects the type of defects and their concentration. The multiple Lorentzian peaks were used for D–G spectral region fitting. The best deconvolution result for GO sample was achieved for four Lorentzian fitting (Figure 1A). D* peak at about 1100–1200 cm^{-1} was previously observed in disordered amorphous carbons with high content of sp^3 bonds.[29] The origin of the D** peak in our case can be assigned to contribution from the electronic state in graphitic nanocrystals.[30] The fitting parameters of Raman spectra component are presented in Table S1 and Table S2. The

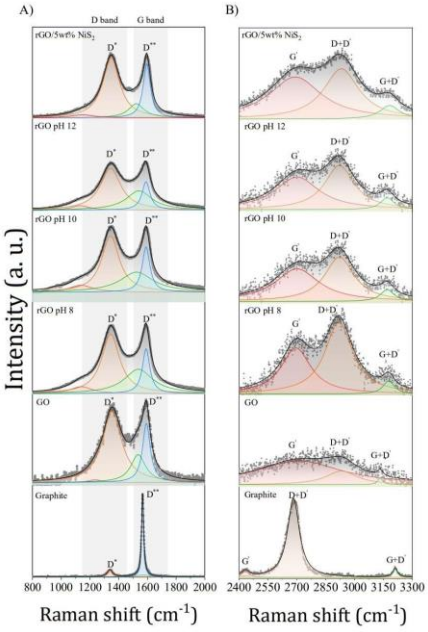

Figure 1. (A) Multiple peak fitting for D–G region of the graphite, GO and rGO materials hydrothermally reduced at different pH values and rGO with NiS_2 deposited. (B) Multiple peak fitting for 2D band regions of the graphite, GO, rGO materials hydrothermally reduced at different pH values and rGO (pH 12) with NiS_2 deposited.

© 2022 The Authors. ChemElectroChem published by Wiley-VCH GmbH

21960216, 2022, 21, Downloaded from https://chemistry-europe.onlinelibrary.wiley.com/doi/10.1002/celc.202200834 by POLITECHNIKA POZNANSKA, Wiley Online Library on [11/06/2024]. See the Terms and Conditions (https://onlinelibrary.wiley.com/terms-and-conditions) on Wiley Online Library for rules of use; OA articles are governed by the applicable Creative Commons License

ChemElectroChem | Research Article
doi.org/10.1002/celc.202200834
Chemistry Europe
European Chemical Societies Publishing

21960216, 2022, 21, Downloaded from https://chemistry-europe.onlinelibrary.wiley.com/doi/10.1002/celc.202200834 by POLITECHNIKA POZNANSKA, Wiley Online Library on [11/06/2024]. See the Terms and Conditions (https://onlinelibrary.wiley.com/terms-and-conditions) on Wiley Online Library for rules of use; OA articles are governed by the applicable Creative Commons License

intensities of D and D* modes for all samples of reduced graphene materials are comparable. At the same time, the relative intensities of G mode for all rGO materials are decreasing with pH.

The G band of rGO pH 12/5 wt% NiS_2 composite is shifted to a slightly higher value (~1596 cm^{-1}) compared to the G band of carbon (~1590 cm^{-1}), which signifies the strong synergistic effect between metal sulfides with carbon.[31] Figure S1 shows the Raman spectra of NiS_2 material. The bands at 270, 282, 470, 509, 549 and 1048 cm^{-1} are assigned to the A_{1g} and E_g modes of NiS_2.[36] It is known that the linear dependence between the total intensity of D component A_D and the intensity of G mode (A_G) allows to estimate the average lateral size L_a (equation 2 – average length of crystallite along to basal (002) crystallographic plane of graphitic lattice).[32]

$$L_a(nm) = (2.4 \times 10^{-10})\lambda^4 \left(\frac{I_D}{I_G}\right)^{-1} \quad (2)$$

where, λ (nm) is a laser line wavelength. The average size of graphite crystallites for GO sample is about 6.39 nm. The reducing procedure causes the decrease of L_a values to 5.48 nm, 5.25 nm, 5.06 nm for rGO pH 8, rGO pH 10 and rGO pH 12 whereas for rGO pH 12/5 wt% NiS_2 is 7.43 nm. The lateral size of crystallites strongly depends on the pH. Complex 2D band observed on Raman spectra in a range of 2400–3300 cm^{-1} is a second order of D band which is caused by overtone of two phonon lattice vibrational processes and is sensitive to the electronic band structure of the graphitic materials, but not associated with defects.[33] This band intensity is sensitive to the stacking order of graphene sheets along the c-axis to the basal plane and for single layer graphene 2D band shows strong single Lorentzian peak at about 2696 ± 5 cm^{-1}.[34] Increase of layers causes the variation of electronic structure, additional modes are formed with simultaneous blue-shift of all 2D band.[35] Bulk graphite has a two peak profile of 2D band.[36] The fitting procedure of 2D region with three Lorentzian functions was performed (Figure 1B) and obtained results are presented in Table S2. Peaks observed for Raman spectra of reduced materials at about 2692–2701 cm^{-1} are assigned to 2D (G') Raman modes. The peaks at 2917–2921 cm^{-1} correspond to D + D' or D + G' modes which are associated to defected structure.[31] Low intensity peaks at 3170–3183 cm^{-1} are attributed to 2D' and G + D' modes or 2G overtones.[37] The reducing process leads to the increase of G' and decrease of D + D' mode intensity. It means that with the increase of the pH, the structure of the resultant sample is less defected. At the same time, 2D band structure for all rGO samples indicates that the pH value does not affect the graphene layers stacking and we can estimate the average number of layers close to 3–4. The specific surface area (SSA) and pore size distribution of the obtained samples were analysed using nitrogen sorption at 77 K. Table S3 shows sorption properties for prepared materials. The sorption isotherms correspond to type IV of IUPAC classification which is typically assigned to monolayer-multilayer adsorption on the mesopore walls.[38] The evolution of hysteresis loop for materials obtained at pH 8 to 12 can be associated with filling of micropores with the simultaneous increase of mesoporosity (Figure 2A). The density functional theory (DFT) calculation (slit pore model) of pore size distribution confirms this assumption (Figure 2B). All hydrothermally obtained materials are characterized with comparable textural properties, whereas higher pH of GO solution prior reduction causes enlarging the meso and micropores volume with the decrease of the average micropore size. Pores in the range of 0.4–5.0 nm are formed by interconnection of graphene packages within the particles. At the same time the large mesopores in a range of 25–45 nm correspond to interparticle cavities. All samples show comparable characteristics of pore size distribution. The pH values affect the porous texture and the reduction degree of rGO. Furthermore, mesopores of the graphene-based structure can accommodate the NiS_2 volume changes during charging/discharging. Thus, it provides effective ions diffusion path contributing to the increase of the power-rate response as well as cycling performance.[24]

For evaluation of electronic properties of the prepared materials, the more detailed characterization was completed. Mott-Schottky characterization was performed in order to estimate the donor or acceptor concentration (N_D) and flat band potential.[39,40] Mott-Schottky plots were prepared with the

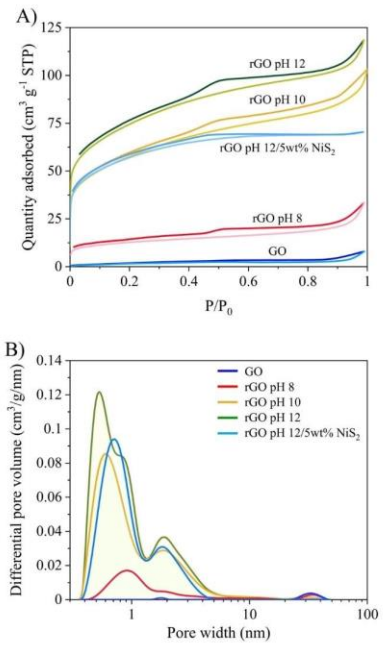

Figure 2. (A) N_2 adsorption/desorption isotherms for rGO and composite samples obtained at different pH; (B) DFT pore size distributions.

© 2022 The Authors. ChemElectroChem published by Wiley-VCH GmbH

ChemElectroChem | Research Article
doi.org/10.1002/celc.202200834
Chemistry Europe
European Chemical Societies Publishing

21960216, 2022, 21, Downloaded from https://chemistry-europe.onlinelibrary.wiley.com/doi/10.1002/celc.202200834 by POLITECHNIKA POZNANSKA, Wiley Online Library on [11/06/2024]. See the Terms and Conditions (https://onlinelibrary.wiley.com/terms-and-conditions) on Wiley Online Library for rules of use; OA articles are governed by the applicable Creative Commons License

assumption of ideal semiconductor characteristics following equation 3:

$$\frac{1}{C^2} = \frac{2}{\varepsilon\varepsilon_0 A^2 e N_D}\left(E - E_{fb} - \frac{K_B T}{E}\right) \quad (3)$$

where ε refers to the relative permittivity (dielectric constant taken as $\varepsilon = 6$,[41] ε_0 is the vacuum permittivity, e is the charge of the electron, N_D is the donor concentration, N_A is the acceptor concentration), E is the applied potential and E_{fb} is the flat band potential. By means of this equation, the flat band potential of the material can be determined by evaluating the interception of the linear region with the axis representing the applied potential.

Figure 3 shows Nyquist (A) and corresponding Mott-Schottky (B) plots for rGO pH 12/5 wt% NiS_2. These plots for GO and rGO materials are also compiled in Figure S2. Nyquist plot consists of two distinct regions, a semi-circle at high frequency related to the electron transfer processes where the diameter of the semicircle is related to the electron transfer resistance whereas a linear region at lower frequencies corresponds to diffusion-controlled processes.[42] Electrochemical impedance spectroscopy (EIS) spectrum for the GO electrode is practically linear throughout the frequency range studied, showing that the GO electrode has low ability to transfer electrons. The sample exhibited negative slope, suggesting that it was p-type semiconductor. Band potential value was calculated and it is equal to 0.79 V. The acceptor charge density of GO was $6.59 \cdot 10^{26}$ m^{-3} (1 kHz).[43] Contrary, the Nyquist plots of all rGO materials show that the bias potential is nearly vertical and at high frequency shows a very small semicircle, which indicates an ideal capacitive behavior, i.e., very low charge-transfer resistance with high electrolyte diffusion inside the rGO electrode.[44] Mott-Schottky analysis of rGO exhibits a positive slope indicating n-type semiconductive nature of material.[45] The semicircle radius for rGO pH 12/5 wt% NiS_2 composite electrode is lower than for rGO. It indicates that incorporation of NiS_2 into rGO effectively reduces its charge transfer resistance.[40] The flat-band potential (E_{fb}) of rGO pH 8–0.21 V, rGO pH 10–0.03 V, and of rGO pH 12–0.02 V (vs. SHE) but shifted anodically to ca 0.41 V for the rGO pH 12/5 wt% NiS_2 material. Thermodynamically, E_{fb} of an n-type rGO pH 12 semiconductor determines the conduction band position, and the positive shift of the conduction band suggests narrowing of the energy barrier of hydrogen evolution (H^+/H_2 –0.83 V vs. SHE in 6 M KOH), leading to enhanced electrocatalytic performance of the material.[46] The donor concentration was estimated from the slope of Mott-Schottky plots for GO – $6.59 \cdot 10^{26}$ m^{-3}, rGO pH 8–$2.63 \cdot 10^{23}$ m^{-3}, rGO pH 10–$1.16 \cdot 10^{20}$ m^{-3}, rGO pH 12–$1.5 \cdot 10^{15}$ m^{-3}, and rGO pH 12/5 wt% NiS_2 – $5.9 \cdot 10^{20}$ m^{-3} (1 kHz).[40,47,48] The decrease of donor concentration can be connected with better graphene material reduction, losing oxide groups on the graphene surface with higher pH levels, and higher specific surface area. Further characterization of samples was performed by using X-ray diffraction (XRD). Characteristic crystallographic parameters [interlayer space (d_{002}), crystal stack height (L_c), in-plane crystallite size (L_a), and number of graphene layers in the crystal (N_c)] were determined as follows (equation 4–7):

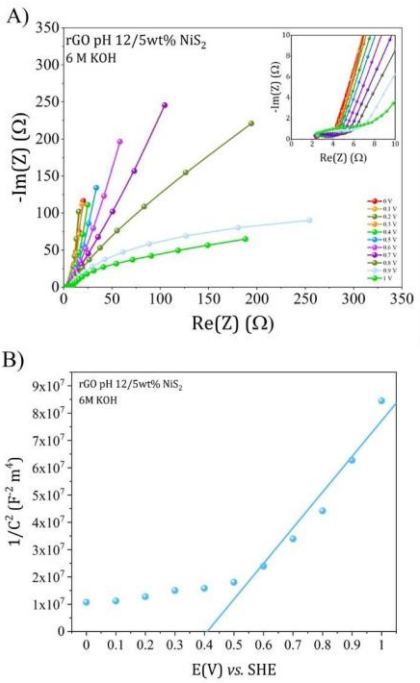

Figure 3. (A) Nyquist plot; (B) Mott-Schottky plot for the rGO pH 12/5 wt% NiS_2.

$$d_{002} = \frac{\lambda}{2sin\theta_1} \quad (4)$$

$$L_c = \frac{k_1 \cdot \lambda}{FWHM \cdot cos\theta_1} \quad (5)$$

$$L_a = \frac{k_2 \cdot \lambda}{FWHM \cdot cos\theta_2} \quad (6)$$

$$N_c = \frac{L_c}{d_{002}} \quad (7)$$

where: λ – radiation wavelength, θ_1 – (002) diffraction peak position (°), θ_2 – (100) diffraction peak position (°), k_1 – form factor ($k_1 = 0.9$), k_2 – Warren form factor constant ($k_2 = 1.84$), FWHM – width at half height of the corresponding diffraction peak (rad).[49,50] Figure 4 shows XRD studies for rGO and rGO/5 wt% NiS_2 and NiS_2 samples.

© 2022 The Authors. ChemElectroChem published by Wiley-VCH GmbH

ChemElectroChem | Research Article
doi.org/10.1002/celc.202200834
Chemistry Europe
European Chemical Societies Publishing

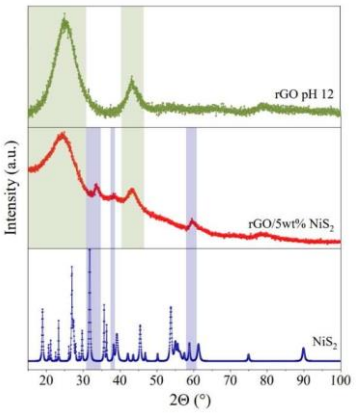

Figure 4. XRD patterns for rGO pH 12, rGO/5 wt% NiS_2 and NiS_2.

The peak observed at $2\theta = 25.21$ confirms partial restoration of the graphitic structure in the rGO sample[51] and it is consistent with a separation between layers (d_{002}) of 0.35 nm. Another peak in the 2θ range of 44°, is due to (100) reflection. Crystallite dimensions as well as average number of sheets in crystallite[52] were determined and are shown in Table S4. Spectra characteristic for cubic, pyrite NiS_2 structure containing discrete S_2 units were revealed. The S–S distance of these S_2 units is very close to that of a single S–S bond.[53] Peaks for NiS_2 observed at 26,9°, 31.8°, 35.6°, 39.1°, 45.4°, 53.8°, 58.8°, 61.3° and 74.9° were assigned to the (111), (200), (210), (211), (220), (311), (230), (321) and (420) diffraction peaks of NiS_2 (JCPDS No. 11-0099).[54] The crystallite dimension of the NiS_2 was calculated using the Scherrer formula giving approximately 23.7 nm what is close to results reported in works.[55,56] Peaks occurring at 19° and 29.7° could be identified as NiS, 23.3° for Ni_2S_3.[57] XRD pattern for composite rGOpH12/5 wt%NiS_2 confirms presence of NiS_2. In addition, NiS_2 nanoparticles attached onto the surface of rGO prevented the aggregation and restacking of rGO sheets and thus weakened the diffraction intensity of rGO sheets.[58] The morphology of the samples was examined by scanning electron microscopy (SEM). Figure 5 shows that graphene oxide has packed structure consisting of thin and homogeneous layers.

Such layers are folded and sequential with individual sheets that are characterized by kinked and wrinkled areas. The rGO pH 12 presents more ordered structure with folding and curling. Composite rGO pH 12/5 wt% NiS_2 reveals that the rGO particles are entirely wrapped by the NiS_2 material. During the hydrothermal reaction, negatively charged GO sheets with high content of oxygen functionalities electrostatically attract positively charged Ni^{2+} ions. At elevated temperature, sodium thiosulfate can act both, as a reductive agent and a source of sulfur ions able to react with Ni^{2+}, forming NiS_2 structures on

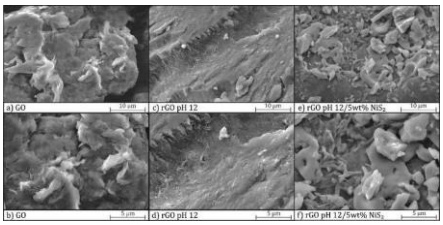

Figure 5. SEM images of GO, rGO pH 12 and rGO pH 12/5 wt% NiS_2 at different magnifications.

the surface of the GO sheets. Simultaneously, the GO is reduced to rGO.[59] It can be seen that the NiS_2 particles are distributed with the rGO sheets uniformly. Transmission electron microscopy (TEM) images with selected area electron diffraction (SAED) pattern are shown in Figure 6. At lower magnification (Figure 6A), various morphology of the composite is observed. It could be caused by the low content of NiS_2 in the structure as well as amorphous character of the rGO. At higher magnification (Figure 6B), it is possible to distinguish two distinct areas with different order stacking. The area with high crystallographic order can be attributed to the closely packed NiS_2 layers with calculated interlayer spacing of ca. ~0.32 nm which is in good agreement with determined d_{002} value. The amorphous part of the material should be attributed to the rGO. It is worth notifying that only part of the rGO surface is covered by the NiS_2 material. Synthesis of the rGO/NiS_2 composite is initiated with electrostatic attraction between negatively charged GO layer and Ni^{2+} ions with a consequent reduction of GO to rGO. SAED diffraction (Figure 6C) shows rich diffraction patterns assigned to (111), (211), and (230) which could be attributed to the presence of the bulk NiS_2 in accordance with the XRD results. Additionally, the UV spectra of the samples were performed. Figure 7 shows the UV-spectra of GO, rGO, and composite rGO pH 12/5 wt% NiS_2.

Based on the absorbance spectra of GO, the main absorption peak at 229 nm indicates the π-π* transition of the aromatic C–C ring, whereas the weak absorption at 300 nm was due to the n-π* transition of C=O bonds.[60] When GO was reduced, a red shift within the UV region was observed for rGO pH 8, 10 and 12; the decrease in oxygenated functional groups and the increase of aromatic C–C bonds facilitated the electrons

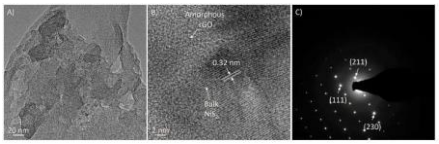

Figure 6. TEM images at different magnifications. (A) Magnification of 20 nm, (B) magnification of 2 nm with distinct areas corresponding to rGO and NiS_2 structures, and (C) SAED pattern along the (011) axis.

© 2022 The Authors. ChemElectroChem published by Wiley-VCH GmbH

21960216, 2022, 21, Downloaded from https://chemistry-europe.onlinelibrary.wiley.com/doi/10.1002/celc.202200834 by POLITECHNIKA POZNANSKA, Wiley Online Library on [11/06/2024]. See the Terms and Conditions (https://onlinelibrary.wiley.com/terms-and-conditions) on Wiley Online Library for rules of use; OA articles are governed by the applicable Creative Commons License

ChemElectroChem | Research Article
doi.org/10.1002/celc.202200834
Chemistry Europe
European Chemical Societies Publishing

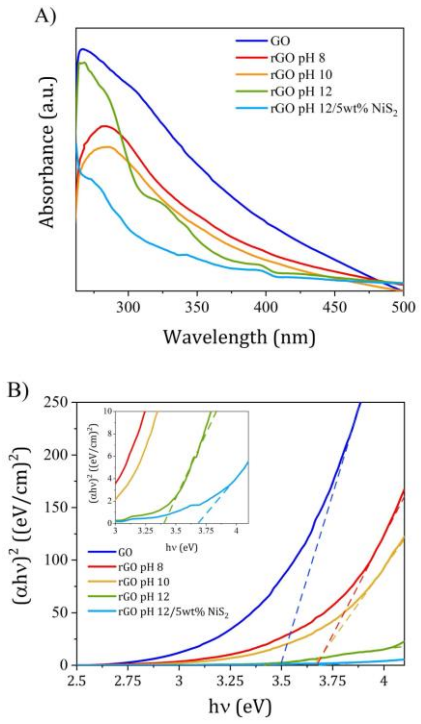

Figure 7. (A) UV spectra; (B) Tauc plots of GO, rGO and rGO pH 12/5 wt% NiS_2 samples.

to be easily excited at low energy. The band gap of material (equation 8) can affect its catalytic properties.

$$(\alpha h\nu)^{1/n} = A(h\nu - E_g) \quad (8)$$

where, h is Planck's constant, ν is the photon's frequency, α is the absorption coefficient, E_g is the band gap and A is the slope of the Tauc plot in the linear region. The value of the exponent denotes the nature of the electronic transition. Typically, the allowed transitions dominate the basic absorption processes, giving either $n = 1/2$ or $n = 2$, for direct and indirect transitions, respectively.[61,62] The results for band gap energy, equivalent series resistance (ESR) and conductivity of solid materials (measured by four point resistance test) of GO, rGO materials[62,63] and rGO pH 12/5 wt% NiS_2[64] were shown in Table 1. The variation of band gap of the rGO can be associated with pore structure and surface oxygen functionality. The effect of pore size could be attributed to quantum confinement effect, and the surface oxygen functionality might be ascribed to the localization effect similarly to doped semiconductors.[65] It could

Table 1. Values of band gap energy, ESR and conductivity of solid materials for GO, rGO and rGO pH 12/5 wt% NiS_2 samples.

Sample	Band gap energy [eV]	ESR [Ω]	Conductivity of solid materials [mS cm^{-1}]
GO	4.3	0.78	–
rGO pH 8	4.3	1.03	0.76
rGO pH 10	3.4	0.77	0.93
rGO pH 12	3.3	0.43	2.14
rGO pH 12/5 wt% NiS_2	3.8	0.58	1.53

be linked with ESR and conductivity of solid materials. Addition of NiS_2 to the rGO structure affects slight increase of ESR.

Physicochemical characterization was completed by the electrochemical studies. Electrochemical comparison between the prepared carbon materials were performed by using standard electrochemical techniques. The results for symmetric cells assembled with GO and rGO samples are presented in Figure 8. It can be observed that with the increase of pH during the hydrothermal reduction, the shape of each CV becomes more rectangular (A). GO surface is rich with oxygen functional groups that are known to be responsible for various redox reactions. Strongly oxidized surface is not participating in the physisorption of ions during EC charge/discharge. Additionally, it decreases the conductivity as well as the reachable capacitance of the cell. During hydrothermal reduction these functional groups are removed from the surface. The structural, textural and morphological properties of the samples will vary depending on the pH of the GO solution. Thus, these differences will affect the electrochemical behaviour of the cell. It can be observed on the CV and galvanostatic charge/discharge with potential limitation (GCPL) curves (B) that the cell with GO is characterized with significantly lower capacitance (16 F g^{-1} at 0.2 A g^{-1} with 57% of energetic efficiency) as well as poor conductivity in comparison to cells with rGO samples. Cells with rGO pH 8 and 10 showed significantly better capacitive response than cell based on GO (both 117 F g^{-1} at 0.2 A g^{-1}, but with 79% and 82% energetic efficiency, respectively). Yet, the voltammograms are typical for cell with material exhibiting surface redox phenomena attributed to activity of remaining oxygen surface groups. High equivalent series resistance (ESR) values as well as diffusion limited character of impedance curve at high frequencies suggests redox activity (C, D). Cell with rGO pH 12 exhibited the highest capacitance and charge propagation (130 F g^{-1} at 1 A g^{-1} with 81% of energetic efficiency) as well as good conductivity, in turn, the rectangular shape of the CV. In addition, we have performed tests of rGO pH 12 in 1 M Li_2SO_4 (Figure S3) which showed slightly higher operational window, but with smaller capacitance. Cells assembled with 6 M KOH and 1 M Li_2SO_4 were also subjected for cycle-life study (Figure S4). The cell with 6 M KOH reached 2500 cycles, and cell with 1 M Li_2SO_4 5000 cycles until 20% of capacitance decay. Obtained values of capacitance are comparable to other works (Table 2). The best performance was obtained for rGO through electrochemical reduction[72] and operating in 6 M KOH

© 2022 The Authors. ChemElectroChem published by Wiley-VCH GmbH

21960216, 2022, 21, Downloaded from https://chemistry-europe.onlinelibrary.wiley.com/doi/10.1002/celc.202200834 by POLITECHNIKA POZNANSKA, Wiley Online Library on [11/06/2024]. See the Terms and Conditions (https://onlinelibrary.wiley.com/terms-and-conditions) on Wiley Online Library for rules of use; OA articles are governed by the applicable Creative Commons License

ChemElectroChem | Research Article
doi.org/10.1002/celc.202200834
Chemistry Europe
European Chemical Societies Publishing

21960216, 2022, 21, Downloaded from https://chemistry-europe.onlinelibrary.wiley.com/doi/10.1002/celc.202200834 by POLITECHNIKA POZNANSKA, Wiley Online Library on [11/06/2024]. See the Terms and Conditions (https://onlinelibrary.wiley.com/terms-and-conditions) on Wiley Online Library for rules of use; OA articles are governed by the applicable Creative Commons License

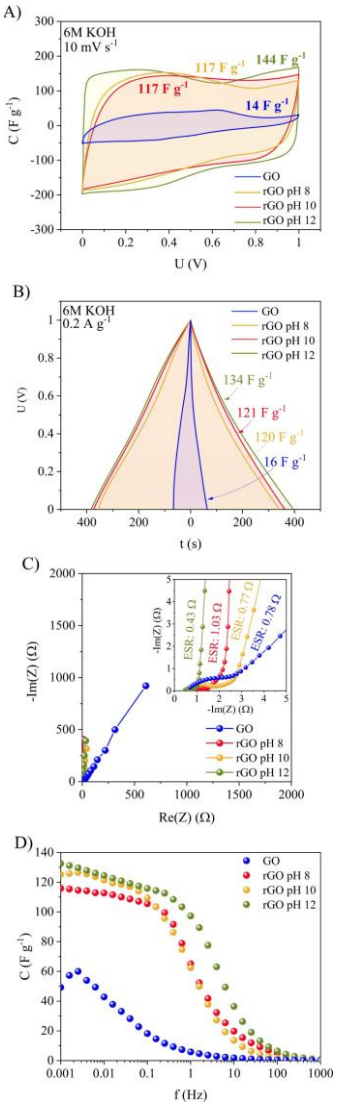

Figure 8. Comparison of electrochemical results. (A) Cyclic voltammograms; (B) galvanostatic charge/discharge curves; (C) Nyquist plots; (D) capacitance *vs.* frequency dependence.

(147 F g^{-1} at 1 A g^{-1}). Comparable electrochemical performance is reported in this work.

Table 2. Electrochemical performance of rGO prepared through different techniques.

Technique	Electrolyte	Specific capacitance [F g^{-1}]	Reference
Electrochemical reduction	1 M $NaNO_3$	67.5 at 1 A g^{-1}	[66]
	1 M H_2SO_4	72 at 0.5 A g^{-1}	[67]
	6 M KOH	147 at 1 A g^{-1}	[68]
Temperature reduction	0.5 M KCl buffer	26 at 25 mV s^{-1}	[69]
Hydrothermal reduction	6 M KOH	130 at 1 A g^{-1}	Our work

Presence of structural defects on the surface of the material will negatively affect the electrochemical performance of the cell. Raman spectroscopy confirmed that with the increase of the pH, the structure of the resulted material is less defected. The sample rGO pH 12 was proven by the Raman spectroscopy to be the least defected by the presence of low intensity D + D′ or D + G′ modes. Less defected structure led to high conductivity and lesser tendency to decompose electrolyte on the defect sites. Comparable conclusions can be obtained from nitrogen sorption results as the highest capacitance exhibited sample with the most developed SSA. Based on XRD results, average size of particles was determined. It can be observed that with the increase of the crystallites size, the conductivity, thus frequency response of the cell is increasing. Based on the determined values of band gaps, cells characterized with lower *E*g values were able to reach higher specific capacitance and conductivity, which is in accordance to the measured conductivity of solid materials by four point resistivity test.

Based on the above considerations, rGO pH 12 (named rGO for easier recognition) was selected for further electrochemical characterization and modification with NiS_2. Figure 9 shows the effect of scan rate (A) and application of different current density (B). It can be observed that the cell exhibited very high charge retention and was able to retain original shape of the CV up to 200 mV s^{-1}. Galvanostatic charge/discharge curves show linear response owing to the high conductivity of the material proven by four point resistivity test and low ESR values. Then, the cell was subjected to voltage expansion from 0.8 V to 1.2 V with 1 mV s^{-1} while observing both, negative and positive electrode (Figure 9C, D). Capacitive response suggests that the cell is able to withstand voltage regime (1.2 V) due to lack of active sites which could lead to electrolyte decomposition.

At the beginning, different loadings of NiS_2 in the composite, i.e., 5 wt%, 10 wt% and 50 wt%, were prepared and studied by CV technique (Figure 10A). It occurred that just 5 wt% content of NiS_2 in the composite was sufficient to improve the performance of the cell. Comparable result was obtained for the cell with rGO/10 wt% NiS_2. After deposition of 50 wt% of NiS_2 on the rGO surface, significant decay of electrochemical performance was observed. It can be explained by blocking the porous structure of the rGO by bulky pyrite structure of NiS_2 during composite synthesis. Interestingly, the improvement of the capacitance is only observed at low voltage range 0–0.6 V. Slightly lower response is registered at higher

© 2022 The Authors. ChemElectroChem published by Wiley-VCH GmbH

ChemElectroChem
Research Article
doi.org/10.1002/celc.202200834
Chemistry Europe
European Chemical Societies Publishing

21960216, 2022, 21, Downloaded from https://chemistry-europe.onlinelibrary.wiley.com/doi/10.1002/celc.202200834 by POLITECHNIKA POZNANSKA, Wiley Online Library on [11/06/2024]. See the Terms and Conditions (https://onlinelibrary.wiley.com/terms-and-conditions) on Wiley Online Library for rules of use; OA articles are governed by the applicable Creative Commons License

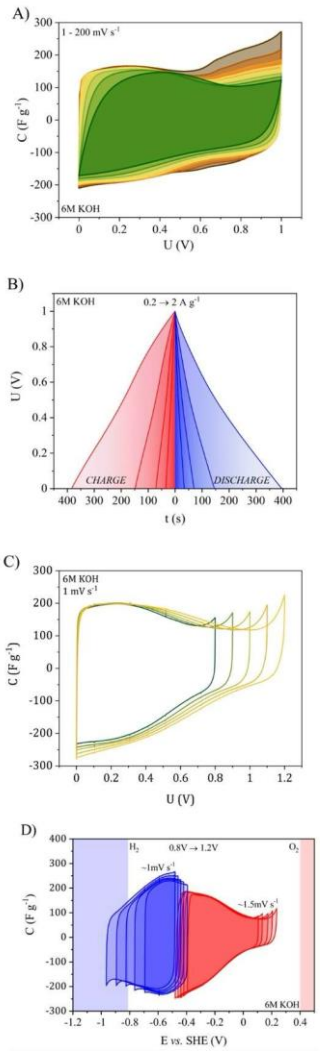

Figure 9. (A) Effect of scan rate; (B) effect of current density; (C) voltage extension; (D) operation of negative and positive electrode; for cell with rGO pH 12 at 6 M KOH.

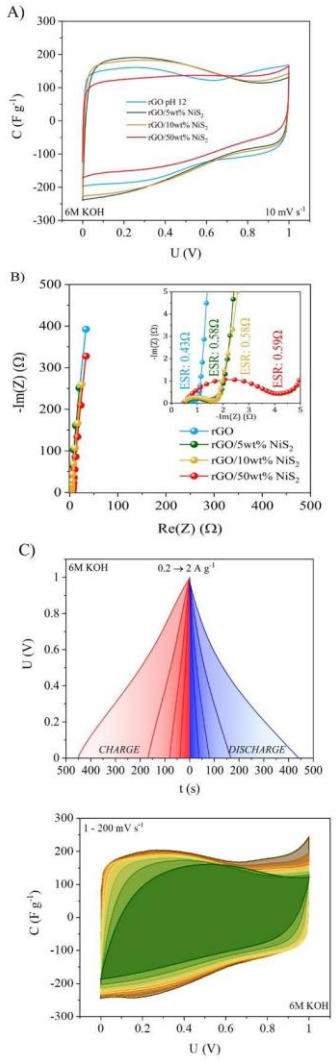

Figure 10. (A) CV comparison of symmetric cells with different loading of NiS_2 composites; (B) comparison of impedance spectroscopy; (C) effect of current density for rGO/5 wt% NiS_2; (D) effect of scan rate for rGO/5 wt% NiS_2. Studies performed in 6 M KOH.

voltage range 0.6–1 V. Nyquist plot (Figure 10B) at high frequency revealed relatively low values of equivalent series resistance (ESR) for each sample. Linear increase of resistance can be observed with higher content of NiS_2 in the composite. After deposition of NiS_2 on the rGO, a clear presence of higher semi-circle related to the sluggish penetration of ions at electrode/electrolyte interface was observed. The higher

© 2022 The Authors. ChemElectroChem published by Wiley-VCH GmbH

ChemElectroChem | Research Article
doi.org/10.1002/celc.202200834
Chemistry Europe
European Chemical Societies Publishing

21960216, 2022, 21, Downloaded from https://chemistry-europe.onlinelibrary.wiley.com/doi/10.1002/celc.202200834 by POLITECHNIKA POZNANSKA, Wiley Online Library on [11/06/2024]. See the Terms and Conditions (https://onlinelibrary.wiley.com/terms-and-conditions) on Wiley Online Library for rules of use; OA articles are governed by the applicable Creative Commons License

amount of NiS_2 in the composite material, the higher the semicircle diameter of Nyquist plot. Composite of rGO/5 wt% NiS_2 was further characterized at various scan rates and different current densities (Figure 10C–D). Cell cycling with higher scan rates showed lower charge retention typically for system with redox reactions. Cell subjected to different current density presented a small deviation from the linear profile at low voltage. Capacitance vs. frequency chart (Figure S5) displayed higher initial capacitance for composite in comparison to rGO pH 12, but lower retention at 1 Hz of 54% and 73%, respectively.

Generally, TMDs are known to be an excellent promoter of hydrogen evolution reaction (HER). They can negatively affect the electrochemical performance of the cell by electrolyte decomposition at elevated voltage. Therefore, it was decided to assemble asymmetric cells with rGO/5 wt% NiS_2 as a positive electrode and rGO pH 12 as a negative one. Comparison of electrochemical performance between asymmetric and symmetric cells is presented in Figure 11A. The highest capacitance was observed for asymmetric cell with (−) rGO||rGO/5 wt% NiS_2 (+) which reached 146 F g^{-1} at 1 A g^{-1} with 73% of energetic efficiency. The summary of reached capacitance for each cell is shown in Table S5. The rGO presented better electrochemical behaviour while working as a negative electrode than the composite material rGO/NiS_2 because of the blockage of porous structure by bulky pyrite structure NiS_2. Contrary, due to utilization of redox processes, the composite material rGO/NiS_2 disclosed improved electrochemical performance while acting as a positive electrode. Despite deposition of only 5 wt% of redox active material, it has significant influence on capacitance increase. Interestingly, the capacitive response is significantly higher for the asymmetric cell at low voltages. Comparable capacitance is observed at higher voltages for asymmetric and symmetric cell with pristine material. This effect can be explained by the activity of redox reactions on the positive electrode.

It was decided to conduct voltage extension of the asymmetric cell from 0.8–1.2 V while tracking positive and negative electrode response (Figure 12).

In comparison to the symmetric cell with pristine rGO, the negative electrode showed the same behaviour. However, positive electrode exhibited improved electrochemical performance with small redox peaks occurring from −0.45 to −0.3 V *vs.* SHE. The system presents stable operation at 1 V. At higher voltages, start of electrode oxidation is observed on the positive electrode. Therefore, it was decided to evaluate life-time of the assembled asymmetric system by galvanostatic charge/discharge at 1 V with 1 A g^{-1} current density (Figure S6). The system was able to operate for only ~2000 cycles until 20% of initial capacitance fade. Mass balancing of both electrodes could give further benefit towards better EC performance. Figure 13 shows Ragone plot of symmetric and asymmetric system. The highest values of the energy and power have been obtained for the hybrid cell with NiS_2 composite on the positive electrode (5.73 Wh kg^{-1} and 378.4 W kg^{-1}, respectively). We have also compared the electrochemical performance of other works based on asymmetric devices with NiS_2 composites on positive electrode (Table 3).

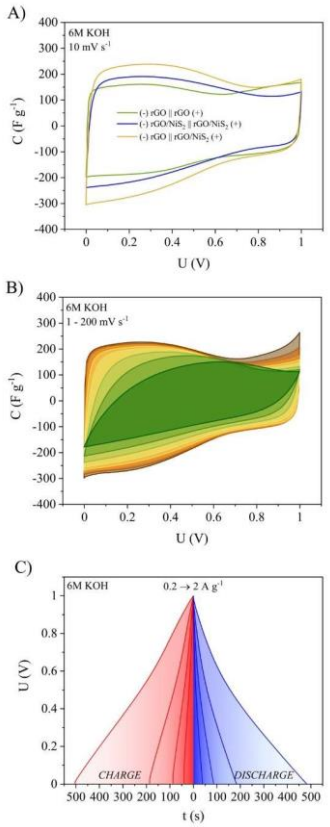

Figure 11. (A) Comparison of symmetric *vs.* asymmetric cells; (B) effect of scan rate for (−) rGO||rGO/5 wt% NiS_2 (+); (C) effect of current density for the same configuration.

Conclusion

This study provides a better understanding of how the morphology and structural properties of rGO are affected by the pH of the GO reaction medium, and this will help to develop novel graphene-like hybrid composites under hydrothermal conditions. Our results show that a higher pH of reaction solution decreases the size of crystallites of reduced graphene and for rGO pH 12 it is 5.06 nm. In addition, better

© 2022 The Authors. ChemElectroChem published by Wiley-VCH GmbH

ChemElectroChem | Research Article
doi.org/10.1002/celc.202200834
Chemistry Europe
European Chemical Societies Publishing

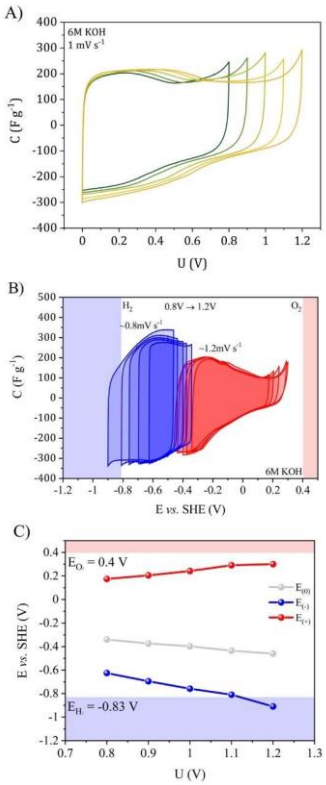

Figure 12. (A) Voltage extension; (B) operation of individual electrodes; (C) electrode potentials *vs.* voltage for cell with (−) rGO||rGO/5 wt% NiS_2 (+) operating in 6 M KOH.

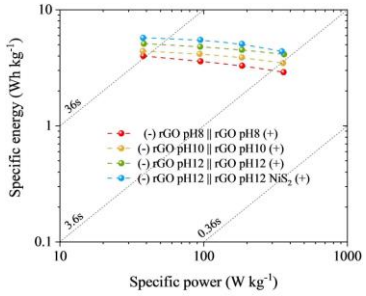

Figure 13. Ragone plot of symmetric and asymmetric systems.

Table 3. Comparison of previously reported asymmetric systems.

System (−)||(+)	Specific capacitance [F g^{-1}]	Energy density [Wh kg^{-1}]	Specific power [W kg^{-1}]	Reference
TRGO||NCC2	146 at 3 A g^{-1}	50.4	2360	[26]
AC||CoS_2@NiS_2	91 at 0.5 A g^{-1}	5	4016	[70]
SC||MXene NiS_2	102 at 1 A g^{-1}	32.1	749.9	[71]
rGO||rGO NiS_2	146 at 1 A g^{-1}	5.7	378	Our work

reduction of graphene material led to higher electrical conductivity, thus demonstrating the restoration of the sp^2 electronic structure. Also, it increases specific surface area of rGO (257 $m^2 g^{-1}$), and in consequence, the specific capacitance for this material was 134 F g^{-1} at a current density of 0.2 A g^{-1} with 54% of energetic efficiency. Such rGO served as a support for NiS_2 by application of hydrothermal method. Utilization of rGO/5 wt% NiS_2 composite as (+) electrode and rGO as (−) one allowed the system to increase the specific capacitance to 165 F g^{-1} at a current density of 0.2 A g^{-1} with 79% of energetic efficiency. Application of carbon/NiS_2 composite seems to be an interesting option as positive electrode; however, further balancing of the hybrid system is necessary.

Experimental Section

Materials preparation

Graphene oxide (GO) synthesis

Graphite powder (4 g) was added to a mixture of H_2SO_4 (150 mL) and H_3PO_4 (30 mL). The resulting colloidal solution was cooled to 0 °C and stirred for 4 h. $KMnO_4$ (24 g) was added to the solution at temperature < 5 °C. The mixture was heated to 35–40 °C and stirred for 2 h. Next, 360 mL of distilled water was added dropwise, followed by addition of H_2O_2 (30% aqueous solution) until the solution changed a color to yellow. Large graphite particles were separated by centrifugation. The resultant material was washed with distilled water and HCl solution to reach a pH of about 6.5–7.

Reduced graphene oxide (rGO) synthesis

2 M NaOH solution was added to 50 mL of colloidal GO to obtain the value of pH = 8, 10 and 12. Then, colloid was stirred for 30 min and ultrasonicated for 2 h. The mixture was transferred into Teflon-lined autoclave and heated at 160 °C for 15 h. The resulting rGO was collected from the bottom of the autoclave in the form of a black solid. It was centrifuged and thoroughly washed with water. Finally, it was filtered over cellulose nitrate membrane and dried in oven at 70 °C for 12 h.

NiS_2 and rGO/NiS_2 synthesis

First, $NiCl_2 \cdot 6H_2O$ (2.37 g, 0.005 mol) were stirred in 25 mL distilled water for 30 min. In the same way, $Na_2S_2O_3 \cdot 5H_2O$ (4.96 g, 0.01 mol) were stirred in 25 mL distilled water for 30 min. Next step, both

© 2022 The Authors. ChemElectroChem published by Wiley-VCH GmbH

21960216, 2022, 21, Downloaded from https://chemistry-europe.onlinelibrary.wiley.com/doi/10.1002/celc.202200834 by POLITECHNIKA POZNANSKA, Wiley Online Library on [11/06/2024]. See the Terms and Conditions (https://onlinelibrary.wiley.com/terms-and-conditions) on Wiley Online Library for rules of use; OA articles are governed by the applicable Creative Commons License

ChemElectroChem | Research Article
doi.org/10.1002/celc.202200834
Chemistry Europe
European Chemical Societies Publishing

21960216, 2022, 21, Downloaded from https://chemistry-europe.onlinelibrary.wiley.com/doi/10.1002/celc.202200834 by POLITECHNIKA POZNANSKA, Wiley Online Library on [11/06/2024]. See the Terms and Conditions (https://onlinelibrary.wiley.com/terms-and-conditions) on Wiley Online Library for rules of use; OA articles are governed by the applicable Creative Commons License

solutions were mixed together and stirred for 30 min to form a clear green solution. This solution was put into the autoclave and maintained at 160 °C for 15 h. As-prepared black precipitate was collected by filtering, washed with distilled water, and dried at 70 °C for 12 h.

The synthesis of rGO/NiS_2 composite materials was realized hydrothermally by the addition of GO solution (pH 12) to a solution of nickel chloride hexahydrate and sodium thiosulfate pentahydrate.[51,72–74] The percentage of NiS_2 in composite was calculated from the proportion of dried materials. We used known mass of colloidal GO, which was the source material in rGO pH 12 synthesis. After successful synthesis of rGO, we could obtain its final mass. The same methodology was used to determine the NiS_2 loading in the composite material. Hence, the percentage of expected NiS_2 in the composite was reached. XRD spectra confirmed presence of nickel sulfides only.

Physicochemical characterization

The powder X-ray diffraction (XRD) analysis was performed on a diffractometer BRUKER D8 Advanced, equipped with Johansson monochromator using Cu Kα radiation (Cu Kα, $\lambda = 1.5406$ Å) and silicon strip detector Lynx Eye. The minimum measurement angle was 0.6 of 2θ degree.

Raman spectra were obtained by Thermo Scientific DXR Raman Microscope with a laser emitting at 532 nm and a power of 5 mW. The total exposure time was 60 s with 3 measurements each lasting 20 s. Measurements were repeated 3 times for each sample ensuring the homogeneity of the sample.

UV-visible spectra were analyzed in UV-9000S UV/VIS spectrophotometer at room temperature. To prepare solutions of graphene materials and composite, the same quantity of powders was added to a given volume of solvent, with an initial concentration of 0.5 mg mL^{-1}. N-methyl-2-pyrrolidone (NMP) was used as solvent.[74]

The isotherms of N_2 adsorption/desorption were recorded at 77 K with the use of porosity analyser ASAP 2460 (Micromeritics, USA). Each sample was degassed for 24 h at 100 °C (He atmosphere) prior the measurements. Pore size distribution was evaluated using 2D-NLDFT model. The range of 0.01–0.05 relative pressure (p/p_0) was selected for calculation of the specific surface area.

The morphology and the surface characterization of the samples were investigated using a FEI Quanta 250 FEG Scanning Electron Microscope.

Electrochemical characterization

For electrochemical studies, all electrodes contained 90 wt% of active material, 5 wt% of conductive agent (C-Nergy Super C65, Imerys), and 5 wt% of binder (polytetrafluoroethylene, 60 wt% dispersion in water, Sigma Aldrich). Each component was mixed together in mortar with isopropanol to form dough-like material. Then, it was rolled on a calendaring machine to obtain a uniform 200 μm thickness foil which was later cut into 10 mm diameter round electrodes. Prepared electrodes were dried during 24 h at 70 °C. Two alike electrodes (ca. 10 mg) and separator (GF/A, Whatman™, thickness of 260 μm and disc diameter of 12 mm) were soaked with 6 M KOH and put together between two stainless steel 316 L current collectors assembled in two- and three-electrodes Swagelok® cells. Ag/AgCl reference electrode ($E = 0.226$ V *vs.* SHE) was used to record performance of each electrode during cell operation. Such assembled cells were subjected to cyclic voltammetry (CV), galvanostatic charge/discharge with potential limitation (GCPL), and electrochemical impedance spectroscopy (EIS) by VMP (Biologic, France). The specific capacitance per one electrode was calculated according to well-known methodology.[75]

Acknowledgements

The authors would like to acknowledge OPUS project of the National Science Centre, Poland (Project No. 2018/31/B/ST4/01852) for the financial support.

Conflict of Interest

The authors declare no conflict of interest.

Data Availability Statement

The data that support the findings of this study are available from the corresponding author upon reasonable request.

Keywords: composite · electrochemical capacitor · nickel sulphide · reduced graphene oxide · transition metal dichalcogenides

[1] P. Xiong, J. Zhu, X. Wang, *J. Power Sources* **2015**, *294*, 31–50.
[2] E. Frackowiak, F. Beguin, *Carbon* **2001**, *6*, 937–950.
[3] M. Inagaki, H. Konno, O. Tanaike, *J. Power Sources* **2010**, *195*, 7880–7903.
[4] L. Wei, G. Yushin, *Nano Energy* **2012**, *1*, 552–565.
[5] C. Vix-Guterl, E. Frackowiak, K. Jurewicz, M. Friebe, J. Parmentier, F. Beguin, *Carbon* **2005**, *43*, 1293–1302.
[6] A. G. Pandolfo, A. F. Hollenkamp, *J. Power Sources* **2006**, *157*, 11–27.
[7] F. Beguin, V. Presser, A. Balducci, E. Frackowiak, *Adv. Mater.* **2014**, *4*, 2219–2251.
[8] D. A. C. Brownson, D. K. Kampouris, C. E. Banks, *J. Power Sources* **2011**, *196*, 4873–4885.
[9] A. T. Lawal, *Biosens. Bioelectron.* **2019**, *141*, 1111384.
[10] Q. Mahmood, S. K. Park, K. D. Kwon, S.-J. Chang, J.-Y. Hong, G. Shen, Y. M. Jung, T. J. Park, S. W. Kahng, W. S. Kim, J. Kong, H. S. Park, *Adv. Energy Mater.* **2015**, *6*, 1501115.
[11] W. Choi, N. Choudhary, G. H. Han, J. Park, D. Akinwande, Y. H. Lee, *Mater. Today* **2017**, *20*, 116–130.
[12] M. Chhowalla, H. S. Shin, G. Eda, L.-J. Li, K. P. Loh, H. Zhang, *Nat. Chem.* **2013**, *5*, 263–275.
[13] L. Lin, W. Lei, S. Zhang, Y. Liu, G. G. Wallace, J. Chen, *Energy Storage Mater.* **2019**, *19*, 408–423.
[14] M. Chhowalla, D. Voiry, J. Yang, H. S. Shin, K. P. Loh, *MRS Bull.* **2015**, *40*, 585–591.
[15] S. A. Han, R. Bhatia, S.-W. Kim, *Nano Convergence* **2015**, *2*, 1–14.
[16] B. Xu, S. Yue, Z. Sui, X. Zhang, S. Hou, G. Cao, Y. Yang, *Energy Environ. Sci.* **2011**, *4*, 2826–2830.
[17] Y. Lin, Z. Qiu, D. Li, S. Ullah, Y. Hai, H. Xin, W. Liao, B. Yang, H. Fan, J. Xu, C. Zhu, *ACS Appl. Nano Mater.* **2021**, *4*, 6093–6102.
[18] W. Ni, B. Wang, J. Cheng, X. Li, Q. Guan, G. Gu, L. Huang, *Nanoscale* **2014**, *6*, 2618–2623.
[19] D. Zhang, X. Zhou, K. Ye, Y. Li, C. Song, K. Cheng, D. Cao, G. Wang, Q. Li, *Electrochim. Acta* **2015**, *173*, 209–2014.
[20] Y. Ji, W. Liu, Z. Zhang, Y. Wang, X. Zhao, B. Li, X. Wang, X. Liu, B. Liu, S. Feng, *RSC Adv.* **2017**, *70*, 44289–44295.
[21] K. Zhu, C. Li, Z. Jing, X. Liu, Y. He, X. Lv, Y. Wang, K. Liu, *Flatchem* **2019**, *18*, 1–15.
[22] B. Hinnemann, P. G. Moses, J. Bonde, K. P. Jorgensen, J. H. Nielsen, S. Horch, I. Chorkendorff, J. K. Norskov, *J. Am. Chem. Soc.* **2005**, *127*, 5308–5309.

© 2022 The Authors. ChemElectroChem published by Wiley-VCH GmbH

ChemElectroChem | Research Article
doi.org/10.1002/celc.202200834
Chemistry Europe
European Chemical Societies Publishing

[23] D. Y. Chung, S.-K. Park, Y.-H. Chung, S.-H. Yu, D.-H. Lim, N. Jung, H. C. Ham, H.-Y. Park, Y. Piao, S. J. Yoo, Y.-E. Sung, *Nanoscale* **2014**, *6*, 2131.
[24] H. Pang, C. Wei, X. Li, G. Li, Y. Ma, S. Li, J. Chen, J. Zhang, *Sci. Rep.* **2013**, *4*, 1–8.
[25] H. Liu, Q. He, H. Jiang, Y. Lin, Y. Zhang, M. Habib, S. Chen, L. Song, *ACS Nano* **2017**, *11*, 11574–11583.
[26] S. Ghosh, J. S. Kumar, N. C. Murmu, R. S. Ganesh, H. Inokawa, T. Kuila, *Composites Part B* **2019**, *15*, 1–11.
[27] N. M. S. Hidayah, W.-W. Liu, C.-W. Lai, N. Z. Noriman, C.-S. Khe, U. Hashim, H. C. Lee, *AIP Conf. Proc.* **2017**, *1892*, 1–8.
[28] V. Boychuk, V. Kotsyubynsky, A. Kachmar, S. Budzulyak, I. Budzulyak, B. Rachiy, L. Yablon, *Nano Res.* **2019**, *59*, 112–125.
[29] J. Schwan, S. Ulrich, V. Batori, H. Ehrhardt, *J. Appl. Phys.* **1996**, *80*, 440–447.
[30] A. Kaniyoor, S. Ramaprabhu, *AIP Adv.* **2012**, *2*, 1–12.
[31] T. Suzuki, K. Uchinokura, T. Sekine, E. Matsuura, *Solid State Commun.* **1977**, *23*, 847–852.
[32] M. A. Pimenta, G. Dresselhaus, M. S. Dresselhaus, L. G. Cancado, A. Jorio, R. Saito, *Phys. Chem. Chem. Phys.* **2007**, *11*, 1276–1290.
[33] M. Ikram, A. Raza, M. Imran, A. Ul-Hamid, A. Shahbaz, S. Ali, *Nanoscale Res. Lett.* **2020**, *15*, 1–11.
[34] J. Hong, M. K. Park, E. J. Lee, D. Lee, D. S. Hwang, S. Ryu, *Sci. Rep.* **2013**, *3*, 1–5.
[35] D. Yoon, H. Moon, H. Cheong, *J. Korean Phys. Soc.* **2009**, *55*, 1299–1303.
[36] A. C. Ferrari, J. C. Meyer, V. Scardaci, C. Casiraghi, M. Lazzeri, F. Mauri, S. Piscanec, D. Jiang, K. S. Novoselov, S. Roth, A. K. Geim, *Phys. Rev. Lett.* **2006**, *97*, 1–14.
[37] A. Niilisk, J. Kozlova, H. Alles, J. Aarik, V. Sammelselg, *Carbon* **2016**, *98*, 658–665.
[38] M. Thommes, K. Kaneko, A. V. Neimark, J. P. Olivier, F. Rodriquez-Reinoso, J. Rouquerol, K. S. W. Sing, *Pure Appl. Chem.* **2015**, *87*, 1–19.
[39] A. Adan-Mas, T. M. E. Silva, L. Guerlou-Demourgues, M. Montemor, *Electrochim. Acta* **2018**, *289*, 47–55.
[40] M. Tayebi, M. Kolaei, A. Tayyebi, Z. Masoumi, Z. Belbasi, B.-K. Lee, *Sol. Energy* **2019**, *190*, 185–194.
[41] R. Bessler, U. Duerig, E. Koren, *Nanoscale Adv.* **2019**, *1*, 1702–1706.
[42] T. A. Silva, H. Zanin, E. Saito, R. A. Medeiros, F. C. Vicentini, E. J. Corat, O. Fatibello-Filho, *Electrochim. Acta* **2014**, *119*, 114–119.
[43] V. L. E. Siong, X. H. Tai, K. M. Lee, J. C. Juan, C. W. Lai, *RSC Adv.* **2020**, *62*, 37905–37915.
[44] P. K. Jha, S. K. Singh, V. Kumar, S. Rana, S. Kurungot, N. Ballav, *Chem* **2017**, *3*, 846–860.
[45] A. I. Kachmar, V. M. Boichuk, I. M. Buchulyak, V. O. Kotsyubynsky, B. I. Rachiy, R. P. Lisovskiy, *Fullerenes Nanotubes Carbon Nanostruct.* **2019**, *27*, 669–676.
[46] Y. Peng, W. Pan, N. Wang, J.-E. Lu, S. Chen, *ChemSusChem* **2017**, *11*, 130–136.
[47] S. Upadhyay, S. Bagheri, S. B. A. Hamid, *Int. J. Hydrogen Energy* **2014**, *39*, 11027–11034.
[48] A. Adan-Mas, T. M. Silva, L. Guerlou-Demourgues, M. F. Montemor, *Electrochim. Acta* **2018**, *289*, 47–55.
[49] A. Romero, M. P. Lavin-Lopez, L. Sanchez-Silva, J. L. Valverde, A. Paton-Carrero, *Mater. Chem. Phys.* **2018**, *203*, 284–292.
[50] M. P. Lavin-Lopez, A. Paton-Carrero, L. Sanchez-Silva, J. L. Valverde, A. Romero, *Adv. Powder Technol.* **2017**, *28*, 3195–3203.
[51] C. Bosch-Navarro, E. Coronado, C. Marti-Gastaldo, J. F. Sanchez-Royo, M. G. Gomez, *Nanoscale* **2012**, *4*, 3977–3982.
[52] A. Romero, P. Lavin-Lopez, L. Sanchez-Silva, J. L. Valverde, A. Paton-Carrero, *Mater. Chem. Phys.* **2017**, *203*, 284–292.
[53] N. Jiang, Q. Tang, M. Sheng, B. You, D. Jiang, Y. Sun, *Catal. Sci. Technol.* **2016**, *4*, 1–9.
[54] J. Zheng, W. Zhou, Y. Ma, W. Cao, C. Wang, L. Guo, *Chem. Commun.* **2015**, *64*, 12863–12866.
[55] L. E. Cebisa, M. S. Dalton, C. N. John, M. B. Wakufwa, *J. Alloys Compd.* **2013**, *552*, 345–350.
[56] A. M. Huerta-Flores, L. M. Torres-Martinez, E. Moctezuma, A. P. Singh, B. Wickman, *J. Mater. Sci. Mater. Electron.* **2018**, *29*, 11613–11626.
[57] M. Kristl, S. Gyergyek, J. Kristl, *Chalcogenide Lett.* **2018**, *15*, 55–61.
[58] W. Shi, J. Mao, X. Xu, W. Liu, L. Zhang, X. Cao, X. Lu, *J. Mater. Chem. A* **2019**, *26*, 15654–15661.
[59] Y.-G. Xu, J. Liu, L.-B. Kong, *Ionics* **2021**, *27*, 3315–3325.
[60] F. W. Low, C. W. Lei, S. B. A. Hamid, *Ceram. Int.* **2015**, *41*, 5798–5806.
[61] J. B. Coulter, D. P. Birnie, *Phys. Status Solidi B* **2017**, *255*, 1–7.
[62] F. Zheng, W.-L. Xu, H.-D. Jin, X.-T. Hao, K. P. Ghiggino, *RSC Adv.* **2015**, *109*, 89515–89520.
[63] A. Mathkar, D. Tozier, P. Cox, P. Ong, C. Galande, K. Balakrishnan, A. L. M. Reddy, P. M. Ajayan, *J. Phys. Chem. Lett.* **2012**, *3*, 986–991.
[64] A. Nqombolo, P. A. Ajibade, *J. Chem.* **2016**, *2016*, 1–9.
[65] J. Zhang, H. Song, D. Zeng, H. Wang, Z. Qin, K. Xu, A. Pang, C. Xie, *Sci. Rep.* **2016**, *6*, 1–9.
[66] A. Galal, H. K. Hassan, T. Jacob, N. F. Atta, *Electrochim. Acta* **2018**, *260*, 738–747.
[67] Y.-S. Wang, S.-M. Li, S.-T. Hsaio, W.-H. Liao, P.-H. Chen, S.-Y. Yang, H.-W. Tien, C.-C. M. Ma, C.-C. Hu, *Carbon* **2014**, *73*, 87–98.
[68] J. B. Kim, S. H. Koo, I. H. Kim, J. T. Kim, B. Jayaraman, J. Lim, S. O. Kim, *Chem. Eng. J.* **2022**, *446*, 137390.
[69] L. Buglione, E. L. K. Chng, A. Ambrosi, Z. Sofer, M. Pumera, *Electrochem. Commun.* **2022**, *14*, 5–8.
[70] S.-C. Wang, D. Xiong, C. Chen, M. Gu, F.-Y. Yi, *J. Power Sources* **2020**, *450*, 227712.
[71] X. C. Tang, X.-Y. Li, Z. Ren, M.-J. Zhang, J.-Q. Zhang, *Research Square* **2022**, *preprint*. https://doi.org/10.21203/rs.3.rs-1692144/v1.
[72] V. O. Kotsyubynsky, V. M. Boychuk, I. M. Budzuliak, B. I. Rachiy, R. I. Zapukhlyak, M. A. Hodlevska, A. I. Kachmar, O. R. Bilogubka, A. A. Malakhov, *Phys. Chem. Solids* **2021**, *22*, 31–38.
[73] X. Chen, R. Fan, *Chem. Mater.* **2001**, *13*, 802–805.
[74] D. Konios, M. M. Stylianakis, E. Stratakis, E. Kymakis, *J. Colloid Interface Sci.* **2014**, *430*, 108–112.
[75] A. Laheaar, P. Przygocki, Q. Abbas, F. Beguin, *Electrochem. Commun.* **2015**, *60*, 21–25.

Manuscript received: August 8, 2022
Revised manuscript received: September 23, 2022
Accepted manuscript online: September 28, 2022

© 2022 The Authors. ChemElectroChem published by Wiley-VCH GmbH

21960216, 2022, 21, Downloaded from https://chemistry-europe.onlinelibrary.wiley.com/doi/10.1002/celc.202200834 by POLITECHNIKA POZNANSKA, Wiley Online Library on [11/06/2024]. See the Terms and Conditions (https://onlinelibrary.wiley.com/terms-and-conditions) on Wiley Online Library for rules of use; OA articles are governed by the applicable Creative Commons License

Chapter IV

Covalent modification of 2D material by redox-active species

P4. *Nanostructured MoS_2 grafted by anthraquinone for energy storage*

Authors: Maciej Tobis, Elżbieta Frąckowiak

Journal: Journal of Power Sources, **2024**, 613, 234862

DOI: https://doi.org/10.1016/j.jpowsour.2024.234862

License: The content is available under CC BY 4.0

Contribution: Conceptualization of the article, experiments planning, conducting hydrothermal synthesis of MoS_2, performing grafting reactions, performing physicochemical analyses (Raman spectroscopy, FT-IR spectroscopy, N_2 sorption), outsourced physicochemical data analysis (elemental analysis, XRD, XPS, TEM), electrochemical studies (two and three-electrode cell investigation, b-values, bode plots), data plotting, funding acquisition, writing original draft, writing response to reviewers

Graphical abstract

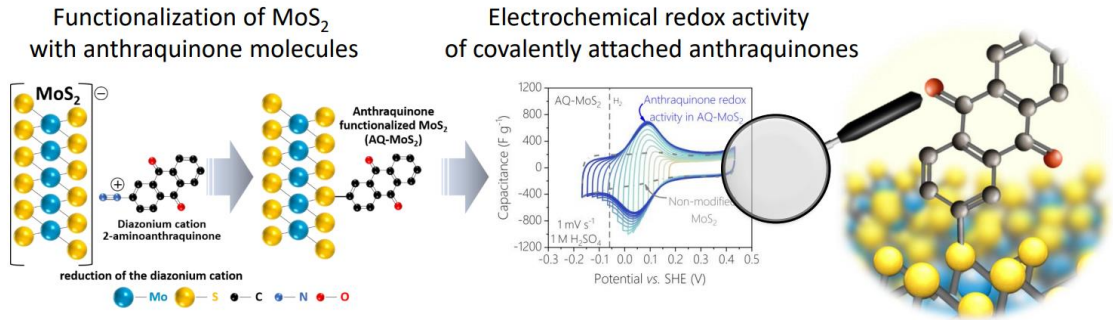

Context of research & summary

Considering previous findings that TMD electrode materials exhibit catalytic activity towards HER, further research focused on the development of methods to inhibit these catalytic properties while enhancing the electrochemical performance of MoS_2.

The hydrothermal preparation method, due to largely uncontrolled reaction kinetics, often produces MoS_2 with a high content of structural defects. These defects are primarily responsible for the material's catalytic properties. Therefore, finding ways to limit these defects or limiting their activity, could be crucial for increasing the operational voltage window of MoS_2-based devices.

Recent discoveries show that the surface of TMDs can be functionalized with various organic and inorganic molecules such as diazonium salts, amines, or thiols. While some of the molecules affect the electronic properties of TMDs, others influence on their physicochemical properties such as interlayer spacing or lattice disorder. Some of these properties were found beneficial for improving the catalytic activity towards HER due to expanded interlayer spacing that facilitates ionic transport [229], other show to suppress the catalytic activity towards HER due to protected S-active sites [230]. Although there is only few reports about using diazonium salts for MoS_2 modification. It was found that S-vacancies on the MoS_2 surface enhance reactivity with diazonium salts (**Fig. 16**) [231]. Thus, hydrothermally prepared MoS_2 with a defect-rich surface is an ideal candidate for modification with redox-active species through diazonium salt chemistry.

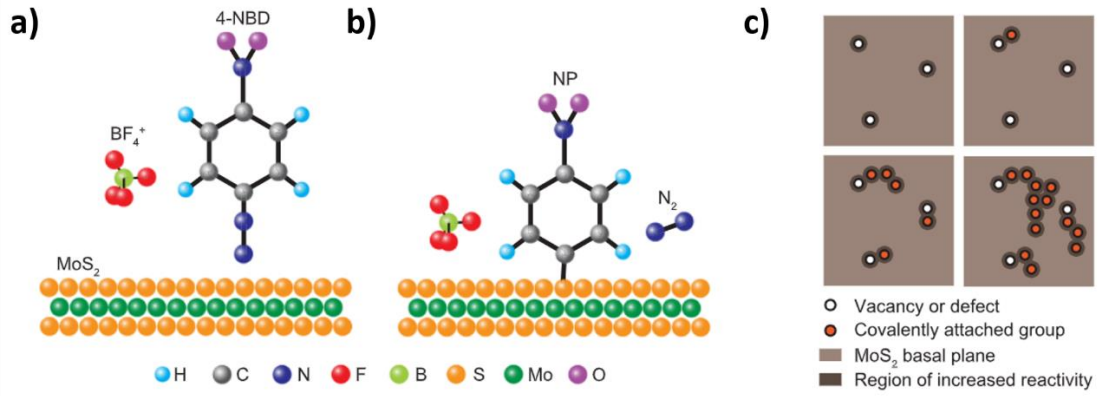

Figure 16 Covalent functionalization of MoS_2 with aryl diazonium salt. a) Schematic reaction of 4-nitrobenzene tetrafluoroborate, b) nitrophenyl is attached to the surface of MoS_2 with a C-S covalent bond, c) reaction starts from an S-vacancy defect on the surface of the MoS_2 due to increased reactivity region around the defect and covalently attached groups. (Adapted from Ref. [231] with permission from American Chemical Society)

Quinones are known for their reversible redox reactions which can significantly enhance the reachable capacitance of an electrode material. Specifically, anthraquinone (AQ) has been studied for grafting onto carbon black (CB) surface.

This article layered nanostructured MoS_2 synthesized *via* hydrothermal reaction and subsequently grafted with anthraquinone molecules during *in-situ* generation of aryl diazonium cations, formation of radicals, and reduction on the MoS_2 surface. X-ray photoelectron spectroscopy (XPS) confirmed covalent bonding between AQ molecules and the MoS_2 surface. X-ray diffraction (XRD) patterns and transmission electron microscopy (TEM) revealed that AQ molecules were grafted onto both the surface

and within the interlayer spacing of MoS_2. Elemental analysis showed that ca. 20 wt% of AQ was grafted onto the MoS_2.

Electrochemical studies demonstrated that AQ-MoS_2 exhibited enhanced capacitance, from 191 F g^{-1} (461 F cm^{-3}) to 263 F g^{-1} (631 F cm^{-3}) at a current density of 0.2 A g^{-1} in a 1 M H_2SO_4 solution which is attributed to the additional AQ redox reactions.

Two-electrode cells were also assembled utilizing carbon electrode (BP2000) as a positive electrode to limit the oxidation of the MoS_2 during positive polarization reaching 1.2 V. Such hybrid cell, (-)AQ-MoS_2||BP2000(+) revealed increased capacitance in comparison to cell with pristine material (-)MoS_2||BP2000(+).

Further analysis using electrochemical impedance spectroscopy (EIS) and *b-value* cyclic voltammogram (CV) analysis revealed that ion intercalation within the interlayer spacing of MoS_2 was not hindered by the presence of AQ. It also showed that the electrochemical behavior has a capacitive response, meaning that the charge storage mechanism could be based on physisorption of ions upon entering the interlayer spacing of MoS_2. The modification primarily occurred at defect sites, reducing the catalytic activity of MoS_2 towards HER and thereby improving the stability of the electrode material.

It is also assumed that the redox reaction of anthraquinone decreases the concentration of hydrogen ions near the electrode/electrolyte interface, thereby shifting the thermodynamic potential of H_2 evolution towards more negative values, artificially suppressing the catalytic activity of MoS_2.

In organic electrolytes, AQ-MoS_2 also demonstrated enhanced pseudocapacitive behavior, indicating its potential for lithium-ion storage applications. This study detailed the synthesis, grafting process, physicochemical and electrochemical characterization of both pristine and modified MoS_2. The results present a novel concept of 2D materials functionalization for improving their energy storage properties. These findings could open new possibilities for further exploitation of TMDs electrochemical behavior.

Publication

P4. *Nanostructured MoS_2 grafted by anthraquinone for energy storage*

Journal of Power Sources 613 (2024) 234862

Contents lists available at ScienceDirect

Journal of Power Sources

journal homepage: www.elsevier.com/locate/jpowsour

Nanostructured MoS_2 grafted by anthraquinone for energy storage

Maciej Tobis **, Elżbieta Frąckowiak *

Institute of Chemistry and Technical Electrochemistry, Poznan University of Technology, 60 – 965, Poznan, Poland

HIGHLIGHTS

- Nanostructured molybdenum sulfide (MoS_2) successfully grafted by anthraquinone (AQ).
- Grafting was on the outer surface of MoS_2 as well as within interlayer spacing.
- AQ-MoS_2 improved capacitance due to redox behavior of grafted molecules.

GRAPHICAL ABSTRACT

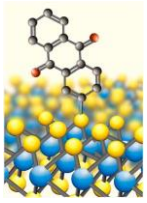

ABSTRACT

Two-dimensional materials such as molybdenum disulfide (MoS_2) can be employed as an electrode material in energy systems due its good electrical conductivity and high reachable capacity/capacitance. We demonstrate the concept of a covalent modification of nanostructured MoS_2 with anthraquinone (AQ) molecules through diazonium salt chemistry for electrochemical capacitors and lithium-ion storage. AQ molecules are chemically bonded to MoS_2 which was proved experimentally by spectroscopic techniques. Here, AQ is grafted (ca. 20 wt%) to the outer surface of nanostructured MoS_2, but also confined within the MoS_2 interlayer spacing. Modified AQ-MoS_2 exhibited faradaic response which improved the overall charge stored from 191 F g^{-1} (461 F cm^{-3}) to 263 F g^{-1} (631 F cm^{-3}) at 0.2 A g^{-1} in 1 M H_2SO_4. The process of intercalation of ions within interlayer spacing of AQ-MoS_2 was not hindered by the presence of confined AQ molecules. Impedance spectroscopy and voltammetry analysis revealed comparable non-diffusion limited response of MoS_2 before and after modification. The MoS_2 modification was likely conducted on the defect sites limiting the catalytic activity of MoS_2 towards hydrogen evolution improving stability of electrodes. In organic medium, the pseudocapacitive response of MoS_2, enhanced by additional redox reactions of grafted AQ was observed during lithium-ion storage.

1. Introduction

Increasing demand for high performance electrochemical energy storage systems has forced the direction of the research towards searching for advanced electrode materials capable of operating at high charge/discharge rate [1–3]. Two-dimensional transition metal dichalcogenides (2D-TMDs), such as molybdenum disulfide (MoS_2), with layered structure and intercalation type charge storage behavior fulfil such requirements [4]. Taking into account that energy storage is based on the efficient insertion of ions in a layered structure, structural and physicochemical properties of this electrode material are the most important factors when designing a battery or a capacitor [5,6]. MoS_2 has a layered structure consisting of molybdenum atoms sandwiched between two layers of sulfur atoms. It usually occurs in a semiconducting phase, i.e., hexagonal (2H) consisting of two adjacent layers in the crystal unit which possesses ~ 10^7 times lower electrical conductivity and higher hydrophobic properties in comparison to its metallic trigonal (1T) counterpart [7,8]. These properties of 1T MoS_2 are

* Corresponding author.
** Corresponding author.
E-mail addresses: maciej.p.tobis@doctorate.put.poznan.pl (M. Tobis), elzbieta.frackowiak@put.poznan.pl (E. Frąckowiak).

https://doi.org/10.1016/j.jpowsour.2024.234862
Received 6 February 2024; Received in revised form 28 May 2024; Accepted 4 June 2024
Available online 8 June 2024
0378-7753/© 2024 The Authors. Published by Elsevier B.V. This is an open access article under the CC BY license (http://creativecommons.org/licenses/by/4.0/).

favorable for aqueous electrochemical capacitors (ECs), but the charge storage mechanism of MoS_2 in aqueous media remains ambiguous. The 2H MoS_2 phase cannot be cycled within the rational potential range in aqueous media to convert this structure to 1T phase which could efficiently host the electrolyte ions during intercalation process. Thus, the charge is mainly stored through formation of electrical double-layer on the basal plane of 2H MoS_2 [9]. The mechanism for 1T MoS_2 in aqueous media is complex, distinct plateau for intercalation of ions is not typically noticed [10]. Instead, rectangular cyclic voltammograms are observed which many authors refer to as pseudocapacitive phenomenon. It is enabled by the fast kinetics of ions diffusion facilitated by the metallic character of MoS_2 phase [11]. However, it has been noticed that after cycling of the electrode material in aqueous media, depending on the ionic radii of solvated cations (i.e., H^+, Li^+, Na^+, K^+), different interlayer spacing is observed, which could indicate a mechanism comparable to sorption of solvated ions within the interlayer spacing [7,12–14]. Though, more studies are required to further validate this concept. In addition, 1T MoS_2 is also already recognized as an efficient promotor of hydrogen evolution reaction (HER) in aqueous media due to the presence of the edge sites, grain boundaries, and sulfur defects [15,16]. Moreover, the major contribution to the overall HER catalytic properties is assigned to the sulfur vacancies in the basal plane of TMDs with the estimated Tafel slopes of 65–85 mV dec^{-1} [16]. Consequently, the use of TMDs in energy storage devices featuring aqueous electrolytes is restricted by the thermodynamic limit of water decomposition (i.e., 1.23 V), which is additionally diminished due to the catalytic activity of the TMDs structure. Such nanostructured composite materials used in a symmetrical, two-electrode system have high capacitance (MoS_2/NTs – 150 F g^{-1} at 0.2 A g^{-1}), but a narrow voltage window (0.8 V) due to the quick HER phenomena on the negative electrode [17,18]. Yet, ECs based on TMDs can offer higher capacitance than carbon and satisfactory level of electrical conductivity, which in consequence could constitute an attractive direction for further development of ECs. There are several reports of integrating MoS_2 with carbon-based materials such as, graphene fibers [19], carbon nanotubes [20], microporous carbons [21], carbon cloths [22], etc., which results into increased overall conductivity and capacitance making them attractive electrode materials for future energy storage devices.

Integration of MoS_2 with surface functionalities has also been tested using various methods including modification with the use of different organic molecules, e.g., thiols, organohalides, or maleimide derivatives [23–28]. Such treatment often leads to altered physicochemical properties of the material. Interestingly, the same catalytically active sulfur defects used as the HER promotors are efficiently exploited during covalent modification as a reaction mediator [29]. This may result in a decreased catalytic activity of modified MoS_2, which could be a promising approach for designing stable MoS_2-based, or generally, TMDs-based electrode materials for high performance energy storage devices. However, in the case of the reports given above, TMDs functionalization was conducted on a model material, i.e., micrometric commercial TMDs converted from 2H to 1T phase during organolithium treatment. Such exfoliated MoS_2 possesses lower content of structural defects, which consequently limits the functionalization kinetics, affecting the total amount of grafted species [29]. Especially, taking into account that dependent on the synthesis methodology, different properties such as particle size, structure, and texture can be found, which might affect the electrochemical behavior of TMDs. Moreover, the electrochemical properties of functionalized TMDs have not been fully elucidated [30]. Y. Zhuo et al. fabricated (EC) electrode materials by electrochemically exfoliating 2H MoS_2 and subsequently functionalizing it with 4-nitro-benzenediazonium tetrafluoroborate (NBD). Their study demonstrated enhanced capacitance values, but without providing the explanations regarding the impact of the functional groups on the electrochemical electrode performance [30].

Besides direct functionalization with diazonium salt, there is a lack of reports describing the spontaneous grafting of quinones onto the nanostructured TMDs. Quinones are aromatic compounds with conjugated aryl groups existing in different molecular configurations. Due to the high reactivity of the double-bonded oxygen in the aryl group, quinones can undergo reversible redox reactions, enhancing system capacitance. Quinones such as 1,2-dihydroxybenzene (catechol) [31], anthraquinone (AQ) [32], or chloroanthraquinone [33] have been grafted onto the surface of carbonaceous materials during the in-situ diazotization of the corresponding amino-substituted molecules into diazonium cations and subsequent reduction at the carbon surface with the release of N_2. Various carbonaceous materials have been employed for grafting, including glassy carbon [34], carbon fabrics [32], and carbon blacks [35], resulting in improved capacitance through participation in reversible redox reactions [36,37].

At the same time, the quinone family is also recognized in non-aqueous systems for improving the reachable capacity through reactions with metal ions, especially lithium [38]. Depending on the atomic composition and carbonyl group arrangement, the additional capacity and redox reaction potential *vs.* Li/Li^+ can slightly vary [39,40]. Therefore, quinone-containing composites can offer a wide versatility in terms of pairing with other energy storage materials with the desired potential region of redox reaction in a full cell design. From the layered material approach, conjugation with quinone compounds could also be performed under confinement where the functional groups are grafted within the interlayer spacing. Consequently, the potential of the electrochemical redox reaction of confined species could be controlled and induced by the process of metal ion intercalation [41]. Lithiation of MoS_2 in organic electrolyte is possible within 3.0–0.0 V *vs.* Li/Li^+ with conversion reaction to Mo and Li_2S occurring below 0.6 V *vs.* Li/Li^+ [42]. Depending on the morphology, i.e., the particle or crystallite size of the MoS_2, the kinetics of ion intercalation will be different with induced fast pseudocapacitive charge storage upon nanostructuring [43,44]. This is caused by the suppression of the first order phase transition and reduction of diffusion pathway resulting in nearly ideal MoS_2 pseudocapacitive performance. Having in mind the layered nature of TMDs, controlling the redox behavior of quinone molecules could be an interesting direction for further research.

Herein, we present an original concept of functionalization of 2D materials with redox active species for energy storage application. We have selected MoS_2 as a typical representative of the TMDs family for covalent functionalization with anthraquinone (AQ), which is known for redox activity in aqueous media. AQ has never been previously used for grafting onto 2D-TMDs. Our study shows that AQ has been successfully grafted on the outer surface of MoS_2 but also confined within interlayer spacing. The physicochemical as well as electrochemical properties of the sole and functionalized MoS_2 have been studied in detail.

2. Experimental section

2.1. Synthesis of pristine MoS_2

Nanostructured MoS_2 was prepared during hydrothermal reaction using 1.2 g L-Cysteine (Sigma-Aldrich, 97 %), 0.9 g sodium molybdate tetrahydrate (Sigma Aldrich, 98 %) in 180 ml of water. Once the substrates were dissolved, the pH of the solution was adjusted to 4.5, changing the color of the solution to orange. The reaction was carried out in a hydrothermal reactor with monitored temperature and pressure (Parr Instruments – High-Pressure Compact Reactor 5521). The reaction was conducted at 180 °C during 24h with stirring at 300 rpm. Once the reaction was finished, black precipitate was collected by filtration and washed with water and isopropanol. Obtained MoS_2 was dried in 70 °C overnight.

2.2. Chemical grafting of MoS_2

The modification of the nanostructured MoS_2 was conducted *via in-situ* generation of aryl diazonium cations and their consequent reduction

on MoS_2. Previously synthetized MoS_2 (300 mg) was sonicated (Hielsher UPH50, 40 % Watts output) for 1h in 5 ml of acetonitrile (Sigma Aldrich, HPLC gradient grade) which formed a stable black suspension. 560 mg of 2-aminoanthraquinone (Sigma Aldrich, 98 %) was dissolved in 450 ml of acetonitrile under N_2 flow for 1h. Then, 300 μL of tert-buthyl nitrile (Acros Organics, 90 %) was added to the 2-aminoanthraquinone solution. After 30 min of stirring, the freshly sonicated MoS_2 was added to the solution of 2-aminoanthraquinone. 300 μL of tert-buthyl nitrite was added two more times, each after 30min. The reaction mixture was left for 2.5h under N_2 flow and without access to light. Finally, the solution was filtered over nylon membrane (Whatman, 0.45 μm diameter). Collected powder was then cleansed with aliquots of acetonitrile, acetone and N,N-dimethylformamide using a Soxhlet system. The non-attached anthraquinone molecules are removed with the solvent during Soxhlet extraction. Repeated washing of AQ-MoS_2 surely eliminate all the non-covalently bonded anthraquinone molecules from AQ-MoS_2 compound. For clarity, this material is not a composite of AQ and MoS_2, but a covalently bonded AQ to the surface of MoS_2. The collected powder was dried in 70 °C overnight under vacuum (Büshi, B-585).

2.3. Structural and morphological characterization

Surface chemistry was investigated by the X-ray photoelectron spectroscopy PHI VersaProbell Scanning XPS system, using a monochromatic source of radiation (Al $K_\alpha = 1486.6$ eV) with a resolution of 0.5 eV and an analysis spot size of 400 μm. The morphology of the samples was studied using TEM FEI Titan 80–300 operating at 80 kV. Elemental composition of the prepared samples was evaluated using Thermo Fisher Scientific FlashSmart™ Elemental Analyzer. The content of C, H, N, S was evaluated in a column filled with copper and copper (II) oxide during incineration at 950 °C. The content of O was determined in a separate measurement in a column filled with nickel plated carbon during pyrolysis at 1060 °C. The crystallinity of the samples was examined by Bruker D8 Advanced X-ray diffractometer with Cu K_α radiation ($\lambda = 1.5406$ Å). Measurements were taken for 1h in the range of 6–60 2theta. Infrared spectrometer (Nicolet iS5 FT-IR) in the 600-1800 cm^{-1} wavenumber range was used to obtain infrared spectra of grafted materials. Raman spectroscopy analysis was performed using Thermo Scientific DXR Raman Microscope with laser emitting at $\lambda = 532$ nm set for 1 mW power. Each measurement lasted for 300 s during 3 scan series. The textural properties of the prepared materials were evaluated through N_2 sorption at 77 K using ASAP 2460 (Micromeritics, USA). Samples were degassed by helium gas flow at 100 °C for 12h. Before recording the isotherms, samples were degassed during 5h under vacuum. The specific surface area (SSA) was determined using Brunauer-Emmett-Teller model using 0.01 to 0.05 P/P_0 range. The pore size distribution (PSD) was evaluated using SAIEUS program (Micromeritics, USA), employing 2D-NLDFT heterogenous surface model.

2.4. Electrodes and electrochemical cell setup

The electrodes consisted of 80 wt% active material, 10 wt% conductive carbon (Super C65, C-NERGY™, Imerys), and 10 wt% binder (polytetrafluoroethylene – PTFE, 60 % dispersion in water, Sigma Aldrich). The constituents were mixed in 5 ml of isopropanol and sonicated for 30 min. The suspension was transferred into a mortar and mixed until solvent's evaporation. After dough-like consistency was obtained, the material was rolled between two sheets of plastic foil and passed through a hot roller to obtain a uniform thickness. The resulting sheet of prepared material was cut into 10 mm diameter discs, and subsequently dried at 70 °C overnight. The electrode mass ranged from 3 to 6 mg with a thickness of approximately 10–20 μm. The electrochemical behavior of the prepared electrodes in an aqueous environment was evaluated using a custom made three-electrode cell made from PTFE. The setup utilized a golden current collector for the working electrode, while a platinum mesh served as a counter electrode. For full cell characterization, PTFE Swagelok® type of cell was used. The negative electrode (MoS_2 or AQ-MoS_2) was paired with a positive electrode made from carbon – BP2000 (commercially available carbon black typically used as an electrochemical capacitor electrode material, from Cabot) and separated by a porous membrane (Whatman GF/A). The MoS_2 negative electrode was matched with the BP2000 positive electrode with the same mass. In the case of the negative electrode prepared from AQ-MoS_2, a twice heavier positive carbon electrode was used to balance the additional charge from the redox reaction. In both cell configuration, 1 M H_2SO_4 was utilized as an electrolyte, and to monitor the potential of the electrodes, Hg/Hg_2SO_4 reference electrode (640 mV *vs.* SHE) was employed. The electrochemical behavior of the prepared electrodes in an organic environment was studied in a stainless steel Swagelok® setup. The inner part of the cell was covered by the polyether ether ketone (PEEK) casing to prevent the stainless steel current collector from short circuiting. The electrodes were dried at 120 °C under vacuum in Büshi (B-585) prior to introducing into an argon filled glovebox introduction (Jacomex, H_2O and O_2 content below 1 ppm). Working electrode was separated by Whatman GF/D porous membrane from a 10 mm lithium disc (Sigma Aldrich, 0.38 mm thickness) and soaked with 200 μL of 1 M $LiPF_6$ dissolved in ethyl carbonate and dimethyl carbonate (EC:DMC, 1/1 v/v) (Sigma Aldrich, battery grade) used as an electrolyte.

2.5. Electrochemical characterization

At the beginning, the electrodes in the three-electrode custom made volume cell were subjected to a gradual potential extension (20 mV per 5 scan series beginning from +0.2 V *vs.* open circuit potential) using cyclic voltammetry (CV) at a scan rate 1 mV s^{-1} to evaluate the operational potential window. For the assembled full cell, the operational voltage window was evaluated using alternately CV (2 mV s^{-1} scan rate) and galvanostatic cycling with potential limitation (GCPL) (0.2 A g^{-1}) from 0.4 V to 1.2 V. Based on the potential measured by the reference electrode, the scan rate and potential window of negative and positive electrode were determined. The cycle lifetime of electrode materials was evaluated by using CV at a scan rate of 5 mV s^{-1}. The ability to withstand high charge/discharge regimes, for both kinds of cells, was evaluated using CV and GCPL at different scan rates (1–200 mV s^{-1}) and current densities (0.1–10 A g^{-1}). The electrochemical impedance spectroscopy (EIS) was performed at 0.1 V *vs.* SHE and 0.36 V *vs.* SHE in a frequency range between 100 kHz and 1 mHz. The cycle lifetime of the cells was investigated by using GCPL with 1 A g^{-1} at 1.2 V. All electrochemical measurements were conducted using a computer controlled multichannel potentiostat/galvanostat (VMP3, Biologic®, France). The capacitance in the three-electrode cell is expressed per one electrode and is calculated as follows:

$$C_{CV(m)} = \frac{I}{\frac{dU}{dt} \cdot m} \text{ and } C_{CV(V)} = \frac{I}{\frac{dU}{dt} \cdot v} \quad (1)$$

$$C_{GC/D(m)} = \frac{2 \cdot I \cdot A}{U^2 \cdot m} \text{ and } C_{GC/D(V)} = \frac{2 \cdot I \cdot A}{U^2 \cdot v} \quad (2)$$

$$C_{EIS(V)} = \frac{-1}{2 \cdot \pi \cdot f \cdot Z'' \cdot v} \quad (3)$$

where, $C_{CV(m)}$: gravimetric electrode capacitance calculated from CV in F g^{-1}, $C_{CV(V)}$: volumetric electrode capacitance calculated from CV in F cm^{-3}, $C_{GC/D(m)}$: gravimetric electrode capacitance calculated from GCPL in F g^{-1}, $C_{CV(V)}$: volumetric electrode capacitance calculated from GCPL in F cm^{-3}, $C_{EIS(V)}$: volumetric electrode capacitance calculated from EIS (F cm^{-3}), f: frequency (Hz), Z'': resistance taken from the imaginary part of the Nyquist plot (Ω), I: current (A), dU/dt: scan rate (V s^{-1}), m: mass of working electrode (g), A: area under discharge (V s), U: potential (V), v: volume (cm^3).

The capacitance, energy, and power in the two-electrode cell is

expressed per both electrodes, i.e., per full device and is calculated accordingly:

$$C_{CV} = \frac{I}{\frac{dU}{dt} \cdot m} \quad (3)$$

$$C_{GC/D} = \frac{2 \cdot I \cdot A}{U^2 \cdot m} \quad (4)$$

$$E = \frac{C_{GC/D} \cdot U^2}{7200} \quad (5)$$

$$P = \frac{E}{t_{dis}} \quad (6)$$

where, C_{CV}: cell capacitance calculated from cyclic voltammetry (F g^{-1}), $C_{GC/D}$: cell capacitance calculated from galvanostatic charge/discharge (F g^{-1}), I: current (A), dU/dt: scan rate (V s^{-1}), m: mass of positive and negative electrode (g), A: area under discharge (V s), U: voltage (V), E: energy (Wh g^{-1}), P: power (W g^{-1}), t_{dis}: cell discharge time (h).

3. Results & discussion

3.1. Synthesis and functionalization of MoS_2 nanosheets

Nanostructured MoS_2 was synthetized *via* facile hydrothermal reaction which is an important bottom-up synthesis method for obtaining various TMDs. After filtration and drying, the black powder was dispersed and suspended in acetonitrile (ACN) during sonication to uniform the MoS_2 particles and provide even access of the reagents to the layered MoS_2. The process of AQ grafting can be expressed by the following reaction mechanism (eqs. (7)–(9)). The AQ diazonium cations, generated by aromatic amine (AQ-NH_2) and tertbutyl nitrite (Fig. S1), lead to the formation of aryl radicals through the loss of nitrogen gas (eq. (8)). In the next step, the formed radicals react with the MoS_2 surface, through a radical addition mechanism, resulting in the attachment of AQ moieties to the MoS_2 surface (eq. (9)).

$$AQ - NH_2 + (CH_3)_3CONO \rightarrow AQ - N \equiv N^+ \quad (7)$$

$$AQ - N \equiv N^+ \rightarrow AQ^\bullet + N_2^\uparrow \quad (8)$$

$$AQ^\bullet + MoS_2 \rightarrow AQ - MoS_2 \quad (9)$$

Covalent attachment of anthraquinone (AQ) species to the surface of MoS_2 forms AQ-MoS_2 is shown in Fig. 1.

X-ray photoelectron spectroscopy (XPS) analysis was performed to determine the type of interaction between AQ and MoS_2 (Fig. 2 a-b). For the non-modified sample, the S2p spectrum confirms the presence of MoS_2 in both phases (1T at 161.9 eV and 2H at 164.0 eV) with a dominant 1T metallic phase (~85 wt%) (Table S1). Peaks positioned at 164 eV on the S2p and 287.7 eV on the C1s spectra show C–S type of bonding, which within the TMDs family could be referred as sulfur defects within MoS_2 crystal lattice [24]. It could be also related to the traces of precursor (L-Cysteine) after synthesis. The C–C bonding on the C1s spectra at 288 eV can be assigned to the amorphous carbons formed during the decomposition of the MoS_2 precursor during the hydrothermal reaction. After functionalization, the ratio of 1T/2H-phase remains comparable, indicating that both phases could undergo covalent grafting, which is also confirmed in the Mo 3d region (Fig. S2). The very low content of MoO_2 and MoO_3 on the surface of the MoS_2 is also a proof that the hydrothermal synthesis allows for the preparation of high purity MoS_2 material. A significant increase in the C–C bonding can be observed due to the presence of the AQ molecules on the surface of MoS_2. It also explains the low intensity of the signals in the S2p region.

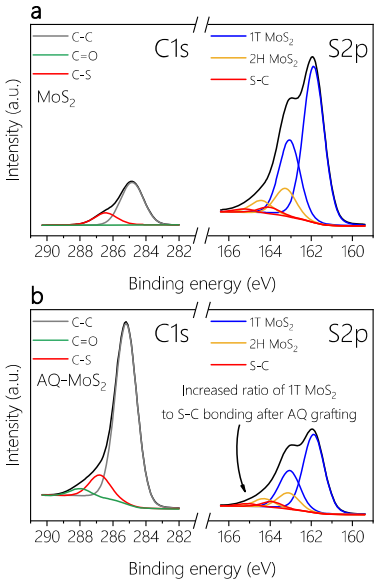

Fig. 2. XPS spectra of pristine and functionalized MoS_2. (a) High-resolution spectra from the C1s and S2p regions corresponding to MoS_2, and (b) AQ-MoS_2.

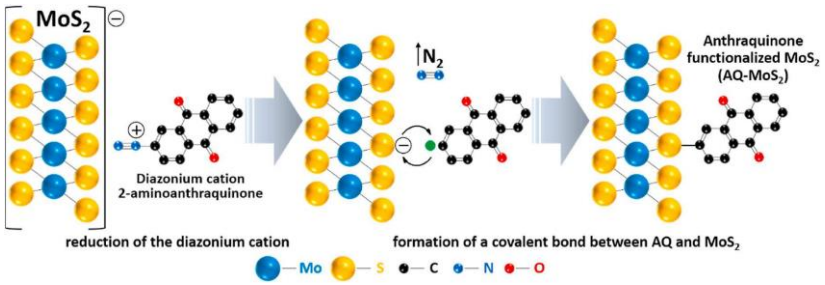

Fig. 1. Synthesis scheme of covalently functionalized MoS_2 with anthraquinone molecules *via in-situ* formation of diazonium salt.

The intensity of the peak indicating the C–S bonding in the C1s and S2p region has changed upon functionalization which implies the chemical interaction between AQ molecule and MoS_2. This means that the MoS_2 can be successfully functionalized by AQ molecules *via* diazonium salt chemistry. By calculating the ratio of the C–S bonding to the content of MoS_2 in the 1T and 2H phases, it is possible to estimate the content of the covalently attached anthraquinones at ca. 20 %.

Transmission electron microscopy (TEM) was used to study the samples morphology and local arrangement of layers. Both samples at lower magnifications (Fig. 3a and d) revealed a structure organized in a few layers' packs. Images of the modified material show no structural impact of the chemical modification on the particle morphology or separation. Typically, liquid phase sonication of MoS_2 in ACN does not provide enough shear force to efficiently exfoliate high quantity of MoS_2 into single layers [45]. At higher magnifications (Fig. 3 b-c and e-f), both materials showed a layered structure with different sheets separation. For pristine MoS_2, we observed around 0.6 nm interlayer distance between the individual layers. However, by analyzing the interlayer spacing at different regions of AQ-MoS_2, we found various interlayer distance ranging from 0.6 nm to 1.2 nm. This could mean that the MoS_2 has been partially grafted by AQ within the interlayer spacing. It appears that part of the MoS_2 has been modified on the outer surface where the interlayer spacing remains intact (ca. 0.6 nm). In the other regions of the MoS_2 with altered the interlayer spacing (ca. 0.9–1.2 nm), anthraquinones could be at least partially confined within the interlayer spacing. Interestingly, different layer separation could indicate various arrangement of anthraquinone molecules between the MoS_2 layers, such as, horizontal, perpendicular or tilted positions. The interlayer spacing values of the modified MoS_2 are in good agreement with dimensions of the AQ molecule model presented in Fig. S3 with length of 1.16 nm, height of 0.83 nm and depth of 0.39 nm.

Fig. 4 a shows the elemental analysis of pristine and AQ modified MoS_2. The elemental weight content of C, H, N, S, and O contains important information about the elemental composition of MoS_2 and the quantity of grafted anthraquinones. It can also allow to estimate the total amount of AQs, regardless of the molecule's position, whether grafted on the surface or within the interlayer spacing. Hydrothermally obtained MoS_2 usually contains a small amount of amorphous carbon (3.90 wt%) due to the usage of alkyl sulfur precursor (L-Cysteine). Some content of oxygen in the sample (8.20 wt%) was detected, which could originate from unreduced molybdenum oxide during the reaction. After modification, AQ-MoS_2 showed increased carbon content (19.60 wt%), which can be attributed to the grafted AQ molecules. Considering that 81.16 % of anthraquinone's molar mass is carbon, we can estimate that the modified sample contains ca. 20 wt% of covalently attached anthraquinones. X-ray diffraction (XRD) was used to evaluate the crystallographic properties of the pristine and modified MoS_2 (Fig. 4 b). Pristine MoS_2 exhibits a semi-crystalline pattern with peaks positioned at $2\theta = 14^\circ$, 35°, 42°, and 58° corresponding to the (002), (100), (103), (110) planes, respectively, assigned to the trigonal (1T) MoS_2 indexed by the JCPDS card no. 04-017-0898. The peak (002) at $2\theta = 14^\circ$ indicates an interlayer distance which in pristine MoS_2 is ca. $d_{(002)} = 0.6$ nm. No presence of MoO_2 or MoO_3 impurities was observed in the XRD pattern. After modification, the position of the (002) peak shifted from 14° to 6.8°, indicating an interlayer spacing of ca. $d_{(002)} = 1.3$ nm in AQ-MoS_2. The shift confirms the presence of AQ molecules not only on the surface of MoS_2, but within the interlayer spacing too. Interestingly, the (002) peak was broadened after functionalization, suggesting a reduction in the crystallographic domains size. This broadening could also be a non-uniform arrangement of AQ molecules within the interlayer spacing, leading to variations in the interlayer distance of AQ-MoS_2. Moreover, there was no presence of unwashed 2-aminoanthraquinone. To further verify whether the process of functionalization affects the porous texture properties of AQ-MoS_2, we have performed N_2 sorption measurements. The isotherms (Fig. 4 c) display the typical shape of isotherm type II, which is commonly observed in nonporous, or mesoporous samples [46]. The comparable shape of the isotherms suggests that the porous texture of the AQ-MoS_2 sample remains intact after the modification. The SSA has slightly increased after the modification (from 39 to 64 $m^2 g^{-1}$) which confirms our assumptions about the reduction of the

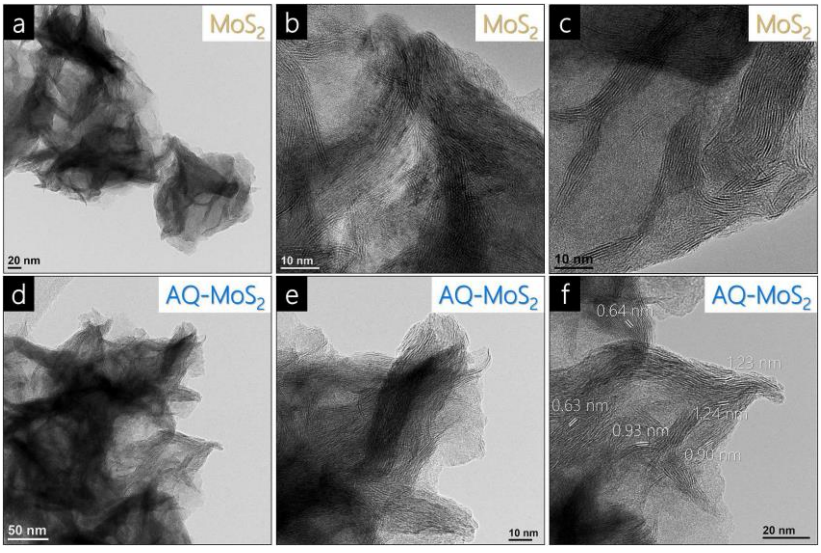

Fig. 3. TEM images of pristine and modified MoS_2 with marked interlayer spacing. (a), (b), (c) pristine MoS_2. (d), (e), (f), AQ-MoS_2.

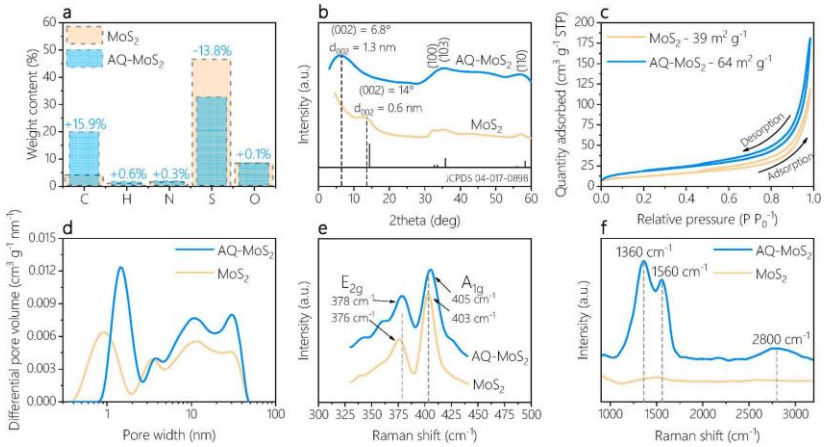

Fig. 4. Materials characterization of pristine and AQ modified MoS_2. (a) Elemental analysis showing content of C, H, N, S, O in the sample. (b) X-ray diffraction patterns. (c) Isotherms of nitrogen sorption. (d) Corresponding pore size distributions. (e), (f), Raman spectra at different regions.

crystallite sizes after functionalization observed in the XRD pattern. This consequently leads to the separation of MoS_2 stacks, revealing the SSA previously unavailable for nitrogen adsorption. It is worth noting that such a small SSA before and after modification also suggests that the AQ molecules are most likely positioned within the interlayer spacing of MoS_2 due to small total adsorption area. In comparison, the functionalization of carbon materials (e.g., activated carbon xerogel) has led to a significant decrease of the SSA from 2350 $m^2\ g^{-1}$ to 1317 $m^2\ g^{-1}$ with 16.9 wt% loading of AQ [47]. This suggests, that in our case, the AQ molecules are distributed within the interlayer spacing and on the surface of the MoS_2 particles. Comparable pore size distribution (Fig. 4 d) indicates that the textural properties of the prepared materials remain comparable. However, the onset of the microporous range in the structure has shifted from 0.40 nm to 0.80 nm, suggesting that the AQ molecules are blocking the access to microporosity of MoS_2 (Table S2). Further confirmation of the presence of AQ molecules on MoS_2 was obtained through Fourier-transform infrared spectroscopy (FT-IR). The spectra (Fig. S4) showed a strong signal corresponding to the C═O stretching vibration at 1674 cm^{-1}. Raman spectroscopy (Fig. 4 e-f) revealed the presence of two characteristic bands for MoS_2, i.e., E^1_{2g}, resulting from S atoms vibrations in the opposite direction with respect to the molybdenum atom, and A_{1g}, out-of-plane S atoms vibrations [48]. The position of these peaks on the Raman spectra could suggest the number of successive layers in the crystal lattice. In our case, pristine MoS_2 shows E^1_{2g} and A_{1g} at 376 cm^{-1} and 403 cm^{-1}, respectively, indicating 4 adjacent layers. After the modification, peaks positions shifted to 378 cm^{-1} and 405 cm^{-1} for E^1_{2g} and A_{1g}, correspondingly, indicating the decrease of the number of layers in the particle to ca. 2–3. Raman spectra of AQ-MoS_2 show strong signals at 1360 cm^{-1}, 1560 cm^{-1}, and 2800 cm^{-1} which can be attributed to the D, G, and 2D bands, correspondingly. The presence of bands typical for carbonaceous materials could be a proof that the MoS_2 has been functionalized by AQ molecules. Functional groups are most likely burned off during the laser exposure, giving the signals usually attributed to the carbonaceous materials. This can be also explained by the stretching and vibrational signal from uncoordinated sp^2 and sp^3 bands which is enhanced by the MoS_2 lattice.

3.2. Covalently linked AQ to nanostructured MoS_2 for energy storage applications

Subsequently, nanostructured MoS_2 and AQ-MoS_2 materials were prepared in a form of 10 mm round self-standing electrodes. The initial evaluation of the electrochemical behavior was conducted in a three-electrode setup with 1 M H_2SO_4 as the aqueous electrolyte. Typically, MoS_2 in acidic media exhibits a well-defined electrochemical response due to high ionic conductivity and great proton ion mobility [7,49]. Moreover, cycling in 1 M H_2SO_4 does not cause significant expansion of the interlayer spacing [7]. The abundance of H^+ ions in the electrolyte bulk is the most conducive for quinone/hydroquinone redox reaction as well. Non-modified MoS_2, as a layered material presents electrochemical characteristics typical for a pseudocapacitive material, i.e., square-shape cyclic voltammograms (Fig. 5 a-b) and isosceles galvanostatic charge/-discharge (Fig. 5 c). The rapid kinetics of charge/discharge is primarily attributed to the nanostructured crystalline domains, where the process of ion intercalation is not limited by diffusion within the interlayer spacing of the host crystal lattice, especially with the small ion size. In pristine MoS_2, two different charge storage mechanisms could be occurring, i.e., sorption of ions at the MoS_2 basal planes and intercalation within the interlayer spacing, described by the following equation (eq. (10)) [50].

$$MoS_2 + H^+ + e^- \leftrightarrow MoS - SH \tag{10}$$

Fig. 5 d shows a cyclic voltammogram with the potential expansion of AQ-MoS_2, revealing characteristic peak (from −0.1 to 0.1 V *vs.* SHE) corresponding to the redox reaction of carbonyl groups originating from grafted AQ molecules, given by the equation below (eq. 11) [51,52].

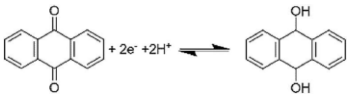

(11)

Interestingly, the rectangular shape of the CV, besides the AQ redox peak, is preserved as showed by the grey dotted line (Fig. 5 d). This observation could support the concept that the intercalation of ions vastly contributes to the total capacitance rather than the sorption of

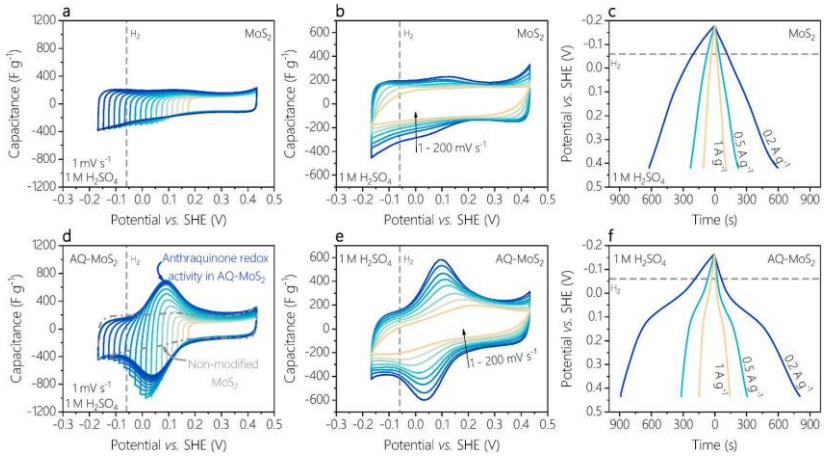

Fig. 5. Electrochemical characterization of MoS_2 and AQ-MoS_2 electrodes in 1 M H_2SO_4 aqueous medium. (a) Cyclic voltammetry potential extension for MoS_2 collected at 1 mV s^{-1}. (b) Cyclic voltammetry performance for MoS_2 recorded at different scan rates from 1 to 200 mV s^{-1}. (c) Galvanostatic charge/discharge profiles for MoS_2 collected at different current densities from 0.2 to 1 A g^{-1}. (d) Cyclic voltammetry potential extension for AQ-MoS_2 collected at 1 mV s^{-1}, performance of pristine MoS_2 is shown for comparison. (e) Cyclic voltammetry performance for AQ-MoS_2 recorded at different scan rates from 1 to 200 mV s^{-1}. (f) Galvanostatic charge/discharge profiles for AQ-MoS_2 collected at different current densities from 0.2 to 1 A g^{-1}. The theoretical hydrogen evolution potential is marked as H_2.

ions at the basal plane of MoS_2 [53]. Furthermore, the presence of grafted AQs within the interlayer spacing does not alter the electrochemical response of MoS_2. The transport properties of ions in the crystal lattice during charge/discharge are not kinetically disrupted by the presence of confined AQs, but it could also be related to the small ionic radii of intercalated ions. It is also worth noting that the oxidation/reduction peaks of the AQ molecules are in the similar position at low scan rates, meaning that the redox reactions are not kinetically limited by the diffusion of ions. The high reversibility of the redox peaks also indicates that the AQ molecules are not detaching from the surface of the MoS_2. After modification, we observed an increase in reachable capacitance from 191 F g^{-1} (461 F cm^{-3}) for MoS_2 to 263 F g^{-1} (631 F cm^{-3}) for AQ-MoS_2 at 0.2 A g^{-1} within the potential range from 0.46 V to −0.16 V *vs.* SHE (Fig. 5e and Fig. 6). Comparing the capacitance at each scan rate (Fig. 5 b and e), we can observe a gradual decrease in capacitance until they become equal at 200 mV s^{-1}, where charge is mainly stored through ion sorption.

So far, AQ grafting has primarily been conducted on carbonaceous materials (e.g., carbon black – BP2000 or SC2A) to incorporate the redox reactions in the EC system which boosted the capacitance (from 100 F g^{-1} to 185 F g^{-1} for BP2000 at 10 mV s^{-1}) [51,52,54]. However, the capacitance originating from EDL decreased, this is mainly associated with a smaller available SSA of the electrode material after modification. In our case, the charge storage behavior is mainly connected with the intercalation of ions which seems to be not kinetically disrupted by the presence of AQ molecules. Therefore, the stored charge originating from the intercalation of ions remains intact after the modification which is in good agreement with the decreasing capacitance during increasing sweep rate (Fig. 6).

We estimate that the grafted AQ molecules could not only significantly boost the capacitance in the functionalized MoS_2 electrode material, but also affect the overall charge storage behavior and ion movement kinetics within the interlayer spacing. The grafted AQ molecules could: decrease the number of the adsorption sites for ions during charge storage and affect the ion movement within the interlayer spacing. Therefore, to further elucidate the nature of the stored charge and determine the limiting parameters for ions intercalation we used the power-law relationship of current to scan rate ($i = av^b$), known *b-value analysis* (Fig. 7 a-b). By determining the slope of the *log(I) vs. log(v)* function, it is possible to assess whether the process is diffusion-controlled (b = 0.5), finite diffusion-controlled (b = 0.6–0.8) or surface-controlled (b = 1) [55,56]. To prove the above hypothesis, we have decided to conduct the *b-value analysis* at two different potentials where the AQ redox reactions were occurring (*AQ region*) and at potential of rectangular voltammogram shape (*flat region*). The results provide crucial insights into how grafted AQ species influence the charge storage behavior and whether they impact the kinetics of ion intercalation. We started by plotting the peak redox current density over different scan rates at different potentials, i.e., *flat region* (at 0.36 V *vs.* SHE) and *AQ region* (at 0.1 V *vs.* SHE) for both materials. It was found that in pristine MoS_2, both regions tend to b = 1, i.e., *AQ region = 0.89* and *flat region = 0.97* (Fig. 7 b) indicating surface-controlled processes. There could be two explanations for this behavior, which include the formation of electrical double layer (EDL) upon intercalation of ions within the interlayer spacing of MoS_2, or the surface redox processes of MoS_2 [57]. In this case, it is difficult to distinguish between those two mechanisms. The formation of an EDL upon intercalation of ions is possible due to the rectangular shape of the CV and the small ion radii of intercalated ion. On the other hand, the change of the oxidation-state of MoS_2 (into MoS–SH, equation (10)) cannot be excluded as well. After AQ modification, by using b-values analysis, *b = 0.79* for *AQ region* and *b = 0.94* for the *flat region* were found. For the *flat region*, the b-values, remain comparable and approach 1. In the *AQ region*, the b-value has shifted towards the intermediate value indicating a finite diffusion-controlled process. This could indicate a mixed contribution from the diffusion-controlled redox reaction of AQ molecules and the surface-controlled charge storage of MoS_2. In our case, the b-value analysis can only give some hints regarding the kinetics of the electrochemical processes. Therefore, we have decided to conduct electrochemical impedance spectroscopy (EIS) to deconvolute the mechanism

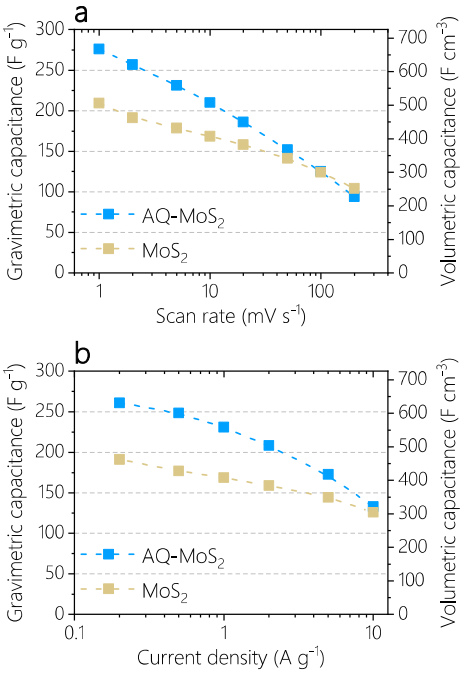

Fig. 6. Comparison of electrode capacitance given in gravimetric (left y-axis) and volumetric (right y-axis). The values obtained from (a) cyclic voltammetry, and (b) galvanostatic charge/discharge techniques recorded at different charge/discharge regimes (from 1 to 200 mV s^{-1}, and from 0.2 to 10 A g^{-1}, correspondingly).

of the charge storage. Fig. 7 shows EIS and corresponding Bode plots dependence (volumetric capacitance and phase angle *vs.* frequency) of pristine and modified MoS_2 recorded at different potentials, i.e., at 0.1 *vs.* SHE (*AQ region*) and 0.36 V *vs.* SHE (*flat region*). Considering pristine MoS_2 (Fig. 7 c), the EIS shows negligible internal resistance (ESR), i.e., 0.74 Ohm. We have also decided to express the capacitance in volumetric, instead of gravimetric metrics to omit the effect related to the increase of the electrode weight after grafting. The linear profile of the EIS spectra at both potentials at high frequency indicates that the process is not limited by the kinetics of the ion diffusion. Corresponding Bode plots (Fig. 7 d) show comparable capacitance at both potentials with slightly higher capacitance at *AQ region* potential. Phase angle (ϕ) represents the balance between the capacitive ($\phi = 90°$), diffusion-limited ($\phi = 45°$), and resistive ($\phi = 0°$) response [57]. Regardless of the applied potential, the phase angle curves are comparable with transition from resistive to ideally capacitive ($\phi = 82°$) response versus frequency accompanied by the increase of the volumetric capacitance (to 601 and 805 F cm^{-3}). It could be an indication that the pristine MoS_2 has a dominant capacitive nature, especially when the profiles of the phase angle do not change at fixed potentials. It means that the charge storage mechanism is based on the reversible adsorption of ions through the formation of an EDL within the interlayer spacing of MoS_2 upon their intercalation. The Nyquist plot for AQ-MoS_2 (Fig. 7 e) presents a low ESR of 0.89 Ohm with a profile indicating a Warburg-type diffusion-limited process. At 0.36 V *vs.* SHE, in the corresponding Bode plot dependence (Fig. 7 f) we could observe a comparable transition from resistive to capacitive characteristics. Interestingly, smaller capacitance is noticed at 0.36 V *vs.* SHE, i.e., 601 F cm^{-3} and 531 F cm^{-3} for MoS_2 and AQ-MoS_2, correspondingly. It could indicate that the number of adsorption sites within the interlayer spacing are occupied by AQ molecules and are not accessible during EDL charge storage. At the region of AQ redox reaction (0.1 V *vs.* SHE), the phase angle versus frequency shows a deviated transition from resistive to capacitive behavior as well. The deviation is most likely due to a mixed contribution from the diffusion of ions and redox reaction. We can also observe a significant capacitance increase from 531 F cm^{-3} for MoS_2 to 1626 F cm^{-3} at *flat* and *AQ regions*, correspondingly. In general, the presence of the AQ molecules does not significantly disrupt the diffusion of ions within the interlayer spacing of MoS_2, neither alters the principal charge storage mechanism of the MoS_2 (Fig. 8).

For a comprehensive comparison of the full cell performance, electrodes made from carbon black (BP2000) were combined with MoS_2 and AQ-MoS_2 electrode, in a hybrid cell configuration, i.e., (−)MoS_2 || BP2000(+) and (−)AQ-MoS_2 || BP2000(+). Constructed cells were subjected to voltage extension from 0.4 V up to 1.2 V (Fig. 9) while observing the operation of positive and negative electrode. Additionally, they were tested at various charge/discharge current load regimes (Fig. S5), which resulted in improved specific cell capacitance (from 41 F g^{-1} to 49 F g^{-1} at 0.1 A g^{-1} for MoS_2 and AQ-MoS_2, correspondingly). It should be underlined that typically the values for specific cell capacitance are four times lower than capacitance per electrode. Thanks to the AQ surface modification of MoS_2, the system with grafted material demonstrated improved values of energy at each specific power charge/discharge rate (Fig. S5 f). It is worth mentioning, that the hybrid cells presented even higher values of energy and power than symmetric cells containing MoS_2 or BP2000 electrodes (Fig. S5 f).

The self-discharge behavior of the assembled cells, i.e., (−)MoS_2 || BP200(+) and (−)AQ-MoS_2 || BP2000(+), was investigated by charging the cells with a 0.2 A g^{-1} current load to different voltages. Subsequently, the circuit was opened, and the voltage of the cells was monitored over a period of 6 h (Fig. S6). At each voltage (1.0 V, 1.2 V, and 1.4 V) the cell with MoS_2 exhibited higher self-discharge, dropping to nearly 0.1 V during the first 2 h. This behavior can be attributed to the high mobility of ions in protic electrolyte (1 M H_2SO_4). In contrast, the cell containing AQ-MoS_2 demonstrated slow self-discharge at all applied voltages. Such discrepancy between the results is due to the presence of redox active AQ groups grafted on the surface and in between the layers of MoS_2 [58]. Immobilized anthraquinone molecules do not show shuttle effect between the electrodes responsible for quicker self-discharge.

Sulfuric acid is problematic electrolyte for commercial application due to the necessity of using costly anti-corrosive cell components. Therefore, researchers are exploring greener alternatives that would not require using expensive current collectors and could operate at a higher potential window. One interesting example suitable for anthraquinone application due to its naturally low pH, is beryllium sulfate. The electrochemical performance of AQ-MoS_2 in 1 M $BeSO_4$ is shown in Fig. S7. During potential extension, a peak related to the anthraquinone redox reaction is also present, but the oxidation-reduction potential wave is shifted by 150 mV, indicating low ionic mobility of H^+ in 1 M $BeSO_4$. At higher scan rates, a gradual decrease of capacitance is observed most likely related to the higher ionic radii of solvated Be^{2+} cations (i.e., 31 pm), in turn, the low-ion mobility and in consequence diffusion related issues [59,60].

Alternatively, integrating polymers (e.g., polyvinyl alcohol – PVA) with acidic electrolyte solutions (1 M H_2SO_4/PVA) allows for reaching higher voltage and potential practical applications of such EC device [61].

The MoS_2 material can also act as a host for lithium ions during the electrochemical intercalation reaction in organic media, showing pronounced redox peaks when bulk electrodes are used [62]. Its

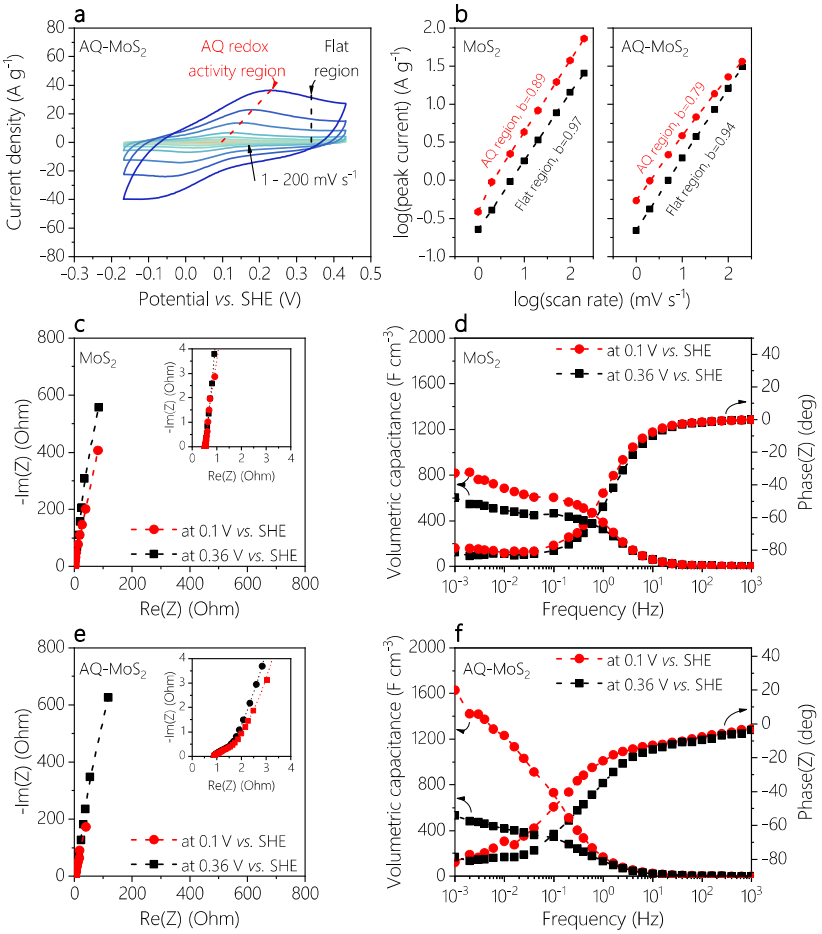

Fig. 7. Analysis of the charge storage mechanism for MoS_2 and AQ-MoS_2 materials. (a) cyclic voltammogram of AQ-MoS_2 obtained at different scan rates. (b) logarithmic peak current variation *vs.* scan rate driven from CV analysis. (c and d) EIS plots at different potential regions with corresponding volumetric capacitance and phase angle – frequency dependence for MoS_2. (e and f) EIS plots at different potential regions with corresponding volumetric capacitance and phase angle – frequency dependence for AQ-MoS_2.

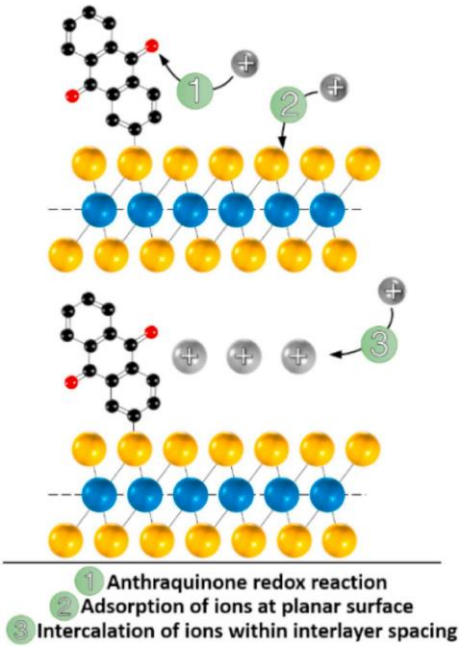

Fig. 8. Proposed mechanism of the charge storage for AQ-MoS_2 electrodes in aq. 1 M H_2SO_4 with AQ molecules grafted on the basal plane and within interlayer spacing of MoS_2. Intercalation of cations is not kinetically disrupted by AQ molecules in MoS_2 structure.

electrochemical intercalation properties, are primarily controlled by the particle size with enhanced pseudocapacitive intercalation of ions upon nanostructuring [63]. Most of the works published on MoS_2 focuses on the four-electron conversion reaction to Mo and Li_2S, or other metal sulfides, however, the cycle life of the electrode materials is often limited [64,65]. Thus, we have decided to exclusively study the intercalation properties of MoS_2 which proceeds in the range of potentials from 1.0 to 3.0 V *vs.* Li/Li^+, with a theoretical capacity of 167 mAh g^{-1} (eq. (12))

$$MoS_2 + xLi^+ + xe^- \leftrightarrow Li_xMoS_2 \quad (0 \leq x \leq 1) \tag{12}$$

As both materials, AQ and MoS_2 are also electrochemically active in organic media, we decided to investigate their electrochemical behavior in half cells *vs.* lithium metal (Fig. 10). The 2H phase of MoS_2 undergoes electrochemical conversion reaction to the 1T phase at 1.1 V *vs.* Li/Li^+, which may induce a strain in the crystal lattice and leads to the detachment of grafted AQ molecules from MoS_2. Despite the relatively low ratio of 2H to 1T phase, we have decided to limit the cut-off potential to 1.5 V *vs.* Li/Li^+, to mitigate the crystal lattice rearrangement. Non-modified MoS_2 shows pseudocapacitive electrochemical performance promoted by the nanosized particles of MoS_2. The short ion diffusion path length allows the nanostructured MoS_2 to behave electrochemically like a pseudocapacitive material [66]. After the modification, AQ-MoS_2 retained its original pseudocapacitive behavior while also presenting broad carbonyl redox reaction peak in the range of 1.9–2.5 V vs Li/Li^+. Similarly to aqueous media, the modification did not alter ion intercalation behavior. Although, the redox reaction peak is broader which could indicate that the process occurs more slowly in the organic medium. The covalently attached AQ to MoS_2 show moderate improvement of capacity. The concept of linking the quinone family to 2D materials could open new possibilities into the new electrode design for energy storage applications.

3.3. *Suppressing hydrogen evolution catalytic activity of MoS_2*

The catalytic activity of MoS_2 towards the HER in aqueous media is the main reason for its narrow operational potential window, i.e., 0.6 V for the negative polarization. To evaluate the long-term electrochemical stability of the prepared materials we, have conducted cyclic voltammetry tests within 0.6 V potential range at a sweep rate of 5 mV s^{-1} using a three-electrode setup (Fig. 11). MoS_2 (Fig. 11a) shows capacitive behavior, with only a 10 % initial capacitance decrease observed after 1000 cycles (from 165 F g^{-1} to 149 F g^{-1}). Interestingly, after ca. 1600 cycles, MoS_2 started to show catalytic activity towards HER which is most likely caused by the structural deterioration of MoS_2. The activation of unsaturated sulfur defects related to the self-regulation effect of Mo–Mo bonds, led to a shift of HER overpotential to ca. −0.1 V *vs.* SHE resulting in a quicker H_2 evolution [67]. Similar tests were conducted for AQ-MoS_2, which showed an initial capacitance of 227 F g^{-1} at 1st cycle (Fig. 11 b). Cycling reveals lack of HER overpotential shift, as it was noticed previously for MoS_2. This can be attributed to the covalently attached AQ molecules occupying defect sites, which are no longer catalytically active towards the HER. In addition, the redox reaction of AQ molecules can locally change the concentration of hydrogen ions at the electrode/electrolyte interface, which could lead to shift of the HER overpotential. It is a proof that the modified material could show improved stability towards parasitic reactions (in this case HER). Additional experiments concerning the cyclability of two-electrode cells (Fig. S8) revealed that the AQ-MoS_2 was able to operate for long lifespan while maintaining the quinone redox reaction. The potential of the negative electrode is shifting over cycling which could be also the reason for the improved overall cycling of the MoS_2-based material.

4. Conclusions

In summary, we synthetized covalently functionalized MoS_2 with anthraquinone molecules *via* diazonium salt chemistry. The chemically bonded redox active species such as quinones were never studied before, especially in terms of their electrochemical behavior in different aqueous and organic media. In our work, the anthraquinones (AQs) were grafted on the outer surface of the layered material as well as within the interlayer spacing of MoS_2. Presence of covalent bonds (C–S) between AQ and MoS_2 was confirmed by spectroscopy techniques such as XPS and FT-IR. Additionally, C═O groups presence proved by FT-IR indicate formation of AQ-MoS_2. Structure and morphology of AQ-MoS_2 was investigated by XRD pattern analysis and TEM imaging. Elemental analysis showed that content of AQ in AQ-MoS_2 was ca. 20 wt%.

We observed a significant capacitance increase of the electrodes after AQ grafting, from 191 F g^{-1} (461 F cm^{-3}) to 263 F g^{-1} (631 F cm^{-3}) at 0.2 A g^{-1} in aqueous media due to the pronounced redox activity of anthraquinones. By testing the cyclability of the electrodes in 1 M H_2SO_4, we found that the catalytic activity of the defect sites on surface of the AQ-MoS_2 was suppressed after functionalization by blocking them with anthraquinones. The grafted anthraquinone molecules do not significantly disturb the transport properties of ions during intercalation processes in aqueous media (1 M H_2SO_4 and 1 M $BeSO_4$). In addition, impedance spectroscopy and *b-value* voltammetry methods allowed us to study the mechanism of charge storage, distinguishing between electrical double layer and faradaic reactions at different potentials. Pristine and modified MoS_2 were used to build hybrid systems (−)MoS_2 || BP2000(+) and (−)AQ-MoS_2 || BP2000(+) for comparison with symmetric cells consisting of MoS_2 and BP2000. Functionalized MoS_2

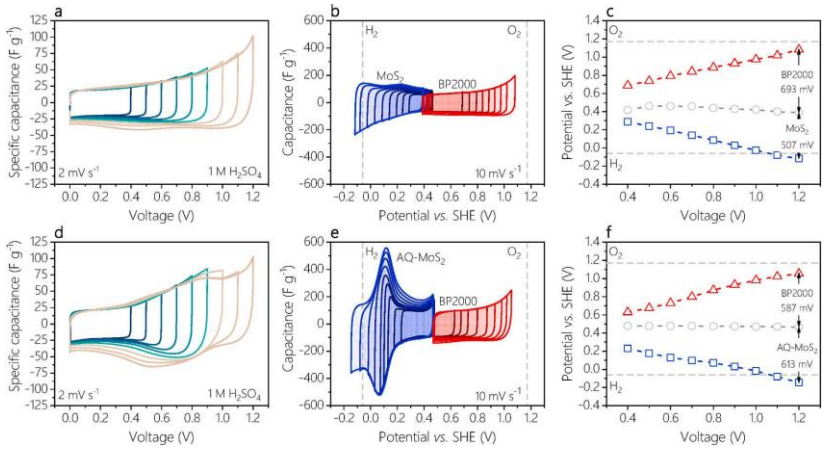

Fig. 9. Electrochemical performance of a hybrid electrochemical capacitor cells in 1 M H_2SO_4 containing. (a), (b), (c) MoS_2, and (d), (e), (f) AQ-MoS_2 as negative electrodes and BP2000 as positive electrodes. (a), (d) profiles of voltage extension. (b), (e) electrochemical behavior of negative and positive electrode during voltage expansion. (c), (f) maximum potential range of electrochemical capacitors during voltage expansion.

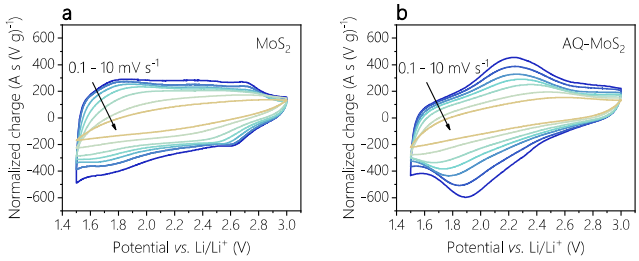

Fig. 10. Electrochemical behavior of MoS_2 based electrodes in half-cells *vs.* lithium metal operating in 1 M $LiPF_6$ (EC:DMC, 1 to 1 v/v) organic media. Cyclic voltammetry performance for (a) MoS_2, and (b) AQ-MoS_2 electrodes recorded at different scan rates from 0.1 to 10 mV s^{-1}.

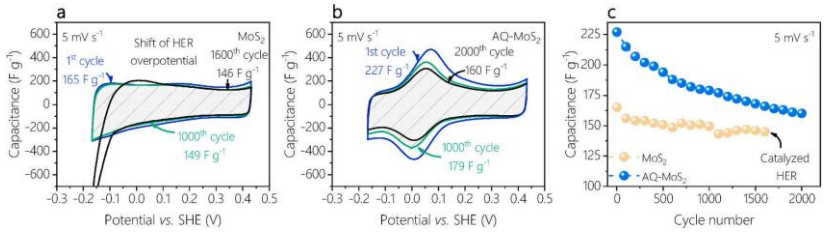

Fig. 11. Cycle-life test of the electrode performed using cycling voltammetry at 5 mV s^{-1} scan rate in 1 M H_2SO_4 aqueous system. Cyclic voltammetry data for (a) MoS_2, and (b) AQ-MoS_2 recorded at different cycle, i.e., 1st, 1000th and 2000th cycle. (c) Electrode capacitance fade over cycle number.

allowed for an improvement of the total specific energy of the hybrid system over symmetric cells. Tests in low pH salt electrolyte (1 M $BeSO_4$) also revealed redox activity of anthraquinone molecules, but at higher charge/discharge rates, a gradual decrease of capacitance is observed mainly due to the diffusion issues connected with the high solvation ionic radius of the Be^{2+} cation. The redox activity of anthraquinone molecules was also confirmed in an organic medium in 1 M $LiPF_6$ (EC:DMC 1:1 v/v), together with the pseudocapacitive behavior of MoS_2.

These findings could open new possibilities for designing advanced 2D energy storage materials.

CRediT authorship contribution statement

Maciej Tobis: Writing – original draft, Methodology, Investigation, Funding acquisition, Conceptualization. **Elżbieta Frąckowiak:** Writing – review & editing, Supervision, Conceptualization.

Declaration of competing interest

The authors declare that they have no known competing financial interests or personal relationships that could have appeared to influence the work reported in this paper.

Data availability

Data will be made available on request.

Acknowledgements

We would like to acknowledge National Science Centre, Poland, for the financial support in the frame of the project Preludium 20 2021/41/N/ST5/01364. We would like to thank prof. Miroslawa Pawlyta from Silesian University of Technology for performing TEM analysis.

Appendix A. Supplementary data

Supplementary data to this article can be found online at https://doi.org/10.1016/j.jpowsour.2024.234862.

References

[1] M.R. Lukatskaya, S. Kota, Z. Lin, M.-Q. Zhao, N. Shpigel, M.D. Levi, J. Halim, P.-L. Taberna, M.W. Barsoum, P. Simon, Y. Gogotsi, Ultra-high-rate pseudocapacitive energy storage in two-dimensional transition metal carbides, Nat. Energy 2 (8) (2017) 17105–17112, https://doi.org/10.1038/nenergy.2017.105.
[2] P. Simon, Y. Gogotsi, Perspectives for electrochemical capacitors and related devices, Nat. Mater. 19 (11) (2020) 1151–1163, https://doi.org/10.1038/s41563-020-0747-z.
[3] M.F. Koudahi, E. Frackowiak, Fast response supercapacitor based on carbon-VS_2 electrodes with a wide operating voltage range, Energy Storage Mater. 49 (2022) 255–267, https://doi.org/10.1016/j.ensm.2022.04.021.
[4] K. Leng, Z. Chen, X. Zhao, W. Tang, B. Tian, C.T. Nai, W. Zhou, K.P. Loh, Phase restructuring in transition metal dichalcogenides for highly stable energy storage, ACS Nano 10 (10) (2016) 9208–9215, https://doi.org/10.1021/acsnano.6b05746.
[5] Y. Zhu, L. Peng, D. Chen, G. Yu, Intercalation pseudocapacitance in ultrathin $VOPO_4$ nanosheets: toward high-rate Alkali-ion-based electrochemical energy storage, Nano Lett. 16 (1) (2016) 742–747, https://doi.org/10.1021/acs.nanolett.5b04610.
[6] V. Augustyn, J. Come, M.A. Lowe, J.W. Kim, P.-L. Taberna, S.H. Tolbert, H. D. Abruña, P. Simon, B. Dunn, High-rate electrochemical energy storage through Li^+ intercalation pseudocapacitance, Nat. Mater. 12 (6) (2013) 518–522, https://doi.org/10.1038/nmat3601.
[7] M. Acerce, D. Voiry, M. Chhowalla, Metallic 1T phase MoS_2 nanosheets as supercapacitor electrode materials, Nat. Nanotechnol. 10 (4) (2015) 313–318, https://doi.org/10.1038/nnano.2015.40.
[8] M. Chhowalla, H.S. Shin, G. Eda, L.-J. Li, K.P. Loh, H. Zhang, The chemistry of two-dimensional layered transition metal dichalcogenide nanosheets, Nat. Chem. 5 (4) (2013) 263–275, https://doi.org/10.1038/nchem.1589.
[9] B. Zhang, X. Ji, K. Xu, C. Chen, X. Xiong, J. Xiong, Y. Yao, L. Miao, J. Jiang, Unraveling the different charge storage mechanism in T and H phases of MoS_2, Electrochim. Acta 217 (2016) 1–8, https://doi.org/10.1016/j.electacta.2016.09.059.
[10] M.A. Bissett, S.D. Worrall, I.A. Kinloch, R.A.W. Dryfe, Comparison of two-dimensional transition metal dichalcogenides for electrochemical supercapacitors, Electrochim. Acta 201 (2016) 30–37, https://doi.org/10.1016/j.electacta.2016.03.190.
[11] X. Yu, S. Yun, J.S. Yeon, P. Bhattacharya, L. Wang, S.W. Lee, X. Hu, H.S. Park, Emergent pseudocapacitance of 2D nanomaterials, Adv. Energy Mater. 8 (13) (2018) 1702930, https://doi.org/10.1002/aenm.201702930.
[12] C. Costentin, J.-M. Savéant, Energy storage: pseudocapacitance in prospect, Chem. Sci. 1 (22) (2019) 5656–5666, https://doi.org/10.1039/C9SC01662G.
[13] S. Fleischmann, J.B. Mitchell, R. Wang, C. Zhan, D.-e. Jiang, V. Presser, V. Augustyn, Pseudocapacitance: from fundamental understanding to high power energy storage materials, Chem. Rev. 120 (14) (2020) 6738–6782, https://doi.org/10.1021/acs.chemrev.0c00170.
[14] Z. Liang, C. Zhao, W. Zhao, Y. Zhang, P. Srimuk, V. Presser, G. Feng, Molecular understanding of charge storage in MoS_2 supercapacitors with ionic liquids, Energy Environ. Mater. 4 (4) (2021) 631–637, https://doi.org/10.1002/eem2.12147.
[15] B. Hinnemann, P.G. Moses, J. Bonde, K.P. Jørgensen, J.H. Nielsen, S. Horch, I. Chorkendorff, J.K. Nørskov, Biomimetic hydrogen evolution: MoS_2 nanoparticles as catalyst for hydrogen evolution, J. Am. Chem. Soc. 127 (15) (2005) 5308–5309, https://doi.org/10.1021/ja0504690.
[16] G. Li, D. Zhang, Q. Qiao, Y. Yu, D. Peterson, A. Zafar, R. Kumar, S. Curtarolo, F. Hunte, S. Shannon, Y. Zhu, W. Yang, L. Cao, All the catalytic active sites of MoS_2 for hydrogen evolution, J. Am. Chem. Soc. 138 (51) (2016) 16632–16638, https://doi.org/10.1021/jacs.6b05940.
[17] M. Tobis, S. Sroka, E. Frackowiak, Supercapacitor with carbon/MoS_2 composites, Front. Energy Res. 9 (2021), https://doi.org/10.3389/fenrg.2021.647878.
[18] E. Frąckowiak, M. Foroutan Koudahi, M. Tobis, Electrochemical capacitor performance of nanotextured carbon/transition metal dichalcogenides composites, Small 17 (48) (2021) 2170255, https://doi.org/10.1002/smll.202006821.
[19] X. Zhu, H. Qiu, Y. Zhang, Z. Man, W. Li, N. Bao, G. Wu, Vertical-aligned and ordered-active architecture of heterostructured fibers for high electrochemical capacitance, Adv. Fiber Mater. 6 (2024) 312–328, https://doi.org/10.1007/s42765-023-00349-6.
[20] X. Chen, J. Ding, J. Jiang, G. Zhang, Z. Zhang, P. Yang, Preparation of a MoS_2/carbon nanotube composite as an electrode material for high-performance supercapacitors, RSC Adv. 8 (2018) 29488–29494, https://doi.org/10.1039/c8ra05158e.
[21] Q. Weng, X. Wang, X. Wang, C. Zhang, X. Jiang, Y. Bando, D. Golberg, Supercapacitive energy storage performance of molybdenum disulfide nanosheets wrapped with microporous carbons, J. Mater. Chem. A 3 (2015) 3097–3102, https://doi.org/10.1039/C4TA06303A.
[22] H. Yu, G. Jiang, J. Ni, L. Li, Architecting core-shell nanosheets of MoS_2-polypyrrole on carbon cloth as a robust sodium anode, Sustain. Mater. Technol. 28 (2021) e00255, https://doi.org/10.1016/j.susmat.2021.e00255.
[23] L. Daukiya, J. Teyssandier, S. Eyley, S. El Kazzi, M.C. Rodríguez González, B. Pradhan, W. Thielemans, J. Hofkens, S. De Feyter, Covalent functionalization of molybdenum disulfide by chemically activated diazonium salts, Nanoscale 13 (5) (2021) 2972–2981, https://doi.org/10.1039/D0NR07310E.
[24] R. Canton-Vitoria, Y. Sayed-Ahmad-Baraza, M. Pelaez-Fernandez, R. Arenal, C. Bittencourt, C.P. Ewels, N. Tagmatarchis, Functionalization of MoS_2 with 1,2-dithiolanes: toward donor-acceptor nanohybrids for energy conversion, NPJ 2D Mater. Appl. 1 (1) (2017) 1–9, https://doi.org/10.1038/s41699-017-0012-8.
[25] K.C. Knirsch, N.C. Berner, H.C. Nerl, C.S. Cucinotta, Z. Gholamvand, N. McEvoy, Z. Wang, I. Abramovic, P. Vecera, M. Halik, S. Sanvito, G.S. Duesberg, V. Nicolosi, F. Hauke, A. Hirsch, J.N. Coleman, C. Backes, Basal-plane functionalization of chemically exfoliated molybdenum disulfide by diazonium salts, ACS Nano 9 (6) (2015) 6018–6030, https://doi.org/10.1021/acsnano.5b00965.
[26] M. Vázquez Sulleiro, A. Develioglu, R. Quirós-Ovies, L. Martín-Pérez, N. Martín Sabanés, M.L. Gonzalez-Juarez, I.J. Gómez, M. Vera-Hidalgo, V. Sebastián, J. Santamaría, E. Burzurí, E.M. Pérez, Fabrication of devices featuring covalently linked MoS_2–graphene heterostructures, Nat. Chem. 14 (6) (2022) 695–700, https://doi.org/10.1038/s41557-022-00924-1.
[27] D. Voiry, A. Goswami, R. Kappera, C.d.C.C. e Silva, D. Kaplan, T. Fujita, M. Chen, T. Asefa, M. Chhowalla, Covalent functionalization of monolayered transition metal dichalcogenides by phase engineering, Nat. Chem. 7 (1) (2015) 45–49, https://doi.org/10.1038/nchem.2108.
[28] X. Chen, A.R. McDonald, Functionalization of two-dimensional transition-metal dichalcogenides, Adv. Mater. 28 (27) (2016) 5738–5746, https://doi.org/10.1002/adma.201505345.
[29] D.O. Li, X.S. Chu, Q.H. Wang, Reaction kinetics for the covalent functionalization of two-dimensional MoS_2 by aryl diazonium salts, Langmuir 35 (17) (2019) 5693–5701, https://doi.org/10.1021/acs.langmuir.8b04288.
[30] Y. Zhuo, I.A. Kinloch, M.A. Bissett, Simultaneous electrochemical exfoliation and functionalization of 2H-MoS_2 for supercapacitor electrodes, ACS Appl. Nano Mater. 6 (19) (2023) 18062–18070, https://doi.org/10.1021/acsanm.3c03322.
[31] Z. Algharaibeh, P.G. Pickup, An asymmetric supercapacitor with anthraquinone and dihydroxybenzene modified carbon fabric electrodes, Electrochem. Commun. 13 (2011) 147–149, https://doi.org/10.1016/j.elecom.2010.11.036.
[32] K. Kalinathan, D.P. DesRoches, X. Liu, P.G. Pickup, Anthraquinone modified carbon fabric supercapacitors with improved energy and power densities, J. Power Sources 181 (2008) 182–185, https://doi.org/10.1016/j.jpowsour.2008.03.032.
[33] A. Le Comte, T. Brousse, D. Bélanger, Chloroanthraquinone as a grafted probe molecule to investigate grafting yield on carbon powder, Electrochim. Acta 197 (2016) 139–145, https://doi.org/10.1016/j.electacta.2016.01.219.
[34] A. Sarapuu, K. Vaik, D.J. Schiffrin, K. Tammeveski, Electrochemical reduction of oxygen on anthraquinone-modified glassy carbon electrodes in alkaline solution, J. Electroanal. Chem. 541 (2003) 23–29, https://doi.org/10.1016/S0022-0728(02)01311-6.
[35] E. Lebègue, C. Benoit, T. Brousse, J. Gaubicher, C. Cougnon, Effect of the porous texture of activated carbons on the electrochemical properties of molecule-grafted carbon products in organic media, J. Electrochem. Soc. 162 (2015) A2289–A2295, https://doi.org/10.1149/2.0481512jes.
[36] T. Brousse, C. Cougnon, D. Bélanger, Grafting of quinones on carbons as active electrode materials in electrochemical capacitors, J. Braz. Chem. Soc. 29 (5) (2018) 989–997, https://doi.org/10.21577/0103-5053.20180015.
[37] P. Allongue, M. Delamar, B. Desbat, O. Fagebaume, R. Hitmi, J. Pinson, J.-M. Savéant, Covalent modification of carbon surfaces by aryl radicals generated

from the electrochemical reduction of diazonium salts, J. Am. Chem. Soc. 119 (1) (1997) 201–207, https://doi.org/10.1021/ja963354s.
[38] A. Jaffe, A. Saldivar Valdes, H.I. Karunadasa, Quinone-functionalized carbon black cathodes for lithium batteries with high power densities, Chem. Mater. 27 (10) (2015) 3568–3571, https://doi.org/10.1021/acs.chemmater.5b00990.
[39] Y. Wu, R. Zeng, J. Nan, D. Shu, Y. Qiu, S.L. Chou, Quinone electrode materials for rechargeable lithium/sodium ion batteries, Adv. Energy Mater. 7 (24) (2017) 1700278, https://doi.org/10.1002/aenm.201700278.
[40] J.E. Bachman, L.A. Curtiss, R.S. Assary, Investigation of the redox chemistry of anthraquinone derivatives using density functional theory, J. Phys. Chem. 118 (38) (2014) 8852–8860, https://doi.org/10.1021/jp5060777.
[41] M. Jaugstetter, N. Blanc, M. Kratz, K. Tschulik, Electrochemistry under confinement, Chem. Soc. Rev. 51 (7) (2022) 2491–2543, https://doi.org/10.1039/D1CS00789K.
[42] T. Stephenson, Z. Li, B. Olsen, D. Mitlin, Lithium ion battery applications of molybdenum disulfide (MoS_2) nanocomposites, Energy Environ. Sci. 7 (1) (2014) 209–231, https://doi.org/10.1039/C3EE42591F.
[43] J.B. Cook, T.C. Lin, H.-S. Kim, A. Siordia, B.S. Dunn, S.H. Tolbert, Suppression of electrochemically driven phase transitions in nanostructured MoS_2 pseudocapacitors probed using operando X-ray diffraction, ACS Nano 13 (2) (2019) 1223–1231, https://doi.org/10.1021/acsnano.8b06381.
[44] J.B. Cook, H.S. Kim, T.C. Lin, C.H. Lai, B. Dunn, S.H. Tolbert, Pseudocapacitive charge storage in thick composite MoS_2 nanocrystal-based electrodes, Adv. Energy Mater. 7 (2) (2017), https://doi.org/10.1002/aenm.201601283 n/a.
[45] A. Jawaid, D. Nepal, K. Park, M. Jespersen, A. Qualley, P. Mirau, L.F. Drummy, R. A. Vaia, Mechanism for liquid phase exfoliation of MoS_2, Chem. Mater. 28 (1) (2016) 337–348, https://doi.org/10.1021/acs.chemmater.5b04224.
[46] M. Thommes, K. Kaneko, A.V. Neimark, J.P. Olivier, F. Rodriguez-Reinoso, J. Rouquerol, K.S.W. Sing, Physisorption of gases, with special reference to the evaluation of surface area and pore size distribution (IUPAC Technical Report), Pure Appl. Chem. 87 (9) (2015) 1051–1069, https://doi.org/10.1515/pac-2014-1117.
[47] B. Gorska, P. Ratajczak, F. Béguin, Faradaic processes on quinone-grafted carbons in protic ionic liquid electrolyte, Electrochim. Acta 328 (2019) 135090, https://doi.org/10.1016/j.electacta.2019.135090.
[48] H. Li, Q. Zhang, C.C.R. Yap, B.K. Tay, T.H.T. Edwin, A. Olivier, D. Baillargeat, From bulk to monolayer MoS_2: evolution of Raman scattering, Adv. Funct. Mater. 22 (7) (2012) 1385–1390, https://doi.org/10.1002/adfm.201102111.
[49] F. Béguin, V. Presser, A. Balducci, E. Frackowiak, Carbons and electrolytes for advanced supercapacitors, Adv. Mater. 26 (14) (2014) 2219–2251, https://doi.org/10.1002/adma.201304137.
[50] M. Mohan, N.P. Shetti, T.M. Aminabhavi, Phase dependent performance of MoS_2 for supercapacitor applications, J. Energy Storage 58 (2023) 106321, https://doi.org/10.1016/j.est.2022.106321.
[51] G. Pognon, T. Brousse, L. Demarconnay, D. Bélanger, Performance and stability of electrochemical capacitor based on anthraquinone modified activated carbon, J. Power Sources 196 (8) (2011) 4117–4122, https://doi.org/10.1016/j.jpowsour.2010.09.097.
[52] K. Brousse, C. Martin, A.L. Brisse, C. Lethien, P. Simon, P.L. Taberna, T. Brousse, Anthraquinone modification of microporous carbide derived carbon films for on-chip micro-supercapacitors applications, Electrochim. Acta 246 (2017) 391–398, https://doi.org/10.1016/j.electacta.2017.06.037.
[53] J.M. Soon, K.P. Loh, Electrochemical double-layer capacitance of MoS_2 nanowall films, Electrochem. Solid State Lett. 10 (11) (2007) A250, https://doi.org/10.1149/1.2778851.
[54] E. Pameté Yambou, B. Gorska, P. Ratajczak, F. Béguin, Hybrid capacitor with anthraquinone-grafted carbon as a battery-type electrode operating in a low pH aqueous salt solution, J. Mater. Chem. A 8 (27) (2020) 13548–13557, https://doi.org/10.1039/D0TA03158E.
[55] H. Lindström, S. Södergren, A. Solbrand, H. Rensmo, J. Hjelm, A. Hagfeldt, S.-E. Lindquist, Li^+ ion insertion in TiO2 (Anatase). 2. Voltammetry on nanoporous films, J. Phys. Chem. B 101 (39) (1997) 7717–7722, https://doi.org/10.1021/jp970490q.
[56] P. Daum, J.R. Lenhard, D. Rolison, R.W. Murray, Diffusional charge transport through ultrathin films of radiofrequency plasma polymerized vinylferrocene at low temperature, J. Am. Chem. Soc. 102 (14) (1980) 4649–4653, https://doi.org/10.1021/ja00534a014.
[57] J.S. Ko, C.-H. Lai, J.W. Long, D.R. Rolison, B. Dunn, J. Nelson Weker, Differentiating double-layer, psuedocapacitance, and battery-like mechanisms by analyzing impedance measurements in three dimensions, ACS Appl. Mater. Interfaces 12 (12) (2020) 14071–14078, https://doi.org/10.1021/acsami.0c02020.
[58] G. Shul, D. Bélanger, Self-discharge of electrochemical capacitors based on soluble or grafted quinone, Phys. Chem. Chem. Phys. 18 (2016) 19137–19145, https://doi.org/10.1039/c6cp02356h.
[59] A. Hattab, Z. Dhaouadi, S. Lahmar, A. Malloum, J. Jules Fifen, N. Russo, M. Toscano, Beryllium ion coordination in Ammonia, methanol and water solvents, J. Mol. Liq. 360 (2022) 119414, https://doi.org/10.1016/j.molliq.2022.119414.
[60] E.H. James, Chapter 11 - chemistry of metallic elements, in: E.H. James (Ed.), Inorganic Chemistry, third ed., Academic Press, 2020, pp. 395–444.
[61] X. Zhu, Y. Zhang, Z. Man, W. Lu, W. Chen, J. Xu, N. Bao, W. Chen, G. Wu, Microfluidic-assembled covalent OrganicFrameworks@$Ti_3C_2T_x$MXene vertical fibers for high-performance electrochemical supercapacitors, Adv. Mater. 35 (2023) 2307186, https://doi.org/10.1002/adma.202307186.
[62] X. Fang, C. Hua, X. Guo, Y. Hu, Z. Wang, X. Gao, F. Wu, J. Wang, L. Chen, Lithium storage in commercial MoS_2 in different potential ranges, Electrochim. Acta 81 (2012) 155–160, https://doi.org/10.1016/j.electacta.2012.07.020.
[63] J.B. Cook, H.-S. Kim, Y. Yan, J.S. Ko, S. Robbennolt, B. Dunn, S.H. Tolbert, Mesoporous MoS_2 as a transition metal dichalcogenide exhibiting pseudocapacitive Li and Na-ion charge storage, Adv. Energy Mater. 6 (2016) 1501937, https://doi.org/10.1002/aenm.201501937.
[64] I.S. Kwon, I.H. Kwak, H.G. Abbas, G. Jung, Y. Lee, J. Park, S.J. Yoo, J.-G. Kim, H. S. Kang, Intercalation of aromatic amine for the 2H–1T′ phase transition of MoS_2 by experiments and calculations, Nanoscale 10 (2018) 11349–11356, https://doi.org/10.1039/c8nr02365d.
[65] H. Yu, Z. Wang, J. Ni, L. Li, Freestanding nanosheets of 1T-2H hybrid MoS_2 as electrodes for efficient sodium storage, J. Mater. Sci. Technol. 67 (2011) 237–242, https://doi.org/10.1016/j.jmst.2020.08.030.
[66] H.D. Yoo, Y. Li, Y. Liang, Y. Lan, F. Wang, Y. Yao, Intercalation pseudocapacitance of exfoliated molybdenum disulfide for ultrafast energy storage, ChemNanoMat : chemistry of nanomaterials for energy, biology and more 2 (7) (2016) 688–691, https://doi.org/10.1002/cnma.201600117.
[67] X. Guo, E. Song, W. Zhao, S. Xu, W. Zhao, Y. Lei, Y. Fang, J. Liu, F. Huang, Charge self-regulation in 1T‴-MoS_2 structure with rich S vacancies for enhanced hydrogen evolution activity, Nat. Commun. 13 (1) (2022), https://doi.org/10.1038/s41467-022-33636-8, 5954-5954.

Chapter V

Emergence of pseudocapacitive properties of 2D materials

5. *Controlling structure and morphology of MoS_2 via sulfur precursor for optimized pseudocapacitive lithium intercalation hosts*

Authors: Maciej Tobis, Mennatalla Elmanzalawy, Jaehoon Choi, Elżbieta Frąckowiak, Simon Fleischmann

Journal: publicly accessible as a preprint, sent for review

DOI: https://doi.org/10.26434/chemrxiv-2024-7hz4h

License: The content is available under CC BY 4.0

Contribution: Conceptualization, investigation, methodology, data curation, funding acquisition, writing (original draft)

Author notes: Results presented in this chapter were originally obtained during scientific internship in *Helmholtz Institute Ulm*, Germany. Data presented here are complementary to the dissertation topic and consist of additional outcomes.

Graphical abstract

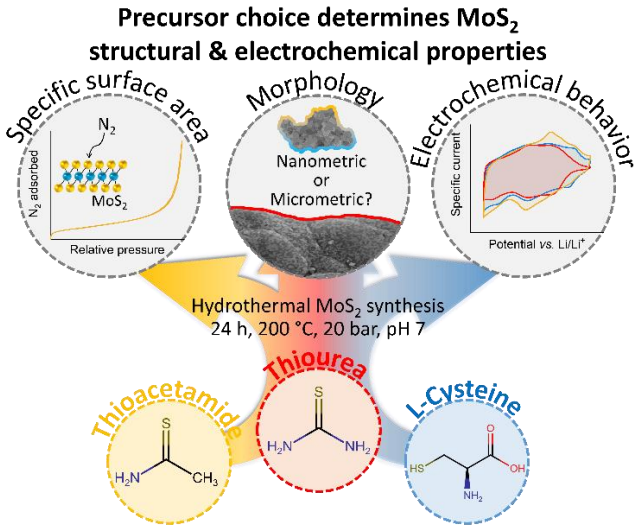

Context of research & summary

Traditional battery materials often face kinetic limitations of charge storage, which impede the realization of the fast charging/discharging devices. MoS_2 with its layered structure shows emergence of the pseudocapacitive intercalation of ions

in organic media upon nanosizing the particle size. Nanosized particles enable faster ion transport in the crystal lattice of the host material due to shortened diffusion ion path.

Hydrothermal synthesis is an effective method for producing nanostructured MoS_2, offering significant control over the material's properties. **This study presents unpublished data** on how different sulfur precursors – thiourea (TU), thioacetamide – (TAA), and L-cysteine (LC) – used during hydrothermal synthesis affect the resultant MoS_2 structure, morphology, and lithium intercalation properties. By systematic evaluation of these effects, this study focuses on clear understanding of the relationship between synthesis conditions and the electrochemical behavior of MoS_2. This knowledge is essential for designing MoS_2-based electrodes that can deliver superior performance in terms of energy density, power density, and cycling stability, thereby contributing to the development of next-generation energy storage devices.

The resulting MoS_2 materials were characterized using scanning electron microscopy (SEM), transmission electron microscopy (TEM), X-ray diffraction (XRD), and Raman spectroscopy. These techniques revealed significant differences in the morphology and crystallite size of MoS_2 depending on the sulfur precursor used. MoS_2 synthesized with TU showed larger, micron-sized architectures, while TAA and LC precursors produced nanosized flakes with higher specific surface area and increased porosity.

The electrochemical properties of the synthesized MoS_2 were evaluated through lithium intercalation experiments and compared to the commercial, bulk MoS_2 (Comm). These experiments, conducted in the 1 to 3 V *vs.* Li/Li^+ potential range, allowed for studying the electrochemical intercalation reaction. MoS_2 synthesized with TAA and LC exhibited improved capacity and superior capacity retention up to ca. 100 mAh g^{-1} at 10 A g^{-1} compared to those synthesized with TU (60 mAh g^{-1}) and commercial MoS_2 (20 mAh g^{-1}). The nanosized flakes from TAA and LC precursors provided a larger electrode/electrolyte interface area, which facilitated faster lithium ion transport and improved intercalation kinetics. Techniques such as o*perando* X-ray diffraction, *operando* dilatometric height change and 3D Bode plot analyses allowed detailed studies of the charge storage mechanism.

In conclusion, selecting appropriate precursors it is possible to produce nanostructured MoS_2 with optimized pseudocapacitive performance. These findings offer valuable insights for designing and development of advanced MoS_2-based electrode materials for high-performance energy storage devices.

Additional results

5. *Controlling structure and morphology of MoS_2 via sulfur precursor for optimized pseudocapacitive lithium intercalation hosts*

Research Article

Controlling structure and morphology of MoS_2 via sulfur precursor for optimized pseudocapacitive lithium intercalation hosts

Maciej Tobis,[1,2,3] Mennatalla Elmanzalawy,[2,3] Jaehoon Choi,[2,3]

Elżbieta Frąckowiak,[1*] Simon Fleischmann,[2,3*]

[1] Poznan University of Technology (PUT), Poznan 60965, Poland

[2] Helmholtz Institute Ulm (HIU), Ulm 89081, Germany

[3] Karlsruhe Institute of Technology (KIT), Karlsruhe 76021, Germany

* Corresponding authors' emails: simon.fleischmann@kit.edu; elzbieta.frackowiak@put.poznan.pl

Abstract

Molybdenum disulfide (MoS_2)-based electrode materials can exhibit a pseudocapacitive charge storage mechanism induced by nanosized dimension of the crystalline domains. This effect is achievable through hydrothermal synthesis of MoS_2, which often yields different properties of the final material, thereby affecting its electrochemical lithium intercalation behavior. In this study, we investigate how the use of different sulfide precursors, specifically thiourea (TU), thioacetamide (TAA), and L-cysteine (LC), during the hydrothermal synthesis of MoS_2, affects its physicochemical, and consequently, electrochemical properties. The three materials obtained exhibit distinct morphologies, ranging from micron-sized architectures (MoS_2 TU), to nanosized flakes (MoS_2 TAA and LC), which influence their available specific surface area and tortuosity. Consequently, the choice of hydrothermal synthesis parameters allows to control the resulting electrochemical signature. The individual charge storage properties are analyzed by operando X-ray diffraction, dilatometry, and 3D Bode analysis, revealing a correlation between the morphology, porosity, and the electrochemical intercalation behavior of the obtained electrode materials. The results demonstrate a facile strategy to control MoS_2 structure and related functionality by choice of hydrothermal synthesis precursors.

https://doi.org/10.26434/chemrxiv-2024-7hz4h **ORCID:** https://orcid.org/0000-0001-9475-3692 Content not peer-reviewed by ChemRxiv. **License:** CC BY 4.0

1. Introduction

Molybdenum disulfide (MoS_2) is among the most studied transition metal dichalcogenides, a family of materials characterized by their two-dimensional character with individual layers stacked by van der Waals forces[1]. MoS_2 has gained attention due to its applicability in a wide range of fields like electrochemical energy storage[2, 3] and electrocatalysis[4, 5]. There are several polytypes of MoS_2, with the naturally occurring, semiconducting 2H-MoS_2 and 3R-MoS_2 polytypes, and the synthetically accessible, metallic 1T-MoS_2[6]. The functional properties of MoS_2 are highly dependent on the polytype, as well as on the morphology and crystallite size of the material, which is why synthesis strategies able to control these properties are required[7, 8].

In the field of electrochemical energy storage, MoS_2 has been employed as an anode material suitable for lithium and sodium ion storage, with the possibility to store charge via electrochemical intercalation and/or conversion reactions, depending on the utilized voltage window[9-12]. When used as an intercalation host, it was found that kinetically favorable intercalation properties are obtained when MoS_2 crystallite size is reduced[13]. For such nanosized MoS_2, Cook et al. report the emergence of solid-solution intercalation with pseudocapacitive properties, that is, Faradaic charge storage with a capacitor-like signature over a wide voltage range in absence of kinetic diffusion limitations[13, 14]. It was also found that the introduction of crystal defects, as well as the increase of the MoS_2 d-spacing via hexanediamine pillars amplifies the pseudocapacitive electrochemical lithiation response[15, 16]. For 2H-MoS_2, an irreversible transition to 1T-MoS_2 during the first electrochemical lithiation cycle at around 1.1 V *vs.* Li^+/Li leads to an unfavorably low initial Coulombic efficiency[17]. The findings underline the significance of controlling MoS_2 crystal structure, crystallite size, and morphology, to obtain desired functional properties.

Not only electrochemical charge storage, but also the electrocatalytic hydrogen evolution (HER) performance is dependent on MoS_2 crystal structure and morphology[18]. This led to the exploration of various hydrothermal synthesis routes controlling MoS_2 structure by choice of sulfur-precursor[19-22]. Liu et al. found that thioacetamide (TAA) and L-cysteine (LC) possess lower decomposition temperatures than thiourea (TU), thereby releasing sulfur more readily, leading to smaller particle sizes and the tendency to form the 1T-polytype, which in turn, leads to a favorable HER activity[23].

https://doi.org/10.26434/chemrxiv-2024-7hz4h **ORCID:** https://orcid.org/0000-0001-9475-3692 Content not peer-reviewed by ChemRxiv. **License:** CC BY 4.0

The findings motivated us to explore the impact of sulfur precursors on the electrochemical lithium intercalation performance of hydrothermally synthesized MoS_2 materials. Given the relative ease and scalability of hydrothermal synthesis over synthesis routes like vapor deposition or thermal conversion of molybdenum oxides in sulfidizing atmospheres, gaining better understanding of the relation between hydrothermal synthesis route, MoS_2 microstructure and the electrochemical performance are crucial to further develop MoS_2 as a promising electrode material in (pseudocapacitive) ion intercalation hosts.

In this study, we highlight the role of sulfur precursor selection in the hydrothermal synthesis of MoS_2 materials, showing its profound influence on their final structural, morphological, and porous texture characteristics. The choice of the precursor dictates the morphology of MoS_2 with secondary particle size ranging from micro- to nano-sized dimensions, consequently impacting the available interfacial area. The resulting physicochemical properties of the synthesized MoS_2 are linked with their electrochemical response, revealing emergence of pseudocapacitive intercalation phenomena upon nanostructuring. Lithiation kinetics of MoS_2 with improved values of capacity at higher currents are linked with greater electrode/electrolyte interface area. Comprehensive analyses, employing techniques such as *operando* XRD, 3D Bode plot analysis, and dilatometric studies reveal solid-solution charge storage mechanism induced by the nanostructured particle size dimensions and different electrode volume change upon de/lithiation. The insights of the study can guide synthesis development of MoS_2-based materials for application in electrochemical energy storage, conversion, and beyond.

https://doi.org/10.26434/chemrxiv-2024-7hz4h **ORCID:** https://orcid.org/0000-0001-9475-3692 Content not peer-reviewed by ChemRxiv. **License:** CC BY 4.0

2. Experimental section

2.1. Materials synthesis

Different nanostructured molybdenum disulfides (MoS_2) were prepared during separate hydrothermal reactions using 1.6 g of sulfur source, i.e., thiourea (Sigma Aldrich, 99%), thioacetamide (Sigma Aldrich, 99%), or L-cysteine (Sigma Aldrich, 97%) and 1.6 g of sodium molybdate (Sigma Aldrich, 98%). Both precursors were dissolved together in 160 ml of deionized water and the pH of the solution was adjusted to 7 with the use of 1 M hydrochloric acid (POCH S.A). Hydrothermal syntheses were conducted in hydrothermal reactor (Parr 5500 HP) with stirring at 200 rpm during 24 h at 200 °C with 20 bar of internal pressure. After the reaction, black precipitate was collected through vacuum filtration and washing with aliquots of deionized water and ethanol. Powder materials were dried at 80 °C overnight. Micrometric-sized MoS_2 was purchased from Sigma-Aldrich (particle size below 2 µm, 99 %).

2.2. Physicochemical characterization

A Crossbeam x340 (Zeiss) scanning electron microscope (SEM) was used to analyze the morphology of the samples at different magnifications using 5 kV acceleration voltage. Transmission electron microscopy (TEM) analysis was performed using a Talos F200i microscope (Thermo Fisher Scientific) operating at 80 kV. Samples were prepared through sonication in ethanol and deposition on a lacey carbon-coated copper TEM grid by drop-casting. Powder X-ray diffraction (XRD) patterns of the MoS_2 materials were obtained by using a Bruker D8 Advance diffractometer operating in Bragg-Brentano geometry with a Cu Kα radiation source (λ = 1.5406 Å). Raman spectroscopy measurements were obtained by using a Renishaw InVia confocal Raman microscope with a 532 nm laser at a low power of 100 µW. Sorption isotherms of N_2 at 77 K were recorded with the use of ASAP 2460 (Micromeritics, USA). The materials were degassed in a flow of helium at 100 °C for 12 h. Prior the N_2 sorption, the samples were degassed in vacuum for 6 h. Brunauer-Emmett Teller (BET) model was utilized to evaluate the specific surface area (SSA) using 0.01 to 0.05 P/P_0 range. The elemental composition of prepared samples was evaluated by using Thermo Fisher Scientific FlashSmart Elemental Analyzer. The elemental content of C, H, N, S was estimated in the column filled with copper and copper (II) oxide during incineration at 950 °C. Separate pyrolysis of samples at 1060 °C in a column filled with nickel coated carbon was used to estimate the content of O.

https://doi.org/10.26434/chemrxiv-2024-7hz4h **ORCID:** https://orcid.org/0000-0001-9475-3692 Content not peer-reviewed by ChemRxiv. **License:** CC BY 4.0

2.3. Electrochemical cell setup and characterization

2.3.1. Electrode preparation

Electrode slurries consisted of 80 wt.% of active material, 10 wt.% of conductive agent (C65, C-NERGY), and 10 wt.% of binder (polyvinylidene fluoride, PVDF, Solvay) dispersed in a N-Methyl-2-pyrrolidone (NMP, Thermo Scientific). Prior to the mixing, powder components were ground in a mortar to uniform the particles. All constituents were added to a plastic container and transferred to a speed mixer (ARE-250, Thinky) and mixed for 10 min at 10.000 rpm. Electrode slurries were later cast on carbon-coated aluminum foils with a wet thickness of about 60 µm by using a doctor blade. Wet films were dried at 80 °C overnight, followed by punching circular electrodes with a diameter of 12 mm. Such prepared electrodes were further dried at 80 °C under vacuum overnight before being transferred to an argon filled glovebox (MBraun, H_2O and O_2 content below 1 ppm).

2.3.2. Electrochemical studies

Electrochemical behavior of prepared electrodes was examined in a coin cell (CR2032, Hohsen Corp.) configuration employing 14 mm lithium metal disc (Honjo) as the negative electrode separated by a porous membrane (GF/A, Whatman) soaked with 200 µL of LP30 electrolyte (1 M $LiPF_6$ in a 1:1 vol.% mixture of ethylene carbonate/dimethyl carbonate (EC:DMC)). Assembled coin cells were studied by cyclic voltammetry at different sweep rates (from 0.2 to 20 mV s^{-1}), where the measured current is normalized by the active material mass and the sweep rate, resulting in the unit of A s $(V\ g)^{-1}$, allowing for easier estimation of the stored charge at various sweep rates, and galvanostatic charge/discharge at different specific currents (20 mA g^{-1} to 10 A g^{-1}) between 3 - 1 V *vs.* Li/Li^+. Staircase potential-electrochemical impedance spectroscopy (SPEIS) was performed in a frequency range between 1 MHz and 10 mHz in 20 steps, i.e., 100 mV increments between 3 to 1 V *vs.* Li/Li^+, with 10 min chronoamperometric steps between potential increments before each EIS measurement. The impedance was analyzed according to prior work[24], with the real capacitance being calculated according to equation (1):

$$C'(\omega) = -\frac{Z''(\omega)}{\omega|Z(\omega)|^2 m} \quad (1)$$

https://doi.org/10.26434/chemrxiv-2024-7hz4h **ORCID:** https://orcid.org/0000-0001-9475-3692 Content not peer-reviewed by ChemRxiv. **License:** CC BY 4.0

where $C'(\omega)$ is the real part of the capacitance, $Z''(\omega)$ the imaginary part of the impedance, ω the angular frequency ($\omega=2\pi f$, with f as the frequency), $|Z(\omega)|$ is the magnitude of the impedance, and m the electrode active mass. All the electrochemical measurements were performed through a multichannel potentiostat/galvanostat (VMP3, Biologic)

2.3.3. Electrochemical operando XRD measurements

Electrode slurries for operando XRD measurements were prepared as described above, but with a weight ratio of active material to conductive carbon to binder of 7:2:1 in order to ensure sufficient electric conductivity throughout the thicker coating. The slurry was then drop-cast onto Ti mesh, with mass loading of ca. 5 mg cm^{-2}, and left to dry under air circulation, then later under vacuum at 80 °C. Operando XRD patterns were recorded during galvanostatic cycling of the electrodes against Li metal in LP30 electrolyte with a specific current of 50 mA g^{-1}, in a modified coin cell setup with thin Kapton windows on both sides of the coin cell. The diffractograms were obtained using a STOE STADI-p diffractometer in Debye-Scherrer geometry with Mo Kα radiation source (λ=0.70932 Å), equipped with a MYTHEN 1K detector and a STOE coin cell holder. The electrochemical measurements were performed using a potentiostat (SP-300, Biologic).

2.3.4. Electrochemical operando dilatometry measurements

For dilatometry studies, selected electrode materials were prepared in form of self-standing electrodes containing 80 wt.% of active material, 10 wt.% of conductive carbon (C65, C-NERGY), and 10 wt.% of binder (polytetrafluoroethylene – PTFE, 60 wt.% dispersion in water, Sigma Aldrich). Constituents were mixed in 20 ml of isopropanol, grounded in a mortar and mixed until isopropanol has evaporated. After a dough-like consistency has been formed, the material was calendared to obtain a sheet of material with uniform thickness. The sheet was cut into 8 mm diameter discs and subsequently dried at 80 °C overnight under vacuum. Before transferring the electrodes inside the glovebox, the thickness of each electrode was measured (ca. 60 μm). Operando electrochemical dilatometry experiments were performed by using ECD-3-nano electrochemical dilatometer (EL-Cell). The working electrode was separated by a stiff glass frit and a porous membrane (GF/A, Whatman) from a 10 mm lithium disc (Honjo). After assembly, the cell was maintained at OCV for period of 6 h to obtain a stable electrode height measurement. The electrode height change is expressed in a form of percentage

https://doi.org/10.26434/chemrxiv-2024-7hz4h **ORCID:** https://orcid.org/0000-0001-9475-3692 Content not peer-reviewed by ChemRxiv. **License:** CC BY 4.0

calculated from the first measurements. The electrochemically-induced height-changes were evaluated with the dilatometer during galvanostatic charge/discharge at 20 mA g^{-1} between 3 to 1 V *vs.* Li/Li^+. Electrochemical experiments were performed with a multichannel potentiostat/galvanostat (VMP3, Biologic).

https://doi.org/10.26434/chemrxiv-2024-7hz4h **ORCID:** https://orcid.org/0000-0001-9475-3692 Content not peer-reviewed by ChemRxiv. **License:** CC BY 4.0

3. Results and discussion

3.1. Physicochemical characterization

Different MoS_2 materials are synthesized from various sulfur precursors, namely thiourea (TU), thioacetamide (TAA), and L-cysteine (LC), by a hydrothermal approach at the same temperature, time, pH of the solution and precursor mass (**Fig. 1A**). Scanning electron microscopy (SEM) shows that dependent on the type of the precursor, different surface morphologies are obtained (**Fig. 1B-E**). Commercially available MoS_2 (Comm) (**Fig. 1B**) utilized for comparison presents micrometer-sized secondary particles consisting of primary flakes with layered features shown at higher magnifications. In contrast, materials obtained via hydrothermal reactions show different morphologies and particle size distributions dependent on the type of precursor. MoS_2 obtained from TU (**Fig. 1C**) shows tens of microns large structures with bump-like surface features, on which nanosized, perpendicularly oriented flakes are visible. In sharp contrast, MoS_2 obtained from TAA (**Fig. 1D**) and from LC (**Fig. 1E**) show 0.5 – 1 micron-sized secondary particle agglomerates consisting of smaller, below 100 nm sized primary particles. They follow a similar trend as previous reports, with MoS_2 derived from TU precursor yielding the largest secondary particle sizes[23]. The observed differences of the samples show a high dependence of resulting macroscopic MoS_2 structure and morphology from the sulfur precursor employed in the hydrothermal synthesis.

The purity of hydrothermally synthetized samples is analyzed in terms of their elemental composition (**Table 1**) showing comparable formulation to MoS_2 Comm. Often, hydrothermal preparation of MoS_2 using organic precursors leads to formation of some amorphous carbon impurities[25]. In this case, each material shows low content of carbon in comparable quantity to MoS_2 Comm. Lack of nitrogen content in MoS_2 TAA and MoS_2 LC suggests the absence of unreacted precursor residue in the samples, whereas MoS_2 TU shows a small quantity of nitrogen (1.6 wt.%), which was previously reported to increase the interlayer distance of MoS_2[26]. The findings show correlation between the lower decomposition temperatures of TAA and LC compared to TU and the resulting nitrogen impurity content. MoS_2 samples derived from TU and LC show some oxygen residue (ca. 4 wt.%), which can be a consequence of the relatively high precursor decomposition temperature (TU) and/or the high oxygen content of the precursor (LC). The analysis reveals that purity of hydrothermally synthesized MoS_2 samples can be affected to some extent by the choice of sulfur precursor.

https://doi.org/10.26434/chemrxiv-2024-7hz4h **ORCID:** https://orcid.org/0000-0001-9475-3692 Content not peer-reviewed by ChemRxiv. **License:** CC BY 4.0

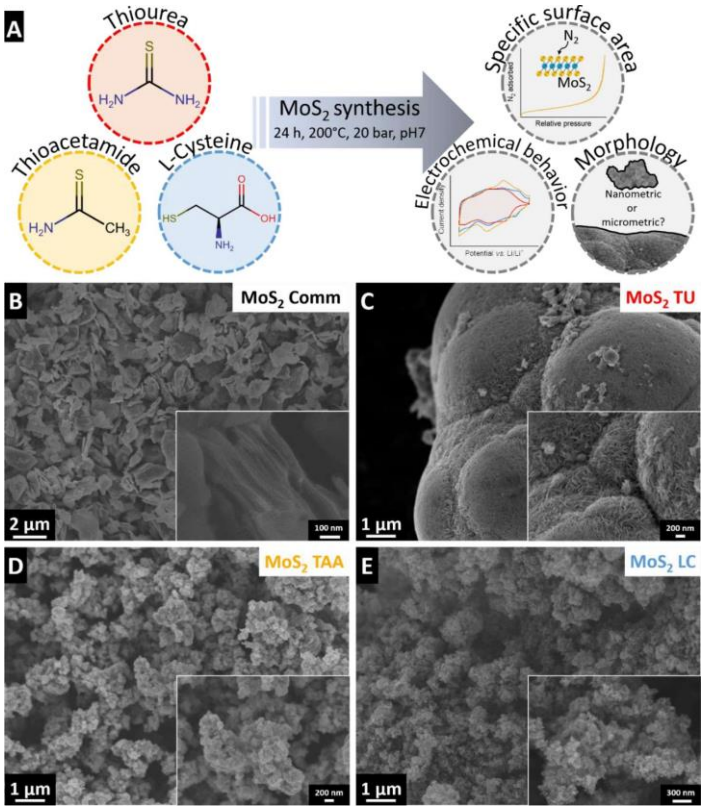

Fig. 1: (A) Schematic illustration of the hydrothermal synthesis of MoS_2 materials from different precursors. Scanning electron micrographs of (B) MoS_2 Comm, (C) MoS_2 TU, (D) MoS_2 TAA, and (E) MoS_2 LC.

Table 1: Elemental composition of prepared materials from CHNSO analysis.

Sample	C (wt.%)	H (wt.%)	N (wt.%)	S (wt.%)	O (wt.%)	Sum (wt.%)
MoS_2 Comm	1.3	0.2	0.0	51.8	0.1	53.4
MoS_2 TU	1.3	0.7	1.6	48.4	3.9	55.8
MoS_2 TAA	0.9	0.3	0.0	52.4	0.8	54.3
MoS_2 LC	2.0	0.5	0.0	46.7	3.8	53.0

https://doi.org/10.26434/chemrxiv-2024-7hz4h **ORCID:** https://orcid.org/0000-0001-9475-3692 Content not peer-reviewed by ChemRxiv. **License:** CC BY 4.0

Investigation of the crystal structure of the formed samples is carried out by powder X-ray diffraction (XRD), presented in **Fig. 2A**. MoS_2 Comm shows sharp and well-defined diffraction peaks corresponding to the crystallographic planes of hexagonal MoS_2 (2H) indexed by ICDD PDF card no. #01-071-9809. Sharp, high intensity diffraction signals indicate large crystallite sizes of MoS_2 Comm. In contrast, hydrothermally prepared MoS_2 samples display broadening of the diffraction peaks indicating reduced crystallite sizes and/or increased structural disorder compared to MoS_2 Comm. The position of the (002) diffraction signal corresponding to the interlayer distance varies depending on the utilized sulfur precursor, with maxima of the broad signals between 2θ values of ca. 11.9 – 13.7°, indicative of average interlayer spacings of the obtained MoS_2 materials between ca. 0.64-0.75 nm, which is above that of commercial MoS_2 Comm at 0.61 nm. The irregular, slightly expanded interlayer spacing measured by XRD does not correlate with the impurity content, since MoS_2 TAA as the sample with most deviation of the interlayer distance from MoS_2 Comm contains least impurities (Table 1). Therefore, the expanded interlayer spacing may be a result of partial water adsorption between the MoS_2 layers, as was observed previously for TAA-derived MoS_2[23]. Diffraction peaks corresponding to the (100), (103), and (110) sets of planes are in comparable position to MoS_2 Comm, indicating that lattice parameter modification resulting from hydrothermal synthesis is mostly limited to the interlayer spacing.

Fig. 2B shows Raman spectra for samples in two different regions corresponding to the 1T (J_1, J_2, J_3 modes) and 2H phases (A_{1g}, E^1_{2g} and E_{1g} modes) of MoS_2, respectively. In case of MoS_2 Comm, distinct peaks positioned at 407 cm^{-1}, 381 cm^{-1}, and 284 cm^{-1} can be assigned to the A_{1g}, E^1_{2g} and E_{1g} modes which are consistent with the characteristic vibrational and stretching modes of 2H phase[27]. Their presence and position are a confirmation of well-defined crystalline domains. Raman spectra of hydrothermally synthesized MoS_2 samples also show the presence of E^1_{2g} and A_{1g} modes, confirming the presence of 2H-MoS_2 in these samples. However, peak broadening and shifting can be observed, specifically for MoS_2 TAA and MoS_2 LC samples. Typically, Raman analysis shows strong relationship between the number of successive layers in the MoS_2 crystallites and position of the A_{1g} and E^1_{2g} modes[27]. Shifts of the peaks are commonly observed when increasing the number of adjacent layers in the crystal unit starting from mono to multilayer (from 385 to 381 cm^{-1} for E^1_{2g} and from 403 to 407 cm^{-1} for A_{1g})[28]. A_{1g} mode corresponding to out-of-plane S atoms vibrations for MoS_2

https://doi.org/10.26434/chemrxiv-2024-7hz4h **ORCID:** https://orcid.org/0000-0001-9475-3692 Content not peer-reviewed by ChemRxiv. **License:** CC BY 4.0

TAA and LC is positioned at 385 cm^{-1}, which suggests multilayer MoS_2, whereas the position of the E^1_{2g} shifts to 403 cm^{-1} suggesting MoS_2 monolayer. Such effect could be the result of the nanostructuring of the MoS_2 TAA and LC crystallites. No shift of A_{1g} mode is observable for MoS_2 TU, showing comparable peak positions to MoS_2 Comm possibly related to the micron-sized particles. At the same time, peaks positioned at 226 cm^{-1} corresponding to the J_2 mode suggest the simultaneous existence of the 1T phase in the hydrothermally synthesized samples. This is in agreement with other works on hydrothermally synthesized MoS_2[29, 30].

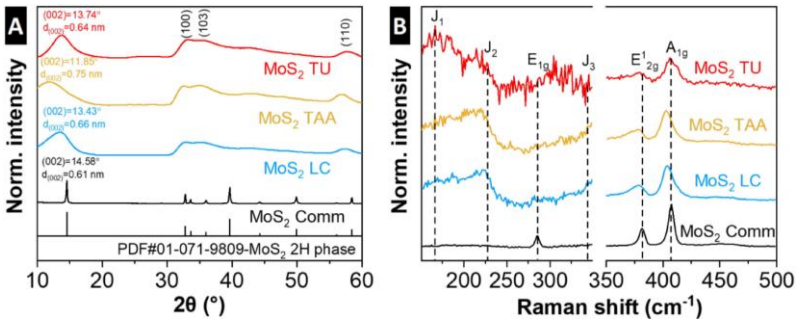

Fig. 2: Physicochemical characterization of MoS_2-based materials. (A) X-ray diffraction patterns and (B) Raman characterization of MoS_2 in 1T and 2H phase regions. In the 1T region (below 350 cm^{-1}), the intensity is multiplied by a factor of 8 for clarity.

Using transmission electron microscopy (TEM) analysis, morphological and crystallographic properties of the hydrothermally synthesized MoS_2 samples are studied at a nanoscale. Morphological features are shown in TEM (**Fig. 3A, C, E**), where all samples exhibit relatively small crystallites with only few MoS_2 layers (in line with broad (002) signal from XRD). The directly measured interlayer distances are closer to the value of ideal 2H-MoS_2 of 0.61 nm (±0.03 nm) for all samples than suggested by the XRD results, which may be a result of volatile interlayer species removal (such as interlayer water) in the microscope (ultra-high vacuum and high-energy electron beam conditions). Utilizing selected area electron diffraction (SAED, **Fig. 3B, D, F**), broad diffraction rings corresponding to the (100) and (110) MoS_2 planes are observed with only small differences of the average lattice parameters between the samples. Overall, TEM investigation reveals that on a nanoscopic level, the crystallite size and shape of MoS_2 domains are more comparable, whereas on a macroscopic level observed by SEM, particle size and/or shape showed stronger differences between these samples.

https://doi.org/10.26434/chemrxiv-2024-7hz4h **ORCID:** https://orcid.org/0000-0001-9475-3692 Content not peer-reviewed by ChemRxiv. **License:** CC BY 4.0

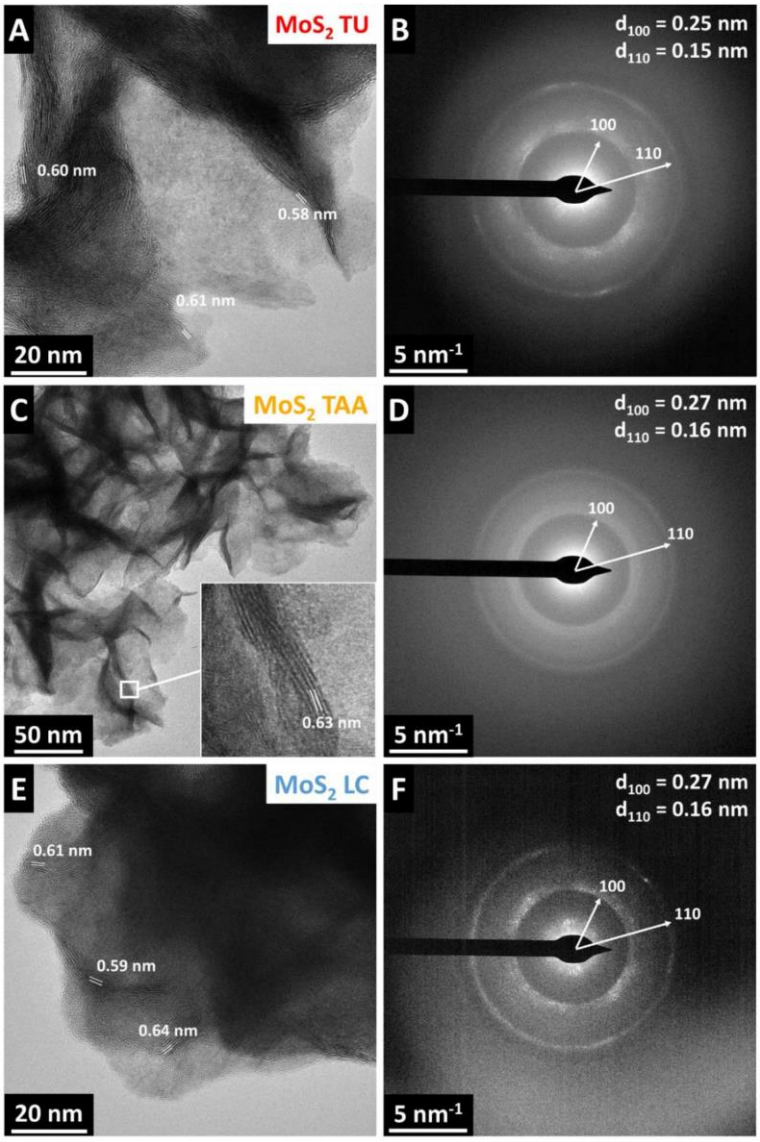

Fig. 3: TEM images and corresponding selected area electron diffraction patterns of (A-B) MoS_2 TU, (C-D) MoS_2 TAA, and (E-F) MoS_2 LC.

https://doi.org/10.26434/chemrxiv-2024-7hz4h **ORCID:** https://orcid.org/0000-0001-9475-3692 Content not peer-reviewed by ChemRxiv. **License:** CC BY 4.0

Nitrogen sorption is conducted to evaluate the porosity and specific surface area (SSA) of the MoS_2 samples. Sorption isotherms of all samples exhibit a type II shape according to IUPAC classification (**Fig. 4**), typically ascribed to nonporous or macroporous samples[31]. For MoS_2 TAA, MoS_2 LC and MoS_2 TU samples, the emergence of H3-type hysteresis loops confirms the presence of aggregated plate-like particles (**Fig. 4B-D**), as already observed in electron micrographs. However, hysteresis loop for MoS_2 TU (**Fig. 4B**) shows a much steeper desorption branch in comparison to the other two samples, reminiscent of H2(a) loops where the behavior is ascribed to blocked pores and/or narrow pore necks[31], which could be formed within the micron-sized secondary particles of MoS_2 TU. This strongly suggests significantly hindered accessibility of pores within the large particles of TU-derived MoS_2, exhibiting a different morphology than MoS_2 TAA and MoS_2 LC despite similar hydrothermal synthesis parameters and despite similarly small crystalline domain sizes observed from TEM and from broadened XRD peaks. The observations are further reflected in the different specific surface areas derived from BET method (Brunauer-Emmett-Teller, ref. [32]), ranging from relatively small SSA of 8 and 5 $m^2 g^{-1}$ for MoS_2 Comm and MoS_2 TU, to larger SSA of 84 and 34 $m^2 g^{-1}$ for MoS_2 TAA and MoS_2 LC, respectively. The results underline the possibility to tune both porosity and SSA of hydrothermally synthesized MoS_2 via choice of sulfur precursor, which can have significant implications on the materials' functional properties[16].

Overall, structural investigation over several length scales demonstrates that the choice of sulfur precursor for hydrothermally synthesized MoS_2 has a large impact on the macroscopic secondary and primary particle morphology, the resulting sample porosity, as well as accessible surface area (TAA > LC > TU). On a microscopic level, however, crystallite size and lattice parameters remain comparable across the three samples.

https://doi.org/10.26434/chemrxiv-2024-7hz4h **ORCID:** https://orcid.org/0000-0001-9475-3692 Content not peer-reviewed by ChemRxiv. **License:** CC BY 4.0

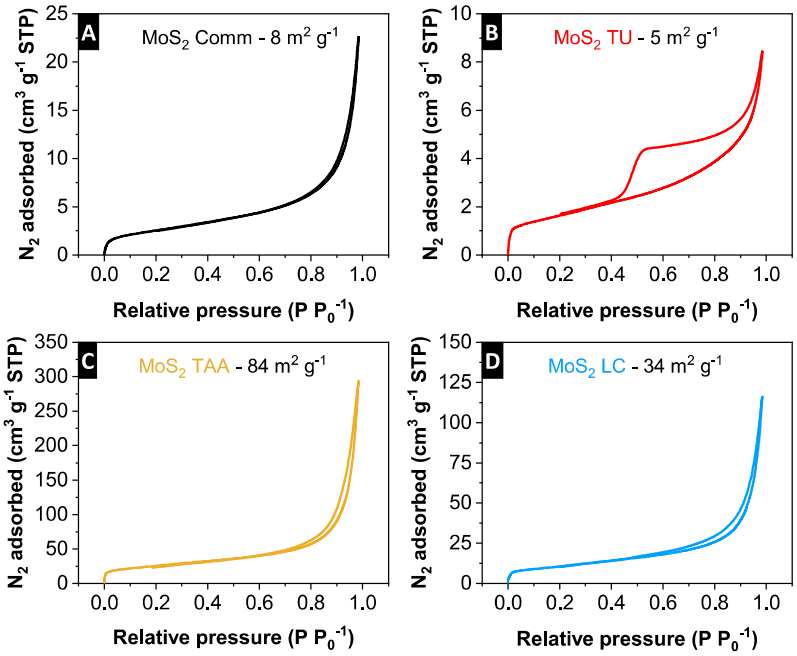

Fig. 4: Nitrogen sorption isotherms at 77 K of MoS_2 based materials prepared from (A) Comm, (B) TU, (C) TAA, (D) LC.

3.2 Electrochemical characterization

While it is demonstrated that the morphology, specific surface area and porosity of hydrothermally synthesized MoS_2 materials are strongly dependent on the utilized sulfur precursor, the samples show comparable, few-layer nano-crystallites with mixed 2H-/1T-phases. The materials therefore allow to study the impact of MoS_2 structural parameters on electrochemical lithium ion intercalation properties, allowing to draw conclusions on the preferred hydrothermal synthesis precursors and set the materials in relation to commercially available, pristine 2H-MoS_2 Comm.

Initial evaluation of electrochemical lithium intercalation behavior of MoS_2 electrode materials is conducted by galvanostatic charge/discharge technique between 3.0 to 1.0 V *vs.*

https://doi.org/10.26434/chemrxiv-2024-7hz4h **ORCID:** https://orcid.org/0000-0001-9475-3692 Content not peer-reviewed by ChemRxiv. **License:** CC BY 4.0

Li/Li^+, a potential range where reversible lithium intercalation into the MoS_2 interlayer space is expected according to[33]:

$$MoS_2 + xLi^+ + xe^- \leftrightarrow Li_xMoS_2, \text{with } 0 \leq x \leq 1 \quad (2)$$

The theoretical maximum capacity for the intercalation of 1 Li^+ per MoS_2 is 167 mAh g^{-1}. Potential profiles of the first five galvanostatic cycles at a constant specific current of 20 mA g^{-1} for each MoS_2 sample are presented in **Fig. 5A-D**. MoS_2 Comm (**Fig. 5A**) exhibits a plateau at ca. 1.1 V *vs.* Li/Li^+ during first cycle associated with the irreversible phase transition from semi-conductive 2H phase to metallic 1T phase, resulting in an initial Coulombic efficiency (ICE) of 76 %, well aligned to the literature values[17]. It is a consequence of the sulfur plane gliding upon intercalation of lithium ions which turns the molybdenum atom into the octahedral coordination environment[34, 35]. In the consecutive few cycles, completion of the irreversible phase transition can still be observed, before a stable (de)lithiation profile with the main redox plateau in the potential region around 1.7 - 1.9 V *vs.* Li/Li^+ is observed, presenting a reversible anodic/delithiation capacity of 152 mAh g^{-1}, close to the theoretical capacity. Comparable behavior can be also observed when tested by cyclic voltammetry (**Fig. S1A**), which shows high cathodic current peak corresponding to phase transition in the first cycle and consequent de/intercalation behavior in the consecutive cycles.

The three samples prepared *via* hydrothermal synthesis (**Fig. 5B-D**) exhibit linear/sloping galvanostatic profiles in absence of clear plateaus which are observed in MoS_2 Comm. The profiles electrically resemble capacitive-type charge storage processes that can be induced by nanosizing effects of the crystallites, leading to pseudocapacitive intercalation behavior. Thermodynamically, the effect can be explained by contributions of excess chemical potential of lithium at (near-)surface sites of MoS_2 nanocrystals dispersing the resulting redox potential[36, 37]. While the sloping potential profile of MoS_2 TU is observed between ca. 2.4 – 1.0 V *vs.* Li/Li^+, the sloping potential region of MoS_2 TAA and MoS_2 LC is further expanded in the positive range to about 2.7 V. The pseudocapacitive behavior of the hydrothermally synthesized MoS_2 samples, especially in contrast to commercial MoS_2 Comm, can also be observed by cyclic voltammograms at various sweep rates between 0.2 mV s^{-1} and 20 mV s^{-1} (**Fig. 5G-H**). The effect of scan rates for each material is presented in **Fig. S2**.

https://doi.org/10.26434/chemrxiv-2024-7hz4h **ORCID:** https://orcid.org/0000-0001-9475-3692 Content not peer-reviewed by ChemRxiv. **License:** CC BY 4.0

In a comparison to MoS_2 Comm, hydrothermally synthesized MoS_2 materials do not show the pronounced plateau behavior of the 2H-to-1T phase transition at 1.1 V during first cycle, likely as a consequence of their high 1T phase content demonstrated by Raman. Only in MoS_2 TU it is visible to some extent. It can be also observed on the cyclic voltammograms during the first few cycles (**Fig. S1B-D**). The ICEs of the samples are 70% for MoS_2 TU, 59% for MoS_2 TAA and 67% for MoS_2 LC, possibly caused by irreversible parasitic reactions at the electrode/electrolyte interface (considering lower ICE for samples with higher SSA) and remaining 2H-to-1T phase transition (specifically for MoS_2 TU). Each hydrothermally synthesized MoS_2 shows higher reversible (de)lithiation capacity than commercial MoS_2 Comm with around 200 mAh g^{-1} (corresponds to ca. 1.2 Li^+ per MoS_2), indicating additional charge storage for nanocrystalline MoS_2 materials. While this effect has been observed before for nanostructured MoS_2 and is attributed to surface redox reactions, it is remarkably also observed for MoS_2 TU with a SSA even smaller than that of commercial MoS_2 Comm, clearly demonstrating the significance of nano-crystallinity over accessible surface area for maximizing the reversible (de)lithiation capacity of MoS_2[16].

All MoS_2-based materials are galvanostatically cycled at different specific currents to investigate the rate capability of the (de)lithiation reaction (**Fig. 5E**). As discussed above, hydrothermally synthesized MoS_2 samples exhibit higher anodic capacity than MoS_2 Comm over the entire range of specific currents. MoS_2 TAA and MoS_2 LC exhibit similar capacity as MoS_2 TU up to specific currents of around 1 - 2 A g^{-1}, but at higher currents these samples show superior capacity retention (**Fig. S3**). This is likely due to their higher specific surface area, leading to an increased electrode/electrolyte interface with reduced diffusion-limitations even at high rates due to smaller diffusion path lengths[13]. The galvanostatic cycling stability is tested at an intermediate specific current rate of 1 A g^{-1} (**Fig. 5F**). After 1,000 cycles, two groups can be identified according to their capacity retention. MoS_2 TAA and MoS_2 LC show comparably stable cycling behavior with about 86 % of initial capacity retention, whereas MoS_2 Comm and MoS_2 TU only exhibit about 80 % of capacity retention. Remarkably, this behavior is opposite to their increasing SSA, which is often hypothesized to be a source of capacity fading due to increased parasitic side reactions[38]. It is demonstrated that MoS_2 materials with higher SSA exhibit improved cycling stability, regardless of crystallite size. We

https://doi.org/10.26434/chemrxiv-2024-7hz4h **ORCID:** https://orcid.org/0000-0001-9475-3692 Content not peer-reviewed by ChemRxiv. **License:** CC BY 4.0

hypothesize that this behavior is a consequence of reduced volumetric electrode changes during cycling (*vide infra*).

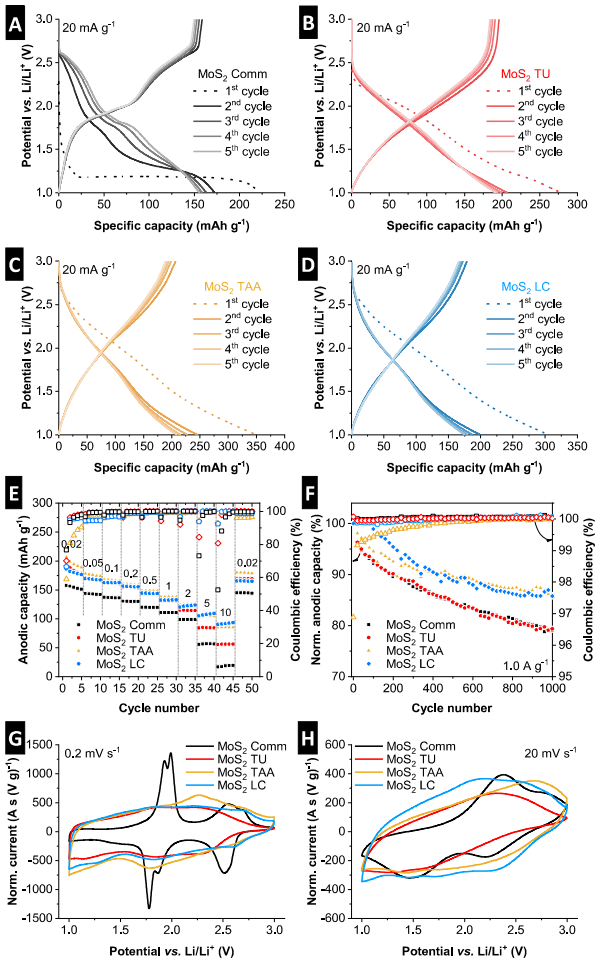

Fig. 5: Electrochemical characterization of MoS_2 based materials. (A-D) First 5 cycles of galvanostatic charge/discharge profiles, (E) Anodic capacity recorded at different specific currents (from 20 mA g^{-1} to 10 A g^{-1}), (F) Galvanostatic charge/discharge stability at a specific current of 1 A g^{-1}, (G-H) Cyclic voltammograms at 0.2 mV s^{-1} and 20 mV s^{-1}. All tests are carried out in coin cells versus lithium metal in LP30 electrolyte at a constant temperature of 20 °C.

https://doi.org/10.26434/chemrxiv-2024-7hz4h **ORCID:** https://orcid.org/0000-0001-9475-3692 Content not peer-reviewed by ChemRxiv. **License:** CC BY 4.0

To gain deeper insights into the kinetics of the MoS_2-based samples during lithium intercalation, electrochemical impedance spectroscopy (EIS) is carried out at various states of charge along the entire potential range from 3 – 1 V *vs.* Li/Li^+ (**Fig. S4**). The capacitor-like electrical response (i.e., pseudocapacitive or electrical double-layer contributions to the charge storage process) can be extracted from EIS by employing a simple equivalent circuit consisting of a capacitor and resistor in series[39]. Then, the (pseudo)capacitive response can be presented over a wide potential range as a function of frequency *via* a so-called 3D Bode plot (**Fig. S5**) with real capacitance representation (**Fig. 6**).

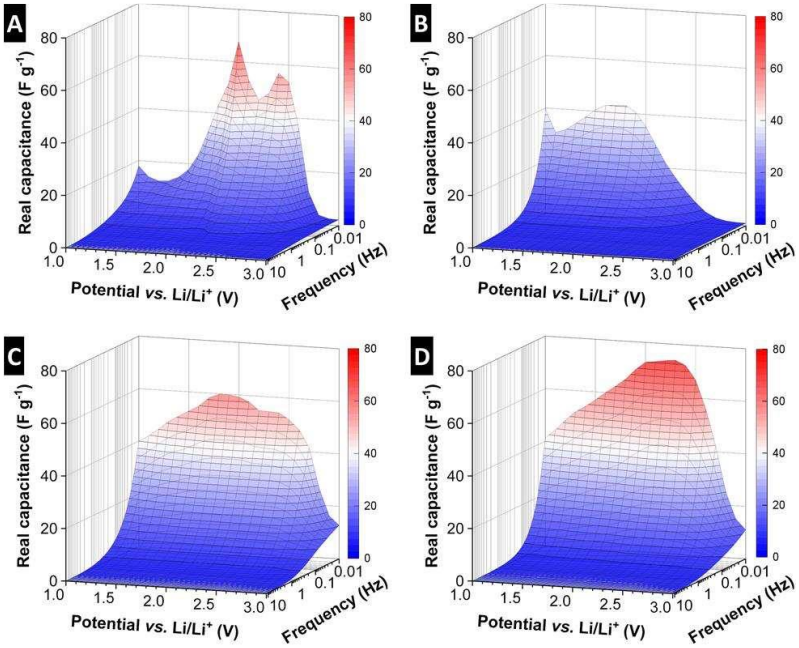

Fig. 6: 3D Bode representation of real capacitance *vs.* frequency at different potentials during discharge for different MoS_2 materials (A) Comm, (B) TU, (C) TAA, (D) LC.

For commercial MoS_2 Comm, two clear maxima of the real capacitance curve can be found corresponding to the two redox peak potentials (**Fig. 6A**). Outside of these peak potentials, there is a significant drop in the real capacitance, in line with a typical battery-like electrochemical response like for example in $LiFePO_4$[24]. Contrarily, for all three

https://doi.org/10.26434/chemrxiv-2024-7hz4h **ORCID:** https://orcid.org/0000-0001-9475-3692 Content not peer-reviewed by ChemRxiv. **License:** CC BY 4.0

hydrothermally synthesized MoS_2 samples (**Fig. 6B-D**), the real capacitance curve changes towards a "waterfall" shape indicating a (pseudo)capacitive charge storage process over a wider potential range. Notably, potential range is narrower for MoS_2 TU as compared to the other two samples, MoS_2 TAA and MoS_2 LC. Overall, 3D Bode analysis gives a comprehensive overview of electrode kinetics over a wide potential and frequency range, with pseudocapacitive lithium intercalation properties for hydrothermally synthesized MoS_2 samples[40].

To better understand the origin of the different electrochemical response of the materials, operando XRD during the galvanostatic cycling is carried out to study the crystallographic changes during lithium (de)intercalation. MoS_2 Comm (**Fig. 7A**) shows the initial (002) plane peak of 2H-MoS_2, with a corresponding d-spacing of d_{002}=0.61 nm, decreasing in intensity during the discharge plateau at 1.1 V *vs.* Li/Li^+, while another peak emerges at corresponding to the (001) plane of the 1T-MoS_2 phase (d_{001}=0.63 nm), in good agreement with the values reported in the literature for the 1T-$LiMoS_2$ phase[41]. The subsequent deintercalation process appears as a solid-solution reaction, with the prominent (001) plane peak shifting to lower angles, corresponding to an expansion in the interlayer spacing (d_{001}=0.65 nm), followed by a contraction to d_{001}=0.62 nm at the end of the deintercalation. The initial 2H-MoS_2 (002) peak is not recovered after the first cycle, which indicates an irreversible transformation from 2H-MoS_2 to 1T-MoS_2, in close agreement with previous reports[17].

In MoS_2 TU (**Fig. 7B**), the initial interlayer distance is 0.65 nm and only expands slightly to 0.67 nm upon lithiation. At the end of the first delithiation, the d-spacing remains at roughly 0.67 nm. The XRD signature is characterized by a minimal, but continuous shifts of the (001) set of planes of 1T-MoS_2, rather than the emergence of new diffraction signals, demonstrating solid-solution lithium (de)intercalation. While Raman results suggest that MoS_2 TU consists of a mixture of 1T-MoS_2 and 2H-MoS_2, a phase transformation is not observed *via* operando XRD. This is likely due to the nanosizing effect of MoS_2 crystallites suppressing the transformation[14]. Overall, crystallographic changes in MoS_2 TU are minimal during (de)lithiation, providing an explanation for the superior kinetics of the material compared to MoS_2 Comm, despite its small SSA. The operando XRD patterns of MoS_2 TAA and MoS_2 LC provide very little peak intensity during cycling, indicating a high degree of structural disorder, making interpretation of the results more challenging. While for MoS_2 TAA a continuous shift

https://doi.org/10.26434/chemrxiv-2024-7hz4h **ORCID:** https://orcid.org/0000-0001-9475-3692 Content not peer-reviewed by ChemRxiv. **License:** CC BY 4.0

of the (001) plane of 1T-MoS_2 could be interpreted from the heatmap representation, somewhat comparable to MoS_2 TU, no clear signals can be observed for MoS_2 LC. However, the absence of any new XRD signals during cycling points towards a solid-solution intercalation process without the formation of a new phase for both samples. Thus, it can be summarized that in the case of hydrothermally synthesized MoS_2, lithium (de)intercalation proceeds *via* a solid-solution type mechanism regardless of the specific surface area of the samples.

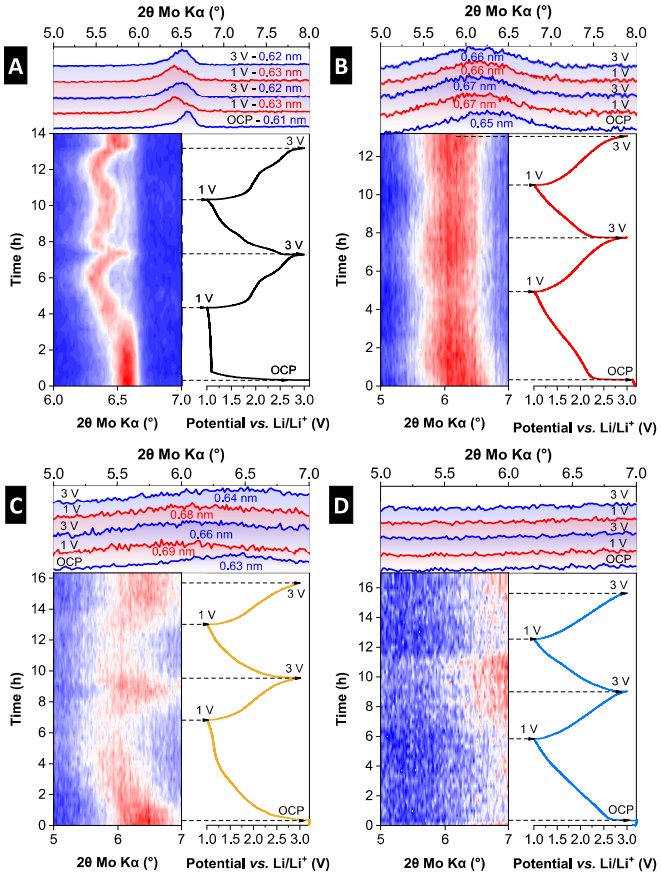

Fig. 7: *Operando* XRD profiles for different MoS_2-based materials: (A) MoS_2 Comm, (B) MoS_2 TU, (C) MoS_2 TAA, (D) MoS_2 LC. Measurements are carried out in Debye-Scherrer geometry using custom-designed coin cells with Kapton-taped holes allowing for X-ray penetration.

https://doi.org/10.26434/chemrxiv-2024-7hz4h **ORCID:** https://orcid.org/0000-0001-9475-3692 Content not peer-reviewed by ChemRxiv. **License:** CC BY 4.0

To elucidate the volumetric changes in electrode materials on a macroscopic level, electrochemical dilatometry (ECD) is employed. The method is useful to investigate morphology/porosity-induced effects, which cannot be easily captured by methods like operando XRD. Thus, ECD is employed to compare the expansion/contraction behavior of MoS_2 Comm, the host material that undergoes a phase transformation during the first lithiation step, with MoS_2 LC which is the host material of the fastest kinetics that showed improved stability during long-term cycling. For MoS_2 Comm (**Fig. 8A**), a large increase in electrode thickness of about 19 % can be observed during the irreversible phase transformation from 2H-to-1T. In subsequent cycles, contraction/expansion of about 2-3 % can be observed during delithiation and lithiation, respectively. The initial irreversible thickness change is very significant and could not be explained by crystallographic expansion (using operando XRD), indicating that this expansion is potentially the consequence of significant solid electrolyte interphase (SEI) formation. Further work will more closely investigate the origin of the significant expansion behavior during the first lithiation cycle.

For MoS_2 LC, very minimal height changes are observed (**Fig. 8B**). During the first lithiation process, the electrode expands by ca. 1 % and subsequently exhibits reversible height changes around 1 %. The significantly reduced height change of MoS_2 LC, especially during the first cycle, is a likely explanation for the improved cycling stability over MoS_2 Comm.

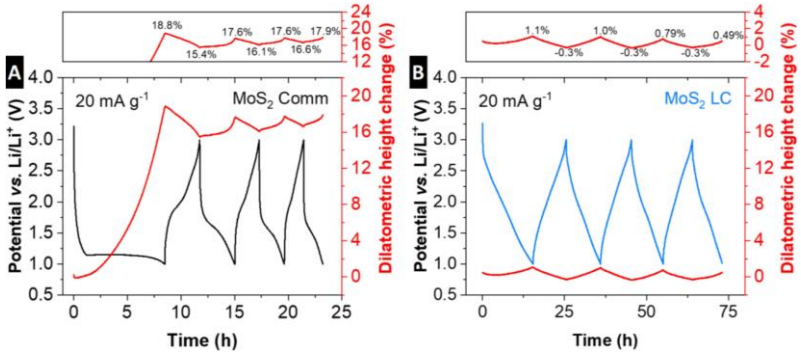

Fig. 8: Dilatometric height change of the electrode materials over first few consecutive cycles. (A) MoS_2 Comm, (B) MoS_2 LC.

https://doi.org/10.26434/chemrxiv-2024-7hz4h **ORCID:** https://orcid.org/0000-0001-9475-3692 Content not peer-reviewed by ChemRxiv. **License:** CC BY 4.0

4. Conclusions

In this work, the choice of sulfur precursor is demonstrated as a facile route to control the structure and morphology of hydrothermally synthesized MoS_2 over several length scales. From a macroscopic point of view, morphology is affected by the precursor choice, with thiourea (MoS_2 TU) yielding micron-sized secondary particle architectures, whereas thioacetamide and L-cysteine provide reduced secondary particles with nano-sized, flake-like morphology (MoS_2 TAA and MoS_2 LC). Further, the resulting sample porosity and (accessible) surface area follows the same trend (TAA > LC > TU). Contrarily, on a microscopic level, crystallite size and lattice parameters remain comparable across all three samples demonstrating nanoscopic crystalline domains with a mixture of 2H- and 1T-phases.

When employed as a host material for electrochemical lithium intercalation, each material shows fast pseudocapacitive charge storage behavior with slightly different electrochemical response showing strong correlation to the available adsorption area and particle size of the crystalline domains explained by 3D bode plot analysis. Each hydrothermally prepared sample shows higher maximum anodic capacity of ca. 200 mAh g^{-1} at a rate of 20 mA g^{-1} in comparison to commercially available MoS_2 with 152 mAh g^{-1}. MoS_2 TAA and MoS_2 LC demonstrate significantly improved rate capability, with higher charge retention at 10 A g^{-1} (related to ca. 34 s discharge) up to 90 mAh g^{-1} in comparison to MoS_2 TU (50 mAh g^{-1}) and MoS_2 Comm (25 mAh g^{-1}). Long term cycling reveals that the samples with high specific surface area and small secondary particle size show slightly better stability over 1,000 cycles, possibly due to smaller volumetric expansion of the electrode material during the first cycles revealed during dilatometric studies.

The study demonstrates the ability to influence electrochemical charge storage properties of MoS_2 by the choice of hydrothermal precursor, offering a facile strategy to control materials structure and functionality. Such insights can be useful for researchers in the field of high-power electrochemical energy storage materials, but can also be of value to materials developed in other fields of electrochemistry such as electrocatalytic hydrogen evolution and beyond.

https://doi.org/10.26434/chemrxiv-2024-7hz4h **ORCID:** https://orcid.org/0000-0001-9475-3692 Content not peer-reviewed by ChemRxiv. **License:** CC BY 4.0

Conflict of interest

There are no conflicts of interest to declare.

Acknowledgements

M.T. and E.F. acknowledge financial support from National Science Centre, Poland within the project Preludium 20 2021/41/N/ST5/01364 and Polish National Agency for Academic Exchange (NAWA) under STER programme, Towards Internationalization of Poznan University of Technology Doctoral School (2022-2024). M.E., J.C, and S.F. acknowledge funding from the German Federal Ministry of Education and Research (BMBF) in the NanoMatFutur program (grant No. 03XP0423). S.F. would like to thank the Daimler and Benz Foundation for financial support in the Scholarship program. The authors are thankful for basic funding from the Helmholtz Association.

https://doi.org/10.26434/chemrxiv-2024-7hz4h **ORCID:** https://orcid.org/0000-0001-9475-3692 Content not peer-reviewed by ChemRxiv. **License:** CC BY 4.0

References

[1] A. V. Kolobov, J. Tominaga, *Two-Dimensional Transition-Metal Dichalcogenides*, Springer Series in Materials Science, vol 239. Springer, Cham **2016**, p. 7-27.

[2] M. A. Bissett, S. D. Worrall, I. A. Kinloch, R. A. W. Dryfe, Electrochimica Acta **2016** 201, 30-37.

[3] M. Acerce, D. Voiry, M. Chhowalla, Nature Nanotechnology, **2015** 10, 313-318.

[4] C. Tsai, F. Abild-Pedersen, J. K. Nørskov, Nano Letters **2014**, 14, 1381-1387.

[5] J. Zhu, Z. C. Wang, H. Dai, Q. Wang, R. Yang, H. Yu, M. Liao, J. Zhang, W. Chen, Z. Wei, N. Li, L. Du, D. Shi, W. Wang, L. Zhang, Y. Jiang, G. Zhang, Nature Communications **2019**, 10, 1348-1348.

[6] M. Chhowalla, H. S. Shin, G. Eda, L. J. Li, K. P. Loh, H. Zhang, Nature Chemistry **2013**, 5, 263-275.

[7] R. Lv, J. A. Robinson, R. E. Schaak, D. Sun, Y. Sun, T. E. Mallouk, M. Terrones, Accounts of Chemical Research **2015**, 48, 56.

[8] M. Zeng, Y. Xiao, J. Liu, K. Yang, L. Fu, Chemical Reviews **2018**, 118, 6236-6296.

[9] T. Stephenson, Z. Li, B. Olsen, D. Mitlin, Energy & Environmental Science **2014**, 7, 209-231.

[10] G. Wang, J. Zhang, S. Yang, F. Wang, X. Zhuang, K. Müllen, X. Feng, Advanced Energy Materials **2018**, 8, 1-8

[11] C. George, A. J. Morris, M. H. Modarres, M. De Volder, Chemistry of Materials **2016**, 28, 7304-7310.

[12] H. D. Yoo, Y. Li, Y. Liang, Y. Lan, F. Wang, Y. Yao, ChemNanoMat **2016**, 2, 688-691.

[13] J. B. Cook, H. S. Kim, T. C. Lin, C. H. Lai, B. Dunn, S. H. Tolbert, Advanced Energy Materials **2017**, 7, 1-12.

[14] J. B. Cook, T. C. Lin, H.-S. Kim, A. Siordia, B. S. Dunn, S. H. Tolbert, ACS Nano **2019**, 13, 1223-1231.

[15] J. Choi, H. Moon, S. Fleischmann, Electrochimica Acta **2024**, 476, 143774.

[16] Y. Yao, H. Cumberbatch, D. D. Robertson, M. A. Chin, R. Lamkin, S. H. Tolbert, Advanced Functional Materials **2023**, 2304896.

[17] X. Fang, C. Hua, X. Guo, Y. Hu, Z. Wang, X. Gao, F. Wu, J. Wang, L. Chen, Electrochimica Acta **2012**, 81, 155-160.

[18] L. Zhou, T. Xia, T. Cao, L. Wang, Y. Chen, S. Li, R. Wang, H. Guo, Journal of Alloys and Compounds **2020**, 818, 152909.

[19] Z. Ali, Q. Hussain, M. A. Yawer, M. Mehmood, R. Hussain, A. Shah, H. Kanwal, A. Yawer, S. Ahmad, S. Zahid, Journal of Molecular Structure **2023**, 1278, 134929.

[20] X. Zheng, Y. Zhu, Y. Sun, Q. Jiao, Journal of Power Sources **2018**, 395, 318-327.

[21] Y. Liu, K. Wu, X.-l. Guo, W.-y. Wang, Y.-q. Yang, Journal of Fuel Chemistry and Technology **2018**, 46, 535-542.

[22] I. S. Waskito, B. Kurniawan, M. I. Amal, M. Hanifuddin, Materials Science and Engineering **2019**, 546, 042048.

https://doi.org/10.26434/chemrxiv-2024-7hz4h **ORCID:** https://orcid.org/0000-0001-9475-3692 Content not peer-reviewed by ChemRxiv. **License:** CC BY 4.0

[23] J. Liu, J. Wang, B. Wei, Y. Xue, L. Ma, R. Jiang, Inorganic Chemistry **2023**, 62, 9749-9757.

[24] J. S. Ko, C.-H. Lai, J. W. Long, D. R. Rolison, B. Dunn, J. Nelson Weker, ACS Applied Materials & Interfaces **2020**, 12, 14071-14078.

[25] K. Chang, W. Chen, ACS Nano **2011**, 5, 4720-4728.

[26] S. Guo, Y. Zhang, S. Tang, B. Wang, Y. Wang, Y. Song, X. Xin, Y. Zhang, X. Li, Journal of Alloys and Compounds **2011**, 864, 158581.

[27] H. Li, Q. Zhang, C. C. R. Yap, B.K. Tay, T.H.T. Edwin, A. Olivier, D. Baillargeat, Advanced Functional Materials **2012**, 22, 1385-1390.

[28] C. Lee, H. Yan, L. E. Brus, T.F. Heinz, J. Hone, S. Ryu, ACS Nano **2010**, 4, 2695-2700.

[29] X. Zang, Y. Qin, T. Wang, F. Li, Q. Shao, N. Cao, ACS Applied Materials & Interfaces **2020**, 12, 55884-55893.

[30] X. Geng, Y. Zhang, Y. Han, J. Li, L. Yang, M. Benamara, L. Chen, H. Zhu, Nano Letters **2017**, 17, 1825-1832.

[31] M. Thommes, K. Kaneko, A. V. Neimark, J. P. Olivier, F. Rodriguez-Reinoso, J. Rouquerol, K. S. W. Sing, Pure and Applied Chemistry **2015**, 87, 1051-1069.

[32] S. Brunauer, P.H. Emmett, E. Teller, Journal of the American Chemical Society **1938**, 60, 309-319.

[33] T. Wang, S. Chen, H. Pang, H. Xue, Y. Yu, Advanced Science **2017**, 4, 1600289.

[34] F. Wypych, R. Schollhorn, Journal of the Chemical Society **1992**, 1386-1388.

[35] Q. Jin, N. Liu, B. Chen, D. Mei, Journal of Physical Chemistry. C **2018**, 122, 28215-28224.

[36] J. Maier, Journal of Power Sources **2007**, 174, 569-574.

[37] J. Nanda, V. Augustyn, Nanostructured Transition Metal Oxides for Electrochemical Energy Storage, John Wiley & Sons **2022**, pp. 183-212.

[38] E. Pomerantseva, Y. Gogotsi, Nature Energy **2017**, 2, 17089.

[39] P. L. Taberna, P. Simon, J. F. Fauvarque, Journal of the Electrochemical Society **2003**, 150, A292-A300.

[40] R. Holze in *Electrochemical Methods. Fundamentals and Applications*, 2nd Edition (Eds: A. J. Bard, L. R. Faulkner), Angewandte Chemie International, **2002**, 41, pp. 655-657.

[41] M. A. Py, R. R. Haering, Canadian Journal of Physics **1983**, 61, 76-84.

https://doi.org/10.26434/chemrxiv-2024-7hz4h **ORCID:** https://orcid.org/0000-0001-9475-3692 Content not peer-reviewed by ChemRxiv. **License:** CC BY 4.0

Chapter VI

Concluding remarks

General summary

ECs are attractive energy storage devices due to their exceptional power density and longevity. However, they suffer from moderate energy density which can be increased by enhancing the capacitance or voltage window of the device. This can be achieved by utilizing different EC components, such as in the context of this PhD dissertation, using different electrode materials.

Recently, 2D materials have become highly appealing for use as electrode materials in energy storage applications due to their faradaic behavior, which is promising for achieving high capacitance. This PhD dissertation explores the concept of utilizing 2D TMDs as electrode materials in electrochemical energy storage applications such as ECs. The study presents an overview on TMDs with respect to their synthesis, material characterization, electrochemical behavior, potential limitations in aqueous media, strategies to address these limitations, and utilization of layered TMDs as lithium-ion hosts in organic electrolytes.

In **Chapter III**, the focus is on developing hydrothermal routes for preparing TMDs, such as MoS_2, ReS_2, NiS_2 and FeS_2 and integrating them with various carbonaceous materials (e.g., NTs, CB, rGO and 3DG) to form composites. It was found that the morphology of the carbon support morphology significantly affects the final properties of the composite materials and their electrochemical behavior. Carbons with open porosity, such as NTs and CB, allow for the perpendicular positioning of MoS_2 and ReS_2 nanoflakes, enhancing their catalytic activity in symmetrical ECs in aqueous media. Despite showing higher capacitance and conductivity than the parent materials (TMDs and carbons), the voltage window of the symmetrical cell was limited to below 1 V. Contrary, 3DG/FeS_2 composite, demonstrated high capacitance and conductivity while operating at 1.5 V. It strongly points toward the importance of the carbon-support choice and its effect on the electrochemical behavior of the carbon/TMDs composites.

Chapter IV addresses the catalytic activity of 2D TMDs. The hydrothermal synthesis route is convenient for preparing nanostructured and layered TMDs, although it often results in materials with structural defects such as sulfur vacancies, which induce TMDs catalytic properties. These vacancies can locally increase reactivity, enabling functionalization which diazonium salts to form covalent bonds between foreign redox molecules and TMDs. This chapter presents a novel approach of using hydrothermally prepared nanostructured MoS_2 for covalent functionalization with AQ molecules during

the *in-situ* generation of diazonium salts. XPS measurements confirmed the covalent AQ linkage to MoS_2, while XRD and TEM studies showed that MoS_2 was grafted both on the surface and within its interlayer spacing. The AQ-MoS_2 material exhibited improved capacitance due to the redox activity of AQ molecules. Further studies featuring *b-value* analysis and EIS, revealed that the presence of AQ molecules within the interlayer spacing did not disrupt ion movement inside the layered structure. A hybrid cell utilizing pristine and grafted MoS_2 as a negative electrode and CB as a positive electrode showed higher energy than symmetric CB cells. Electrochemical studies using an aqueous electrolyte, i.e., 1 M $BeSO_4$, revealed the redox activity of AQ, indicating a promising approach for safe and stable high-performance ECs. Initial studies featuring organic electrolyte revealed redox activity of AQ in organic media as well.

Chapter V explores the electrochemical behavior of MoS_2 materials in organic electrolytes. It was found that the choice of sulfur precursor strongly affects the resultant material's morphology, structure, microporous texture, and electrochemical behavior. Different MoS_2 was hydrothermally synthetized from three various precursors, namely thioacetamide, thiourea, and L-cysteine. As reported in the literature, higher decomposition temperatures of thiourea resulted in materials with different morphology and microporous texture compared to MoS_2 obtained from thioacetamide and L-cysteine. In terms of electrochemical behavior, each hydrothermally prepared material shows pseudocapacitive features during lithium intercalation studies which was in-depth analyzed by *operando* XRD, dilatometry and EIS studies.

The main findings of this PhD dissertation include:

i) the hydrothermal route is an attractive synthesis method that allows for the preparation of nanostructured TMDs with controllable properties depending on the precursors used,
ii) the morphology of carbon supports significantly influences the electrochemical behavior of carbon/TMD composites,
iii) sulfur vacancies in TMDs can be exploited for functionalization with diazonium salts,
iv) catalytic properties of TMDs can be suppressed by the redox reaction of AQ at the electrode/electrolyte interface,
v) the sulfur precursor used for hydrothermal synthesis allows for controlling the structure, morphology, and microporous texture of MoS_2 material, affecting its electrochemical properties.

Scientific track records

All publications

1. E. Frackowiak*, M. Foroutan Koudahi, **M. Tobis**,
   Electrochemical capacitor performance of nanotextured carbon/transition metal dichalcogenides composites, Small 17 (**2021**) 2006821,
   https://doi.org/10.1002/smll.202006821 **IF: 13.3, MNiSW: 200**

2. **M. Tobis**, S. Sroka, E. Frąckowiak*,
   Supercapacitor with Carbon/MoS_2 Composites,
   Frontiers in Energy Research 9 (**2021**) 647878,
   https://doi.org/10.3389/fenrg.2021.647878 **IF: 3.4, MNiSW: 100**

3. A. Kachmar, **M. Tobis**, E. Frackowiak*,
   Electrochemical Capacitor Based on Reduced Graphene Oxide/NiS_2 Composite,
   ChemElectroChem 9 (**2022**) e202200834,
   https://doi.org/10.1002/celc.202200834 **IF: 4.0, MNiSW: 100**

4. A. Klimek, **M. Tobis**, E. Frackowiak*,
   Effect of buffer/iodide electrolyte on electrochemical capacitor performance,
   Green Chemistry 26 (**2024**) 6684-6695,
   https://doi.org/10.1039/D4GC01748J **IF: 9.8, MNiSW: 200**

5. **M. Tobis**, J. Piwek, A. Platek-Mielczarek, L. Przypis, D. Janas*, E. Frackowiak*,
   Probing iodide/iodonium salt interactions with single-walled carbon nanotubes for resilient electrochemical capacitor,
   Electrochimica Acta 492 (**2024**) 144386,
   https://doi.org/10.1016/j.electacta.2024.144386 **IF: 6.6, MNiSW: 100**

6. **M. Tobis***, E. Frackowiak*,
   Nanostructured MoS_2 grafted by anthraquinone for energy storage,
   Journal of Power Sources 613 (**2024**) 234862,
   https://doi.org/10.1016/j.jpowsour.2024.234862
   IF: 9.2, MNiSW: 140

7. **M. Tobis**, M. Elmanzalawy, J. Choi, E. Frackowiak*, S. Fleischmann*,
   Controlling structure and morphology of MoS_2 via sulfur precursor for optimized pseudocapacitive lithium intercalation hosts,
   Submitted as invited paper Batteries & Supercaps, under review,
   https://doi.org/10.26434/chemrxiv-2024-7hz4h
   IF: 5.7, MNiSW: 20

Total Impact Factor of published papers: 46.3
Impact Factor Including Co-authors: 15.9
Total MNiSW of published papers: 840
***denotes corresponding author**

Oral presentations at conferences (as a speaker)

1. **M. Tobis***, M. F. Koudahi, A. Kachmar, S. Azmi, E. Frackowiak, *High frequency response electrochemical capacitors based on carbon/dichalcogenides electrodes,* XIII Konferencja Naukowo-Techniczna – Materiały węglowe i kompozyty polimerowe, Nauka i Przemysł, Ustroń-Jaszowiec, Polska, 23.11.2021 – 26.11.2021

2. **M. Tobis***, A. Płatek-Mielczarek, J. Piwek, D. Janas, L. Przypis, E. Frackowiak, *Single walled-carbon nanotubes empowered with iodonium salts used as an electrochemical capacitors electrodes*, European Materials Research Society (EMRS) Spring Meeting, Virtual Conference (on-line), 30.05.2022 – 03.06.2022

3. **M. Tobis***, E. Frackowiak, *Anthraquinone modified carbon/MoS_2 composites as an electrode materials in supercapacitors,* III Warsztaty Naukowe "Nowe trendy w nauce o węglu" Polskie Towarzystwo Węglowe, Kraków, Polska 24.06.2022.

4. **M. Tobis***, M. F. Koudahi, A. Kachmar, S. Azmi, E. Frackowiak, *Carbon materials as a support for TMD based supercapacitor electrodes,* The World Conference on Carbon, Carbon 2022 'Carbon for Cleaner Future', London, Great Britain, 03.07.2022 – 08.07.2022

5. **M. Tobis***, E. Frackowiak, *Covalent functionalization of layered MoS_2 with redox species as electrode materials for supercapacitors,* International Society of Electrochemistry (ISE), Lyon, France, 03.09.2023 – 08.09.2023

6. **M. Tobis***, E. Frackowiak, *Layered MoS_2 with covalently linked redox species as supercapacitor electrode material,* International Conference on Advanced Capacitors (ICAC), Kamakura, Japan, 26.09.2023 – 29.09.2023

***denotes presenting author**

Poster presentations at conferences (as a presenter)

1. **M. Tobis***, E. Frackowiak,
   Molybdenum selenide/sulfide with carbon nanotubes as attractive electrode materials for electrochemical capacitors, International Society of Electrochemistry, Belgrade, Serbia, Virtual Conference (on-line), 30.08.2020 – 04.09.2020.

2. **M. Tobis***, E. Frackowiak,
   Carbon/ReS_2 composite as an Electrochemical Capacitor Electrode material operating in different aqueous and organic electrolytes, International Society of Electrochemistry,
   Jeju Island, South Korea, Virtual Conference (on-line), 29.08.2021 – 03.09.2021.
   The poster presentation was selected as a poster prize winner.

3. **M. Tobis***, E. Frackowiak,
   Carbon/MoS_2 composites modified with redox agents as an electrode material in supercapacitors, European Materials Research Society (EMRS) Spring Meeting, Virtual Conference (on-line), 30.05.2022 – 03.06.2022.

4. **M. Tobis***, E. Frackowiak,
   Redox response at electrode/electrolyte interface in carbon/TMDs composites, International Symposium on Enhanced Electrochemical Capacitors (ISEECAP) 2022, Bologna, Italy, 11.07.2022 – 15.07.2022.

5. **M. Tobis***, E. Frackowiak, S. Fleischmann
   Interlayer space optimization in MoS_2 for improved lithium intercalation kinetics, International Conference on Advanced Capacitors (ICAC), 26.09.2023 – 29.09.2023, Kamakura, Japan.
   The poster presentation was selected as a poster prize winner.

***denotes presenting author**

Participation in scientific projects

1. **Preludium 20** (2021/41/N/ST5/01364), National Science Centre
   Project title: *Influence of redox pairs on hydrogen evolution overpotential of dichalcogenides*
   Role: Principal investigator

2. **OPUS 16** (2018/31/B/ST4/01852), National Science Centre
   Project title: *Study of electrode/electrolyte interface of high stability and quick charge response*
   Principal investigator: Prof. Elżbieta Frąckowiak
   Role: Young scientist

3. **TEAM TECH**, Foundation for Polish Science
   Project title: *A new generation of high Energy hybrid capacitors – HYCAP*
   Principal investigator: Prof. Francois Beguin
   Role: Master student

Short scientific internship

1. **Funding institution:** Research internship under the STER Mobility program (co-financed by NAWA)
   Place of stay: Karlsruhe Institute of Technology (KIT),
   Helmholtz Institute Ulm (HIU), Ulm, Germany,
   Project title: *Investigation of energy storage mechanism of transition metal dichalcogenides (TMDs) with designed interlayer spacing*
   Scientific advisor: dr. Simon Fleischmann
   Role: Visiting PhD Student
   30.03.2023 – 30.06.2023 (3 months)

Awards

1. **Master thesis award:**
   2nd place award in “Competition for an outstanding diploma thesis in the field of technology and organization of production and services” conducted by Federation of Scientific and Technical Associations – 2020, Poznan Council, Poland

2. **Cover picture of Small journal magazine:**
   E. Frackowiak, M. Foroutan Koudahi, **M. Tobis**,
   Electrochemical capacitor performance of nanotextured carbon/transition metal dichalcogenides composites, Small 17 (2021) 2006821

3. **Poster prize**:
   M. Tobis, E. Frackowiak, S. Fleischmann
   Interlayer space optimization in MoS_2 for improved lithium intercalation kinetics, International Conference on Advanced Capacitors (ICAC), 26.09.2023 – 29.09.2023, Kamakura, Japan

4. **Poster prize:**
   M. Tobis, E. Frackowiak,
   Carbon/ReS_2 composite as an Electrochemical Capacitor Electrode material operating in different aqueous and organic electrolytes, International Society of Electrochemistry,
   Jeju Island, South Korea, Virtual Conference (on-line), 29.08.2021 – 03.09.2021

5. **1st place in the PUT START UP competition for the best business idea**
   "PUT START UP" aims to select the most promising and innovative projects and promote academic entrepreneurship

Other

1. Member of the Polish Carbon Society
2. Member of the International Society of Electrochemistry
3. Participation in the course 'Battery energy storages in smart grids' – Eunice European University
4. Participation in the gas adsorption training, ASAP 2460 – Gas Adsorption - Training Micromeritics Instrument Corporation

References

[1] P. Weingart, A. Engels, P. Pansegrau, Risks of communication: discourses on climate change in science, politics, and the mass media, Public understanding of science 3 (2000), 261-283.

[2] M. Lineman, Y. Do, J.Y. Kim, G.-J. Joo, Talking about Climate Change and Global Warming, PloS one 9 (2015) 138996.

[3] S. Li, Y.W. Siu, G. Zhao, Driving Factors of CO_2 Emissions: Further Study Based on Machine Learning, Frontiers in Environmental Science 9 (2021) 721517.

[4] https://climate.ec.europa.eu/climate-change/causes-climate-change_en.

[5] P. Ratajczak, M. E. Suss, F. Kaasik, F. Beguin, Carbon electrodes for capacitive technologies, Energy Storage Materials 16 (2019) 126-145.

[6] M. Winter, R.J. Brodd, What Are Batteries, Fuel Cells, and Supercapacitors?, Chemical reviews 10 (2004) 4245-4270.

[7] P. Simon, Y. Gogotsi, Perspectives for electrochemical capacitors and related devices, Nature materials 11 (2020) 1151-1163.

[8] B. E. Conway, Electrochemical Supercapacitors: Scientific Fundamentals and Technological Applications, 1 ed., Springer, Boston, MA, 1999.

[9] J. R. Miller, P. Simon, The Chalkboard: Fundamentals of Electrochemical Capacitor Design and Operation, The Electrochemical Society interface 1 (2008) 31-32.

[10] R. Kötz, M. Carlen, Principles and applications of electrochemical capacitors, Electrochimica acta 15 (2000) 2483-2498.

[11] H. Shao, Y.-C. Wu, Z. Lin, P.-L. Taberna, P. Simon, Nanoporous carbon for electrochemical capacitive energy storage, Chemical Society reviews 1 (2020) 3005-339.

[12] A. Balducci, D. Belanger, T. Brousse, J. W. Long, W. Sugimoto, Perspective-A Guideline for Reporting Performance Metrics with Electrochemical Capacitors: From Electrode Materials to Full Devices, Journal of the Electrochemical Society 164(7) (2017) A1487-A1488.

[13] A. Burke, Ultracapacitors: why, how, and where is the technology, Journal of power sources 91(1) (2000) 37-50.

[14] L. L. Zhang, X. S. Zhao, Carbon-based materials as supercapacitor electrodes, Chemical Society reviews 38(9) (2009) 2520-2531.

[15] T. Placke, R. Kloepsch, S. Dühnen, M. Winter, Lithium ion, lithium metal, and alternative rechargeable battery technologies: the odyssey for high energy density, Journal of solid state electrochemistry 21(7) (2017) 1939-1964.

[16] Z. Du, D.L. Wood, C. Daniel, S. Kalnaus, J. Li, Understanding limiting factors in thick electrode performance as applied to high energy density Li-ion batteries, Journal of applied electrochemistry 47(3) (2017) 405-415.

[17] H. Helmholtz, Ueber einige Gesetze der Vertheilung elektrischer Ströme in körperlichen Leitern mit Anwendung auf die thierisch-elektrischen Versuche, Annalen der Physik 165(6) (1853) 211-233.

[18] F. Béguin, V. Presser, A. Balducci, E. Frackowiak, Carbons and Electrolytes for Advanced Supercapacitors, Advanced materials (Weinheim) 26(14) (2014) 2219-2251.

[19] J. R. Miller, Introduction to electrochemical capacitor technology, IEEE electrical insulation magazine 26(4) (2010) 40-47.

[20] C. L. David, A contribution to the theory of electrocapillarity, The London, Edinburgh, and Dublin Philosophical Magazine and Journal of Science 25(148) (1913) 475-481.

[21] S. Otto, Zur Theorie der Elektrolytischen Doppelschnicht, Zeitschrift für Elektrochemie und angewandte Physikalische Chemie 30(21-22) (1924) 508-516.

[22] D. C. Grahame, The Electrical Double Layer and the Theory of Electrocapillarity, Chemical reviews 41(3) (1947) 441-501.

[23] J. Bockris, M. Devanathan, K. Müller, On the Structure of Charged Interfaces, Proceedings of the Royal Society of London. Series A, Mathematical and physical sciences 274(1356) (1963) 55-79.

[24] D. C. Grahame, Properties of the Electrical Double Layer at a Mercury Surface. I. Methods of Measurement and Interpretation of Results, Journal of the American Chemical Society 63(5) (1941) 1207-1215.

[25] P. R. Bandaru, H. Yamada, R. Narayanan, M. Hoefer, Charge transfer and storage in nanostructures, Materials Science and Engineering: R: Reports 96 (2015) 1-69.

[26] P. M. Biesheuvel, S. Porada, J.E. Dykstra, The difference between Faradaic and non-Faradaic electrode processes. Preprint at https://arxiv.org/abs/1809.02930 (2018).

[27] C. Costentin, J.-M. Savéant, Energy storage: pseudocapacitance in prospect, Chemical science 1(22) (2019) 5656-5666.

[28] B. E. Conway, Transition from supercapacitor to battery behavior in electrochemical energy storage, Journal of The Electrochemical Society 138(6) (1991) 1539-1548.

[29] V. Augustyn, P. Simon, B. Dunn, Pseudocapacitive oxide materials for high-rate electrochemical energy storage, Energy & Environmental Science 7(5) (2014) 1597-1614.

[30] B. E. Conway, Two-dimensional and quasi-two-dimensional isotherms for Li intercalation and upd processes at surfaces, Electrochimica Acta 38(9) (1993) 1249-1258.

[31] P. Bhojane, Recent advances and fundamentals of Pseudocapacitors: Materials, mechanism, and its understanding, Journal of Energy Storage 45 (2022) 103654.

[32] P. Simon, Y. Gogotsi, B. Dunn, Where Do Batteries End and Supercapacitors Begin?, Science 343(6176) (2014) 1210-1211.

[33] S. Deebansok, J. Deng, E. Le Calvez, Y. Zhu, O. Crosnier, T. Brousse, O. Fontaine, Capacitive tendency concept alongside supervised machine-learning toward classifying electrochemical behavior of battery and pseudocapacitor materials, Nature communications 15(1) (2024) 1133-1133.

[34] S. Fleischmann, J. B. Mitchell, R. Wang, C. Zhan, D.-E. Jiang, V. Presser, V. Augustyn, Pseudocapacitance: From Fundamental Understanding to High Power Energy Storage Materials, Chemical Reviews 120(14) (2020) 6738-6782.

[35] B. E. Conway, H. Angerstein-Kozlowska, The electrochemical study of multiple-state adsorption in monolayers, Accounts of Chemical Research 14(2) 49-56.

[36] A. Szczepanska, N. Vasiljevic, Surface Alloying During Pb Underpotential Deposition on Au(111), Journal of the Electrochemical Society 169(11) (2022) 112509.

[37] B. Łosiewicz, R. Jurczakowski, A. Lasia, Kinetics of hydrogen underpotential deposition at iridium in sulfuric and perchloric acids, Electrochimica Acta 225 (2017) 160-167.

[38] L. Demarconnay, E. Raymundo-Piñero, F. Béguin, A symmetric carbon/carbon supercapacitor operating at 1.6 V by using a neutral aqueous solution, Electrochemistry Communications 12(10) (2010) 1275-1278.

[39] M. J. Bleda-Martinez, J. M. Perez, A. Linares-Solano, E. Morallon, D. Cazorla-Amoros, Effect of surface chemistry on electrochemical storage of hydrogen in porous carbon materials, Carbon 46(7) (2008) 1053-1059.

[40] Q. Abbas, B. Gollas, V. Presser, Reduced Faradaic Contributions and Fast Charging of Nanoporous Carbon Electrodes in a Concentrated Sodium Nitrate Aqueous Electrolyte for Supercapacitors, Energy Technology 7(9) (2019) 1900430.

[41] C. Vix-Guterl, E. Frackowiak, K. Jurewicz, M. Friebe, J. Parmentier, F. Béguin, Electrochemical energy storage in ordered porous carbon materials, Carbon 43(6) (2005) 1293-1302.

[42] Q. Gao, L. Demarconnay, E. Raymundo-Piñero, F. Béguin, Exploring the large voltage range of carbon/carbon supercapacitors in aqueous lithium sulfate electrolyte, Energy & Environmental Science 5(11) (2012) 9611-9617.

[43] F. Béguin, K. Kierzek, M. Friebe, A. Jankowska, J. Machnikowski, K. Jurewicz, E. Frackowiak, Effect of various porous nanotextures on the reversible electrochemical sorption of hydrogen in activated carbons, Electrochimica Acta 51(11) (2006) 2161-2167.

[44] D. Qu, Mechanism for electrochemical hydrogen insertion in carbonaceous materials, Journal of power sources 179(1) (2008) 310-316.

[45] G. Lota, K. Fic, K. Jurewicz, E. Frackowiak, Correlation of hydrogen capacity in carbon material with the parameters of electrosorption, Central European Journal of Chemistry 9(1) (2011) 20-24.

[46] K. Jurewicz, E. Frackowiak, F. Béguin, Nanoporous H-sorbed carbon as anode of secondary cell, Journal of power sources 188(2) (2009) 617-620.

[47] B. E. Conway, V. Birss, J. Wojtowicz, The role and utilization of pseudocapacitance for energy storage by supercapacitors, Journal of power sources 66(1) (1997) 1-14.

[48] T. Brousse, M. Toupin, D. Belanger, A hybrid activated carbon-manganese dioxide capacitor using a mild aqueous electrolyte, Journal of the Electrochemical Society 151(4) (2004) 614-622.

[49] H. Y. Lee, J. B. Goodenough, Supercapacitor Behavior with KCl Electrolyte, Journal of Solid State Chemistry 144(1) (1999) 220-223.

[50] M. Toupin, T. Brousse, D. Bélanger, Charge Storage Mechanism of MnO_2 Electrode Used in Aqueous Electrochemical Capacitor, Chemistry of Materials 16(16) (2004) 3184-3190.

[51] J. P. Zheng, P. J. Cygan, T. R. Jow, Hydrous ruthenium oxide as an electrode material for electrochemical capacitors, Journal of the Electrochemical Society 142(8) (1995) 2699-2703.

[52] J. W. Long, K. E. Swider, C. I. Merzbacher, D. R. Rolison, Voltammetric Characterization of Ruthenium Oxide-Based Aerogels and Other RuO_2 Solids: The Nature of Capacitance in Nanostructured Materials, Langmuir 15(3) (1999) 780-785.

[53] W. Dmowski, T. Egami, K. E. Swider-Lyons, C. T. Love, D. R. Rolison, Local Atomic Structure and Conduction Mechanism of Nanocrystalline Hydrous RuO_2 from X-ray Scattering, The Journal of Physical Chemistry. B 106(49) (2002) 12677-12683.

[54] B. E. Conway, W. G. Pell, Double-layer and pseudocapacitance types of electrochemical capacitors and their applications to the development of hybrid devices, Journal of Solid State Electrochemistry 7(9) (2003) 637-644.

[55] V. Augustyn, J. Come, M. A. Lowe, J. W. Kim, P.-L. Taberna, S. H. Tolbert, H. D. Abruña, P. Simon, B. Dunn, High-rate electrochemical energy storage through Li^+ intercalation pseudocapacitance, Nature Materials 12(6) (2013) 518-522.

[56] M. Weiss, R. Ruess, J. Kasnatscheew, Y. Levartovsky, N. R. Levy, P. Minnmann, L. Stolz, T. Waldmann, M. Wohlfahrt-Mehrens, D. Aurbach, M. Winter, Y. Ein-Eli, J. Janek, Fast Charging of Lithium-Ion Batteries: A Review of Materials Aspects, Advanced Energy Materials 11(33) (2021) 2101126.

[57] T. Ohzuku, K. Sawai, T. Hirai, Electrochemistry of L-niobium pentoxide a lithium/non-aqueous cell, Journal of power sources 19(4) (1987) 287-299.

[58] J.W. Kim, V. Augustyn, B. Dunn, The Effect of Crystallinity on the Rapid Pseudocapacitive Response of Nb_2O_5, Advanced Energy Materials 2(1) (2012) 141-148.

[59] A. A. Lubimtsev, P. R. C. Kent, B. G. Sumpter, P. Ganesh, Understanding the origin of high-rate intercalation pseudocapacitance in Nb_2O_5 crystals, Journal of Materials Chemistry. A 1(47) (2013) 14951.

[60] J. Come, V. Augustyn, J.W. Kim, P. Rozier, P.-L. Taberna, P. Gogotsi, J.W. Long, B. Dunn, P. Simon, Electrochemical Kinetics of Nanostructured Nb_2O_5 Electrodes, Journal of the Electrochemical Society 161(5) (2014) A718-A725.

[61] C. Zhan, D.-e. Jiang, Understanding the pseudocapacitance of RuO_2 from joint density functional theory, Journal of Physics Condensed Matter 28(46) (2016) 464004.

[62] W. Guo, C. Yu, S. Li, Z. Wang, J. Yu, H. Huang, J. Qiu, Strategies and insights towards the intrinsic capacitive properties of MnO_2 for supercapacitors: Challenges and perspectives, Nano Energy 57 (2019) 459-472.

[63] X. Han, Q. Meng, X. Wan, B. Sun, Y. Zhang, B. Shen, J. Gao, Y. Ma, P. Zuo, S. Lou, G. Yin, Intercalation pseudocapacitive electrochemistry of Nb-based oxides for fast charging of lithium-ion batteries, Nano Energy 81 (2021) 105635.

[64] D. Li, H. Zhou, Two-phase transition of Li-intercalation compounds in Li-ion batteries, Materials today 17(9) (2014) 451-463.

[65] A. Van der Ven, J. Bhattacharya, A. A. Belak, Understanding Li Diffusion in Li-Intercalation Compounds, Accounts of Chemical Research 46(5) (2013) 1216-1225.

[66] Y.-M. Choi, S.-I. Pyun, Effects of intercalation-induced stress on lithium transport through porous $LiCoO_2$ electrode, Solid State Ionics 99(3) (1997) 173-183.

[67] M. Okubo, E. Hosono, J. Kim, M. Enomoto, N. Kojima, T. Kudo, H. Zhou, I. Honma, Nanosize Effect on High-Rate Li-Ion Intercalation in $LiCoO_2$ Electrode, Journal of the American Chemical Society 129(23) (2007) 7444-7452.

[68] W. Bergh, M. Stefik, Understanding Rapid Intercalation Materials One Parameter at a Time, Advanced Functional Materials 32(31) (2022) 2204126.

[69] M. R. Lukatskaya, B. Dunn, Y. Gogotsi, Multidimensional materials and device architectures for future hybrid energy storage, Nature communications 7(1) (2016) 12647-12647.

[70] S. Fleischmann, Y. Zhang, X. Wang, P. T. Cummings, J. Wu, P. Simon, Y. Gogotsi, V. Presser, V. Augustyn, Continuous transition from double-layer to Faradaic charge storage in confined electrolytes, Nature Energy 7(3) (2022) 222-228.

[71] B. Pal, S. Yang, S. Ramesh, V. Thangadurai, R. Jose, Electrolyte selection for supercapacitive devices: a critical review, Nanoscale Advances 1(1) (2019) 3807-3835.

[72] S. Samantaray, D. Mohanty, I.M. Hung, M. Moniruzzaman, S.K. Satpathy, Unleashing recent electrolyte materials for next-generation supercapacitor applications: A comprehensive review, Journal of Energy Storage 72 (2023) 108352.

[73] E. Frackowiak, G. Lota, J. Pernak, Room-temperature phosphonium ionic liquids for supercapacitor application, Applied Physics Letters 86(16) (2005) 164104.

[74] S. Azmi, A. Klimek, E. Frackowiak, Why electrochemical capacitor electrolytes should not be ignored?, Electrochimica acta 452 (2023) 142347.

[75] K. Fic, A. Platek, J. Piwek, J. Menzel, A. Slesinski, P. Bujewska, P. Galek, E. Frackowiak, Revisited insights into charge storage mechanisms in electrochemical capacitors with Li_2SO_4-based electrolyte, Energy Storage Materials 22 (2019) 1-14.

[76] K. Fic, M. He, E. J. Berg, P. Novák, E. Frackowiak, Comparative operando study of degradation mechanisms in carbon-based electrochemical capacitors with Li_2SO_4 and $LiNO_3$ electrolytes, Carbon 120 (2017) 281-293.

[77] M. He, K. Fic, E. Frackowiak, P. Novák, E. J. Berg, Ageing phenomena in high-voltage aqueous supercapacitors investigated by in situ gas analysis, Energy & Environmental Science 9(2) (2016) 623-633.

[78] J. Piwek, A. Platek, E. Frackowiak, K. Fic, Mechanisms of the performance fading of carbon-based electrochemical capacitors operating in a $LiNO_3$ electrolyte, Journal of Power Sources 438 (2019) 227029.

[79] A. Platek, J. Piwek, K. Fic, E. Frackowiak, Ageing mechanisms in electrochemical capacitors with aqueous redox-active electrolytes, Electrochimica Acta 311 (2019) 211-220.

[80] V. Ruiz, R. Santamaría, M. Granda, C. Blanco, Long-term cycling of carbon-based supercapacitors in aqueous media, Electrochimica Acta 54(19) (2009) 4481-4486.

[81] E. Frackowiak, Q. Abbas, F. Beguin, Carbon/carbon supercapacitors, Journal of Energy Chemistry 22(2) (2013) 226-240.

[82] L. Köps, F. A. Kreth, D. Leistenschneider, K. Schutjajew, R. Gläßner, M. Oschatz, A. Balducci, Improving the Stability of Supercapacitors at High Voltages and High Temperatures by the Implementation of Ethyl Isopropyl Sulfone as Electrolyte Solvent, Advanced Energy Materials 13(5) (2023) 2203821.

[83] K. Lota, A. Sierczynska, I. Acznik, G. Lota, Effect of aqueous electrolytes on electrochemical capacitor capacitance, Chemik 67(11) (2013) 1138-1145.

[84] P. Ratajczak, K. Jurewicz, F. Béguin, Factors contributing to ageing of high voltage carbon/carbon supercapacitors in salt aqueous electrolyte, Journal of Applied Electrochemistry 44(4) (2014) 475-480.

[85] S. Azmi, A. Klimek, E. Frackowiak, Anticorrosive performance of green deep eutectic solvent for electrochemical capacitor, Chemical Engineering Journal 444 (2022) 136594.

[86] Q. T. Qu, B. Wang, L. C. Yang, Y. Shi, S. Tian, Y. P. Wu, Study on electrochemical performance of activated carbon in aqueous Li_2SO_4, Na_2SO_4 and K_2SO_4 electrolytes, Electrochemistry Communications 10(10) (2008) 1652-1655.

[87] K. Fic, G. Lota, M. Meller, E. Frackowiak, Novel insight into neutral medium as electrolyte for high-voltage supercapacitors, Energy & Environmental Science 5(2) (2012) 5842-585.

[88] R. Chandrasekaran, M. Koh, A. Yamauchi, M. Ishikawa, Electrochemical Study on Aqueous Magnesium Nitrate Electrolyte System for EDLC Applications, Electrochemistry 77(1) (2009) 51-55.

[89] J. Jiang, B. Liu, G. Liu, D. Qian, C. Yang, J. Li, A systematically comparative study on $LiNO_3$ and Li_2SO_4 aqueous electrolytes for electrochemical double-layer capacitors, Electrochimica Acta 274 (2018) 121-130.

[90] S. Gharouel, F. Béguin, Revisiting the performance of electrical double-layer capacitors implementing a sodium perchlorate water-in-salt electrolyte, Electrochimica Acta 450 (2023) 142212.

[91] J. Yin, C. Zheng, L. Qi, H. Wang, Concentrated $NaClO_4$ aqueous solutions as promising electrolytes for electric double-layer capacitors, Journal of Power Sources 196(8) 4080-4087.

[92] S. Azmi, A. Klimek, E. Frackowiak, Electrochemical capacitor in aqueous electrolyte with long lifespan improved by hydrogen bond donor addition, Materials Today 68 (2023) 34-50.

[93] E. Frackowiak, K. Fic, M. Meller, G. Lota, Electrochemistry Serving People and Nature: High-Energy Ecocapacitors based on Redox-Active Electrolytes, ChemSusChem 5(7) (2012) 1181-1185.

[94] K. Fic, S. Morimoto, E. Frąckowiak, M. Ishikawa, Redox Activity of Bromides in Carbon-Based Electrochemical Capacitors, Batteries & Supercaps 3(10) (2020) 1080-1090.

[95] G. Lota, E. Frackowiak, Striking capacitance of carbon/iodide interface, Electrochemistry communications 11(1) (2009) 87-90.

[96] M. Pourbaix, Atlas of Electrochemical Equilibria in Aqueous Solutions, NACE International 1974.

[97] Q. Abbas, H. Fitzek, H. Schröttner, S. Dsoke, B. Gollas, Immobilization of Polyiodide Redox Species in Porous Carbon for Battery-Like Electrodes in Eco-Friendly Hybrid Electrochemical Capacitors, Nanomaterials 9(10) (2019) 1413.

[98] E. Frackowiak, M. Meller, J. Menzel, D. Gastol, K. Fic, Redox-active electrolyte for supercapacitor application, Faraday Discussions 172 (2014) 179-198.

[99] P. Przygocki, Q. Abbas, P. Babuchowska, F. Béguin, Confinement of iodides in carbon porosity to prevent from positive electrode oxidation in high voltage aqueous hybrid electrochemical capacitors, Carbon 125 (2017) 391-400.

[100] J. Menzel, K. Fic, M. Meller, E. Frackowiak, The effect of halide ion concentration on capacitor performance, Journal of Applied Electrochemistry 44(4) (2014) 439-445.

[101] P. Przygocki, Q. Abbas, F. Béguin, Capacitance enhancement of hybrid electrochemical capacitor with asymmetric carbon electrodes configuration in neutral aqueous electrolyte, Electrochimica Acta 269 (2018) 640-648.

[102] P. Simon, Y. Gogotsi, Materials for electrochemical capacitors, Nature materials 7(11) (2008) 845-854.

[103] F. Beguin, E. Frackowiak, Supercapacitors: Materials, Systems, and Applications, John Wiley & Sons, Incorporated, Weinheim, 2013.

[104] J. Krummacher, C. Schütter, L.H. Hess, A. Balducci, Non-aqueous electrolytes for electrochemical capacitors, Current Opinion in Electrochemistry 9 (2018) 64-69.

[105] Skeleton Tech and Siemens ink pact to make supercapacitors, Autocar Professional (2022).

[106] T. Welton, Room-Temperature Ionic Liquids. Solvents for Synthesis and Catalysis, Chemical Reviews 99(8) (1999) 2071-2084.

[107] L. Timperman, F. Béguin, E. Frackowiak, M. Anouti, Comparative Study of Two Protic Ionic Liquids as Electrolyte for Electrical Double-Layer Capacitors, Journal of the Electrochemical Society 161(3) (2014) A228-A238.

[108] P. Przygocki, Q. Abbas, B. Gorska, F. Béguin, High-energy hybrid electrochemical capacitor operating down to −40 °C with aqueous redox electrolyte based on choline salts, Journal of Power Sources 427 (2019) 283-292.

[109] E. Pameté, B. Gorska, F. Béguin, Binary mixtures of ionic liquids based on EMIm cation and fluorinated anions: physico-chemical characterization in view of their application as low-temperature electrolytes, Journal of Molecular Liquids 298 (2020) 111959.

[110] M. Larriba, P. Navarro, J.-B. Beigbeder, J. García, F. Rodríguez, Mixing and decomposition behavior of {[4bmpy][Tf2N]+[emim][EtSO4]} and {[4bmpy][Tf2N]+[emim][TFES]} ionic liquid mixtures, The Journal of Chemical Thermodynamics 82 (2015) 58-75.

[111] E. P. Yambou, B. Gorska, F. Béguin, Electrical Double-Layer Capacitors Based on a Ternary Ionic Liquid Electrolyte Operating at Low Temperature with Realistic Gravimetric and Volumetric Energy Outputs, ChemSusChem 14(4) (2021) 1196-1208.

[112] B. Scrosati, M. Armand, F. Endres, D. R. MacFarlane, H. Ohno, Ionic-liquid materials for the electrochemical challenges of the future, Nature materials 8(8) (2009) 621-629.

[113] R. Futamura, T. Iiyama, Y. Takasaki, Y. Gogotsi, M.J. Biggs, M. Salanne, J. Ségalini, P. Simon, K. Kaneko, Partial breaking of the Coulombic ordering of ionic liquids confined in carbon nanopores, Nature materials 16(12) (2017) 1225-1232.

[114] E. Pameté, B. Gorska, V. Pavlenko, F. Beguin, Fitting the porous texture of carbon electrodes to a binary ionic liquid electrolyte for the realization of low temperature EDLCs, Electrochimica Acta 350 (2020) 136416.

[115] M. Galiński, A. Lewandowski, I. Stępniak, Ionic liquids as electrolytes, Electrochimica Acta 51(26) (2006) 5567-5580.

[116] A. Brandt, S. Pohlmann, A. Varzi, A. Balducci, S. Passerini, Ionic liquids in supercapacitors, MRS Bulletin 38(7) (2013) 554-559.

[117] A. M. O'Mahony, D. S. Silvester, L. Aldous, C. Hardacre, R. G. Compton, Effect of Water on the Electrochemical Window and Potential Limits of Room-Temperature Ionic Liquids, Journal of Chemical and Engineering Data 53(12) (2008) 2884-2891.

[118] C. Arbizzani, M. Biso, D. Cericola, M. Lazzari, F. Soavi, M. Mastragostino, Safe, high-energy supercapacitors based on solvent-free ionic liquid electrolytes, Journal of Power Sources 185(2) (2008) 1575-1579.

[119] A. Balducci, R. Dugas, P. L. Taberna, P. Simon, D. Plée, M. Mastragostino, S. Passerini, High temperature carbon–carbon supercapacitor using ionic liquid as electrolyte, Journal of Power Sources 165(2) (2007) 922-927.

[120] L. Yu, G. Z. Chen, Ionic Liquid-Based Electrolytes for Supercapacitor and Supercapattery, Frontiers in Chemistry 7 (2019) 272-272.

[121] E. Frackowiak, F. Béguin, Carbon materials for the electrochemical storage of energy in capacitors, Carbon 39(6) (2001) 937-950.

[122] H. Shi, Activated carbons and double layer capacitance, Electrochimica Acta 41(10) (1996) 1633-1639.

[123] E. Frackowiak, Carbon materials for supercapacitor application, Physical Chemistry Chemical Physics : PCCP 9(15) (2007) 1774-1785.

[124] E. Frackowiak, K. Metenier, V. Bertagna, F. Beguin, Supercapacitor electrodes from multiwalled carbon nanotubes, Applied Physics Letters 77(15) (2000) 2421-2423.

[125] E. Frackowiak, F. Béguin, Electrochemical storage of energy in carbon nanotubes and nanostructured carbons, Carbon 40(10) (2002) 1775-1787.

[126] P. Simon, Y. Gogotsi, Capacitive Energy Storage in Nanostructured Carbon–Electrolyte Systems, Accounts of Chemical Research 46(5) (2013) 1094-1103.

[127] I. Padron-Ramirez, N. Torres-Figueredo, A. L. Corcho-Valdes, J. P. de Leon-Cabrera, F. J. Chao-Mujica, K. V. Cruz, M. Antuch, J. Deschamps, E. Reguera, L. F. Desdin-Garcia, Methane and carbon dioxide adsorption on carbon nano-onions synthesized by the submerged arc-discharge method, Adsorption 30(1) (2024) 25-38.

[128] M. Giorcelli, M. Bartoli, Carbon Nanostructures for Actuators: An Overview of Recent Developments, Actuators 8(2) (2019) 46.

[129] S. Priyadarsini, S. Mohanty, S. Mukherjee, S. Basu, M. Mishra, Graphene and graphene oxide as nanomaterials for medicine and biology application, Journal of Nanostructure in Chemistry 8(2) (2018) 123-137.

[130] H. Badenhorst, A review of the application of carbon materials in solar thermal energy storage, Solar Energy 192 (2019) 35-68.

[131] M. Zhang, J. Li, Carbon nanotube in different shapes, Materials Today 12(6) (2009) 12-18.

[132] T. Hayashi, M. Endo, Carbon nanotubes as structural material and their application in composites, Composites Part B: Engineering 42(8) (2011) 2151-2157.

[133] T. W. Ebbesen, P. M. Ajayan, Large-scale synthesis of carbon nanotubes, Nature 358(6383) (1992) 220-222.

[134] B. Lobato, L. Suárez, L. Guardia, T. A. Centeno, Capacitance and surface of carbons in supercapacitors, Carbon 122 (2017) 434-445.

[135] A. Peigney, C. Laurent, E. Flahaut, R. R. Bacsa, A. Rousset, Specific surface area of carbon nanotubes and bundles of carbon nanotubes, Carbon 39(4) (2001) 507-514.

[136] J. Wang, X. Guo, R. Cui, H. Huang, B. Liu, Y. Li, D. Wang, D. Zhao, J. Dong, S. Li, B. Sun, MnO_2/Porous Carbon Nanotube/MnO_2 Nanocomposites for High-Performance Supercapacitor, ACS Applied Nano Materials 3(11) (2020) 11152-11159.

[137] L. Du, P. Yang, X. Yu, P. Liu, J. Song, W. Mai, Flexible supercapacitors based on carbon nanotube/MnO_2 nanotube hybrid porous films for wearable electronic devices, Journal of Materials Chemistry A 2(41) (2014) 17561-17567.

[138] H. Zhang, G. Cao, Z. Wang, Y. Yang, Z. Shi, Z. Gu, Growth of manganese oxide nanoflowers on vertically-aligned carbon nanotube arrays for high-rate electrochemical capacitive energy storage, Nano Letters 8(9) (2008) 2664-2668.

[139] J. H. Park, J.M. Ko, O. O. Park, Carbon nanotube/RuO_2 nanocomposite electrodes for supercapacitors, Journal of the Electrochemical Society 150(7) (2003) A864-A867.

[140] P. Wang, Y. Xu, H. Liu, Y. Chen, J. Yang, Q. Tan, Carbon/carbon nanotube-supported RuO_2 nanoparticles with a hollow interior as excellent electrode materials for supercapacitors, Nano Energy 15 (2015) 116-124.

[141] C. Shi, K. Xiang, Y. Zhu, X. Chen, W. Zhou, H. Chen, Preparation and electrochemical properties of nanocable-like Nb_2O_5/surface-modified carbon nanotubes composites for anode materials in lithium ion batteries, Electrochimica Acta 246 (2017) 1088-1096.

[142] D. Thanasamy, D. Jesuraj, V. Avadhanam, K. Chinnadurai, S. K. K. Kannan, Microstructural effect of various polyaniline-carbon nanotube core-shell nanocomposites on electrochemical supercapacitor electrode performance, Journal of Energy Storage 53 (2022) 105087.

[143] A. Cymann, M. Sawczak, J. Ryl, E. Klugmann-Radziemska, M. Wilamowska-Zawlocka, Capacitance Enhancement by Incorporation of Functionalised Carbon Nanotubes into Poly(3,4-Ethylenedioxythiophene)/Graphene Oxide Composites, Materials 13(10) (2020) 2419.

[144] M. Tobis, J. Piwek, A. Platek-Mielczarek, L. Przypis, D. Janas, E. Frackowiak, Probing iodide/iodonium salt interactions with single-walled carbon nanotubes for resilient electrochemical capacitor, Electrochimica Acta 492 (2024) 144386.

[145] V. Khomenko, E. Frackowiak, F. Béguin, Determination of the specific capacitance of conducting polymer/nanotubes composite electrodes using different cell configurations, Electrochimica Acta 50(12) (2005) 2499-2506.

[146] H. Wang, J. Lin, Z.X. Shen, Polyaniline (PANi) based electrode materials for energy storage and conversion, Journal of Science: Advanced Materials and Devices 1(3) (2016) 225-255.

[147] E. Frąckowiak, M. Foroutan Koudahi, M. Tobis, Electrochemical Capacitor Performance of Nanotextured Carbon/Transition Metal Dichalcogenides Composites, Small 17(48) (2021) 2006821.

[148] P. J. F. Harris, New Perspectives on the Structure of Graphitic Carbons, Critical Reviews in Solid State and Materials Sciences 30(4) (2005) 235-253.

[149] S. Ergun, V. Tiensuu, Tetrahedral structures in amorphous carbons, Acta Crystallographica 12(12) (1959) 1050-1051.

[150] P. J. F. Harris, Fullerene-like models for microporous carbon, Journal of Materials Science 48(2) (2013) 565-577.

[151] P. H. Emmett, Adsorption and Pore-Size Measurements on Charcoals and Whetlerites, Chemical Reviews 43(1) (1948) 69-148.

[152] R. E. Franklin, Crystallite growth in graphitizing and non-graphitizing carbons, Proceedings of the Royal Society of London. Series A, Mathematical and physical sciences 209(1097) (1951) 196-218.

[153] M.-M. Titirici, Sustainable carbon materials from Hydrothermal Processes edited by Maria-Magdalena Titirici, 1st ed., Wiley, Chichester, England, 2013.

[154] D. Ye, Y. Yu, J. Tang, L. Liu, Y. Wu, Electrochemical activation of carbon cloth in aqueous inorganic salt solution for superior capacitive performance, Nanoscale 8(19) (2016) 10406-10414.

[155] X. Qu, Y.W. Kwon, S. Jeon, J. Jeong, W. Kang, Z. Jiang, C. Zhang, S.W. Hong, Foldable and wearable supercapacitors for powering healthcare monitoring applications with improved performance based on hierarchically co-assembled CoO/NiCo networks, Journal of Colloid and Interface Science 634 (2023) 715-729.

[156] S. Zhai, W. Jiang, L. Wei, H.E. Karahan, Y. Yuan, A.K. Ng, Y. Chen, All-carbon solid-state yarn supercapacitors from activated carbon and carbon fibers for smart textiles, Materials Horizons 2(6) 598-605.

[157] A. Platek-Mielczarek, C. Nita, C.I. Matei Ghimbeu, E. Frackowiak, K. Fic, Link between Alkali Metals in Salt Templates and in Electrolytes for Improved Carbon-Based Electrochemical Capacitors, ACS Applied Materials & Interfaces 13(2) (2021) 2584-2599.

[158] M. Jerigová, M. Odziomek, N. López-Salas, "We Are Here!" Oxygen Functional Groups in Carbons for Electrochemical Applications, ACS Omega 7(14) (2022) 11544-11554.

[159] X. Yang, Q. Wang, J. Lai, Z. Cai, J. Lv, X. Chen, Y. Chen, X. Zheng, B. Huang, G. Lin, Nitrogen-doped activated carbons via melamine-assisted NaOH/KOH/urea aqueous system for high performance supercapacitors, Materials Chemistry and Physics 250 (2020) 123201.

[160] F. Mo, H. Zhang, Y. Wang, C. Chen, X. Wu, Heteroatom-doped hierarchical porous carbon for high performance flexible all-solid-state symmetric supercapacitors, Journal of Energy Storage 49 (2022) 104122.

[161] J. Chen, Y. Lin, J. Liu, D. Wu, X. Bai, D. Chen, H. Li, Outstanding supercapacitor performance of nitrogen-doped activated carbon derived from shaddock peel, Journal of Energy Storage 39 (2021) 102640.

[162] S.-M. Li, S.-Y. Yang, Y.-S. Wang, H.-P. Tsai, H.-W. Tien, S.-T. Hsiao, W.-H. Liao, C.-L. Chang, C.-C. M. Ma, C.-C. Hu, N-doped structures and surface functional groups of reduced graphene oxide and their effect on the electrochemical performance of supercapacitor with organic electrolyte, Journal of Power Sources 278 (2015) 218-229.

[163] X.-r. Li, Y.-h. Jiang, P.-z. Wang, Y. Mo, W.-d. Lai, Z.-j. Li, R.-j. Yu, Y.-t. Du, X.-r. Zhang, Y. Chen, Effect of the oxygen functional groups of activated carbon on its electrochemical performance for supercapacitors, New Carbon Materials 35(3) (2020) 232-243.

[164] W. Dilokekunakul, P. Teerachawanwong, N. Klomkliang, S. Supasitmongkol, S. Chaemchuen, Effects of nitrogen and oxygen functional groups and pore width of activated carbon on carbon dioxide capture: Temperature dependence, Chemical Engineering Journal 389 (2020) 124413.

[165] Z. Li, H. Wu, D. Zhang, Q. Wang, H. Sun, Q. Sun, B. Wang, Revealing the mechanism of oxygen-containing functional groups on the capacitive behavior of activated carbon, Applied Surface Science 657 (2024).

[166] G. Shul, D. Bélanger, Self-discharge of electrochemical capacitors based on soluble or grafted quinone, Physical Chemistry Chemical Physics (PCCP) 18(28) (2016) 19137-19145.

[167] E. Pameté Yambou, B. Gorska, P. Ratajczak, F. Béguin, Hybrid capacitor with anthraquinone-grafted carbon as a battery-type electrode operating in a low pH aqueous salt solution, Journal of Materials Chemistr A 8(27) (2020) 13548-13557.

[168] K. S. Novoselov, A. K. Geim, S. V. Morozov, D. Jiang, Y. Zhang, S. V. Dubonos, I. V. Grigorieva, A. A. Firsov, Electric Field Effect in Atomically Thin Carbon Films, Science 306(5696) (2004) 666-669.

[169] J. C. Meyer, A. K. Geim, M. I. Katsnelson, K. S. Novoselov, T. J. Booth, S. Roth, The structure of suspended graphene sheets, Nature 446(7131) (2007) 60-63.

[170] M. D. Bhatt, H. Kim, G. Kim, Various defects in graphene: a review, RSC Advances 12(33) (2022) 2152-21547.

[171] R. Raccichini, A. Varzi, S. Passerini, B. Scrosati, The role of graphene for electrochemical energy storage, Nature Materials 14(3) (2015) 271-279.

[172] S. Gadipelli, Z.X. Guo, Graphene-based materials: Synthesis and gas sorption, storage and separation, Progress in materials science 69 (2015) 1-60.

[173] G. H. B. Dommett, R. S. Ruoff, E. J. Zimney, S. T. Nguyen, R. D. Piner, D. A. Dikin, S. Stankovich, K. M. Kohlhaas, E. A. Stach, Graphene-based composite materials, Nature 442(7100) (2006) 282-286.

[174] Q. Ke, J. Wang, Graphene-based materials for supercapacitor electrodes – A review, Journal of Materiomics 2(1) (2016) 37-54.

[175] L. Mao, K. Zhang, H. S. On Chan, J. Wu, Surfactant-stabilized graphene/polyaniline nanofiber composites for high performance supercapacitor electrode, Journal of Materials Chemistry 22(1) (2012) 80-85.

[176] Y. Zhao, H. Hao, T. Song, X. Wang, C. Li, W. Li, MnO_2-graphene based composites for supercapacitors: Synthesis, performance and prospects, Journal of Alloys and Compounds 914 (2022) 165343.

[177] M. Chhowalla, H. S. Shin, G. Eda, L.-J. Li, K. P. Loh, H. Zhang, The chemistry of two-dimensional layered transition metal dichalcogenide nanosheets, Nature chemistry 5(4) (2013) 263-275.

[178] N. S. Arul, V. D. Nithya, Two Dimensional Transition Metal Dichalcogenides Synthesis, Properties, and Applications, edited by Narayanasamy Sabari Arul, Vellalapalayam Devaraj Nithya, 1st ed 2019, Springer Singapore, Singapore, 2019.

[179] J. A. Wilson, A. D. Yoffe, The transition metal dichalcogenides discussion and interpretation of the observed optical, electrical and structural properties, Advances in Physics 18(73) (1969) 193-335.

[180] N. S. Arul, V. D. Nithya, Two-Dimensional Transition Metal Dichalcogenides: An Overview, Springer Singapore, Singapore, 2019, pp. 1-27.

[181] Q. H. Wang, K. Kalantar-Zadeh, A. Kis, J. N. Coleman, M. S. Strano, Electronics and optoelectronics of two-dimensional transition metal dichalcogenides, Nature Nanotechnology 7(11) (2012) 699-712.

[182] K. F. Mak, C. Lee, J. Hone, J. Shan, T.F. Heinz, Atomically thin MoS_2: a new direct-gap semiconductor, Physical Review Letters 105(13) (2010) 136805-136805.

[183] A. Splendiani, L. Sun, Y. Zhang, T. Li, J. Kim, C.-Y. Chim, G. Galli, F. Wang, Emerging Photoluminescence in Monolayer MoS_2, Nano letters 10(4) (2010) 1271-1275.

[184] M. Acerce, D. Voiry, M. Chhowalla, Metallic 1T phase MoS_2 nanosheets as supercapacitor electrode materials, Nature Nanotechnology 10(4) (2015) 313-318.

[185] Y. H. Lee, X. Q. Zhang, W. Zhang, M. T. Chang, C. T. Lin, K. D. Chang, Y. C. Yu, J. T. W. Wang, C. S. Chang, L. J. Li, T. W. Lin, Synthesis of Large-Area MoS_2 Atomic Layers with Chemical Vapor Deposition, Advanced materials 24(17) (2012) 2320-2325.

[186] Y. Zhan, Z. Liu, S. Najmaei, P. M. Ajayan, J. Lou, Large-Area Vapor-Phase Growth and Characterization of MoS_2 Atomic Layers on a SiO_2 Substrate, Small 8(7) (2012) 966-971.

[187] L. Seravalli, M. Bosi, A Review on Chemical Vapour Deposition of Two-Dimensional MoS_2 Flakes, Materials 14(24) (2021) 7590.

[188] X. Zheng, Y. Zhu, Y. Sun, Q. Jiao, Hydrothermal synthesis of MoS_2 with different morphology and its performance in thermal battery, Journal of Power Sources 395 (2018) 318-327.

[189] H. Cao, Z. Bai, Y. Li, Z. Xiao, X. Zhang, G. Li, Solvothermal Synthesis of Defect-Rich Mixed 1T-2H MoS_2 Nanoflowers for Enhanced Hydrodesulfurization, ACS Sustainable Chemistry & Engineering 8(19) (2020) 7343-7352.

[190] H. Huang, N. Liu, X. Wang, M. Zhong, X. Huang, Application of Hydrothermal and Solvothermal Method in Synthesis of MoS_2, Revista de Chimie 73(4) (2022) 26-35.

[191] Y. Liu, K. Wu, X.-l. Guo, W.-y. Wang, Y.-q. Yang, A comparison of MoS_2 catalysts hydrothermally synthesized from different sulfur precursors in their morphology and hydrodeoxygenation activity, Journal of Fuel Chemistry and Technology 46(5) (2018) 535-542.

[192] X. Luo, N. Li, X. Guo, K. Wu, One-pot hydrothermal synthesis of MoS_2 anchored corncob-derived carbon nanospheres for use as a high-capacity anode for reversible Li-ion battery, Journal of Solid State Chemistry 296 (2021) 122020.

[193] S. Duraisamy, A. Ganguly, P.K. Sharma, J. Benson, J. Davis, P. Papakonstantinou, One-Step Hydrothermal Synthesis of Phase-Engineered MoS_2/MoO_3 Electrocatalysts for Hydrogen Evolution Reaction, ACS Applied Nano Materials 4(3) (2021) 2642-2656.

[194] W.-J. Li, E.-W. Shi, J.-M. Ko, Z.-z. Chen, H. Ogino, T. Fukuda, Hydrothermal synthesis of MoS_2 nanowires, Journal of Crystal Growth 250(3-4) (2003) 418-422.

[195] H. Lin, X. Chen, H. Li, M. Yang, Y. Qi, Hydrothermal synthesis and characterization of MoS_2 nanorods, Materials Letters 64(15) (2010) 1748-1750.

[196] S. S. Karim, A. Sudais, M. S. Shah, S. Farrukh, S. Ali, M. Ahmed, Z. Salahuddin, X. F. Fan, A contemplating review on different synthesis methods of 2D-Molybdenum disulfide (MoS_2) nanosheets, Fuel 351 (2023) 128923.

[197] M. Tamulewicz-Szwajkowska, S. J. Zelewski, J. Serafińczuk, R. Kudrawiec, Geometric progress in the thickness of exfoliated van der Waals crystals on the example of MoS_2, AIP advances 12(2) (2022) 025328,1-7.

[198] R. A. Vaia, H. Ishii, E. P. Giannelis, Synthesis and properties of two-dimensional nanostructures by direct intercalation of polymer melts in layered silicates, Chemistry of Materials 5(12) (1993) 1694-1696.

[199] A. Jawaid, D. Nepal, K. Park, M. Jespersen, A. Qualley, P. Mirau, L. F. Drummy, R. A. Vaia, Mechanism for Liquid Phase Exfoliation of MoS_2, Chemistry of Materials 28(1) (2016) 337-348.

[200] D. Sahoo, B. Kumar, J. Sinha, S. Ghosh, S. S. Roy, B. Kaviraj, Cost effective liquid phase exfoliation of MoS_2 nanosheets and photocatalytic activity for wastewater treatment enforced by visible light, Scientific Reports 10(1) (2020) 10759-10759.

[201] A. Gupta, V. Arunachalam, S. Vasudevan, Liquid-Phase Exfoliation of MoS_2 Nanosheets: The Critical Role of Trace Water, The Journal of Physical Chemistry Letters 7(23) (2016) 4884-4890.

[202] F. Jiang, J. Xiong, W. Zhou, C. Liu, L. Wang, F. Zhao, H. Liu, J. Xu, Use of organic solvent-assisted exfoliated MoS_2 for optimizing the thermoelectric performance of flexible PEDOT:PSS thin films, Journal of Materials Chemistry A 4(14) (2016) 5265-5273.

[203] I. Janica, D. Iglesias, S. Ippolito, A. Ciesielski, P. Samori, Effect of temperature and exfoliation time on the properties of chemically exfoliated MoS_2 nanosheets, Chemical Communications 56(99) (2020) 15573-15576.

[204] Y. Liang, H. D. Yoo, Y. Li, J. Shuai, H. A. Calderon, F. C. Robles Hernandez, L. C. Grabow, Y. Yao, Interlayer-Expanded Molybdenum Disulfide Nanocomposites for Electrochemical Magnesium Storage, Nano letters 15(3) (2015) 2194-2202.

[205] M. Samadi, N. Sarikhani, M. Zirak, H. Zhang, H.-L. Zhang, A.Z. Moshfegh, Group 6 transition metal dichalcogenide nanomaterials: synthesis, applications and future perspectives, Nanoscale Horizons 3(2) (2018) 9-24.

[206] G. Eda, H. Yamaguchi, D. Voiry, T. Fujita, M. Chen, M. Chhowalla, Photoluminescence from Chemically Exfoliated MoS_2, Nano Letters 11(12) (2011) 5111-5116.

[207] A. S. Golub, G. A. Protsenko, L. V. Gumileva, A. G. Buyanovskaya, Y. N. Novikov, The formation of intercalation compounds of MoS_2 with cations of alkali metals and alkylammonium from monolayer dispersion of molybdenum disulfide, Russian Chemical Bulletin 42(4) (1993) 632-634.

[208] W. M. R. Divigalpitiya, R. F. Frindt, S. R. Morrison, Inclusion Systems of Organic Molecules in Restacked Single-Layer Molybdenum Disulfide, Science 246(4928) (1989) 369-371.

[209] X. Chen, A. R. McDonald, Functionalization of Two-Dimensional Transition-Metal Dichalcogenides, Advanced Materials 28(27) (2016) 5738-5746.

[210] K. C. Knirsch, N. C. Berner, H. C. Nerl, C. S. Cucinotta, Z. Gholamvand, N. McEvoy, Z. Wang, I. Abramovic, P. Vecera, M. Halik, S. Sanvito, G. S. Duesberg, V. Nicolosi, F. Hauke, A. Hirsch, J. N. Coleman, C. Backes, Basal-Plane Functionalization of Chemically Exfoliated Molybdenum Disulfide by Diazonium Salts, ACS Nano 9(6) (2015) 6018-6030.

[211] X. Chen, N. C. Berner, C. Backes, G. S. Duesberg, A. R. McDonald, Functionalization of Two-Dimensional MoS_2: On the Reaction Between MoS_2 and Organic Thiols, Angewandte Chemie 128(19) (2016) 5897-5902.

[212] M. Liu, H. Zhu, Y. Wang, C. Sevencan, B.L. Li, Functionalized MoS_2-Based Nanomaterials for Cancer Phototherapy and Other Biomedical Applications, ACS Materials Letters 3(5) (2021) 462-496.

[213] M. S. Whittingham, Electrical Energy Storage and Intercalation Chemistry, Science 192(4244) (1976) 1126-1127.

[214] M. S. Whittingham, History, Evolution, and Future Status of Energy Storage, Proceedings of the IEEE 100 (2012) 1518-1534.

[215] A. H. Thompson, Electron-Electron Scattering in TiS_2, Physical Review Letters 35(26) (1975) 1786-1789.

[216] G. A. Muller, J. B. Cook, H.-S. Kim, S. H. Tolbert, B. Dunn, High Performance Pseudocapacitor Based on 2D Layered Metal Chalcogenide Nanocrystals, Nano Letters 15(3) (2015) 1911-1917.

[217] S. Fleischmann, H. Shao, P.-L. Taberna, P. Rozier, P. Simon, Electrochemically Induced Deformation Determines the Rate of Lithium Intercalation in Bulk TiS_2, ACS energy letters 6(12) (2021) 4173-4178.

[218] J. B. Cook, T. C. Lin, H.-S. Kim, A. Siordia, B. S. Dunn, S. H. Tolbert, Suppression of Electrochemically Driven Phase Transitions in Nanostructured MoS_2 Pseudocapacitors Probed Using Operando X-ray Diffraction, ACS nano 13(2) (2019) 1223-1231.

[219] L. Zhang, D. Sun, J. Kang, J. Feng, H.A. Bechtel, L.-W. Wang, E.J. Cairns, J. Guo, Electrochemical Reaction Mechanism of the MoS_2 Electrode in a Lithium-Ion Cell Revealed by in Situ and Operando X-ray Absorption Spectroscopy, Nano letters 18(2) (2018) 1466-1475.

[220] X. Fang, C. Hua, X. Guo, Y. Hu, Z. Wang, X. Gao, F. Wu, J. Wang, L. Chen, Lithium storage in commercial MoS_2 in different potential ranges, Electrochimica Acta 81 (2012) 155-160.

[221] J. B. Cook, H. S. Kim, T. C. Lin, C. H. Lai, B. Dunn, S. H. Tolbert, Pseudocapacitive Charge Storage in Thick Composite MoS_2 Nanocrystal-Based Electrodes, Advanced Energy Materials 7(2) (2017) 1601283.

[222] S. J. Panchu, K. Raju, H. C. Swart, B. Chokkalingam, M. Maaza, M. Henini, M. K. Moodley, Luminescent MoS_2 Quantum Dots with Tunable Operating Potential for Energy-Enhanced Aqueous Supercapacitors, ACS omega 6(7) (2021) 4542-4550.

[223] G. Li, D. Zhang, Q. Qiao, Y. Yu, D. Peterson, A. Zafar, R. Kumar, S. Curtarolo, F. Hunte, S. Shannon, Y. Zhu, W. Yang, L. Cao, All The Catalytic Active Sites of MoS_2 for Hydrogen Evolution, Journal of the American Chemical Society 138(51) (2016) 16632-16638.

[224] Z. Liang, C. Zhao, W. Zhao, Y. Zhang, P. Srimuk, V. Presser, G. Feng, Molecular Understanding of Charge Storage in MoS_2 Supercapacitors with Ionic Liquids, Energy & Environmental Materials 4(4) (2021) 631-637.

[225] Q. Mahmood, S. K. Park, K. D. Kwon, S. J. Chang, J. Y. Hong, G. Shen, Y. M. Jung, T. J. Park, S. W. Khang, W. S. Kim, J. Kong, H. S. Park, Transition from Diffusion-Controlled Intercalation into Extrinsically Pseudocapacitive Charge Storage of MoS_2 by Nanoscale Heterostructuring, Advanced Energy Materials 6(1) (2016).

[226] Skeleton launches its SuperBattery and unveils Shell as partner, Contify Automotive News (2022).

[227] S. Liu, Y. Liu, L. Wanwan, X. Zhou, K. Xu, Q. Qiao, W.-H. Zhang, Few-layered ReS_2 nanosheets vertically aligned on reduced graphene oxide for superior lithium and sodium storage, Journal of Materials Chemistry A 6(41) (2018) 20267-20276.

[228] M. Rahman, K. Davey, S.Z. Qiao, Advent of 2D Rhenium Disulfide (ReS_2): Fundamentals to Applications, Advanced Functional Materials 27(10) (2017) 1606129.

[229] V.K. Singh, B. Mukherjee, S. Assa Aravindh, S. Das, Sulfonic acid (SO_3H) functionalized two-dimensional MoS_2 nanosheets for electrocatalytic hydrogen generation, Applied Surface Science 609 (2023) 155354.

[230] J. Chen, F. Li, Y. Tang, Q. Tang, Tuning the phase stability and surface HER activity of 1T '-MoS_2 by covalent chemical functionalization, Journal of materials chemistry C 8(44) (2020) 15852-15859.

[231] D.O. Li, X.S. Chu, Q.H. Wang, Reaction Kinetics for the Covalent Functionalization of Two-Dimensional MoS_2 by Aryl Diazonium Salts, Langmuir 35(17) (2019) 5693-5701.

Co-authorship statements

POLITECHNIKA POZNAŃSKA

Prof. Elżbieta Frąckowiak
Institute of Chemistry and Technical Electrochemistry
Poznan University of Technology, Berdychowo 4
60-965 Poznan, PL +48 61 665 36 32
e-mail: elzbieta.frackowiak@put.poznan.pl

Poznan, 14.05.2024

Declaration of individual contribution in publications

As the co-author of the following paper, I hereby declare that my contribution to this work was:

Article:	*Electrochemical Capacitor Performance of Nanotextured Carbon/Transition Metal Dichalcogenides Composites*
Authors:	**Elżbieta Frąckowiak**, Masoud Foroutan Koudahi, Maciej Tobis
Journal:	Small
DOI:	https://doi.org/10.1002/smll.202006821
Contribution:	Supervision, conceptualization, methodology, data curation, funding acquisition, writing (review and editing)

E. Frąckowiak

Signature

POLITECHNIKA POZNAŃSKA
Faculty of Chemical Technology
Institute of Chemistry and Technical Electrochemistry
ul. Berdychowo 4, 60-965 Poznan

Poznan, 27.03.2024

Declaration of individual contribution in publications

As the co-author of the following paper, I hereby declare that my contribution to this work was:

Article: *Electrochemical Capacitor Performance of Nanotextured Carbon/Transition Metal Dichalcogenides Composites*

Authors: Elżbieta Frąckowiak, **Masoud Foroutan Koudahi,** Maciej Tobis

Journal: Small

DOI: https://doi.org/10.1002/smll.202006821

Contribution: Synthesis of three-dimensional graphene, synthesis of FeS_2-based composites, physicochemical analysis, electrochemical characterization, data plotting, writing original draft

Signature

POLITECHNIKA POZNAŃSKA

mgr inż. Maciej Tobis
Instytut Chemii i Elektrochemii Technicznej
ul. Berdychowo 4, 60-965 Poznań
tel. +48 61 665 39 77
e-mail: maciej.p.tobis@doctorate.put.poznan.pl

Poznan, 14.05.2024

Declaration of individual contribution in publications

As the co-author of the following paper, I hereby declare that my contribution to this work was:

Article:	*Electrochemical Capacitor Performance of Nanotextured Carbon/Transition Metal Dichalcogenides Composites*
Authors:	Elżbieta Frąckowiak, Masoud Foroutan Koudahi, **Maciej Tobis**
Journal:	Small
DOI:	https://doi.org/10.1002/smll.202006821
Contribution:	Synthesis of ReS_2-based composites, physicochemical analysis, electrochemical characterization, data plotting, writing original draft

M. Tobis

Signature

POLITECHNIKA POZNAŃSKA
mgr inż. Maciej Tobis
Instytut Chemii i Elektrochemii Technicznej
ul. Berdychowo 4, 60-965 Poznań
tel. +48 61 665 39 77
e-mail: maciej.p.tobis@doctorate.put.poznan.pl

Poznan, 14.05.2024

Declaration of individual contribution in publications

As the co-author of the following paper, I hereby declare that my contribution to this work was:

Article: *Supercapacitor with Carbon/MoS_2 Composites*

Authors: **Maciej Tobis**, Sylwia Sroka, Elżbieta Frąckowiak

Journal: Frontiers in Energy Research

DOI: https://doi.org/10.3389/fenrg.2021.647878

Contribution: Conceptualization of the article, planning experiments, synthesis of carbon/MoS_2 composites, physicochemical analysis of prepared samples (Raman spectra, XRD, SEM/EDX, TEM), electrochemical investigation (two, and three-electrode cells), data plotting, writing original draft

M. Tobis
Signature

POLITECHNIKA POZNAŃSKA
Faculty of Chemical Technology
Institute of Chemistry and Technical Electrochemistry
ul. Berdychowo 4, 60-965 Poznan

Poznan, 14.05.2024

Declaration of individual contribution in publications

As the co-author of the following paper, I hereby declare that my contribution to this work was:

Article: *Supercapacitor with Carbon/MoS_2 Composites*

Authors: Maciej Tobis, **Sylwia Sroka**, Elżbieta Frąckowiak

Journal: Frontiers in Energy Research

DOI: https://doi.org/10.3389/fenrg.2021.647878

Contribution: Synthesis of carbon/MoS_2 composites, physicochemical analysis of prepared samples (Raman spectroscopy), electrochemical investigation (two, and three-electrode cells), writing original draft

Signature

POLITECHNIKA POZNAŃSKA

Prof. Elżbieta Frąckowiak
Institute of Chemistry and Technical Electrochemistry
Poznan University of Technology, Berdychowo 4
60-965 Poznan, PL +48 61 665 36 32
e-mail: elzbieta.frackowiak@put.poznan.pl

Poznan, 14.05.2024

Declaration of individual contribution in publications

As the co-author of the following paper, I hereby declare that my contribution to this work was:

Article:	*Supercapacitors with Carbon/MoS_2 Composites*
Authors:	Maciej Tobis, Sylwia Sroka, **Elżbieta Frąckowiak**
Journal:	Frontiers in Energy Research
DOI:	https://doi.org/10.3389/fenrg.2021.647878
Contribution:	Supervision, conceptualization, methodology, funding acquisition, writing (review and editing)

E. Frąckowiak
Signature

Louvain-la-Neuve, 31.05.2024

Declaration of individual contribution in publications

As the co-author of the following paper, I hereby declare that my contribution to this work was:

Article:	*Electrochemical Capacitor Based on Reduced Graphene Oxide/NiS_2 Composite*
Authors:	**Andrii Kachmar**, Maciej Tobis, Elżbieta Frąckowiak
Journal:	ChemElectroChem
DOI:	https://doi.org/10.1002/celc.202200834
Contribution:	Synthesis of reduced graphene oxide at different pH, synthesis of rGO/NiS_2 composites, performing and evaluation of physicochemical analyses (Raman spectroscopy, UV spectroscopy, XRD), conducting electrochemical studies in two- and three-electrode cells by different techniques, data plotting, writing original draft

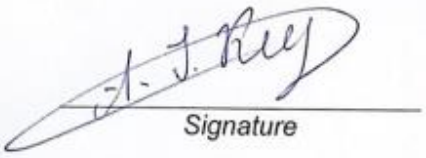

Signature

POLITECHNIKA POZNAŃSKA

mgr inż. Maciej Tobis
Instytut Chemii i Elektrochemii Technicznej
ul. Berdychowo 4, 60-965 Poznań
tel. +48 61 665 39 77
e-mail: maciej.p.tobis@doctorate.put.poznan.pl

Poznan, 14.05.2024

Declaration of individual contribution in publications

As the co-author of the following paper, I hereby declare that my contribution to this work was:

Article: *Electrochemical Capacitor Performance of Nanotextured Carbon/Transition Metal Dichalcogenides Composites*

Authors: Andrii Kachmar, **Maciej Tobis**, Elżbieta Frąckowiak

Journal: ChemElectroChem

DOI: https://doi.org/10.1002/celc.202200834

Contribution: Responsible for obtaining physicochemical characterization results (XRD patterns, N_2 sorption, SEM imaging, TEM imaging), evaluation of the physicochemical data (N_2 sorption, SEM and TEM imaging), performing electrochemical studies in two- and three-electrode cells by different techniques, data plotting, writing original draft

M. Tobis
Signature

POLITECHNIKA POZNAŃSKA

Prof. Elżbieta Frąckowiak
Institute of Chemistry and Technical Electrochemistry
Poznan University of Technology, Berdychowo 4
60-965 Poznan, PL +48 61 665 36 32
e-mail: elzbieta.frackowiak@put.poznan.pl

Poznan, 14.05.2024

Declaration of individual contribution in publications

As the co-author of the following paper, I hereby declare that my contribution to this work was:

Article:	*Electrochemical Capacitor Performance of Nanotextured Carbon/Transition Metal Dichalcogenides Composites*
Authors:	Andrii Kachmar, Maciej Tobis, **Elżbieta Frąckowiak**
Journal:	ChemElectroChem
DOI:	https://doi.org/10.1002/celc.202200834
Contribution:	Supervision, conceptualization, funding acquisition, methodology, writing (review and editing)

E. Frąckowiak

Signature

POLITECHNIKA POZNAŃSKA

mgr inż. Maciej Tobis
Instytut Chemii i Elektrochemii Technicznej
ul. Berdychowo 4, 60-965 Poznań
tel. +48 61 665 39 77
e-mail: maciej.p.tobis@doctorate.put.poznan.pl

Poznan, 14.05.2024

Declaration of individual contribution in publications

As the co-author of the following paper, I hereby declare that my contribution to this work was:

Article: *Nanostructured MoS_2 grafted by anthraquinone for energy storage*

Authors: **Maciej Tobis**, Elżbieta Frąckowiak

Journal: Journal of Power Sources

DOI: https://doi.org/10.1016/j.jpowsour.2024.234862-

Contribution: Conceptualization of the article, experiments planning, conducting hydrothermal synthesis of MoS_2, performing grafting reactions, performing physicochemical analyses (Raman spectroscopy, FT-IR spectroscopy, N_2 sorption), outsourced physicochemical data analysis (elemental analysis, XRD, XPS, TEM), electrochemical studies (two and three-electrode cell investigation, b-values, bode plots), data plotting, funding acquisition, writing original draft, writing response to reviewers

M. Tobis

Signature

POLITECHNIKA POZNAŃSKA

Prof. Elżbieta Frąckowiak
Institute of Chemistry and Technical Electrochemistry
Poznan University of Technology, Berdychowo 4
60-965 Poznan, PL +48 61 665 36 32
e-mail: elzbieta.frackowiak@put.poznan.pl

Poznan, 14.05.2024

Declaration of individual contribution in publications

As the co-author of the following paper, I hereby declare that my contribution to this work was:

Article:	*Nanostructured MoS_2 grafted by anthraquinone for energy storage*
Authors:	Maciej Tobis, **Elżbieta Frąckowiak**
Journal:	Journal of Power Sources
DOI:	https://doi.org/10.1016/j.jpowsour.2024.234862
Contribution:	Supervision, conceptualization, methodology, writing (review and editing)

E. Frąckowiak
Signature

POLITECHNIKA POZNAŃSKA
mgr inż. Maciej Tobis
Instytut Chemii i Elektrochemii Technicznej
ul. Berdychowo 4, 60-965 Poznań
tel. +48 61 665 39 77
e-mail: maciej.p.tobis@doctorate.put.poznan.pl

Poznan, 14.05.2024

Declaration of individual contribution in publications

As the co-author of the following paper, I hereby declare that my contribution to this work was:

Article: *Controlling structure and morphology of MoS_2 via sulfur precursor for optimized pseudocapacitive lithium intercalation hosts*

Authors: **Maciej Tobis**, Mennatalla Elmanzalawy, Jaehoon Choi, Elżbieta Frąckowiak, Simon Fleischmann

Journal: Submitted

DOI: -

Contribution: Conceptualization, investigation, methodology, data curation, funding acquisition, writing (original draft)

M. Tobis
Signature

Lille, France

Declaration of individual contribution in publications

As the co-author of the following work, I hereby declare that my contribution to this work was:

Article: *Controlling structure and morphology of MoS_2 via sulfur precursor for optimized pseudocapacitive lithium intercalation hosts*

Authors: Maciej Tobis, **Mennatalla Elmanzalawy**, Jaehoon Choi, Elżbieta Frąckowiak, Simon Fleischmann

Journal: Submitted

DOI: -

Contribution: Investigation, methodology, data curation, writing (review & editing)

Signature

Ulm, May 24, 2024

Declaration of individual contribution in publications

As the co-author of the following work, I hereby declare that my contribution to this work was:

Article:	*Controlling structure and morphology of MoS_2 via sulfur precursor for optimized pseudocapacitive lithium intercalation hosts*
Authors:	Maciej Tobis, Mennatalla Elmanzalawy, **Jaehoon Choi**, Elżbieta Frąckowiak, Simon Fleischmann
Journal:	Submitted
DOI:	-
Contribution:	Investigation, methodology, data curation, writing (review & editing)

Signature

POLITECHNIKA POZNAŃSKA

Prof. Elżbieta Frąckowiak
Institute of Chemistry and Technical Electrochemistry
Poznan University of Technology, Berdychowo 4
60-965 Poznan, PL +48 61 665 36 32
e-mail: elzbieta.frackowiak@put.poznan.pl

Poznan, 14.05.2024

Declaration of individual contribution in publications

As the co-author of the following paper, I hereby declare that my contribution to this work was:

Article:	*Controlling structure and morphology of MoS_2 via sulfur precursor for optimized pseudocapacitive lithium intercalation hosts*
Authors:	Maciej Tobis, Mennatalla Elmanzalawy, Jaehoon Choi, **Elżbieta Frąckowiak**, Simon Fleischmann
Journal:	Submitted
DOI:	-
Contribution:	Conceptualization, writing (review & editing)

E. Frąckowiak

Signature

Ulm, 23.05.2024

Declaration of individual contribution in publications

As the co-author of the following work, I hereby declare that my contribution to this work was:

Article:	*Controlling structure and morphology of MoS_2 via sulfur precursor for optimized pseudocapacitive lithium intercalation hosts*
Authors:	Maciej Tobis, Mennatalla Elmanzalawy, Jaehoon Choi, Elżbieta Frąckowiak, **Simon Fleischmann**
Journal:	Submitted
DOI:	-
Contribution:	Conceptualization, methodology, data curation, funding acquisition, writing (original draft, review & editing)

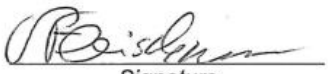

Signature

Copyrights

P1. *Electrochemical Capacitor Performance of Nanotextured Carbon/Transition Metal Dichalcogenides Composites*

Authors: Elżbieta Frąckowiak, Masoud Foroutan Koudahi, Maciej Tobis

Journal: Small, 2021, 17, 2006821

DOI: https://doi.org/10.1002/smll.202006821

License: The content is available under CC BY 4.0

Copyrights statement: Available

Electrochemical Capacitor Performance of Nanotextured Carbon/Transition Metal Dichalcogenides Composites

Author: Elżbieta Frąckowiak, Masoud Foroutan Koudahi, Maciej Tobis

Publication: Small

Publisher: John Wiley and Sons

Date: Mar 19, 2021

© 2021 The Authors. Small published by Wiley-VCH GmbH

Open Access Article

This is an open access article distributed under the terms of the Creative Commons CC BY license, which permits unrestricted use, distribution, and reproduction in any medium, provided the original work is properly cited.

You are not required to obtain permission to reuse this article.

For an understanding of what is meant by the terms of the Creative Commons License, please refer to Wiley's Open Access Terms and Conditions.

Permission is not required for this type of reuse.

Wiley offers a professional reprint service for high quality reproduction of articles from over 1400 scientific and medical journals. Wiley's reprint service offers:

- Peer reviewed research or reviews
- Tailored collections of articles
- A professional high quality finish
- Glossy journal style color covers
- Company or brand customisation
- Language translations
- Prompt turnaround times and delivery directly to your office, warehouse or congress.

Please contact our Reprints department for a quotation. Email corporatesaleseurope@wiley.com or corporatesalesusa@wiley.com or corporatesalesDE@wiley.com.

© 2024 Copyright - All Rights Reserved | Copyright Clearance Center, Inc. | Privacy statement | Data Security and Privacy | For California Residents | Terms and ConditionsComments? We would like to hear from you. E-mail us at customercare@copyright.com

P2. *Supercapacitors with Carbon/MoS_2 Composites*

Authors: Maciej Tobis, Sylwia Sroka, Elżbieta Frąckowiak

Journal: Frontiers in Energy Research, 2021, 9, 647878

DOI: https://doi.org/10.3389/fenrg.2021.647878

License: The content is available under CC BY 4.0

Copyrights statement: Available

Frontiers Copyright Statement

Frontiers publishes its own journals (referred to here as **Frontiers Journals**) and journals owned by third parties (referred to here as **Hosted Journals**). When we refer to **Journals**, we include both Frontiers Journals and Hosted Journals.

In this Copyright Statement, **Websites** (with a capitalised W) refers to all Frontiers websites, including those of Hosted Journals. An **Owner** means Frontiers as owner of all Frontiers Journals, or the respective owner of a Hosted Journal.

All content included on these Websites (including Loop), such as text, graphics, logos, button icons, images, video/audio clips, downloads, data compilations and software, is the property of the person or entity who or which owned it prior to submission to Frontiers or to a Hosted Journal. If not owned by Frontiers or an Owner of a Hosted Journal, it is licensed to Frontiers Media SA ("Frontiers"), such Owner or its or their licensees and/or subcontractors.

The ownership of copyright in the text of individual articles (including research articles, opinion articles, book reviews, conference proceedings and abstracts) is not affected by its submission to or publication by Frontiers, whether for itself or for a Hosted Journal. Frontiers benefits from a general licence over all content submitted. Hosted Journal Owners benefit from a general licence over all content submitted to their respective Hosted Journals. Frontiers, Hosted Journal Owners and all their users benefit from a **Creative Commons CC-BY licence** over all content, as specified below.

Images and graphics not forming part of user-contributed materials are the property of or are licensed to Frontiers and may not be downloaded or copied without Frontiers' explicit and specific permission or in accordance with any specific copyright notice attached to that material.

The combination of all content on Frontiers websites, and the look and feel of the Frontiers websites, is the property of Frontiers Media SA.

As an author or contributor you grant permission to others to reproduce your articles, **including any graphics and third-party materials supplied by you**, in accordance with the Frontiers Terms and Conditions. The licence granted to third parties over all contents of each article, including third-party elements, is a Creative Commons Attribution ("CC BY") licence. The current version is CC-BY, version 4.0 (http://creativecommons.org/licenses/by/4.0/), and the licence will automatically be updated as and when updated by the Creative Commons organisation.

You may include a requirement to reproduce copyright notices but you may not restrict the right to reproduce the entire article, including third-party graphics. This means that you must obtain any necessary third-party consents and permissions to reproduce third-party materials in your articles submitted to Frontiers.

E-books are subject to the same licensing conditions as the articles within them.

Articles published prior to 25th May 2018: Please note that reproduction of third-party graphics and other third-party materials contained in articles published prior to 25th May 2018 may be subject to third-party notices prohibiting their reproduction without permission. You must comply with those notices.

Articles published prior to July 2012: The licence granted for these articles may be different and you should check the pdf version of any article to establish what licence was granted. If an article carries only a non-commercial licence and you wish to obtain a commercial licence, please contact Frontiers at editorial.office@frontiersin.org.

Article metadata, as defined in Frontiers' terms and conditions, are the property of Frontiers or the Owner of the respective Hosted Journal, and are licensed under Creative Commons CC0 terms.

All software used on this site, and the copyright in the code constituting such software, and all intellectual property in all such elements, is the property of or is licensed to Frontiers and its use is restricted in accordance with the Frontiers Terms and Conditions. All copyright, and all rights therein, are protected by national and international copyright laws.

Please also see the Frontiers Terms and Conditions.

Copyright Statement updated with effect from 16th December 2020.

P3. *Electrochemical Capacitor Based on Reduced Graphene Oxide/NiS_2 Composite*

Authors: Andrii Kachmar, Maciej Tobis, Elżbieta Frąckowiak

Journal: ChemElectroChem, 2022, 9, e202200834

DOI: https://doi.org/10.1002/celc.202200834

License: The content is available under CC BY 4.0

Copyrights statement: Available

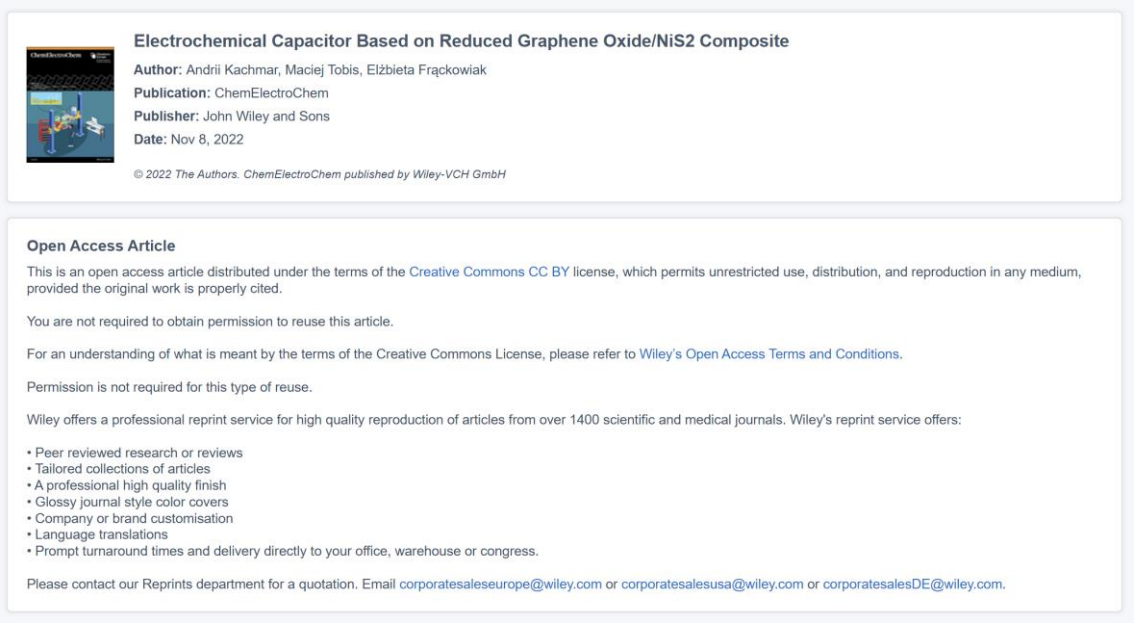

Electrochemical Capacitor Based on Reduced Graphene Oxide/NiS2 Composite

Author: Andrii Kachmar, Maciej Tobis, Elżbieta Frąckowiak

Publication: ChemElectroChem

Publisher: John Wiley and Sons

Date: Nov 8, 2022

© 2022 The Authors. ChemElectroChem published by Wiley-VCH GmbH

Open Access Article

This is an open access article distributed under the terms of the Creative Commons CC BY license, which permits unrestricted use, distribution, and reproduction in any medium, provided the original work is properly cited.

You are not required to obtain permission to reuse this article.

For an understanding of what is meant by the terms of the Creative Commons License, please refer to Wiley's Open Access Terms and Conditions.

Permission is not required for this type of reuse.

Wiley offers a professional reprint service for high quality reproduction of articles from over 1400 scientific and medical journals. Wiley's reprint service offers:

- Peer reviewed research or reviews
- Tailored collections of articles
- A professional high quality finish
- Glossy journal style color covers
- Company or brand customisation
- Language translations
- Prompt turnaround times and delivery directly to your office, warehouse or congress.

Please contact our Reprints department for a quotation. Email corporatesaleseurope@wiley.com or corporatesalesusa@wiley.com or corporatesalesDE@wiley.com.

P4. *Nanostructured MoS_2 grafted by anthraquinone for energy storage*

Authors: Maciej Tobis, Elżbieta Frąckowiak

Journal: Journal of Power Sources, 2024, 613, 234862

DOI: https://doi.org/10.1016/j.jpowsour.2024.234862

License: The content is available under CC BY 4.0

Copyrights statement: Available

Nanostructured MoS2 grafted by anthraquinone for energy storage

Author: Maciej Tobis,Elżbieta Frąckowiak

Publication: Journal of Power Sources

Publisher: Elsevier

Date: 1 September 2024

© 2024 The Authors. Published by Elsevier B.V.

Creative Commons

This is an open access article distributed under the terms of the Creative Commons CC-BY license, which permits unrestricted use, distribution, and reproduction in any medium, provided the original work is properly cited.

You are not required to obtain permission to reuse this article.

To request permission for a type of use not listed, please contact Elsevier Global Rights Department.

Are you the author of this Elsevier journal article?

5. *Controlling structure and morphology of MoS_2 via sulfur precursor for optimized pseudocapacitive lithium intercalation hosts*

Authors: Maciej Tobis, Mennatalla Elmanzalawy, Jaehoon Choi, Elżbieta Frąckowiak, Simon Fleischmann

Journal: publicly accessible as a preprint, sent for review

DOI: https://doi.org/10.26434/chemrxiv-2024-7hz4h

License: The content is available under CC BY 4.0